

ISSN en trámite



Geofísica Internacional

Revista Trimestral Publicada por el Instituto de Geofísica de la
Universidad Nacional Autónoma de México



México

Volume 51 Number 3
July - September
2012

— Geofísica Internacional —

Dr. José Francisco Valdés Galicia
Director of Instituto de Geofísica

Dr. Avto Gogichaishvili
President of Unión Geofísica Mexicana

Editor Chief

Dr. Servando De la Cruz-Reyna
Instituto de Geofísica, UNAM
sdelacrr@geofisica.unam.mx

Technical Editor

Mtra. Andrea Rostan Robledo
Instituto de Geofísica, UNAM
arostan@igeofisica.unam.mx

Editorial Board

Donald Bruce Dingwell
Earth and Environment
Ludwig Maximilian University of Munich,
Germany

Eric Desmond Barton
Departamento de Oceanografía
Instituto de Investigaciones Marinas, Spain

Jorge Clavero
Amawta Consultores, Chile

Gerhardt Jentzsch
Institut für Geowissenschaften
Friedrich-Schiller-Universität Jena, Germany

Peter Malischewsky
Institut für Geowissenschaften
Friedrich-Schiller-Universität Jena, Germany

François Michaud
Géosciences Azur
Université Pierre et Marie Curie, France

Olga Borisovna Popovicheva
Scobeltzine Institute of Nuclear Physics
Moscow State University, Rusia

Jaime Pous
Facultad de Geología
Universidad de Barcelona, Spain

Joaquín Rui
UA Science
University of Arizona, United States

Angelos Vourlidas
Solar Physics Branch
NASA Goddard Space Flight Center, United States

Théophile Ndougsa Mbarga
Department of Physics
University of Yaounde I, Cameroon

Associate Editors
José Agustín García Reynoso
Atmospheric Science Centro de Ciencias de la
Atmósfera UNAM, Mexico

Tereza Cavazos
Atmospheric Science
Departamento de Oceanografía Física CICESE,
Mexico

Dante Jaime Morán-Zenteno
Geochemistry
Instituto de Geología, UNAM, Mexico

Margarita López
Geochemistry
Instituto de Geología UNAM, Mexico

Avto Gogichaisvili
Geomagnetism And Paleomagnetism
Instituto de Geofísica UNAM, Mexico

Jaime Urrutia-Fucugauchi
Geomagnetism And Paleomagnetism
Instituto de Geofísica, UNAM, Mexico

Felipe I. Arreguín Cortés
Hydrology
Instituto Mexicano de Tecnología del Agua IMTA,
Mexico

William Lee Bandy
Marine Geology And Geophysics
Instituto de Geofísica UNAM, Mexico

Fabian García-Nocetti
**Mathematical And Computational
Modeling**
Instituto de Investigaciones en Matemáticas
Aplicadas y en Sistemas UNAM, Mexico

Graciela Herrera-Zamarrón
Mathematical Modeling
Instituto de Geofísica, UNAM, Mexico

Ismael Herrera Revilla
**Mathematical And Computational
Modeling**
Instituto de Geofísica UNAM, Mexico

Rene Chávez Segura
Near-Surface Geophysics
Instituto de Geofísica UNAM, Mexico

Juan García-Abdeslem
Near-Surface Geophysics
División de Ciencias de la Tierra CICESE, Mexico

Alec Torres-Freyermuth
Oceanography
Instituto de Ingeniería, UNAM, Mexico

Jorge Zavala Hidalgo
Oceanography
Centro de Ciencias de la Atmósfera UNAM,
Mexico

Shri Krishna Singh
Seismology
Instituto de Geofísica, UNAM, Mexico

Xyoli Pérez-Campos
Seismology
Servicio Sismológico Nacional, UNAM, Mexico

Blanca Mendoza Ortega
Space Physics
Centro de Ciencias de la Atmósfera, UNAM,
Mexico

Inez Staciari Batista
Space Physics
Pesquisador Senior Instituto Nacional de Pesquisas
Espaciais, Brazil

Roberto Carniel
Volcanology
Laboratorio di misure e trattamento dei segnali
DPIA - Università di Udine, Italy

Miguel Moctezuma-Flores
Satellite Geophysics
Facultad de Ingeniería, UNAM, Mexico

Assistance

Elizabeth Morales Hernández,
Management
eliedit@igeofisica.unam.mx



GEOFÍSICA INTERNACIONAL, Año 51, Vol. 51, Núm. 3, julio - septiembre de 2012 es una publicación trimestral, editada por la Universidad Nacional Autónoma de México, Ciudad Universitaria, Alcaldía Coyoacán, C.P. 04150, Ciudad de México, a través del Instituto de Geofísica, Circuito de la Investigación Científica s/n, Ciudad Universitaria, Alcaldía Coyoacán, C.P. 04150, Ciudad de México, Tel. (55)56 22 41 15. URL: <http://revistagi.geofisica.unam.mx>, correo electrónico: revistagi@igeofisica.unam.mx. Editora responsable: Andrea Rostan Robledo. Certificado de Reserva de Derechos al uso Exclusivo del Título: 04-2022-081610251200-102, ISSN: en trámite, otorgados por el Instituto Nacional del Derecho de Autor (INDAUTOR). Responsable de la última actualización Saúl Armendáriz Sánchez, Editor Técnico. Fecha de la última modificación: 30 de junio 2012, Circuito de la Investigación Científica s/n, Ciudad Universitaria, Alcaldía Coyoacán, C.P. 04150, Ciudad de México.

El contenido de los artículos es responsabilidad de los autores y no refleja el punto de vista de los árbitros, del Editor o de la UNAM. Se autoriza la reproducción total o parcial de los textos siempre y cuando se cite la fuente completa y la dirección electrónica de la publicación.



Esta obra está bajo una Licencia Creative Commons Atribución-NoComercial-SinDerivadas 4.0 Internacional.

Contents

Mass changes from GRACE data in Argentina. A preliminary qualitative analysis.

Ayelen Pereira, María Cristina Pacino, Rene Forsberg

199

Radial S wave velocity structure of the D'' region under a spot of the east central Pacific Ocean.

Luis F. Terán-Mendieta., Raúl. W. Valenzuela

207

Using subsurface geophysical methods in flood control: A resistivity survey to define underground storage capacity of a sand body in ciudad Juárez, Mexico. Oscar S. Dena O., Griselda Obeso.

C., Jesús E. Leyva, Miguel Domínguez A., E. Rascon., Francisco. Gómez, D- Doser.

225

Exploration of subsoil structure in Mexico city using correlation of micrometremors.

Francisco. J. Chávez-García, Jorge Aguirre.

251

Vertical structure of tidal flows at the entrance to Guaymas Bay, Mexico.

José Gómez-Valdés., Heriberto J. Vázquez.

271

Shallow travel-time tomography below southern Mexico.

Eduardo Huesca-Pérez, Allen Husker

281

Trace elements geochemistry and origin of volcanic units from the San /XLV.

Alfredo Aguillón Robles., Margarito Tristán González, Rubén Alfonso López Doncel, María Elena García Arreola, Joselin de Lourdes Almaguer Rodríguez., René C. Maury.

Mass changes from GRACE data in Argentina. A preliminary qualitative analysis

Ayelen Pereira*, María Cristina Pacino and Rene Forsberg

Received: May 05, 2010; accepted: March 07, 2011; published on line: June 29, 2012

Resumen

Las misiones satelitales gravimétricas introducen un nuevo concepto en el modelado del campo gravitacional, ya que proveen valiosa información acerca del comportamiento geodinámico de nuestro planeta. La misión satelital GRACE permite obtener variaciones del campo de gravedad para una región determinada; además, estos cambios pueden relacionarse con el almacenamiento de agua y con el rebote postglacial, por ejemplo.

El objetivo de este trabajo es mostrar las variaciones temporales del campo de gravedad detectadas en Argentina, provistas por los cuatro centros de procesamiento GRACE: CSR, JPL, GFZ y BGI. Todas las soluciones detectaron cambios de masas significativos en la región; sin embargo, existen algunas diferencias entre los cuatro centros de procesamiento de GRACE. Los mapas de tendencia y amplitud de la gravedad para el período 2002- 2008 muestran tres zonas de variaciones importantes: en la Patagonia, en la Cuenca del Plata y en la Cordillera de los Andes. Los cambios de gravedad en las dos primeras regiones están relacionados principalmente con la redistribución de agua continental; y en la tercera, con movimientos sísmicos. Asimismo, se muestran para las tres áreas los perfiles con las variaciones de tendencia y amplitud de la gravedad.

Palabras clave: GRACE, almacenamiento de agua, cambios de masa.

Abstract

Gravimetric satellite missions have introduced a new concept in gravitational field modeling, providing valuable information about the geodynamic behavior of our planet. The GRACE satellite mission allows obtaining monthly variations of the gravity field for a certain region; furthermore, in particular these changes can be related to terrestrial water storage and postglacial rebound, for example.

The aim of this work is to analyze the temporal variation of the gravity field as measured over Argentina, provided by four different GRACE processing centers: CSR, JPL, GFZ and BGI. All the solutions detected the significant mass changes of the area, though there are some discrepancies between the four GRACE processing centers. Gravity trend as well as amplitude maps of these variations for the period 2002- 2008 show important features in three zones: Patagonia, La Plata basin, and the Andes Mountain chain. The gravity changes in the first two areas are mainly related to the continental water redistribution; and in the third one, with seismic movements. Also, the profiles over the three areas with the gravity trend and amplitude variations are shown.

Key words: GRACE, water storage, mass changes.

A. Pereira*
Facultad de Ciencias Exactas
Ingeniería y Agrimensura
Universidad Nacional de Rosario- CONICET
Av. Pellegrini 250, 3º- Rosario
Argentina
**Corresponding author: apereira@fceia.unr.edu.ar*

M.C. Pacino
Facultad de Ciencias Exactas
Ingeniería y Agrimensura
Universidad Nacional de Rosario- CONICET
Av. Pellegrini 250, 3º- Rosario
Argentina

R. Forsberg
National Space Institute
Technical University of Denmark
Juliane Maries vej 30, Building Rockefeller
Office/Room 269
Denmark.

Introduction

The practical use of the theories elaborated a century ago for the study of the Earth by Gauss, Molodensky and Stokes, among others, (Heiskanen and Moritz, 1985; Torge, 2001) was only possible once the advance of satellite technology and computing tools enabled it. In practical specific applications, having a geoid model allows us to use an algorithm from which ellipsoidal heights can be transformed into orthometric heights.

Many countries, including Argentina, are encouraging the investigation and computing of Geoid Models mainly because of the increasing use of GNSS (Global Navigation Satellite Systems) technology. Besides, many geological and geophysical applications demand knowledge of the terrestrial gravity field. Basically, this demand is concentrated in engineering, mining and petroleum companies.

Recent gravity satellite campaigns represent a tool to improve several applications related to the gravity field modeling; moreover, they provide valuable information about the geodynamic behavior of our planet since they offer monitoring the temporal variations of the gravity field (Reigber *et al.*, 2005; Rodell *et al.*, 2007).

GRACE (Gravity Recovery And Climate Experiment) mission can map the mass distribution by measuring the changes in the Earth's gravity field. Most of the monthly gravity changes detected by this mission can be associated with the variations in terrestrial water storage, which includes hydrological reservoir changes, groundwater, soil moisture, lakes, streams, snow, ice and glaciers (Ramillien *et al.*, 2005; Velicogna and Wahr, 2005, 2006). A few years ago, these studies were achieved from ground measurements, obtaining results of low precision and for small areas. Temporal and spatial variations of water storage in large areas (a river basin, a glacier, for example) are difficult to analyze from ground measurements because of its size. With the present development of technologies represented by GRACE mission it is possible to detect the monthly spatial changes in the distribution of water masses in these regions. Furthermore, GRACE can map water storage changes to a height of about 1 centimeter for areas ranging in size on the order of 400 km.

The La Plata Basin is one of the largest in the world, with an area of 3,100,000 km², which is equivalent to the 17% of South America's surface. This basin covers 5 countries: Brazil (1,415,000 km²), Argentina (920,000 km²), Paraguay (410,000 km²), Bolivia (205,000 km²), and Uruguay (150,000 km²).

The main rivers in Argentina that are part of this hydrographic system are the Paraná (its basin is the largest one with an area of 1,510,000 km² and a longitude of 4,000 km), Uruguay and Paraguay.

Also in the La Plata basin lies a large part of the second fresh groundwater reservoir of the world (the Guaraní Water-bearing System), thus the knowledge of its behavior is of extreme importance for being an important environmental, economic and strategic resource.

The Patagonia is located in the southernmost part of Argentina, between 40° and 56° of South latitude. This region is characterized by the presence of a big continental ice extension (the third greater of the world after the Antarctica and Greenland), located in the "Andes Patagónicos" in the border between Argentina and Chile. The continental ice extends throughout 350 km and 49 glaciers descend from them. In Argentina, they have an extension of 3,000 km².

At present, GRACE data is a remarkable tool to study and quantify the variations related to climate change, like the regression of the glaciers in the south of Argentina and the water redistribution in the Paraná River basin and in the Guaraní Water-bearing System.

In this paper, the mass changes for Argentina obtained from different processing centers are shown and compared, analyzing the possible causes of the variations and showing that GRACE mission can actually detect the glaciological and hydrological changes.

Data and methods

Study area

Argentina is the second largest country in South America, with an area of 2,766,891.2 km², and is located between 20° and 56° South Latitude and 53° and 74° West Longitude. It comprises different geological and physiographical areas, presenting mainly plains at the eastern region, hills in the center and mountains at the West (Figure 1). The country is limited at its western extreme by the Andes Mountain chain. The physiography is diverse, with heights ranging from -100 to 7,000 m approximately; the highest point is located at Cerro Aconcagua with 6,962 m above sea level, and the lowest is at Laguna del Carbón (105 m below sea level).

The continental territory includes four major geological regions: the Patagonian massif -a Precambrian basement-; the Andes System -caused by the Andean bending-; the Brazilian massif -Precambrian basement-; and the Pampa

Plain comprising marine and volcanic sediments (Gentili *et al.*, 1980).

The major rivers in Argentina are the Paraná, Uruguay, Paraguay, Bermejo, Pilcomayo, Colorado, Salado and La Plata. Also, there are several lakes, like the Argentino and Viedma; and numerous reservoirs created by dams, like the Esteros del Iberá.

GRACE data

Before this new gravity satellite mission era, the long wavelength of the Earth gravity field was obtained from the tracking measurement of satellites orbiting our planet. These measurements had varied quality and quantity, and had a low geographical coverage density. Therefore, the accuracy and precision of the gravity models that had come up this way was limited and only the important geophysical features of the Earth's structure could be detected. But in the last few years, this scenario has changed and a great advance has been achieved concerning the knowledge of the terrestrial gravity field, thanks to the combined use of GPS (Global Positioning System) receivers, accelerometers and gradiometers.

The successful launching of CHAMP (CHALLENGING Mini-satellite Payload) in 2001 and GRACE in 2002 marked the beginning of a new age in satellite gravimetry (Wahr *et al.*, 1998; Beutler, 2004).

In the present investigation, the GRACE Level-2 data from four processing centers were analyzed and compared to determine the gravity trend and amplitude in Argentina for the period 2002-2008.

GRACE Level-2 data consists of monthly spherical expansions of the Earth's gravity field. Each solution is represented by a set of harmonic coefficients up to a defined order and degree (Bettadpur, 2007).

The data used in this investigation were provided by four processing centers: UTCSR (University of Texas, Center for Space Research), GFZ (GeoForschung Zentrum, Potsdam), JPL (Jet Propulsion Laboratory, NASA) and BGI (Bureau Gravimétrie International, France)¹.

In this research, the following data were used: the released 4 (RL04) from UTCSR and GFZ, the release 4.1 from JPL, and the version 1 from BGI.

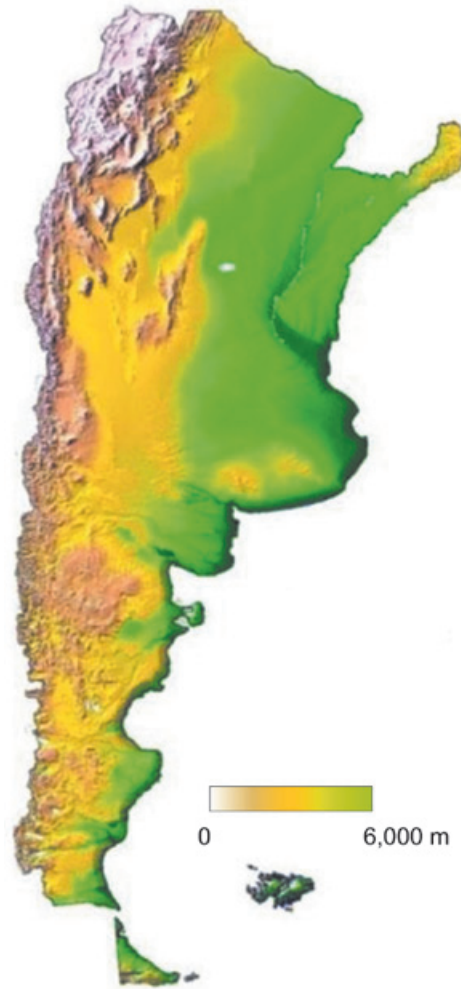


Figure 1. Argentina relief map (Argentinean National Water Information System, 2003).

The CSR RL04 solutions are complete to degree and order 60 in terms of spherical harmonic expansions, the ones from GFZ RL04 and JPL RL04.1, to 120; and the data sets of the BGI, to 50.

The time period used in this study spans from January 2002 to December 2008. The data were filtered by truncating the coefficients at degree and order 30 and by doing the calculation at satellite altitude (500 km). This was made to allow a fair comparison and to reduce the uncertainties of the GRACE data in the higher order coefficients (Forsberg and Reeh, 2006; Sandberg Sørensen and Forsberg, 2010).

¹ These solutions are now computed by the GRGS- CNES (Groupe de Recherche de Géodésie Spatiale, Centre National d'Études Spatiales, Toulouse).

The time- variability of each set is represented by a sequence of 30 days approximately, except for the BGI solutions, where the data are provided every 10 days and are based on the running average of three 10-day periods (Lemoine *et al.*, 2007, 2008). The resulting epochs for each center were 71 for UTCSR, 63 for GFZ, 70 for JPL and 202 for BGI. For the first three data sets, the months June- July of 2002 and June 2003 are missing due to the missing accelerometer data.

Method and results

In general, the trend, amplitude and phase of a time-dependent function can be defined as:

$$x(t) = a + b \cdot t + c \cdot \cos(t) + d \cdot \sin(t) \tag{1}$$

where *b.t* is the trend and it is represented by the slope of the function *x(t)*; and *a* is the origin ordinate.

From (1) the amplitude *A* of the variable and its corresponding phase ϕ would be:

$$c \cdot \cos(t) + d \cdot \sin(t) = A \cos(\phi + t) \tag{2}$$

Where

$$A^2 = c^2 + d^2, \quad \phi = \tan^{-1}(c/d) \tag{3}$$

The first step is to determine the change of the monthly gravity fields, δ_g , in time, which is done by a 4-parameter trend analysis of the gravity disturbances. A bias (*a*), trend (*b.t*) and two yearly seasonal terms (*c.cos t*; *d.sin t*) are estimated in each grid point defined for Argentina, where the amplitude is a combination of *c* and *d* (3). The solutions were processed with software specially developed for GRACE by the National Space Institute, Technical University of Denmark. Finally, the gravity trend and amplitude for the 4 centers, for the period from August 2002 to May 2008 were obtained (Forsberg and Reeh, 2006) with:

$$\delta_g(t) = a + b \cdot t + c \cdot \cos(t) + d \cdot \sin(t) \tag{4}$$

The resulting gravity trends (in μGal per year) and amplitudes (in μGal per year) at satellite altitude (500 km), based on the CSR, JPL, GFZ and BGI epochs respectively, are shown in Figures 2 and 3.

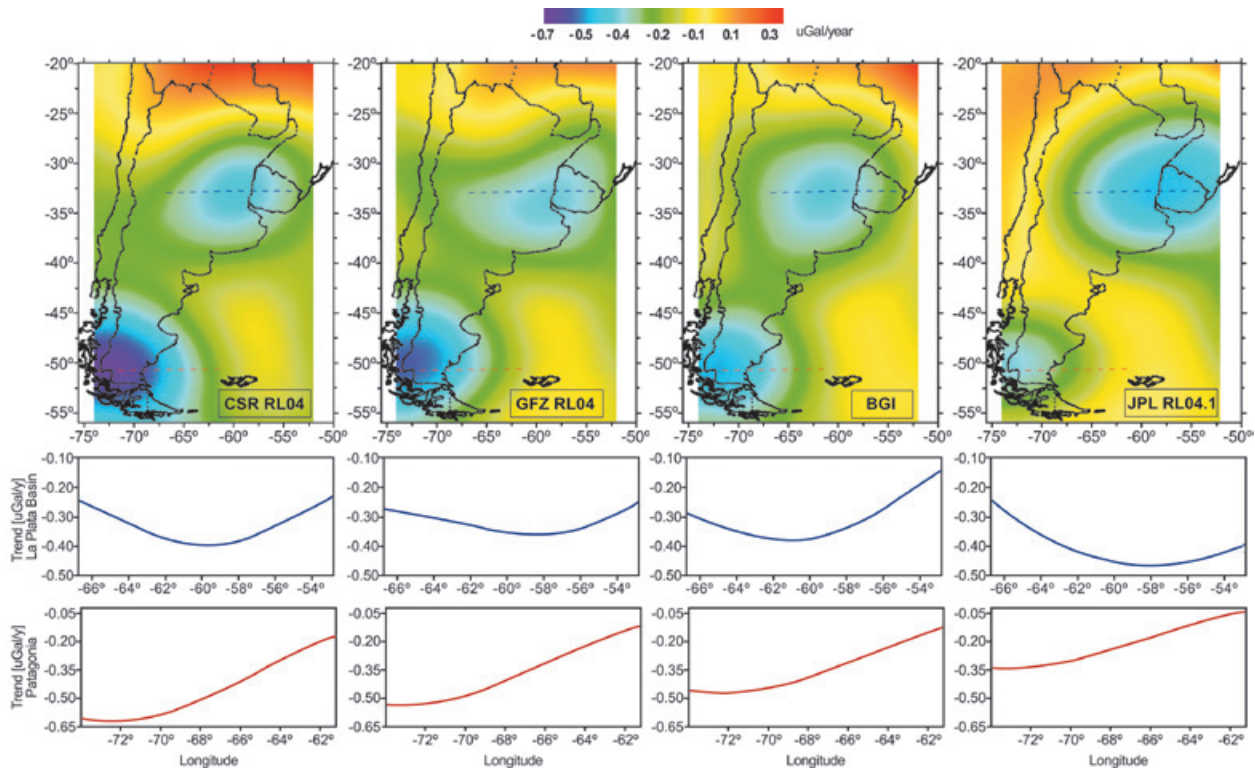


Figure 2. Above: Gravity trends in Argentina from August 2002 to May 2008, given in μGal per year, from the data of the four processing centers. Below: Gravity trend profiles over the La Plata Basin (blue) and the Patagonia (red), from the data of the four processing centers.

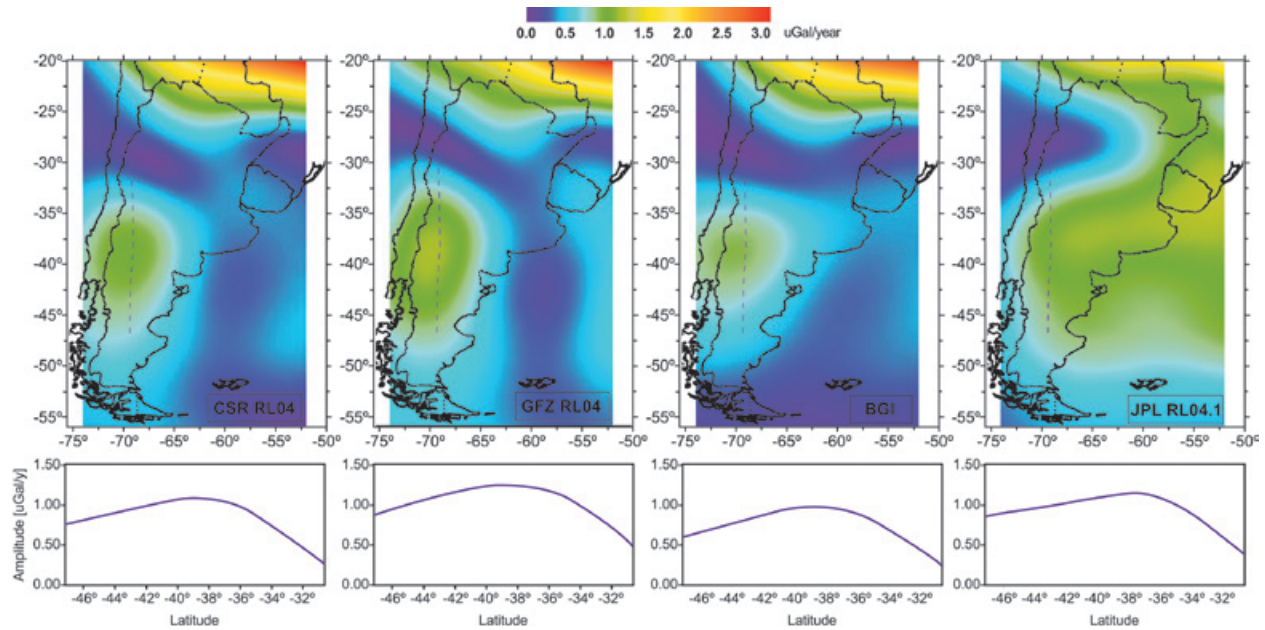


Figure 3. Above: Gravity amplitude in Argentina from August 2002 to May 2008, given in μGal per year, from the data of the four processing centers. Below: Gravity amplitude profiles over the central Andes Mountain chain, from the data of the four processing centers.

The gravity trend maps for Argentina from August 2002 to May 2008, given in μGal per year, from the data of the four processing centers are presented in Figure 2 (above).

The trend plots indicate some differences among the GRACE solutions, but they do agree on a negative trend over two regions, indicating a significant mass loss.

The first one is located in the Patagonian Ice Field. The mass changes detected in this area correspond with the water, ice and snow redistribution. The second one is located in the La Plata basin. In this area, the significant gravity trend variations are mainly related to seasons, drought and flood periods, and at inter-annual scales, with phenomena like El Niño and La Niña (Berbery and Barros, 2002).

Also in Figure 2 (below), the gravity trend profiles over the La Plata Basin and the Patagonia, from the data of the four processing centers, showing the maximum and minimum values reached for each center, are presented.

In Figure 3 (above) the gravity amplitude maps for Argentina from August 2002 to May 2008, given in μGal per year, from the data of the four processing centers, are shown. It can be detected an important gravity amplitude

change in the middle-west part of Argentina, in coincidence with a region of large earthquakes. Gravity amplitude profiles over the central Andes Mountain chain, from the data of the four processing centers, are presented also in Figure 3 (below).

Analyzing the amplitude and trend maps and profiles, the solutions from the JPL is the one that always presents the greatest differences in relation to the others centers. The analysis centers follow different data pre-processing, processing and post-processing strategies, which cause differences in the sets of spherical harmonic coefficients (Klees *et al.*, 2008).

The gravity trend and amplitude statistics can be found in Table 1, which shows that the amplitude ranges from a minimum of 0.040 (BGI) to a maximum of 3.149 (GFZ) μGal per year; and for the trend the values varies from -0.479 (BGI) to 0.281 (CSR) μGal per year.

These results show that the research in Argentina should be extended and the detected mass changes should be validated with hydrological and glacial models, climatic data (temperature, rainfall records) and satellite images series. Also, in a next stage, the variations detected will be estimated in km^3/year of water equivalent.

Table.1. Gravity amplitude and gravity trend statistics, in μGal per year, for Argentina from August 2002 to May 2008 from the data of the four processing centers.

	AMPLITUDE [$\mu\text{Gal}/\text{y}$]			TREND [$\mu\text{Gal}/\text{y}$]		
	Min.	Max.	Mean	Min.	Max.	Mean
CSR	0.063	3.126	0.614	-0.620	0.281	-0.180
GFZ	0.057	3.149	0.660	-0.543	0.151	-0.183
BGI	0.040	2.987	0.562	-0.479	0.278	-0.168
JPL	0.112	1.966	0.848	-0.460	0.127	-0.141

Conclusions

Comparing the results obtained from the four processing centers, the JPL is the one that shows the highest differences for both trend and amplitude variables. The estimated trend and amplitude values are slightly different but the same pattern could be found in the results from the four processing centers, except for JPL amplitude. GRACE products differences are currently being studied in terms of resolution and pre-processing.

From the amplitude figures, an important variation can be seen in the Andes Mountain chain, in an area of oil exploitation and exploration, and also in the north part of the country.

It can be concluded from the analysis of the trend figures that significant mass changes could be detected in two areas in particular: the main one in the glaciers zone in the Patagonia, and the other one corresponding to the La Plata Basin.

There is a clear negative trend (maximum absolute value of $0.25 \mu\text{Gal}$ per year approximately) in the La Plata Basin and another one at the Patagonian Ice Field (maximum absolute value of $0.63 \mu\text{Gal}$ per year approximately). The first one can be related to the Paraná River behavior and the seasonal variations in the basin area that are being affected by extreme weather events. The second variation can be associated with the water, snow and ice redistribution, among others, and partly also by the climatic change that is generating a great regression and loss of mass in most of the Patagonian glaciers. Moreover, the connection between ice mass loss and postglacial rebound signal can be derived from that.

These patterns agree with other preliminary results that are still under study, like altimetry from ENVISAT and equivalent water change grids derived from NASA and GRGS- CNES (Andersen *et al.*, 2008; Pereira, 2011; Pereira *et al.*, 2012).

Acknowledgements

This paper was partially supported by PICT-01590 (ANPCyT).

Bibliography

- Argentinean National Water Information System. Maps and data of Argentina. Available at <http://www.hidricosargentina.gov.ar/InformacionHidrica.html>. July 2003.*
- Andersen O., Berry P., Freeman J., Lemoine F.G., Lutsckhe S., Jakobsen F., Butts M., 2008, Satellite altimetry and GRACE gravimetry for studies of the annual water storage variations in Bangladesh. *Terr. Atmos. Ocean. Sci.*, 19: 47-52.
- Berbery E.H., Barros V.R., 2002, The hydrologic cycle of the La Plata Basin in South America. *J. Hydrometeorology*, 3:630-645.
- Beutler G., 2004, Revolution in Geodesy and Surveying. *FIG Article*, July 2004, pp. 19.
- Bettadpur S., 2007, Level-2 Gravity Field Product User Handbook (Rev. 2.3, February 20, 2007), Center for Space Research, University of Texas at Austin.
- Forsberg R., Reeh N., 2006, Mass change of the Greenland ice sheet from GRACE. *Proc. First Meeting of the International Gravity Field Service: Gravity Field of the Earth 2006*, Springer Verlag.
- Gentili C., Rimoldi H., Di Gregorio J., Ullana M., González Díaz E., Nullo F., Riccardi A., Rolleri E., Russo A., Fabres M., Di Benedetto H., Stepancic P., Methol E., Caminos R., Leste P., Perello R., Theabli W., 1980, *Geología Regional Argentina*. Vol I-II. Academia Nacional de Ciencias.
- Heiskanen W.A., Moritz H., 1985, *Geodesia Física*. Ed. Instituto Geográfico Nacional- Instituto de Astronomía y Geodesia, Madrid. 371 pp.
- Klees R., Liu X., Wittwer T., Gunter B.C., Revtova E.A., Tenzer R., Ditmar P., Winsemius H.C., Savenije H.H.G., 2008, A Comparison of Global and Regional GRACE Models for Land Hydrology. *Survey Geophysics*, 29: 335-359, doi: 10.1007/s10712-008-9049-8.
- Lemoine J.M., Bruinsma S.L., Biancale R., 2008, 10-day gravity field solutions inferred from GRACE data. *Proc. IAG International Symposium on Gravity, Geoid and Earth Observation 2008*.

- Lemoine J.-M., Bruinsma S., Loyer S., Biancale R., Marty J.-C., Perosanz F., Balmino G., 2007, Temporal gravity field models inferred from GRACE data. *Advances in Space Research* 39 (2007) 1620-1629, doi:10.1016/j.asr.2007.03.062.
- Pereira A., 2011, Estudio comparativo de modelos de geopotencial y análisis geodinámico de las variaciones temporales del campo gravitacional para la Argentina. PhD thesis presented in the National University of Rosario, Argentina.
- Pereira A., Miranda S., Pacino M.C., Forsberg R., 2012, Water storage changes from GRACE data in the La Plata Basin. *IAG Series: Geodesy for Planet Earth* 136 (2012) 613-618, doi: 10.1007/978-3-642-20338-1_75, - Springer Berlin Heidelberg Ed.
- Ramillien G., Frappart F., Cazenave A., Güntner A., 2005, Time variations of land water storage from an inversion of 2 years of GRACE geoids. *Earth and Planetary Science Letters*, 283- 301.
- Reigber C., Jochmann H., Wunsch J., Petrovic S., Schwintzer P., Barthelmes F., Neumayer K.-H., König R., Förste Ch., Balmino G., Biancale R., Lemoine J.-M., Loyer S., Perosanz F., 2005, Earth Gravity Field and Seasonal Variability from CHAMP. In: *Reigber, Ch., Lühr, H., Schwintzer, P., Wickert, J. (eds.)*, 2004. Earth Observation with CHAMP - Results from Three Years in Orbit, Springer, Berlin, 25-30.
- Rodell M., Chen J., Kato H., Famiglietti J.S., Nigro J., Wilson C.R., 2007, Estimating groundwater storage changes in the Mississippi River basin (USA) using GRACE. *Hydrogeology Journal*, 15: 159- 166.
- Sandberg Sørensen L., Forsberg R., 2010, Greenland Ice Sheet Mass Loss from GRACE Monthly Models. Proc. IAG Symposium on Gravity, Geoid and Earth Observation, (135), Part 7, 527-532, doi: 10.1007/978-3-642-10634-7_70, Springer.
- Torge W., 2001, Geodesy, 3ª Edición. Ed. De Gruyter. 416 pp.
- Velicogna I., Wahr J., 2005, Greenland mass balance from GRACE. *Geophys. Res. Lett.*, doi: 10.1029/2005GL023955.
- Velicogna I., Wahr J., 2006, Acceleration of Greenland ice mass loss in spring 2004. *Nature*, doi: 10.1038/nature05168.
- Wahr J., Molenaar M., Bryan F., 1998, Time-Variability of the Earth's Gravity Field: Hydrological and Oceanic Effects and their possible detection using GRACE. *J. Geophys. Res.*, 103, 30,205-30,230.

Radial S wave velocity structure of the D'' region under a spot of the east central Pacific Ocean

Luis F. Terán-Mendieta and Raúl W. Valenzuela*

Received: November 19, 2010; accepted: April 10, 2012; published on line: June 29, 2012

Resumen

Se determinó la estructura radial de velocidades para la onda S en la base del manto en un área del Océano Pacífico centro-oriental centrada en los 19°N , 132°O . Se aplicó la técnica de la constante de disipación en el dominio de la frecuencia a las ondas S y S_{diff} de un sismo producido en las islas Tonga y registrado en el noreste de los Estados Unidos. Se trabajó con 29 modelos diferentes, entre los cuales se incluían modelos con una discontinuidad de la velocidad y también el Modelo Preliminar de Referencia de la Tierra (PREM). De acuerdo con el ajuste a la constante de disipación en el dominio de la frecuencia y a las formas de onda en el dominio del tiempo, se consideró que PREM es el mejor modelo. Esto implica que en esta ubicación D'' tiene un espesor de 150 km y un gradiente de velocidad ligeramente negativo conforme aumenta la profundidad. No se encontró una discontinuidad de la velocidad en la parte superior de D'' . La estructura de velocidades observada es consistente con el comportamiento de D'' como una capa térmica limítrofe y también con la posibilidad de que el material del manto se enriquezca en hierro como consecuencia de reacciones químicas con el núcleo. Además este modelo sugiere que en esta región existen temperaturas ligeramente elevadas en la base del manto. Por otra parte, no se esperaría encontrar una discontinuidad en esta zona puesto que ahí no se ha producido subducción en los últimos 180 millones de años.

Palabras clave: ondas difractadas, interfaz núcleo-manto, D'' , constante de disipación, post-perovskita, capa térmica limítrofe.

L.F. Terán-Mendieta
Departamento de Sismología
Instituto de Geofísica
Universidad Nacional Autónoma de México
Ciudad Universitaria
Delegación Coyoacán, 04510
México D.F., México

Now at Colegio de Ciencias y Humanidades Plantel Sur
Universidad Nacional Autónoma de México
México D.F., México
E-mail: luisteran@yahoo.com

Abstract

The S wave radial velocity structure at the base of the mantle was constrained for an area of the east central Pacific Ocean centered at 19°N , 132°W . The decay constant technique was applied in the frequency domain to the S and S_{diff} waves of an earthquake in the Tonga Islands recorded in the northeastern United States. A total of 29 different S wave velocity models were explored, including models with a velocity discontinuity and also the Preliminary Reference Earth Model (PREM). As determined from the fit to the decay constant in the frequency domain and to the waveforms in the time domain, PREM was considered the best model. This choice implies that D'' at this location is 150 km thick and has a slightly negative velocity gradient with increasing depth. No velocity discontinuity was found at the top of D'' . The proposed velocity structure is consistent with D'' acting as a thermal boundary layer and also with the possible existence of mantle enriched in iron through chemical reactions with the core. The preferred model also implies the existence of slightly elevated temperatures at the base of the mantle. The lack of a discontinuity is consistent with the absence of subduction at this location during the last 180 Myr.

Key words: diffracted waves, core-mantle boundary, D'' , decay constant, post-perovskite, thermal boundary layer.

R. W. Valenzuela*
Instituto de Geofísica
Universidad Nacional Autónoma de México
Ciudad Universitaria
Delegación Coyoacán, 04510
México D.F., México
*Corresponding author: raul@ollin.igeofcu.unam.mx

Introduction

A number of different approaches have been pursued in order to determine the velocity structure at the base of the mantle. Core diffracted waves are well suited for studying the velocity at the core-mantle boundary (CMB) because they spend a significant portion of their paths at this interface. Two techniques in particular involve the use of the ray parameter (Doornbos and Mondt, 1979b; Mula and Müller, 1980; Doornbos, 1983; Valenzuela-Wong, 1996; Valenzuela and Wysession, 1998; Valenzuela *et al.*, 2000) and the decay constant (Doornbos and Mondt, 1979a, 1979b; Mula, 1981; Doornbos, 1983; Valenzuela-Wong, 1996; Valenzuela and Wysession, 1998). By measuring the ray parameter in the time domain it is possible to determine the lateral velocity structure at the base of the mantle. On the other hand, the robust decay constant method relies on the frequency domain amplitude decay of diffracted waves and is sensitive to the radial velocity structure. Early work using the decay constant led some investigators to the conclusion that D'' has a negative velocity gradient for both P and S waves (Mondt, 1977; Doornbos and Mondt, 1979b; Doornbos, 1983), while other researchers found slightly positive gradients (Mula and Müller, 1980; Mula, 1981). The velocity structure determined by these studies was based on the assumption that D'' is globally homogeneous, which justified averaging the observations from individual earthquakes around the world. Wright and Lyons (1981) proposed a model with a discontinuous P-wave velocity increase for a region under the Caribbean Sea. Lay and Helmberger (1983) introduced several discontinuous shear wave velocity models for three different regions. It has been further suggested that the discontinuity is a global feature (Lay and Helmberger, 1983; Nataf and Houard, 1993; Sidorin *et al.*, 1999a; Sun and Helmberger, 2008). Although this discontinuity seems to be highly heterogeneous and it has not been observed everywhere, it has now been reported in many studies; see Nataf and Houard (1993), Krüger *et al.* (1995), Loper and Lay (1995), Wysession *et al.* (1998), Helmberger *et al.* (2005), Lay and Garnero (2007, 2011), Garnero and McNamara (2008), and Wookey and Dobson (2008) for a review. One of the leading explanations for the discontinuity is the occurrence of a phase transition from perovskite to post-perovskite under lowermost mantle conditions (Murakami *et al.*, 2004).

Given the uneven distribution of sources and receivers on a global scale, our sampling of the core-mantle boundary is not uniform. Of all the phases used to study D'', core diffracted waves are the best suited for on-land recording, especially in eastern North America and southern

Africa (Wysession, 1996a). The Missouri to Massachusetts (MOMA) array was in a very favorable location for recording diffracted waves from earthquakes in the southwest Pacific (Wysession *et al.*, 1996; Fischer *et al.*, 1996). This study presents the results of forward modeling the radial velocity structure at the base of the mantle in a spot under the east central Pacific Ocean using SH and SH_{diff} waves recorded by the MOMA array. Other authors (e. g., Sun and Helmberger, 2008; Kawai and Geller, 2010) have taken advantage of the new data gathered by the Transportable Array component of the USArray (Ammon and Lay, 2007) in order to obtain improved models of D'' structure using various seismic phases.

Calculating the decay constant

This derivation follows from the work of Mula (1981); the theory is also described by van Loenen (1988) and Valenzuela-Wong (1996). Mathematically, the amplitude of the impulse recorded by a station at an epicentral distance Δ and azimuth ϕ from the source can be described in the frequency domain by the product of the following terms:

$$A(\omega, \phi, \Delta) = S(\omega) R(\phi, \Delta) M_d(\omega, \phi) C(\omega, \phi, \Delta) M_u(\omega, \phi) U(\omega) I(\omega), \quad (1)$$

where ω is angular frequency, $S(\omega)$ is the source time function, assuming that directivity effects are not significant, and $R(\phi, \Delta)$ is the radiation pattern. $C(\omega, \phi, \Delta)$ is the effect of the path along the core-mantle boundary on the waves. $M_d(\omega, \phi)$ and $M_u(\omega, \phi)$ represent, respectively, the effects of the downward and upward paths through the mid-mantle on the waves. $U(\omega)$ is the impulse response of the crust and uppermost mantle under the station. This formulation is slightly different from Mula's (1981) since he used the term $K(\omega)$ and accounted solely for crustal effects. We have allowed for the possibility that the upper mantle sustains significant heterogeneities. Lastly, $I(\omega)$ is the instrument response.

Assuming that the amplitudes along the core-mantle boundary decay exponentially with distance (Phinney and Alexander, 1966; Chapman and Phinney, 1972; Van Loenen, 1988; Aki and Richards, p. 457, 2002) and that the dependence on the azimuth will be averaged for a small enough azimuthal window (less than 20°), let

$$C(\omega, \phi, \Delta) = e^{-\gamma(\omega)\Delta} \sin^{-1/2} \Delta, \quad (2)$$

where $\sin^{-1/2} \Delta$ is the geometrical spreading factor. The term $\gamma(\omega)$ is the decay constant. Anelastic attenuation has the effect of reducing wave

amplitudes. Valenzuela-Wong (1996) carried out tests to evaluate the relative contributions of anelastic attenuation versus velocity structure on the decay constant. He concluded that the amplitude decay due to the diffraction process is clearly more significant than the decay due to anelastic attenuation.

It is possible to solve for the decay constant by obtaining the spectral amplitude ratio of any station j relative to a reference station r . Upon division, the term $S(\omega)$ cancels out because we have assumed no directivity effects, and because we chose a narrow azimuthal window. The term $M_d(\omega, \phi)$ also cancels out upon division because the downgoing path is approximately the same for all stations since a narrow azimuthal window was used; we further consider the mid-mantle to be nearly homogeneous. The term $M_u(\omega, \phi)$ is not considered significant on the premise of mid-mantle homogeneity. Under the previous assumptions, the spectral division takes on the following form:

$$\frac{A_j(\omega)}{A_r(\omega)} = \frac{R_j(\phi, \Delta) e^{-\gamma(\omega)\Delta_j} \sin^{-1/2} \Delta_j U_j(\omega) I_j(\omega)}{R_r(\phi, \Delta) e^{-\gamma(\omega)\Delta_r} \sin^{-1/2} \Delta_r U_r(\omega) I_r(\omega)} \quad (3)$$

Solving for the decay constant, $\gamma(\omega)$, yields

$$\ln \left\{ \frac{A_j(\omega) R_r(\phi, \Delta) U_r(\omega) I_r(\omega) \sin^{1/2} \Delta_r}{A_r(\omega) R_j(\phi, \Delta) U_j(\omega) I_j(\omega) \sin^{1/2} \Delta_j} \right\} = \gamma(\omega) [\Delta_r - \Delta_j] \quad (4)$$

The terms A_j and A_r are the recorded seismograms; R_j and R_r can be calculated from the focal mechanisms, readily available in the literature; and I_j and I_r are the instrument responses, known from manufacturer's specifications or empirically determined. Finally, based on earlier literature, Mula (1981) set the ratio K_j/K_r for crustal effects, equal to 1. Valenzuela-Wong (1996) showed a procedure to obtain the ratio U_j/U_r using data from other earthquakes (at shorter epicentral distances) recorded by the same stations. Additionally, he also explored the effect of setting the ratio $U_j/U_r = 1$. Valenzuela-Wong (1996) could not fit the observed decay constant when he applied crustal and upper mantle corrections. He speculated that the crustal and upper mantle effects are too small and thus applying the corrections would adversely affect the measurement of the decay constant. Alternatively, if the quality of the data he used to evaluate the corrections was not good enough, then the measurement of the decay constant would have been degraded. In this paper the decay constant was determined assuming that $U_j/U_r = 1$.

Data and procedure

Data from the Tonga Islands earthquake of April 7, 1995 was analyzed to determine the radial velocity structure of the D'' region under the east central Pacific Ocean, in a spot centered at 19°N, 132°W (Figure 1). The event parameters are as follows. 22:06:57 UT, 15.20°S, 173.53°W, depth 40 km, $M_w=7.3$, $M_o=1.3 \times 10^{20}$ N m, $\phi=165^\circ$, $\delta=18^\circ$, $\lambda=159^\circ$. The origin time, latitude, and longitude were taken from the National Earthquake Information Center (NEIC) catalog. The moment magnitude and the seismic moment were taken from the Harvard University Centroid Moment Tensor (CMT) catalog (Dziewonski *et al.*, 1996). The event depth as well the nodal plane parameters were constrained through waveform modeling. Reflectivity synthetic seismograms were generated using a technique similar to the one described by Kennett (1980). The source was placed at different depths in order to fit the arrival times of the S and sS waves at the shortest distances, and the S_{diff} and sS_{diff} arrivals later in the profile (Figures 2 and 3). The nodal plane was constrained by keeping the dip and slip taken from the Harvard CMT catalog (Dziewonski *et al.*, 1996) fixed while varying the strike in 5° steps and looking for the best fit to the relative amplitudes between the S and sS (or between S_{diff} and sS_{diff}) phases. Additionally, the source time function (STF) was determined and a double rupture was found for this earthquake. The source time function was convolved with the synthetics to obtain the best fit to the data. This STF is made up of two overlapping trapezoids which amount to a total duration of 23 s. The first trapezoid has the largest amplitude. The amplitude of the second trapezoid is roughly two thirds the amplitude of the first one. The seismograms used were recorded at the temporary stations of the Missouri to Massachusetts (MOMA) broadband array (Wysession *et al.*, 1996; Fischer *et al.*, 1996). The seismometers were provided by the Incorporated Research Institutions for Seismology (IRIS) Program for Array Seismic Studies of the Continental Lithosphere (PASSCAL). Both Streckeisen STS-2 and Güralp CMG3-T broadband seismometers were used. Their amplitude responses in velocity are essentially the same. The amplitude response is flat in the frequency range from 0.0083 to 50 Hz (periods between 120 and 0.02 s). Figure 1 shows the epicenter, the stations, and the region of D'' sampled under the east central Pacific. At the epicentral distances involved, between 94° and 108°, both S and S_{diff} arrivals are observed, as shown in Figure 2 and 3. The profile spans a distance at the core-mantle boundary of 14° and the azimuthal window is extremely narrow, only ~1°, thus providing a very coherent and stable sampling of the base of the mantle. The scale of the region sampled is on the order of 900 km.

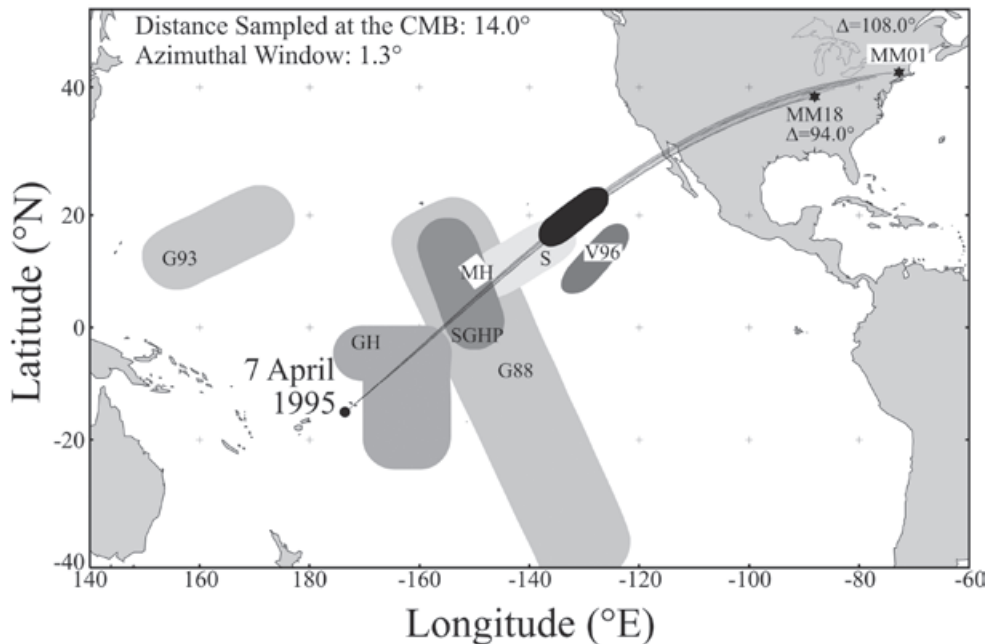


Figure 1. Ray paths of SH and SH_{diff} waves from the Tonga earthquake of 7 April 1995 recorded by the Missouri to Massachusetts (MOMA) broadband array in the northeastern United States. The dot marks the epicenter. Stations MM01 and MM18 served as anchors for the MOMA array. The lowermost mantle is sampled under the east central Pacific Ocean as indicated by the black area along the ray paths. As the epicentral distances vary between 94° and 108° , the farthest arrivals are fully diffracted waves while the nearest ones are direct waves traveling within D'' . The distance sampled at the core-mantle boundary (CMB) is 14° . The azimuthal window is $\sim 1.4^\circ$, providing a very coherent and stable sampling of the CMB. Also shown are the locations of previous studies of D'' under the Pacific. The codes stand for the following work. S: Schlittenhardt *et al.* (1985); G88: Garnero *et al.* (1988); G93 and SGHP: Garnero *et al.* (1993); MH: Mori and Helmberger (1995); GH: Garnero and Helmberger (1995, 1996); V96: Valenzuela-Wong (1996), and Valenzuela and Wysession (1998). For discussion refer to Section 5.1.

The steps followed to determine the decay constant using data from the MOMA array are described below. Figure 3 shows the instrument-deconvolved, displacement waveforms as recorded in the transverse components. The amplitude spectrum for each station was obtained from a 70 s time window containing both the SH_{diff} and the sSH_{diff} pulses (or SH and sSH , depending on the actual distance). Records were bandpass filtered to retain frequencies between 0.005

and 0.500 Hz (i. e., 200 to 2 s period). Figure 4 shows the amplitude spectra at all the stations that recorded this event. The vertical dashed lines bound the frequency range (from 0.014 to 0.043 Hz, or alternatively periods from 71 to 23 s) where the decay constant can be reliably determined following a criterion which will be explained below. The amplitudes are largest within this frequency band, thus providing the best signal-to-noise ratio (SNR). Also noticeable in

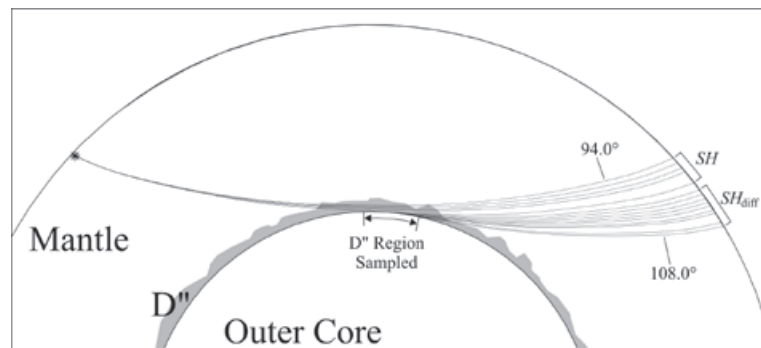


Figure 2. Cross section showing the region of the core-mantle boundary sampled by the Tonga earthquake of 7 April 1995 recorded by the MOMA array in the northeastern United States. The ray paths are also shown. At these epicentral distances, between 94° and 108° , both SH and SH_{diff} waves were recorded.

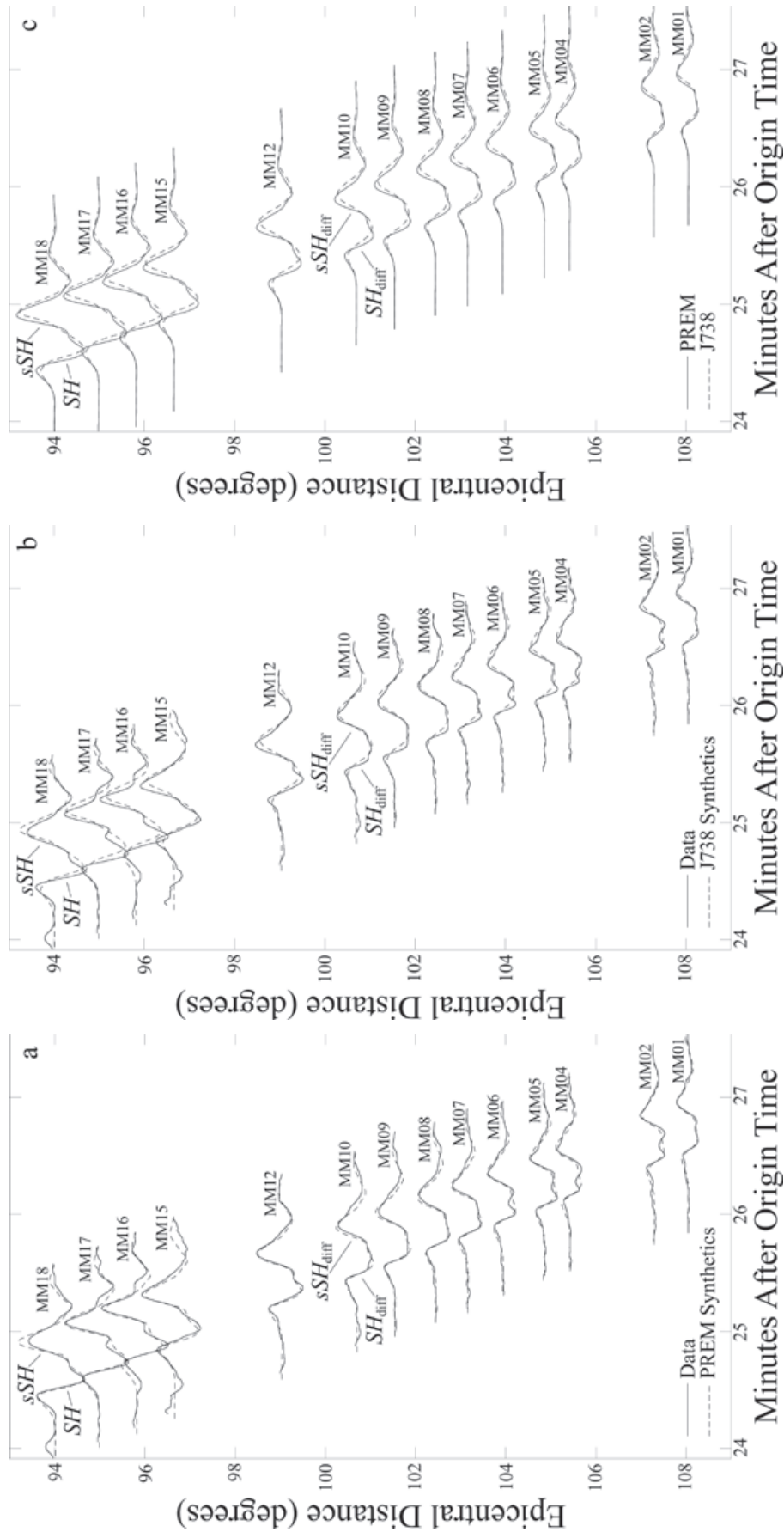


Figure 3. Instrument-deconvolved, displacement, transverse records from the Tonga earthquake of April 7, 1995 recorded by the MOMA array. Records were bandpass filtered between 200 and 2 s (between 0.005 and 0.500 Hz). Synthetic waveforms correspond to models (a) PREM and (b) J738. The synthetics were normalized to match the amplitude of the observed pulses. The depth of the earthquake was constrained through waveform modeling of the surface reflected phases sSH and sSH_{diff} . A source time function with a double rupture was applied. (c) compares PREM to J738 synthetics at the same scale.

Figure 4 is the expected decrease in amplitude with increasing epicentral distance (Phinney and Alexander, 1966; Chapman and Phinney, 1972; Van Loenen, 1988; Aki and Richards, p. 457, 2002). In general the amplitudes (Figure 4) drop to a low at a frequency of 0.05 Hz and are highly variable from station to station at higher frequencies. Figure 5 shows the logarithmic amplitude ratio for each station, relative to the nearest station (MM18) chosen as the reference, plotted as a function of distance at a frequency of 0.0297 Hz (period = 33.7 s). The decay constant is the slope of a straight line, obtained through a least squares fit. At this frequency $\gamma = 0.079$ and the correlation coefficient for the fit is $r = 0.980$. Given that the decay constant is the slope calculated at a certain frequency, it is expected that γ will take different values at different frequencies, as shown in Figure 6 for selected frequencies. A plot of the decay constant, as well as the corresponding correlation coefficient, as a function of frequency is presented in Figure 7. It is necessary to stress the importance of determining the correlation coefficient for the linear fit. In order for a measurement of the decay constant to be considered reliable, a correlation coefficient greater than or equal to 0.9 was required. The square of the correlation coefficient is a measure of how much one variable Y can be accounted for through a linear relationship as a function of the variable X (Walpole and Myers, pp. 403-409, 1993). Thus, using the customary value of $r \geq 0.9$, X accounts for $r^2 \geq 0.81$ (81%) of the values in Y through a linear relationship. The same requirement was imposed on decay constants determined by forward modeling as described in the next section. In this paper the

requirement that $r \geq 0.9$ was used more as a measure to determine if the variables could be appropriately related by the decay constant, i. e., that it was appropriate to fit the data through a straight line (Walpole and Myers, pp. 403-409, 1993), than as a measure of data scatter about a straight line. At certain frequencies $r < 0.9$ and, unlike Figure 5, deviations from a straight line were observed (e. g., sigmoidal or arc-shaped curves, or a decreasing trend followed by a sudden increase). This meant the breakdown of the assumption that the decay constant is a good model for the amplitude decay, and furthermore that Equation (4) was not valid at these frequencies. This effect was especially obvious for decay constants determined from forward models. To a large extent, reliable values of the correlation coefficient ($r \geq 0.9$) were used to determine the range of frequencies where the measurement of the decay constant was valid. In Figure 7, as well as in Figure 4, this range goes from 0.014 to 0.043 Hz. In general γ shows an increasing trend with increasing frequency, except at the highest frequencies (from 0.038 to 0.043 Hz) where a slight drop occurs (Figure 7). Figure 8 shows the measured decay constant and the $1-\sigma$ standard deviation obtained from the least squares fit. For comparison purposes Figure 8 also shows the decay constant observed in nearby region V96 (see Figure 1) where a discontinuity at the top of D'' was previously reported (Valenzuela-Wong, 1996; Valenzuela and Wysession, 1998). The two decay constants show some overlap at low and high frequencies. They clearly differ, however, in the range from 0.018 to 0.031 Hz.

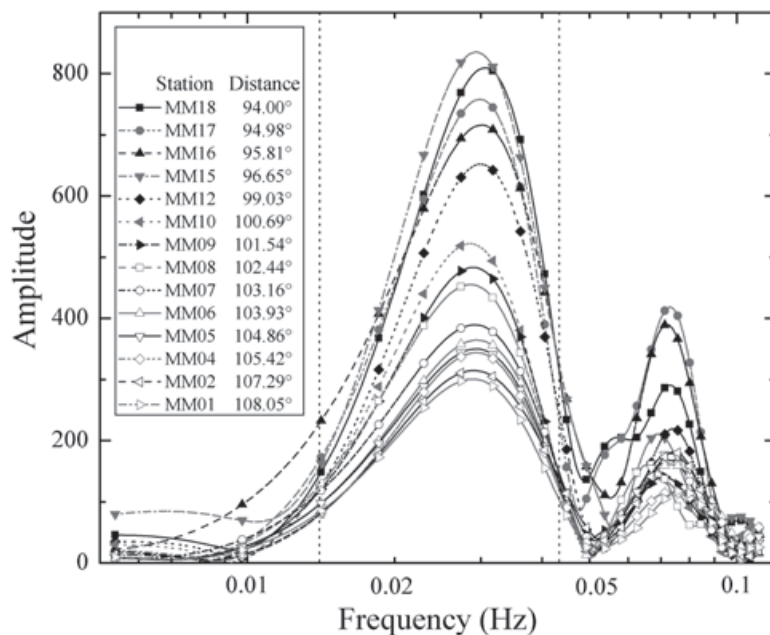


Figure 4. Amplitude spectra for the Tonga earthquake of 7 April 1995 recorded by the MOMA array. Notice the decay of the amplitude as distance increases. Records were bandpass filtered between 200 and 2 s (between 0.005 and 0.500 Hz). SH waves at these distances have most of their energy at periods between 71 and 23 s (between 0.014 and 0.043 Hz) as indicated by the vertical dashed lines.

Figure 5. Logarithmic amplitude ratio for each station, relative to reference station MM18, plotted as a function of distance. The frequency is 0.0297 Hz (33.7 s period). The decay constant is the slope of the straight line, obtained through a least squares fit. The decay constant is $\gamma = 0.079$ and the corresponding correlation coefficient is $r = 0.980$.

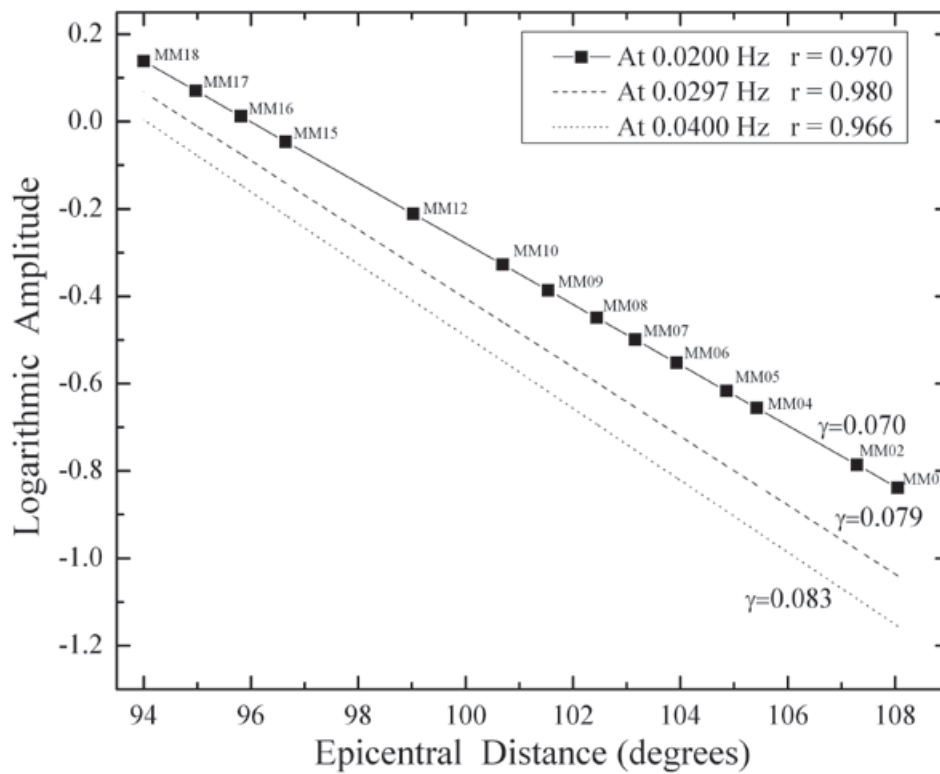
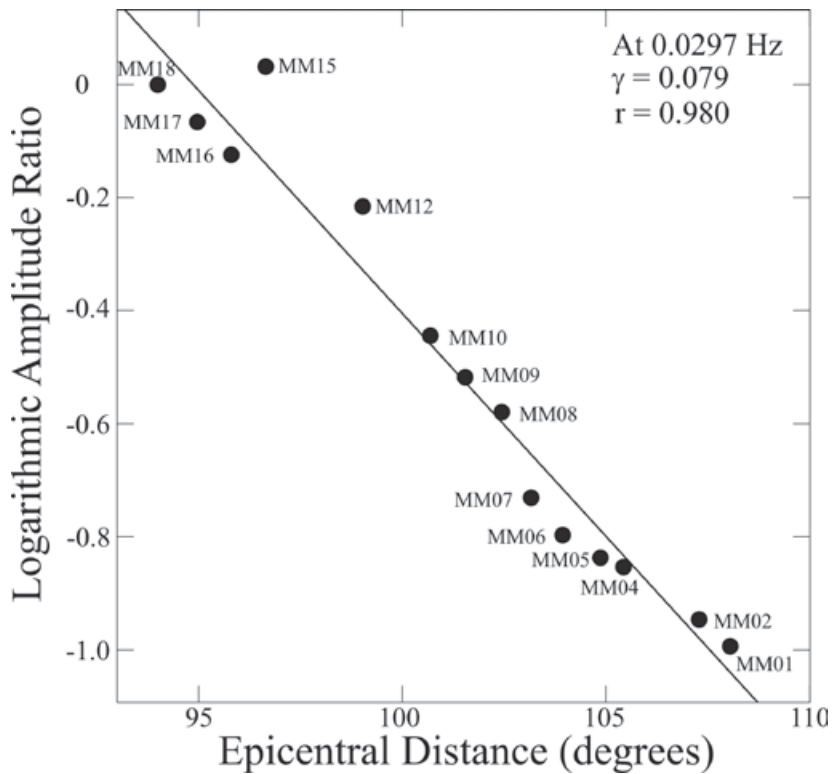


Figure 6. Decay constant obtained as in Figure 5 shown at selected frequencies. The value for γ is different at different frequencies. Squares are not actual data points, they are only intended to show the epicentral distance for each station.

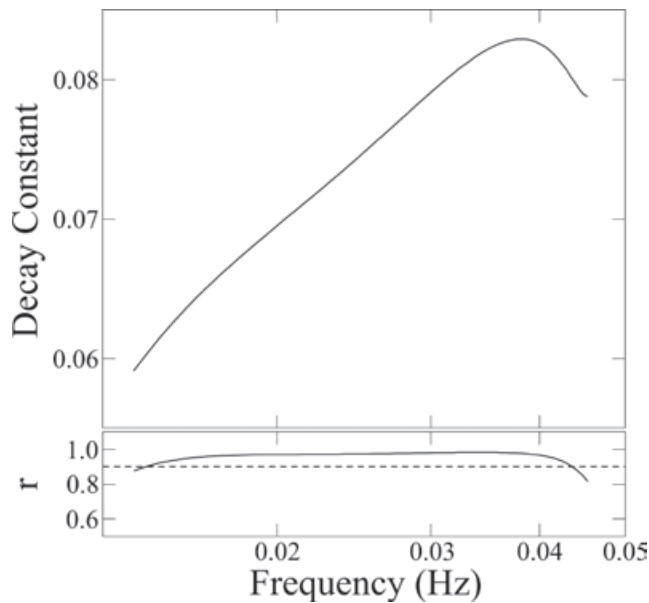


Figure 7. Decay constant plotted as a function of frequency. Also shown is the correlation coefficient for the least squares fit. Decay constants are considered reliable if their correlation coefficients are equal to or greater than 0.9, as indicated by the horizontal dashed line.

The range of frequencies chosen to analyze the decay constant is controlled by the energy content of the diffracted waves. At higher frequencies the effect of scattering is important (Bataille and Flatté, 1988; Bataille *et al.*, 1990; Bataille and Lund, 1996; Stein and Wysession, pp. 168-169, 2003) and consequently diffracted waves have little energy. This makes it impossible to fit the data with the decay constant. At lower frequencies, as the diffracted wave travels farther along the CMB it becomes increasingly depleted in high frequency energy given that the diffraction process is more efficient at low frequencies (Aki and Richards, p. 457, 2002; Stein and Wysession, p. 74, 2003). In this regard the frequency content, between 0.014 and 0.043 Hz (periods between 71 and 23 s), observed in this study for the *SH* wave (at distances between 94° and 108°) agrees with earlier work using diffracted waves (Bolt *et al.*, 1970; Doornbos and Mondt, 1979b; Mula, 1981; Doornbos, 1983; Doornbos *et al.*, 1986; Valenzuela-Wong, 1996; Valenzuela and Wysession, 1998). The third effect controlling the frequency content is the radial velocity structure at the base of the mantle (Mula, 1981; van Loenen, 1988; Valenzuela-Wong, 1996; Valenzuela and Wysession, 1998) and is in fact the reason that the decay constant technique was chosen for this study. In the analysis described herein, the effects of both the diffraction process and the radial velocity structure are accounted for by the forward modeling of reflectivity synthetic seismograms. The resolution of the decay constant method is limited to long wavelength structures (~1000 km) because of the low frequency nature of diffracted waves. This fact has long been known and researchers have been careful not to overinterpret their

data (Bolt *et al.*, 1970; Doornbos and Mondt, 1979b; Mula, 1981; Doornbos, 1983; Doornbos *et al.*, 1986). Nonetheless, the reliability of the method has been firmly established (Bolt *et al.*, 1970; Doornbos and Mondt, 1979b; Mula, 1981; Doornbos, 1983; Doornbos *et al.*, 1986; Van Loenen, 1988; Valenzuela-Wong, 1996; Valenzuela and Wysession, 1998). Given the uneven distribution of sources and receivers around the world, the use of diffracted waves makes it possible to increase the coverage of *D''* afforded by other seismic phases (Wysession, 1996a).

Results

In order to determine the radial velocity structure at the base of the mantle, reflectivity synthetic seismograms were generated by forward modeling while trying a set of proposed models. The algorithm used to generate synthetic seismograms was provided by Tim Clarke and is similar to the one described by Kennett (1980). Three criteria were followed to guarantee the reliability of the best-fitting models. First, a good fit of the modeled decay constant to the observations was sought. Second, the correlation coefficient of the least squares fit to a straight line (decay constant) had to be greater than or equal to 0.9. Third, synthetic and recorded time domain waveforms were compared in order to avoid features which do not correspond with the observations.

Models were organized into the following groups and their effects on the decay constant were explored. (a) The Preliminary Reference Earth Model, PREM, (Dziewonski and Anderson, 1981), models with (b) a gradual decrease of the velocity throughout *D''* with increasing depth, (c) a gradual increase, and (d) a discontinuous increase in the velocity followed by a gradual decrease. Special attention was given to discontinuous models in order to determine the response of the decay constant to changes in (i) the amount of the velocity decrease throughout *D''*, (ii) the thickness of *D''*, (iii) the velocity increase at the discontinuity, and (iv) the velocity gradient above *D''*. Earlier work has shown the importance and prevalence of velocity models with a discontinuity at the top of *D''* (e. g., Lay and Helmberger, 1983; Nataf and Houard, 1993; Krüger *et al.*, 1995; Loper and Lay, 1995; Wysession *et al.*, 1998; Helmberger

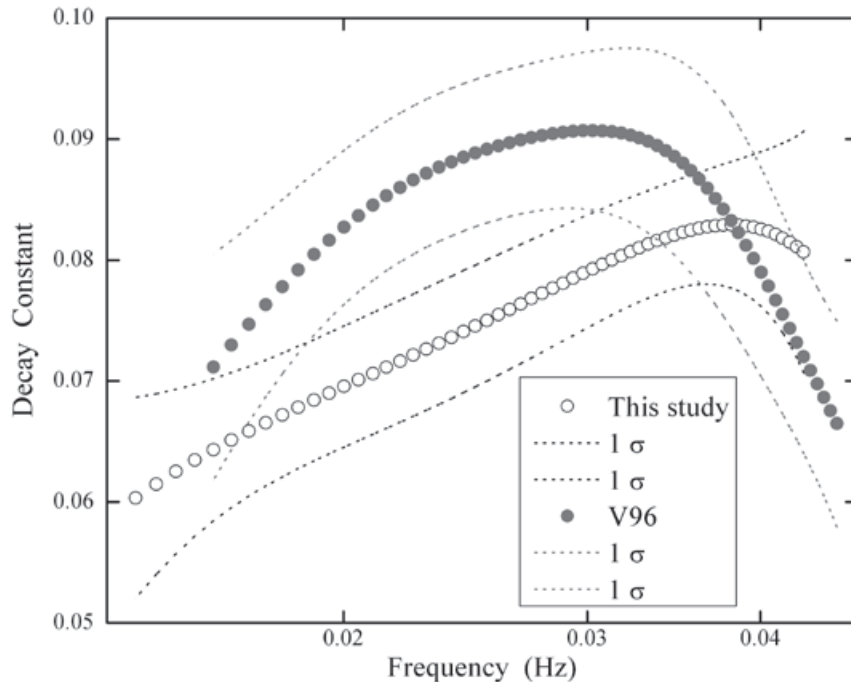


Figure 8. Comparison of the decay constant measured in this study (black, open circles) with the decay constant observed in nearby region V96 (gray, solid circles) as shown in Figure 1. The dashed lines represent one standard deviation for the two measurements. A discontinuity at the top of D'' has been reported in region V96 (Valenzuela-Wong, 1996; Valenzuela and Wyession, 1998). These decay constants overlap somewhat at the low and high frequency ends, but are clearly different at intermediate frequencies.

et al., 2005; and Lay and Garnero, 2007, 2011). Figure 1 shows locations where the discontinuity has been found under the Pacific Ocean (G88 from Garnero *et al.*, 1988; SGHP and G93 from Garnero *et al.*, 1993). In particular, Valenzuela-Wong (1996) and Valenzuela and Wyession (1998) found that a model with a discontinuous increase in the velocity followed by a gradual decrease (RJK2705) best fits the decay constant in a region of D'' located near and to the southeast of the one reported in this study (V96 in Figure 1). In that case the decay constant from PREM is clearly different than that of RJK2705's and does not match the observations at all. Based on the preceding results it was expected that models with a discontinuity at the top of D'' would provide the best fit to the observations. It was indeed possible to fit the data using discontinuous model J738, but as it will be shown, model PREM provided an even better fit to the decay constant and the waveforms. Given that both the diffraction process and anelastic attenuation lead to the amplitude decrease of seismic waves, Valenzuela-Wong (1996) and Valenzuela and Wyession (1998) calculated the decay constant by varying the value of Q , the seismic quality factor, in their models in order to evaluate the relative contribution of the two processes. In this study PREM provided a good fit to the data, therefore trying different values of Q was not deemed necessary. Furthermore, Valenzuela-Wong (1996) concluded that even

for models with a discontinuity, increasing Q_{μ} above 156 has only a small effect on the decay constant. Most of the models available in the literature have values for Q_{μ} in D'' greater than 200 (Anderson and Hart, 1978a, 1978b; Sailor and Dziewonski, 1978; Stein *et al.*, 1981; Dziewonski and Anderson, 1981; Widmer *et al.*, 1991; Bhattacharyya *et al.*, 1995a, 1995b; Durek and Ekström, 1996). For example $Q_{\mu} = 312$ in PREM.

Four different models were initially tested and are shown in Figure 9a. The Preliminary Reference Earth Model (PREM), proposed by Dziewonski and Anderson (1981), was the first one evaluated. It is a global, homogeneous, and one-dimensional model of the seismic velocities, density, and anelastic attenuation as a function of depth. In order to create the model, different kinds of data such as body waves, long period surface waves, and free oscillations were taken into account. The S wave velocity in PREM is shown by the dash-dotted line in Figure 9a. It has a gradual velocity increase with increasing depth throughout most of the lower mantle and a very slight decrease throughout a 150 km-thick D''. Models A, B, and C are variations of PREM in the lowermost 150 km of the mantle, i. e. the D'' region. Model A shows a gradual decrease in the velocity from top to bottom of D'', model B shows a gradual increase, and model C shows a sudden increase at the top of D'' followed by a constant velocity all the way down to the bottom of D''.

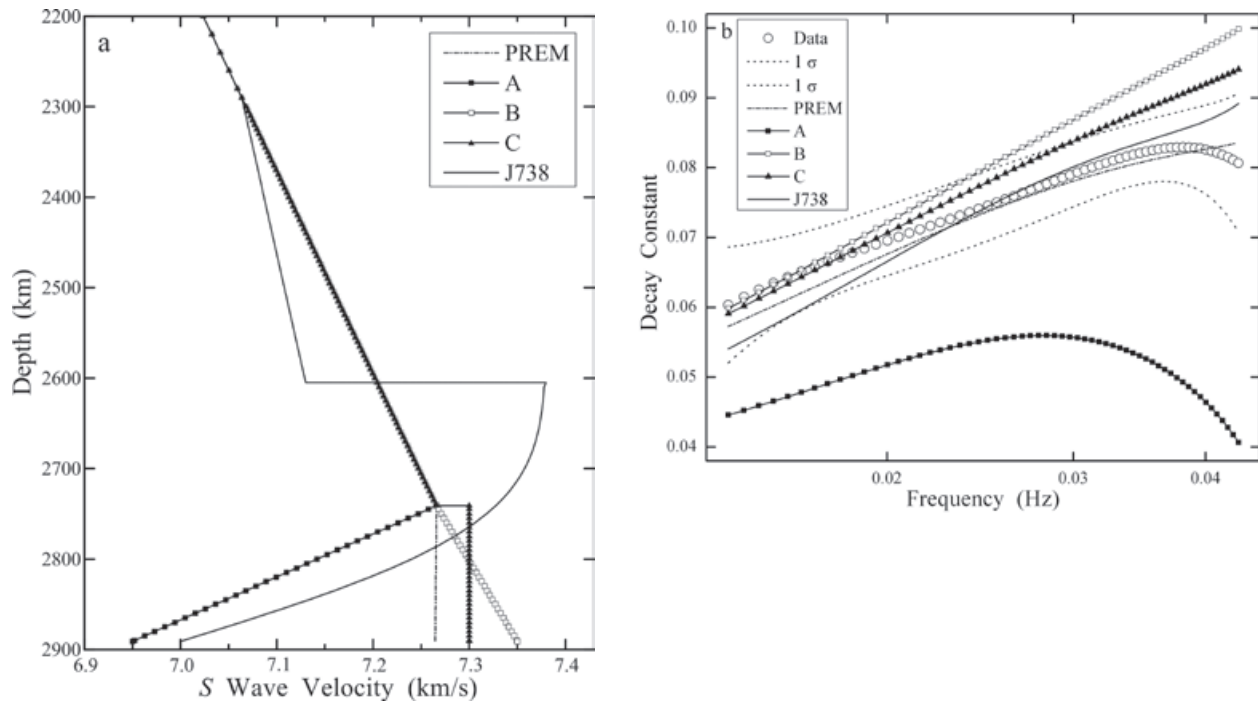


Figure 9. (a) Models of lowermost mantle shear velocity structure. Dot-dashed line is for model PREM. It has a very slight velocity decrease with increasing depth throughout a 150 km-thick D". There is no discontinuity at the top of D". Models A, B and C are variations of PREM in the bottom 150 km. Model A shows a gradually decreasing velocity. Model B, a gradually increasing velocity. Model C, a discontinuous increase at the top of D" followed by a constant velocity down to the CMB. Model J738 is only shown for comparison and will be discussed later. (b) Decay constants obtained from the corresponding models. The open circles show the data and the dashed lines represent one standard deviation. PREM fits the data as it falls within the error bars. The decay constant from model A is too low to fit the data. Model B matches the observations only at low frequencies, and so does model C for a somewhat broader frequency range.

In order to generate reflectivity synthetic seismograms, models for the compressional velocity, the density, and the bulk and shear seismic quality factors were specified in addition to the shear velocity model. The same percentage change in P velocity models was used as for S velocity models. Since changes in seismic wave velocity can be caused by thermal (Stacey and Loper, 1983; Lay and Helmberger, 1983; Doornbos *et al.*, 1986; Lay, 1989; Loper and Lay, 1995; Wyession *et al.*, 1998; Lay *et al.*, 1998; Garnero, 2000) or chemical (Lay and Helmberger, 1983; Lay, 1989; Loper and Lay, 1995) heterogeneities at the base of the mantle, Valenzuela-Wong (1996) tested different density models consistent with both possibilities. He found that the differences caused by the different density models on the decay constant are relatively small, in agreement with earlier work by Doornbos and Mondt (1979a). Therefore, for simplicity all modeling in this paper was done using thermal density models alone. In this way, a velocity increase is correlated with a density increase, and likewise a velocity drop

is correlated with lowered densities. The seismic quality factors, Q_K and Q_{μ} , used for the models of D" in this work were taken from PREM. The models for P and S velocities, density, and Q used in the generation of reflectivity synthetic seismograms are identical to PREM through the crust and the mantle down to 2,300 km depth, and also in the core.

The fits of the synthetic to the observed decay constant are shown in Figure 9b for models PREM, A, B, and C. The dashed lines represent the 1- σ standard deviation for the measured decay constant as obtained from the least squares fit. The decay constant from model A is clearly too low to match the observations. Model B fits the measured decay constant at low frequencies, from 0.014 to 0.023 Hz, whereas model C can fit the data up to frequencies as high as 0.030 Hz. PREM fits the data well because its decay constant falls within the error bars for the data throughout the entire frequency range from 0.014 to 0.043 Hz. Valenzuela-Wong (1996) and Valenzuela and Wyession (1998) found that

certain models with a discontinuous increase in the velocity followed by a gradual decrease with increasing depth best fit the decay constant in a region of D'' near the area of this study (V96 in Figure 1) and also for D'' under easternmost Siberia. Simple models such as PREM, A, or B, or variations of these models, however, could not fit their data. So, next we tried to fit our data using models that have a sudden increase in the velocity followed by a gradual decrease. Some examples are given below.

Figure 10 shows the effect of changing the velocity at the CMB while keeping constant the velocity jump at the discontinuity. Models F02, G02, and H all have a discontinuous S wave velocity increase at the top of D'' from 7.13 to 7.34 km/s (Figure 10a). Next the velocity undergoes a gradual decrease down to the CMB in the form of a complementary error function. The choice of a complementary error function is consistent with the perception of D'' as a thermal boundary layer (Stacey and Loper, 1983; Lay and Helmberger, 1983; Doornbos *et al.*, 1986; Lay, 1989; Loper and Lay, 1995; Wyssession *et al.*, 1998; Lay *et al.*, 1998; Garnero, 2000; Lay and Garnero, 2011). The complementary error function is used to describe the temperature as heat is transferred by conduction through a

thermal boundary layer (Turcotte and Schubert, pp. 153-157, 2002). Both the velocity and density profiles are assumed to depend on the temperature and thus follow a complementary error function within the thermal boundary layer (TBL). The thickness of the basal layer is 286 km. Models F02, G02, and H illustrate the effect of decreasing the velocity at the CMB (Figure 10a). These velocities are 7.19, 7.00, and 6.90 km/s, respectively. The corresponding decay constants are shown in Figure 10b. The decay constant from model F02 fits the data at low frequencies, from 0.014 to 0.019 Hz, but it is too high at higher frequencies. Model G02 does a good job at large frequencies, from 0.020 to 0.043 Hz, but it fails to fit the data at lower frequencies. Lastly, the decay constant from model H is too low throughout the entire frequency range.

Models of the J series explore the effect of varying the velocity increase at the discontinuity (at the top of D''). Figure 11a shows models J724, J734 (which is the same as G02), J738, and J744. The number after the J corresponds to the increased S wave velocity at the discontinuity: 7.24, 7.34, 7.38, and 7.44 km/s, respectively. Therefore the velocity jump at the discontinuity is 1.54, 2.95, 3.51, and 4.35 % for models J724, J734, J738, and J744, respectively. The starting

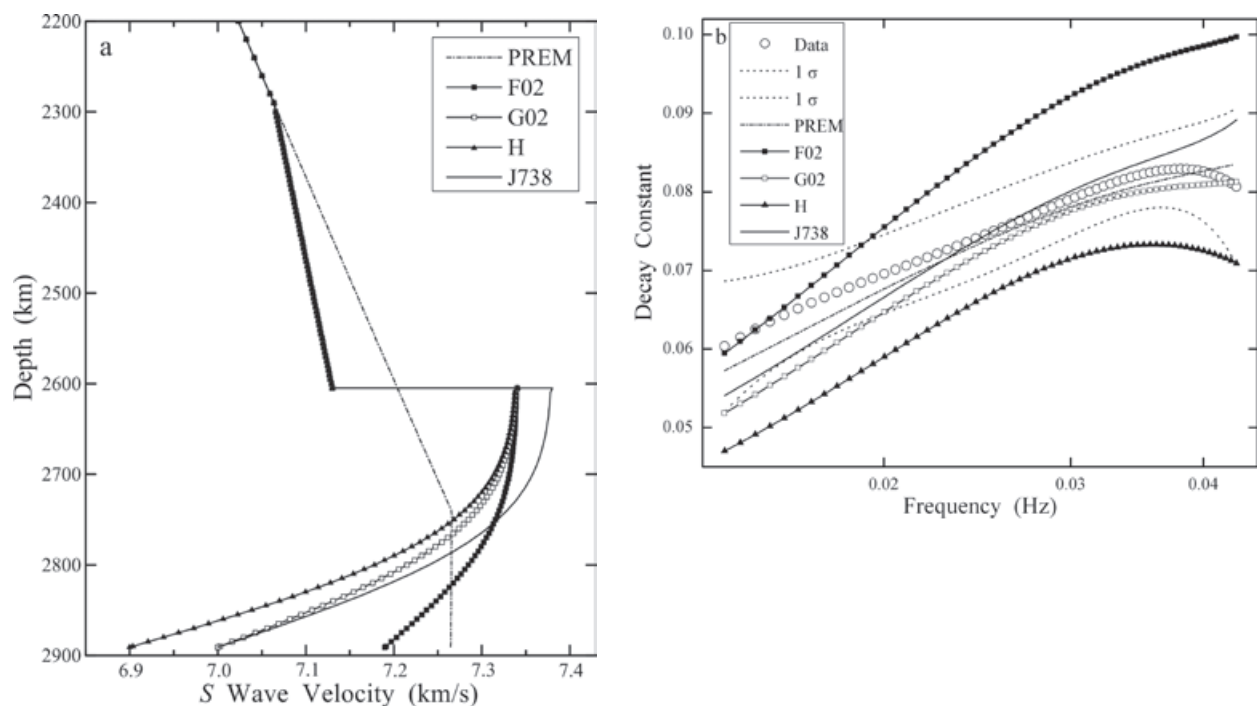


Figure 10. Determining the effect of varying the velocity at the core-mantle boundary. (a) Shown here are models F02, G02 and H in order of decreasing velocity at the CMB. All models use a complementary error function to describe the velocity decrease throughout the lowermost mantle. Model J738 will be discussed later. (b) Corresponding decay constants. Notice the decreasing decay constant with decreasing velocity at the CMB. None of these models fit the observations throughout the entire frequency range.

velocity at the discontinuity is 7.13 km/s. The velocity at the CMB is 7.00 km/s and the basal layer thickness is 286 km. Figure 11b shows the decay constants. These follow a straightforward pattern. Larger velocity jumps are associated with larger decay constants. The decay constant from model J724 is clearly too low to fit the data. Model J734 works well only at high frequencies, from 0.020 to 0.043 Hz. Model J738 does a good job at all frequencies. Model J744 fits the observations at low frequencies, from 0.014 to 0.025 Hz, but breaks down at higher frequencies.

In other models (not shown) the thickness of D'' and the velocity gradient above D'' were changed in order to evaluate their effect on the decay constant. These could not match the observations. Out of a total of 29 different models tested, two fit the data given that their decay constants fall within the error bars for the data. These are PREM and J738 (Figure 11). PREM, however, provides a better fit because its decay constant is closer to the observed decay constant for most frequencies (Figure 11b). The time domain waveforms from PREM are compared to the observations in Figure 3a and also show a good fit. The SH_{diff} (or SH) pulse from the J738 synthetics shows a poorer fit to the data as it is too narrow, especially in the distance range from

99° to 106° (Figure 3b). The PREM and J738 synthetic waveforms are compared in Figure 3c. PREM is our preferred model given that it provides a better fit than J738 in both the time and frequency domains.

Discussion

Under this region of the east central Pacific Ocean PREM implies that D'' is 150 km thick and that the S wave velocity gradient is slightly negative throughout. No discontinuity is observed at the top of D'' . The observation of a PREM velocity structure is consistent with a thermal boundary layer because the velocity gradient is decreased relative to the rest of the lower mantle. Due to its silicate composition, the mantle has a low thermal conductivity and a high viscosity (Loper and Lay, 1995) and is thus expected to act as a TBL. The temperature increases with increasing depth while the seismic velocity gradient drops. A PREM structure is also consistent with chemical reactions between mantle and core materials which could lead to iron enrichment of the silicates in D'' (Knittle and Jeanloz, 1989, 1991). The denser, iron-enriched silicates would accumulate in the lowermost mantle and are seismically slow (Williams and Garnero, 1996; Wyssession *et al.*, 1998), which is consistent with the reduced S

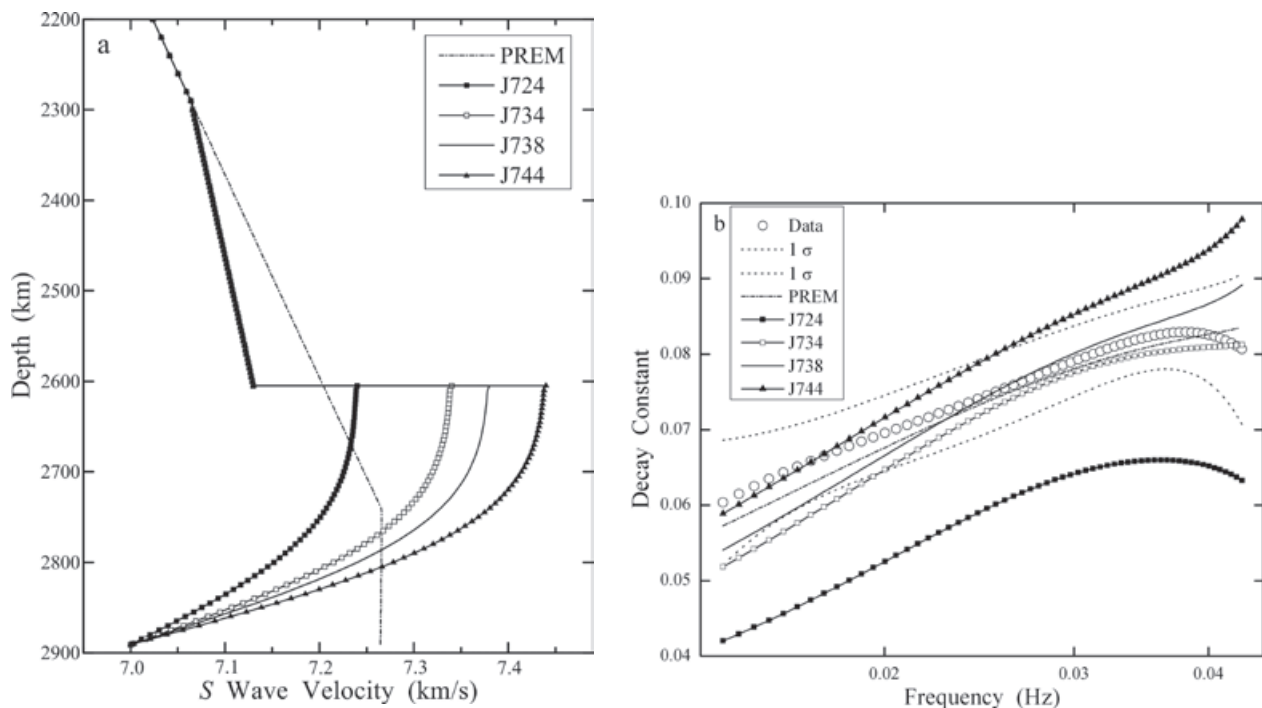


Figure 11. Effect of the velocity increase at the discontinuity. (a) Models of the J series in order of increasing jump in the velocity. D'' thickness is 286 km. The velocity jump at the discontinuity varies between 1.54 and 4.35 %. (b) Corresponding decay constants. Model J738 fits the data as it falls within the error bars. PREM, however, stays closer to the observed decay constant at most frequencies and is thus considered a better model. Also see the fits to the time domain waveforms for these two models in Fig. 3.

wave velocity gradient observed in PREM. The accumulation of subducted slabs at the base of the mantle is expected to produce increased seismic velocities (Wyssession, 1996b) and is thus associated with the seismic discontinuity. Given that no subduction has taken place at this location of the Pacific in the past 180 Myr (Richards and Engebretson, 1992; Ricard *et al.*, 1993; Lithgow-Bertelloni and Richards, 1998) no discontinuity would be expected, in agreement with a PREM structure. Hernlund *et al.* (2005) proposed that a hot profile through the mantle, such as in a mantle upwelling, would remain within the perovskite stability field because its geotherm would not intersect the post-perovskite phase boundary. This mechanism is suggested as an explanation for the absence of the discontinuity. In this location of D'' under the east central Pacific, the temperature is not as high as in the large low-velocity province (LLVP) beneath the Pacific found to the southwest and does not appear to be consistent with the model of Hernlund *et al.* (2005).

Comparison with the radial velocity structure of D'' under the Pacific Ocean

A velocity discontinuity at the top of D'' has been observed in many different regions around the world; see Nataf and Houard (1993); Krüger *et al.* (1995); Loper and Lay (1995); Wyssession *et al.* (1998); Helmberger *et al.* (2005); Lay and Garnero (2007, 2011); Garnero and McNamara (2008); and Wookey and Dobson (2008) for a review. Nonetheless, there exist regions where the discontinuity has not been found (e. g., Wyssession *et al.*, 1998). Studies using the prevalent method for determining the radial velocity structure of the lowermost mantle, i. e. the search for the triplicated *Scd* arrival (e. g., Lay and Helmberger, 1983), argue for the existence of a strong discontinuity at the top of D'' in regions of downwelling mantle and high shear velocities in tomographic models (Helmberger *et al.*, 2005). Assuming that a solid-solid phase transition in the lowermost mantle were to occur, Sidorin *et al.* (1999a, 1999b) developed a method to thermally map shear wave velocities into temperatures and from there to the elevation of a phase/seismic velocity discontinuity above the CMB. Under this model, the discontinuity would be a global feature and it would be found higher above the CMB in regions of high velocities, and closer to the CMB where velocities are low. The experimental observation of a phase transition from perovskite to post-perovskite at 125 GPa (equivalent to 2,700 km depth) and 2,500 K (Murakami *et al.*, 2004) seems generally consistent with seismic observations of the velocity discontinuity at the top of D''. The evidence for a D'' triplication from secondary arrivals between *S* and *ScS*, however,

is less convincing in regions of low velocities and possible upwelling such as under the central Pacific (Helmberger *et al.*, 2005). Newer results, using expanded data sets, as well as a stacking technique to improve the observation of the *SdS* phase, confirm the existence of the discontinuity in certain regions under the central Pacific (Russell *et al.*, 2001; Avants *et al.*, 2006; Lay *et al.*, 2006; and Ohta *et al.*, 2008).

One of the earliest studies that specifically searched for a discontinuity and failed to find it was conducted by Schlittenhardt *et al.* (1985). Amongst others, they used earthquakes in Fiji, recorded by stations in North America, which sampled a patch of D'' to the southwest of, and partially overlapping, the region chosen for this study (their study area is labeled S in Figure 1). They looked for, but did not find, the waveform distortions of P_{diff} and SH_{diff} pulses produced by a triplicated arrival at epicentral distances between 95° and 120°. Schlittenhardt *et al.* (1985) generated reflectivity synthetic seismograms comparing PREM to discontinuous model SLHO (Lay and Helmberger, 1983) and concluded that PREM fits better the time domain waveforms. In the present study, PREM was chosen as the preferred model because it fits both the decay constant (in the frequency domain) and the SH_{diff} waveforms (in the time domain). Garnero *et al.* (1988) proposed a lower mantle model whereby a V_s discontinuity (model B) in regions of the Pacific bordering the coast of North America fades away to no discontinuity (model A) in the mid-Pacific (G88, Figure 1). They based their conclusions on anomalously large *S-SKS* times and on the lack of waveform evidence at 92° for any arrivals from a discontinuity. In later work, however, Garnero *et al.* (1993) concluded, from the triplicated arrival *Scd* and from *ScS-S* differential travel times, that a discontinuity exists under the same region where no discontinuity was found in their previous study (SGHP, Figure 1). Model SGHP (Garnero *et al.*, 1993) shows a discontinuity of ~2.4% and a D'' thickness of 180 km. Model RJK2705 (Valenzuela-Wong, 1996; Valenzuela and Wyssession, 1998) for a region located near and to the southeast of the one reported in this study (V96 in Figure 1) has a thickness (186 km) that closely agrees with that of SGHP but shows a greater velocity jump (~3.4%) at the top of D'' and a lower velocity at the CMB. Just like in this study, they used the decay constant technique. The differing results between their study and ours should not be surprising given the strong heterogeneity of D'' on all scales. Garnero *et al.* (1993) also show evidence for a discontinuity in the west central Pacific to the east of the Mariana Islands and to the north of Vanuatu and the Solomon Islands (G93, Figure 1). The thickness of the basal layer in this region was poorly constrained but appeared to be around 280 km.

Later work (Russell *et al.*, 2001; Avants *et al.*, 2006; Lay *et al.*, 2006; Ohta *et al.*, 2008; and Hutko *et al.*, 2009) used a stacking technique in order to enhance the detection of the triplicated arrival between *S* and *ScS* (or *P* and *PcP*) in the same general region, SGHP, studied by Garnero *et al.* (1993). These studies used earthquakes in the Tonga-Fiji region recorded predominantly by stations in the western United States. Russell *et al.* (2001) found a *D''* layer with a thickness of 230 km and a discontinuity for both *P* and *S* waves with velocity increases of 0.75% and 1.7%, respectively. These velocity jumps are somewhat smaller than in *D''* underneath circum-Pacific regions (Avants *et al.*, 2006). Russell *et al.* (2001) also found an ultralow velocity zone (ULVZ). Avants *et al.* (2006) found a discontinuous velocity jump followed by two discontinuous velocity drops which they interpreted as a lens of post-perovskite material above a ULVZ. They noticed high variability on scale lengths on the order of 130 km such that the *S* wave velocity increase at the discontinuity varied between 0.5 and 2.3% and the depth of the discontinuity ranged from 2,490 to 2,735 km. Further work (Lay *et al.*, 2006; Ohta *et al.*, 2008) using expanded data sets confirmed these findings. The overall *S* wave velocity structure where the post-perovskite lens has been observed is slightly slower than PREM. Hutko *et al.* (2009) observed a small (0.5%) *P* wave velocity jump at a discontinuity 140 km above the CMB and a ULVZ underneath. Unlike the work carried out by Lay's group (Russell *et al.*, 2001; Avants *et al.*, 2006; Lay *et al.*, 2006; Ohta *et al.*, 2008; and Hutko *et al.*, 2009) using forward modeling of data stacks, Kawai and Geller (2010) followed a waveform inversion approach in the same broad region. They observed shear velocity decreases and increases of 1%–1.5% in the zones from 400 to 500 km and from 300 to 400 km above the CMB, respectively. They also reported 0.5%–1% velocity increases and decreases in the zones from 100 to 200 km and from 0 to 100 km above the CMB, respectively. Sun and Helmberger (2008) modeled *Scd* arrivals in a region of the east central Pacific centered around 2°N, 105°W and obtained a velocity distribution with a 3.5% velocity increase at a discontinuity located 220 km above the core-mantle boundary. Wen (2002) studied the central Pacific using the *SH* components of events in Fiji recorded in the western US and by the MOMA array at epicentral distances ranging from 83 to 108°. He found that a negative velocity gradient of 3% relative to PREM at the bottom 300 km of the mantle fits the data. Wen also studied a MOMA profile sampling *D''* under the north Pacific and southern Alaska using SH_{diff} at distances from about 101 to 110° and concluded that PREM satisfactorily explains the observations.

Conclusions

The *S* wave radial velocity structure of the *D''* region was determined for a spot of the east central Pacific Ocean centered at 19°N, 132°W. This area falls in the transition from the large low-velocity province beneath the Pacific to the circum-Pacific high-velocity provinces. The technique of the decay constant was applied in the frequency domain to the *S* and S_{diff} waves of an earthquake in the Tonga Islands recorded by the MOMA array in the northeastern United States. Reflectivity synthetic seismograms were generated by forward modeling while trying different models. These included PREM, models with a gradual decrease of the velocity with increasing depth, models with a gradual increase, and a suite of models with a discontinuous increase at the top of *D''* followed by a gradual decrease in the form of a complementary error function, consistent with a thermal boundary layer. Care was taken to guarantee the reliability of the models by requiring a good fit of the decay constant in the frequency domain, a correlation coefficient for the least squares fit greater than or equal to 0.9, and a good fit of the time domain waveforms. A couple models were found to fit the decay constant data since the calculated γ falls within one standard deviation of the observed γ . PREM, however, is closer to the actual data points than J738, the model with a discontinuity. Comparison of the waveforms in the time domain also shows PREM to be better and it was chosen as the preferred model. Consequently, *D''* at this location is 150 km thick and has a slightly negative velocity gradient with increasing depth. No velocity discontinuity is observed at the top of *D''*. The *S* wave velocity is relatively low and the temperatures at the base of the mantle are high, but not so much as in the LLVP of the Pacific. The velocity structure is consistent with *D''* acting as a thermal boundary layer. Iron enrichment of mantle materials through chemical reactions is also a possibility since it would result in lowered velocities. The downwelling of oceanic slabs is correlated with regions of high velocities in the lowermost mantle and also with the locations of some of the best documented discontinuities. Therefore a discontinuity is not expected in the area of the present study because it is not a subduction zone. Likewise, no subduction has taken place here during the last 180 Myr.

Acknowledgments

We are thankful to Tim Clarke for providing the computer code used to generate the reflectivity synthetic seismograms. Karen Fischer, Tim Clarke and Michael Wyssession were co-PIs of project MOMA. We thank Manuel Velásquez for computer support. We are also thankful to Xyoli Pérez-Campos and two anonymous reviewers whose valuable

comments greatly improved the manuscript. One of us (LFTM) received partial funding for his graduate studies from Mexico's Consejo Nacional de Ciencia y Tecnología through grant 34299-T.

Bibliography

- Aki K., Richards P.G., 2002, *Quantitative Seismology, Second edition*, University Science Books, Sausalito, California, 700 pp.
- Ammon C.J., Lay T., 2007, Nuclear test illuminates USArray data quality, *Eos Trans. AGU*, *88*, 37-38, doi:10.1029/2007EO040001.
- Anderson D.L., Hart R.S., 1978a, Attenuation models of the Earth, *Phys. Earth Planet. Int.*, *16*, 289-306.
- Anderson D.L., Hart R.S., 1978b, *Q* of the Earth, *J. Geophys. Res.*, *83*, 5,869-5,882.
- Avants M., Lay T., Russell S.A., Garnero E.J., 2006, Shear velocity variation within the D" region beneath the central Pacific, *J. Geophys. Res.*, *111*, B05305, doi:10.1029/2004JB003270.
- Bataille K., Flatté S.M., 1988, Inhomogeneities near the core-mantle boundary inferred from short-period scattered PKP waves recorded at the Global Digital Seismograph Network, *J. Geophys. Res.*, *93*, 15,057-15,064.
- Bataille K., Lund F., 1996, Strong scattering of short-period seismic waves by the core-mantle boundary and the *P*-diffracted wave, *Geophys. Res. Lett.*, *23*, 2,413-2,416.
- Bataille K., Wu R.S., Flatté S.M., 1990, Inhomogeneities near the core-mantle boundary evidenced from scattered waves: A review, *Pure Appl. Geophys.*, *132*, 151-173.
- Bhattacharyya J., Masters G., Shearer P., 1995a, Shear wave attenuation in the mantle from long-period body waveforms (abstract), *International Union of Geodesy and Geophysics XXI General Assembly abstracts*, B403.
- Bhattacharyya J., Masters G., Shearer P., 1995b, A Q_b model for the mantle (abstract), *Eos Trans. AGU*, *76* (46), Fall Meeting Suppl., F385.
- Bolt B.A., Niazi M., Somerville M.R., 1970, Diffracted ScS and the shear velocity at the core boundary, *Geophys. J. R. astr. Soc.*, *19*, 299-305.
- Chapman C.H., Phinney R.A., 1972, Diffracted seismic signals and their numerical solution, in *Seismology: Body waves and sources, Methods in computational Physics*, *12*, edited by B. A: Bolt, 165-230, Academic Press, New York City, N. Y.
- Doornbos D.J., 1983, Present seismic evidence for a boundary layer at the base of the mantle, *J. Geophys. Res.*, *88*, 3,498-3,505.
- Doornbos D.J., Mondt J.C., 1979a, Attenuation of *P* and *S* waves diffracted around the core, *Geophys. J. R. astr. Soc.*, *57*, 353-379.
- Doornbos D.J., Mondt J.C., 1979b, *P* and *S* waves diffracted around the core and the velocity structure at the base of the mantle, *Geophys. J. R. astr. Soc.*, *57*, 381-395.
- Doornbos D.J., Spiliopoulos S., Stacey F.D., 1986, Seismological properties of D" and the structure of a thermal boundary layer, *Phys. Earth Planet. Int.*, *41*, 225-239.
- Durek J.J., Ekström G., 1996, A radial model of anelasticity consistent with long-period surface-wave attenuation, *Bull. Seism. Soc. Am.*, *86*, 144-158.
- Dziewonski A.M., Anderson D.L., 1981, Preliminary reference Earth model, *Phys. Earth Planet. Int.*, *25*, 297-356.
- Dziewonski A.M., Ekström G., Salganik M.P., 1996, Centroid-moment tensor solutions for April-June 1995, *Phys. Earth Planet. Int.*, *96*, 1-13.
- Fischer K.M., Wyssession M.E., Clarke T.J., Fouch M.J., Al-Eqabi G.I., Shore P.J., Valenzuela R.W., Li A., Zaslav J.M., 1996, The 1995-1996 Missouri to Massachusetts broadband seismometer deployment, *IRIS Newsletter*, *XV* (2), 6-9.
- Garnero E.J., 2000, Heterogeneity of the lowermost mantle, *Annu. Rev. Earth Planet. Sci.*, *28*, 509-537.
- Garnero E.J., Helmberger D.V., 1995, A very slow basal layer underlying large-scale low-velocity anomalies in the lower mantle beneath the Pacific: Evidence from core phases, *Phys. Earth Planet. Int.*, *91*, 161-176.
- Garnero E.J., Helmberger D.V., 1996, Seismic detection of a thin laterally varying boundary layer at the base of the mantle beneath the central-Pacific, *Geophys. Res. Lett.*, *23*, 977-980.
- Garnero E., Helmberger D., Engen G., 1988, Lateral variations near the core-mantle boundary, *Geophys. Res. Lett.*, *15*, 609-612.

- Garnero E.J., Helmberger D.V., Grand S., 1993, Preliminary evidence for a lower mantle shear wave velocity discontinuity beneath the central Pacific, *Phys. Earth Planet. Int.*, *79*, 335-347.
- Garnero E.J., McNamara A.K., 2008, Structure and dynamics of Earth's lower mantle, *Science*, *320*, 626-628.
- Helmberger D., Lay T., Ni S., Gurnis M., 2005, Deep mantle structure and the postperovskite phase transition, *Proc. Natl. Acad. Sci.*, *102*, 17,257-17,263.
- Hernlund J.W., Thomas C., Tackley P.J., 2005, A doubling of the post-perovskite phase boundary and structure of the Earth's lowermost mantle, *Nature*, *434*, 882-886.
- Hutko A.R., Lay T., Revenaugh J., 2009, Localized double-array stacking analysis of *PcP*: D" and ULVZ structure beneath the Cocos plate, Mexico, central Pacific, and north Pacific, *Phys. Earth Planet. Int.*, *173*, 60-74.
- Kawai K., Geller R.J., 2010, Waveform inversion for localized seismic structure and an application to D" structure beneath the Pacific, *J. Geophys. Res.*, *115*, B01305, doi:10.1029/2009JB006503.
- Kennett B. L. N., 1980, Seismic waves in a stratified half space - II. Theoretical seismograms, *Geophys. J. R. Astr. Soc.*, *61*, 1-10.
- Knittle E., Jeanloz R., 1989, Simulating the core-mantle boundary: An experimental study of high-pressure reactions between silicates and liquid iron, *Geophys. Res. Lett.*, *16*, 609-612.
- Knittle E., Jeanloz R., 1991, Earth's core-mantle boundary: Results of experiments at high pressures and temperatures, *Science*, *251*, 1,438 - 1,443.
- Krüger F., Weber M., Scherbaum M., Schlittenhardt J., 1995, Evidence for normal and inhomogeneous lowermost mantle and core-mantle boundary structure under the Arctic and northern Canada, *Geophys. J. Int.*, *122*, 637-657.
- Lay T., 1989, Structure of the core-mantle transition zone: A chemical and thermal boundary layer, *Eos Trans. AGU*, *70*, 49, 54-55, 58-59.
- Lay T., Garnero E.J., 2007, Reconciling the postperovskite phase with seismological observations of lowermost mantle structure, in *Post-perovskite: The last mantle phase transition*, *Geophys. Monogr.*, *174*, edited by K. Hirose, J. Brodholt, T. Lay and D. Yuen, 129-153, American Geophysical Union, Washington, D. C.
- Lay T., Garnero E.J., 2011, Deep mantle seismic modeling and imaging, *Annu. Rev. Earth Planet. Sci.*, *39*, 91-123.
- Lay T., Helmberger D.V., 1983, A lower mantle S-wave triplication and the shear velocity structure of D", *Geophys. J. R. Astr. Soc.*, *75*, 799-837.
- Lay T., Hernlund J., Garnero E.J., Thorne M.S., 2006, A post-perovskite lens and D" heat flux beneath the central Pacific, *Science*, *314*, 1272-1276.
- Lay T., Williams Q., Garnero E.J., 1998, The core-mantle boundary layer and deep Earth dynamics, *Nature*, *392*, 461-468.
- Lithgow-Bertelloni C., Richards M.A., 1998, The dynamics of Cenozoic and Mesozoic plate motions, *Rev. Geophys.*, *36*, 27-78.
- Loper D.E., Lay T., 1995, The core-mantle boundary region, *J. Geophys. Res.*, *100*, 6,397-6,420.
- Mondt J.C., 1977, *SH* waves: Theory and observations for epicentral distances greater than 90 degrees, *Phys. Earth Planet. Int.*, *15*, 46-59.
- Mori J., Helmberger D.V., 1995, Localized boundary layer below the mid-Pacific velocity anomaly identified from a *PcP* precursor, *J. Geophys. Res.*, *100*, 20,359-20,365.
- Mula A.H.G., 1981, Amplitudes of diffracted long-period *P* and *S* waves and the velocities and *Q* structure at the base of the mantle, *J. Geophys. Res.*, *86*, 4,999-5,011.
- Mula A.H., Müller G., 1980, Ray parameters of diffracted long period *P* and *S* waves and the velocities at the base of the mantle, *Pure Appl. Geophys.*, *118*, 1,272-1,292.
- Murakami M., Hirose K., Kawamura K., Sata N., Ohishi Y., 2004, Post-perovskite phase transition in MgSiO_3 , *Science*, *304*, 855-858.
- Nataf H.-C., Houard S., 1993, Seismic discontinuity at the top of D": A world-wide feature?, *Geophys. Res. Lett.*, *20*, 2,371-2,374.
- Ohta K., Hirose K., Lay T., Sata N., Ohishi Y., 2008, Phase transitions in pyrolite and MORB at lowermost mantle conditions: Implications

- for a MORB-rich pile above the core-mantle boundary, *Earth Planet. Sci. Lett.*, *267*, 107-117.
- Phinney R.A., Alexander S.S., 1966, *P* wave diffraction theory and the structure of the core-mantle boundary, *J. Geophys. Res.*, *71*, 5959-5975.
- Ricard Y., Richards M., Lithgow-Bertelloni C., Le Stunff Y., 1993, A geodynamic model of mantle density heterogeneity, *J. Geophys. Res.*, *98*, 21,895-21,909.
- Richards M.A., Engebretson D.C., 1992, Large-scale mantle convection and the history of subduction, *Nature*, *355*, 437-440.
- Russell S.A., Reasoner C., Lay T., Revenaugh J., 2001, Coexisting shear- and compressional-wave seismic velocity discontinuities beneath the central Pacific, *Geophys. Res. Lett.*, *28*, 2,281-2,284.
- Sailor R.V., Dziewonski A.M., 1978, Measurements and interpretation of normal mode attenuation, *Geophys. J. R. Astr. Soc.*, *53*, 559-581.
- Schlittenhardt J., Schweitzer J., Müller G., 1985, Evidence against a discontinuity at the top of *D''*, *Geophys. J. R. Astr. Soc.*, *81*, 295-306.
- Sidorin I., Gurnis M., Helmberger D.V., 1999a, Evidence for a ubiquitous seismic discontinuity at the base of the mantle, *Science*, *286*, 1,326-1,331.
- Sidorin I., Gurnis M., Helmberger D.V., 1999b, Dynamics of a phase change at the base of the mantle consistent with seismological observations, *J. Geophys. Res.*, *104*, 15,005-15,023.
- Stacey F.D., Loper D.E., 1983, The thermal boundary-layer interpretation of *D''* and its role as a plume source, *Phys. Earth Planet. Int.*, *33*, 45-55.
- Stein S., Mills J.M. Jr., Geller R.J., 1981, Q^{-1} models from data space inversion of fundamental spheroidal mode attenuation measurements, in *Anelasticity in the Earth*, *Geodynamics Ser.*, *4*, edited by F. D. Stacey, M. S. Paterson and A. Nicholas, 39-53, American Geophysical Union, Washington, D. C.
- Stein S., Wysession M., 2003, *An introduction to Seismology, earthquakes, and Earth structure*, 498 pp., Blackwell Publishing, Malden, Massachusetts.
- Sun D., Helmberger D., 2008, Lower mantle tomography and phase change mapping, *J. Geophys. Res.*, *113*, B10305, doi:10.1029/2007JB005289.
- Turcotte D.L., Schubert G., 2002, *Geodynamics, Second edition*, 456 pp., Cambridge University Press, Cambridge, England.
- Valenzuela-Wong R., 1996, Lateral and radial velocity structure at the base of the mantle from diffracted shear waves, Ph. D. thesis, 255 pp., Washington University, St. Louis, Missouri.
- Valenzuela R.W., Wysession M.E., 1998, Illuminating the base of the mantle with diffracted waves, in *The core-mantle boundary region*, *Geodynamics Ser.*, *28*, edited by M. Gurnis, M. E. Wysession, E. Knittle and B. Buffett, 57-71, American Geophysical Union, Washington, D. C.
- Valenzuela R.W., Wysession M.E., Neustadt M.O., Butler J.L., 2000, Lateral variations at the base of the mantle from profiles of digital S_{diff} data, *J. Geophys. Res.*, *105*, 6,201-6,220.
- Van Loenen P.M., 1988, *S* velocity at the base of the mantle from diffracted *SH* waves recorded by the NARS array, M. Sc. thesis, Department of Theoretical Geophysics, Utrecht, The Netherlands, 25 pp.
- Walpole R.E., Myers R.H., 1993, *Probability and Statistics for engineers and scientists, Fifth edition*, 766 pp., Macmillan Publishing Company, New York.
- Wen L., 2002, An *SH* hybrid method and shear velocity structures in the lowermost mantle beneath the central Pacific and South Atlantic oceans, *J. Geophys. Res.*, *107*, B3, 2055, doi:10.1029/2001JB000499.
- Widmer R., Masters G., Gilbert F., 1991, Spherically symmetric attenuation within the Earth from normal mode data, *Geophys. J. Int.*, *104*, 541-553.
- Williams Q., Garnero E.J., 1996, Seismic evidence for partial melt at the base of Earth's mantle, *Science*, *273*, 1,528-1,530.
- Wookey J., Dobson D.P., 2008, Between a rock and a hot place: The core-mantle boundary, *Phil. Trans. R. Soc. A*, *366*, 4,543-4,557.
- Wright C., Lyons J.A., 1981, Further evidence for radial velocity anomalies in the lower mantle, *Pure Appl. Geophys.*, *119*, 137-162.

Wyssession M.E., 1996a, How well do we utilize global seismicity?, *Bull. Seism. Soc. Am.*, 86, 1,207-1,219.

Wyssession M.E., 1996b, Imaging cold rock at the base of the mantle: The sometimes fate of slabs?, in *Subduction: Top to bottom, Geophys. Monogr. 96*, edited by G. E. Bebout, D. W. Scholl, S. H. Kirby and John P. Platt, 369-384, American Geophysical Union, Washington, D. C.

Wyssession M.E., Fischer K.M., Clarke T.J., Al-eqabi G.I., Fouch M.J., Shore P.J., Valenzuela R.W., Li A., Zaslav J.M., 1996. Slicing into the Earth, *Eos Trans. AGU*, 77, 477, 480-482.

Wyssession M.E., Lay T., Revenaugh J., Williams Q., Garnero E.J., Jeanloz R., Kellogg L.H., 1998, The D" discontinuity and its implications, in *The core-mantle boundary region, Geodynamics Ser., 28*, edited by M. Gurnis, M. E. Wyssession, E. Knittle and B. Buffett, 273-297, American Geophysical Union, Washington, D. C.

Using subsurface geophysical methods in flood control: A resistivity survey to define underground storage capacity of a sand body in Ciudad Juárez, Mexico

Oscar S. Dena O.*, Griselda Obeso C., Diane Doser, Jesús E. Leyva, E. Rascon, Francisco Gómez and Miguel Domínguez A.

Received: February 01, 2011; accepted: May 28, 2012; published on line: June 29, 2012

Resumen

En una zona localizada al sur de Ciudad Juárez, Chihuahua, que presenta serios problemas de inundación durante la época de lluvias, se llevó a cabo un estudio geoelectrico de corriente directa, con el objetivo de determinar y evaluar la capacidad de almacenamiento de un estrato subyacente de arenas permeables, para prevenir inundaciones en "El Barreal", el cual se caracteriza por la presencia de naves industriales y desarrollos urbanos de tipo de interés social. En julio del 2008, eventos hidrometeorológicos intensos registraron 68 mm de precipitación en 24 horas, y un acumulado mensual de 146 mm, el cual representa casi el 50% de la precipitación anual media en Ciudad Juárez. Tales niveles de intensidad de precipitación ocasionaron inundaciones en gran parte de la superficie de la laguna "El Barreal", dejando cientos de casas y parques industriales anegados durante la contingencia. Un total de 9 Sondeos Eléctricos Verticales (SEV) se realizaron utilizando el arreglo Schlumberger para generar un modelo geológico. Dos zanjas exploratorias se excavaron para calibrar el método y realizar pruebas de permeabilidad. El método exitosamente diferenció las unidades estratigráficas de grano fino (limos y arcillas) y de grano grueso (arenas), para así inferir la presencia y geometría de cuerpos de arena permeable capaces de almacenar y transportar parte del volumen de los escurrimientos al acuífero, y funcionar así como una estrategia de mitigación para inundaciones en la zona de "El Barreal". Por lo tanto, el implementar una batería o red de pozos de infiltración, localizados estratégicamente en la parte oeste del sistema lagunar y diseñados para alcanzar profundidades mayores a los 12 m, es una solución ingenieril práctica y factible para parcialmente resolver los problemas de inundación en la parte baja de la cuenca el Barreal.

Palabras clave: runoff, flooding, hydrology, VES, permeability, infiltration.

O.S. Dena O.*
G. Obeso C.
J. E. Leyva
M. Domínguez A.
Instituto de Ingeniería y Tecnología
Universidad Autónoma de Ciudad Juárez
*Corresponding author: osdena@gmail.com

Abstract

A DC resistivity survey was conducted over a flood prone area (playa lake) in the southern urbanized area of Ciudad Juárez, Chihuahua, Mexico to locate and evaluate the water storage capacity of a subsurface permeable sand stratum to prevent flooding "El Barreal", a large urban area of housing developments and industrial compounds. Recent major floods in July 2008 record were caused by precipitation levels of 68 mm in 24 hours, and a monthly accumulation of 146 mm. Hundreds of homes and industrial enterprises were flooded. Nine vertical electrical soundings (VES) were conducted utilizing a Schlumberger array to generate a geologic model. Two trenches were excavated to calibrated the method and perform permeability tests. The method successfully discriminated between fine grained clay and silt and coarse sand. The subsurface sand body will be used as a temporary storage facility for flood control during summer storms amounting to up to half the total annual rainfall.

Key words: escurrimiento, inundación, hidrología, SEV, permeabilidad, infiltración.

E. Rascon
F. Gómez
Junta Municipal de Aguas y Saneamiento

D. Doser
Department of Geological Sciences
University of Texas at El Paso

Introduction

Ciudad Juárez, Chihuahua is located in the central Chihuahuan Desert; with El Paso, Texas the cities form the twin Paso Del Norte metroplex (Figure 1a). This region of the Chihuahuan Desert is characterized by a semiarid climate with low precipitation rates (300 mm/yr) (Laboratorio de Climatología y Calidad del Aire-LCCA, 2008) occurring during the rainy season from early June to late August (LCCA, 2008). Summer rains in this area occur mainly in the form of heavy storms of short duration. Some of these storms

can discharge large amounts of water within minutes to a few hours (Comisión Nacional del Agua CNA, 2008).

Hydrologically the region is divided into eight major basins (Instituto Municipal de Investigación y Planeación IMIP, 2004). The 2006 and 2008 floods were caused by intense rainstorms responsible for 30 to 50% of the total yearly precipitation in less than 24 hours (LCCA, 2008). The urban area of El Barreal was developed after 2003 for residential and commercial use (Buró Nacional Inmobiliario BNI,

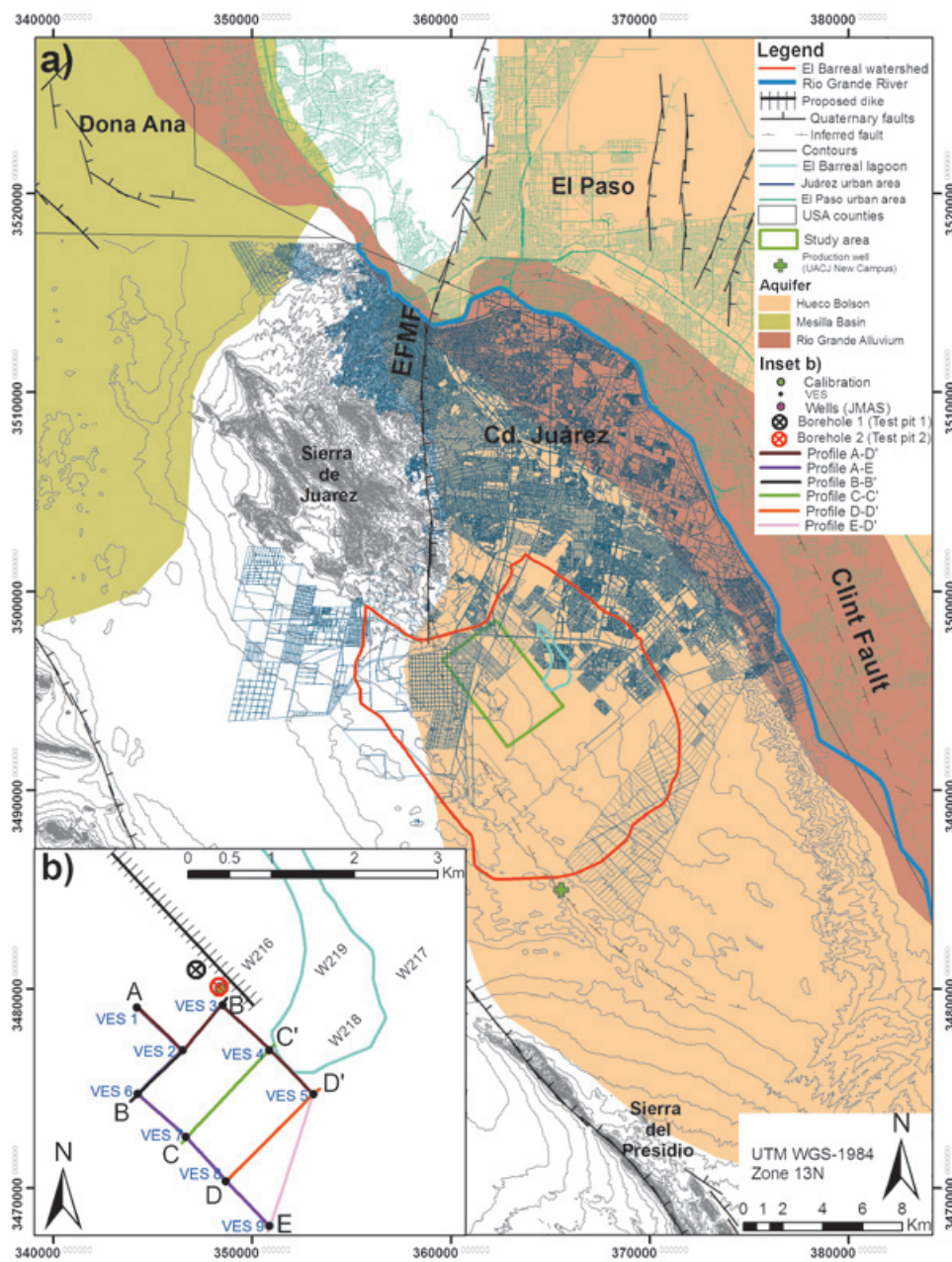


Figure 1. a) Regional location map. b) Inset of the study area (Green square). Letters represent geophysical profiles, the black hatched line represents the proposed dike and the pink dots represent the production well data available in the area. The trenches excavated to calibrate geophysics and perform open pit permeability tests are represented by black and red circles. Black dot represents location of Wenner array VES.

2009). Recommendations of the City Planning and Research Institute (IMIP) suggested preservation of the lake area, based on evidence from both hydrological modeling and historical records that it would flooded. Some small earth dams upstream (BNI, 2009) failed, chiefly due to lack of compaction and presence of impermeable clay cores, and a few absorption wells were unable to remove surface water as fast as it accumulated. During the July 2008 storms, the low lying area was totally flooded.

The State urban development offices (Secretaría de Desarrollo Urbano y Ecología, SEDUE) considered a solution consisting in a partial restoration of the lake area and the injection of excess water volumes into permeable strata of a shallow aquifer. A row of properly designed infiltration wells would be emplaced along a man-made embankment (Figure 1b).

Nine vertical electric soundings (VES) were performed with a Schlumberger array to delineate the depth and extent of non-permeable clay layers and the subsurface geometry of a sand body with enough permeability to store and deflect the excess runoff into the shallow aquifer. Two trenches were excavated to calibrate the geophysical findings and perform permeability tests of the selected strata. The geophysical survey proved to be an economical solution to image the depth and geometry of subsurface strata, which together with permeability results, led to a proper design for the injection of excess runoff during a major storm.

Background Studies

Hydrologic Setting

The Paso Del Norte region is located in the Basin and Range physiographic province. The topography of the Basin and Range is characterized by the presence of NNW trending mountain ranges and intermountain basins (Bolsos) with flat playa lakes (Hawley, 1993; Haenggi, 2002). Some playa lakes were formed as perennial pluvial lakes in late Pleistocene and especially during the last glacial maxima (early Wisconsin) (Hawley, 1993; Reeves, 1969). The largest Pleistocene Lake Palomas, covered an area inundating close to 7,800 km² in the bolson de Los Muertos (Reeves, 1969), approximately 60 kilometers southwest of the study area. These glacial lakes served as sinks for large hydrological basins often drained by two or more fluvial systems. The basin of El Barreal was not mentioned among the large glacial lakes (Reeves, 1969; Hawley, 1993; Allen, 2005; Castiglia and Fawcett, 2006), because of its smaller area (only 164 km²), and the absence of paleoclimatic studies.

El Barreal is a closed basin that drains the southeast Sierra de Juárez and adjacent highland areas (Figure 1a). The center of the basin is occupied by a flat playa covering an area of 2.3 km². There is 15 m of relief between the lowest point at the center of the basin and the highest point near Sierra de Juárez, and 3 m relief from the eastern boundary of the watershed to the center of the basin. Three to four midsize water streams (5-6 m crosssections) discharge into the basin (Figure 2b). Sediments in the basin surface range from sand to silt and clay towards the center of the basin.

The watershed of El Barreal covers approximately 164.114 km² (IMIP, 2004b), yielding an approximate runoff of 1,318.37 m³ (IMIP, 2004), for an average yearly precipitation of 300 mm (LCCA, 2008). This relatively large mass of water is transported by several first and second order intermittent streams that drain the runoff into a lower area defined by the 1,160 m elevation contour line, the historical boundary of the Laguna de Patos (El Barreal) (IMIP, 2004b). However, the flooded area could cover up to 6 km² unless hydraulic facilities are developed to contain the runoff (IMIP, 2004b).

The city granted permits for urban development, on the condition that earth dams were constructed upstream from the playa (IMIP, 2004b). However, this approach was not successful. In July 2008 the dams failed (Juárez Press, 2008).

Geologic Setting

The study area is geomorphologically defined as a flat, low-lying, desert playa flanked to the north by the Sierra de Juárez and to the south by Sierra del Presidio (Figure 2a). These mountain ranges and intervening basins represent the classic setting of the Basin and Range physiographic province, which is an uplifted region that records lithospheric thinning, extension and magmatism during the Tertiary (Keller and Baldrige, 1999). However, despite of the proximity to the Basin and Range province, the area of study actually lies within the southern portion of the Río Grande rift tectonic province as evidenced by a series of geological and geophysical features such as basin size and depth, presence of Quaternary tectonic activity, and crustal thinning (Seager and Morgan, 1979; Sinno *et al.*, 1986; Keller *et al.*, 1990; Averill, 2007), which differentiates the Río Grande rift from the Basin and Range (Keller and Baldrige, 1999).

As consequence of the tectonic setting, several main faults bounding the Hueco Bolson aquifer have been identified (Seager, 1980;

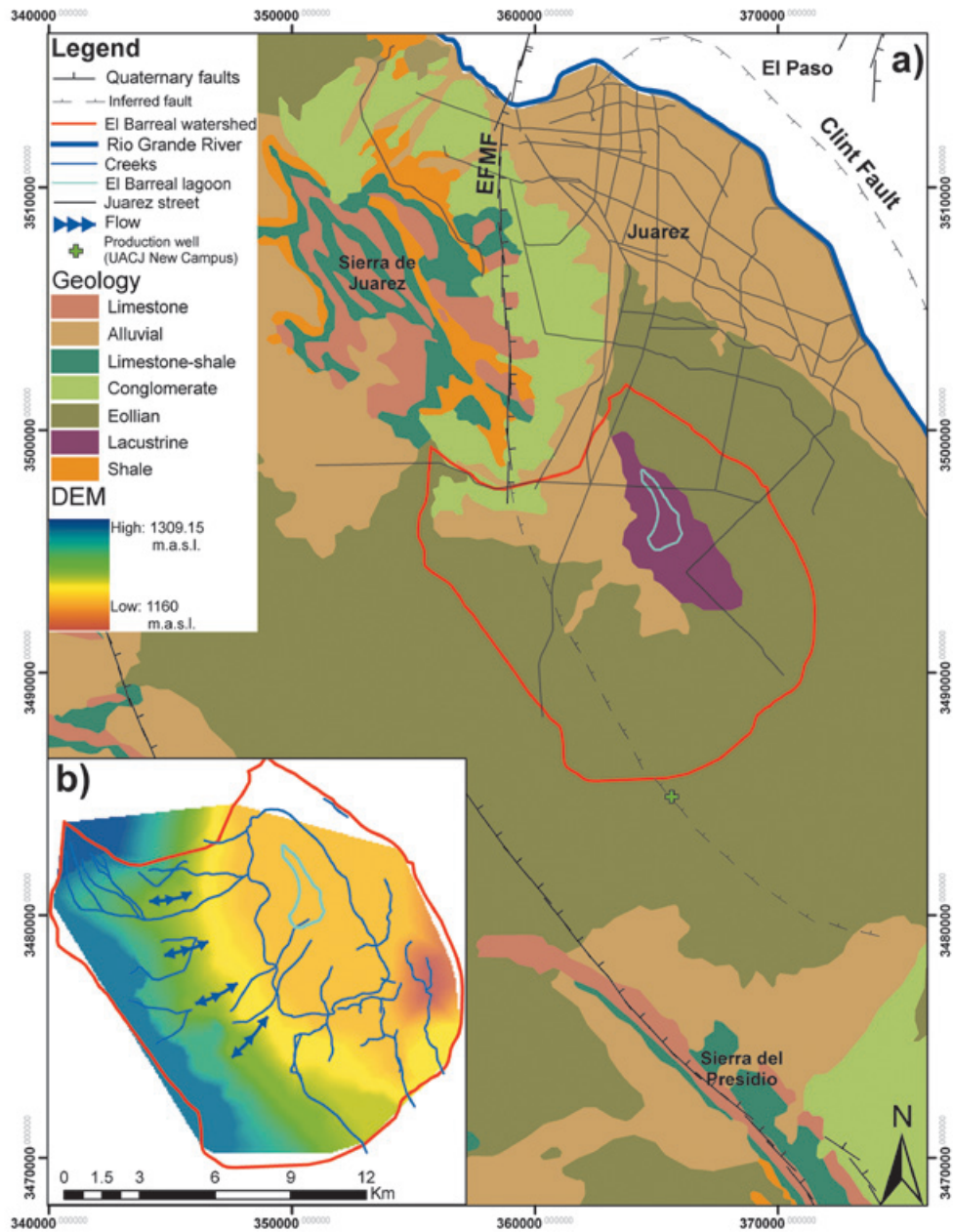


Figure 2. a) Geology of the El Barreal. Black hatched lines represent Quaternary faults and black spaced lines represent an important inferred fault by Burgos (2004) in the region. b) Inset of the El Barreal watershed showing flow patterns and the boundary (navy) of the ephemeral playa lake.

Burgos, 1993). Likewise intrabasin minor faulting, which has surface expressions, has also been reported (Sayre and Livingston, 1945; Knowles and Kennedy, 1956; Seager 1980; Burgos, 1993; McCalpin, 2006). The major faults flanking the basin are, at the western basin boundary, the East Franklin Mountain Fault (EFMF) and its prolongation into the Sierra de Juárez, and the Hueco Mountain fault that bounds the Hueco Bolson to the east (Figures 1 and 2a). The minor intrabasin faults scarps constitute an array of horsts, grabens and tilted

blocks in basin fill deposits (Seager, 1980). The other structural feature in the area is the Clint Fault, which is a major intrabasin fault inferred from analysis of stratigraphic data (Uphoff, 1978) that runs alongside the Río Grande marking the westernmost limit of the Diablo Platform uplift (Burgos, 1993). The age of the fault systems has been dated as 64.1 Ka by recent Infrared-Stimulated Luminescence Geochronology and sedimentology studies (McCalpin, 2006), which are half as old as the age assumed by Keaton and Barnes (1996).

In terms of sedimentation, the stratigraphic record of the area is comprised of varied depositional environments. The bedrock in the vicinity of the area is found approximately at 400 m depth (Burgos 1993; Rascón and Gómez, 2007; Dena, 2007; Obeso, 2008) and is commonly composed of carbonates from the Chihuahua Trough (Haengii, 2002). The sediments atop the basement represent a mixture of fluvial, lacustrine and terminal deltaic deposits derived from the ancient (post-Kansan) Río Grande deposits (Reeves, 1969) as it filled the structural basin formed by the Río Grande Rift, which through continued Neogene uplift again exposed part of the sediment package at the surface (Keller and Baldrige, 1999). The sedimentary depositional environment of the deposits is commonly referred to as "alluvial" (Kernodle, 1992), in spite of the significant amounts of fluvial, lacustrine, and aeolian sediments that form these complex landforms (Hawley 1969; Hawley *et al.*, 2000; Hawley *et al.*, 2001). Modern surficial deposits atop the basin include a varied series of sedimentary environments, resembling at smaller and localized scales the ancient fluvial Río Grande and terminal (alluvial-lacustrine) depositional systems. These deposits, especially near the Sierra de Juárez, commonly accumulate in small endorheic micro-basins (e.g., study area) and are characterized by a series of fluvial (stream) and alluvial (fan) deposits found in the upstream (piedmont) areas of the basin. Terminal fan deposits and their associated feeding streams are found at the upstream margins of the playa lakes commonly located in the center or lowest elevation areas of the basins (Figure 2a). The central areas of the basins are dominated by fine grain size sediments accumulating in thick (several meters) layers intercalated by lenses or thin layers of coarser sand size deposits, as found in the production well data (Figure 3) from wells located close to the area of study (Figure 1b) provided by the Juárez Water Utility office (JMAS). These layered sediments would have been deposited by the progression of a terminal fans feeding streams on to the playa areas and their subsequent abandonment and covering by the continuing deposition of lacustrine deposits. Surficial playa deposits in the study area are surrounded by a thin and non-extensive aeolian sand sheet and overlaying nebkha dunes.

Geophysics

The shallow stratigraphy of El Barreal has not been formally described and there are no published geophysical studies that would aid in the location and visualization of any permeable strata geometry. Only isolated technical reports related to the construction of absorption wells exist, but are not available to the public.

Several previous geophysical studies have examined both the regional tectonic and stratigraphic setting chiefly in the Hueco Bolson; Keller and Baldrige (1999) summarized the geophysical work done in the area that resulted in the geographic distinction, in terms of tectonic provinces, between the Basin and Range and Río Grande Rift as well as an explanation of the rift evolution. More recently, Averill (2007) conducted Wide Angle Reflection and Refraction (WARR) studies that revealed the lithospheric structure beneath the rift, as well as the basin architecture. On a more local scale, O'Donnell (1998) conducted seismic reflection studies that mapped the basement at depths of 400 meters. Gravity studies have also revealed the presence of regional faults (Burgos, 1993), and the presence of Quaternary faults (Khatun *et al.*, 2007) and fracture zones suitable to be infiltrated by brines into the aquifer (Granillo, 2004). On the Mexican side of the border, an undulating bedrock surface formed by a series of horst and grabens at depths greater than 400 meters has been also modeled from gravity studies (Dena, 2007; Obeso, 2008). In the case of magnetic data, the Ciudad Juárez aeromagnetic chart (Servicio Geológico Mexicano (SGM), 2008) reveals the presence of intrusive bodies in the vicinity of the Sierra de Juárez, but the magnetic field intensity is relatively low in the El Barreal area. Time Domain Electromagnetic (TDEM) soundings (Rascón and Gómez, 2007) have mapped the basement at depths of 400 meters in strong agreement with the gravity studies conducted in the same area (e.g., Dena, 2007; Obeso, 2008). The textural discrimination of the sediment package was also inferred from TDEM studies, since it is widely documented (e.g., Telford *et al.*, 1995; Sharma, 1997; Palacky, 1987; Dena, 2000; Doser *et al.*, 2004) that clay dominated textures show lower electrical resistivity and magnetic susceptibility values than sand units. Rascón and Gómez (2007) also correlated the final results of TDEM studies and electrical resistivity logs with the lithology (Figure 4) of an exploration well drilled approximately 10 km south of the southern tip of El Barreal (Figure 1a). Their results showed that low resistivities were indeed associated with fine grain textures. The relatively low resistivity observed at depths ranging between 75 and 200 m was due to the presence of moderately good quality groundwater (Figure 4). This unexpected effect, could be the consequence that in a relatively clay dominated sedimentary units, the low resistivity might be attributed to the clay itself exclusively, and not necessarily to low quality water, as can be concluded from theoretical petrophysical calculations (Shevnin *et al.*, 2003). Nevertheless none of these geophysical studies were conducted specifically at El Barreal, and none of them had the specific goal of discriminating the shallow stratigraphy in the detailed fashion required in this study.

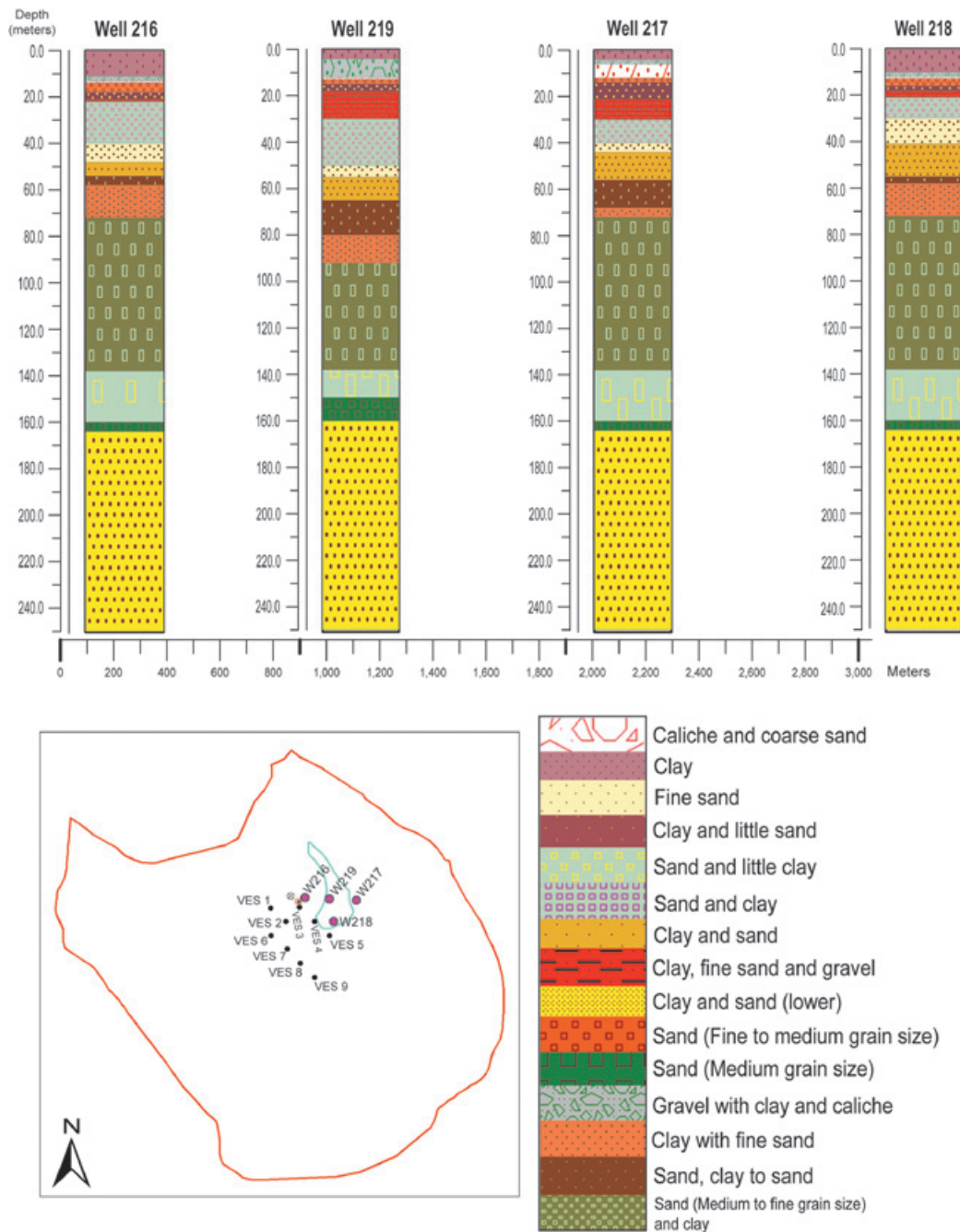


Figure 3. Production well lithology data.

Methodology

The methodological approach consisted of conducting an array sensitivity test to determine the best DC acquisition geometry to be deployed during the survey. The actual data acquisition was conducted utilizing the Schlumberger electrode array since it was shown to be sensitive enough to

discriminate between sand and clay strata, and at the same time be the least time and crew intensive. As a result, a total of 9 Vertical Electrical Soundings (VES), with depths of penetration not deeper than the water table (~100 m) were acquired in the vicinity of the proposed dike (Figure 1b).

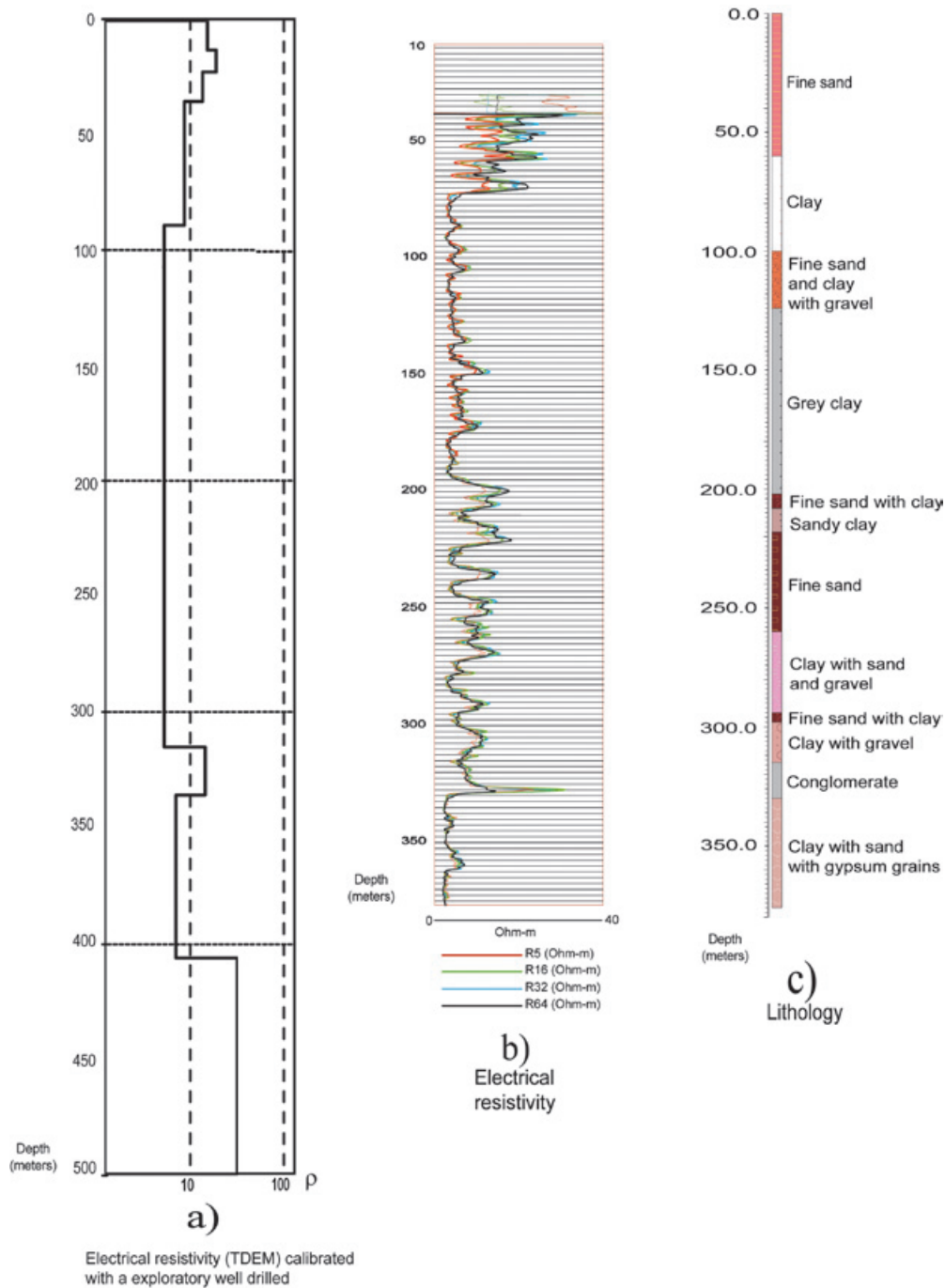


Figure 4. Geophysical and exploratory well studies in the vicinity of El Barreal watershed. a) TDEM 1D model. b) Electrical Resistivity log. c) Exploration well lithology data.

The initial resistivity curves were forward modeled with the software package IPI2win (Shevnin and Modin, 2003) to generate a preliminary geophysical model and to determine the locations of calibration trenches required to validate the geophysical findings. At one of the excavated trenches (borehole 2, Figure 1b) two

extra VES using Wenner arrays, since they are more sensitive to vertical variations at deeper measurements than the Schlumberger electrode configuration (Loke, 2004), were recorded perpendicular to each other in order to test for resistivity anisotropy.

We next used the lithostratigraphic information from borehole number 2 to fix the first 14 meters of the models to known strata thicknesses, and the water table depth (known from the production water wells) was kept also fixed during the inversion process (also carried out with IPI2win), allowing the software to invert exclusively for resistivity using these geologic constraints. For the intermediate layers located at depths between 14 m and ca. 100 m we inverted for both resistivity and thickness. The calibrated 1D geophysical models were correlated to each other by gridding the inverted results using the linear triangulation method. Further post-processing and final graphics for the geophysical model were produced with the software package GMT (Wessel and Smith, 1988). The geological model was produced by assigning stratigraphic horizons to the resistivity layers obtained from inversion of the DC soundings using the software package Rockworks (Rockware, Inc.; 2002). The permeability was determined by pouring water into an open pit and applying a Lefranc variable flow test with the descending hydraulic head method conducted through an open pipe resting on the clean sand layer at the location of borehole 1 (Figure 1b). The subsurface strata infiltration capacity was estimated applying the constant head method. Finally, the study area was zoned in terms of subsurface hydrostratigraphic properties by integrating all the geophysical findings and geomorphologic analysis of satellite imagery into a geographic information system (GIS).

Data and modeling

Resistivity

Resistivity readings were collected with a TERRAMETER SAS 300C instrument (ABEM, 1993) and digitized on a field computer to visualize and determine if the observed slope changes in the apparent resistivity curves were reasonable or if the reading had to be repeated. To generate 1D models relating true resistivity to depth, forward modeling was carried out utilizing the available lithology in the groundwater exploration well database (Figure 3) as starting models. The final 1D model for each sounding was calibrated and inverted constraining the inversion with the lithology observed in the trench of borehole 2 and the water table depth of ca. 100 m as reported by the JMAS (Rascón, 2008). The final 1D inverted models, with RMS fits less than 5%, were correlated by using the triangulation method of linear interpolation between the layered models.

Permeability test

With the data collected in the field-time (min), and depth (m), we calculated each of the required

variables to obtain the average permeability as follows: for each time interval (5 minutes) we determined the change in hydraulic head, and since the shape coefficient and the cross section of the shape are constant, we calculated the permeability for each time interval. After 81 minutes, the water had completely infiltrated into the ground, so we averaged the interval permeability. Once the average permeability was determined, the subsurface strata infiltration capacity was estimated (constant head method) with the following parameters: a 6 m length filtrant gallery, pipelines with inner ring casing diameters of 8, 12, and 16" (20.3, 30.5, 40.6 cm), and a maximum depth of 85 meters. The phreatic level is expected to be found at ca. 100 m and we assumed that it was not unlikely to find a sand dominated strata between depths of 12 m and 85 m since the lithology (Figure 3), and resistivity and gamma logs in nearby production wells supported our hypothesis of finding sand packages with similar grain size (Rascón, 2008).

Results

Apparent resistivity

The apparent resistivity curves (Figure 5) show how the sampled grain size related parameters vary geospatially, reflecting the presence of different resistivity families or domains in terms of the overall shape of the apparent resistivity curves. VES's 1, 5, 6, 7, 8 and 9 show "H" type curves indicating the presence of an anomalous low resistivity bed at intermediate depths (Telford *et al.*, 1995). On the other hand, VES's 2, 3 and 4 show "A" type resistivity patterns that monotonously increase with depth.

Forward modeling

The initial results of the forward modeling (Figure 6a) of VES 3 and VES 4 showed that an interpreted clay layer could be overlaying a possible permeable sand body located at a depth of ca. 14 m. To confirm or reject these results, a trench was excavated at a distance of approximately 20 m NW of the VES 3 location. The observed stratigraphic units (Figure 6b) showed the presence of a coarse sand unit at a depth of 12 m, but a fine grain sand layer embedded in the clay layers was also observed between depths of 1.70 m and 7 m. Additionally, as mentioned earlier, two more VES were conducted next to the trench to detect if any anisotropy was present (Figure 7). Since no significant changes were observed between the soundings, we concluded that, at least with the resolution provided by our electrode array and instrument, homogeneity and isotropy was indicated.

Vertical Electrical Soundings

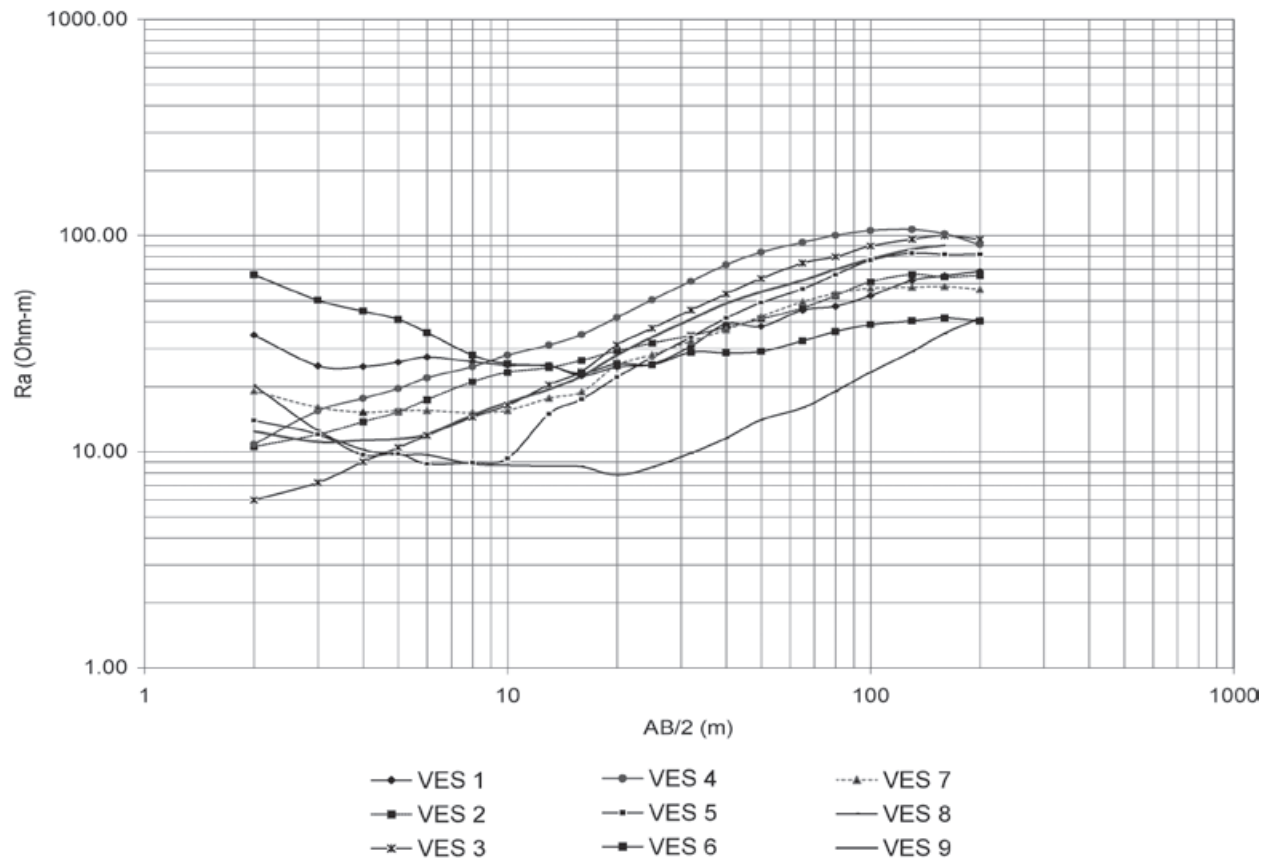


Figure 5. Apparent resistivity curves of the nine VES (Vertical Electrical Soundings) acquired at El Barreal utilizing the Schlumberger array. For sounding location see Figure 1(b).

Borehole tests

Two trenches were excavated (Figure 1b) to corroborate and calibrate the geophysical findings. The observed lithologic columns (Figure 8) are composed of 11 meters of lacustrine deposits at borehole 1 (BH1) (Figure 8a), and 12 meters of lacustrine deposits at borehole 2 (BH2) (Figure 8b). Within this sedimentary sequence, a package of fine sand with clay is found. The thickness of this layer is 5.5 m at BH2 and 9 m at BH1. The bottom of the lacustrine sequence at BH2 is composed of plastic clays and poorly compacted fine sands. These strata are not found at BH1, suggesting that during deposition a strong elevation gradient existed between the boreholes geographic locations because the flooding event is not recorded in both lithologic columns. Finally, a package of sediments with a grain size corresponding to fine to medium sands with no observed clays underlies the lacustrine sequence.

Inverted models

The most remarkable results obtained from the trench-calibrated final 1D inverted models (Figures 9, 10 and 11) are the presence of horizontal variations of the geoelectrical signature, expressed as the logarithm of the inverted resistivity, in the 2D models (Figures 12 and 13).

Based on these results several geoelectric units (G.E.U.) were defined by using ranges of resistivity values documented in global studies (e.g., Palacky, 1987; Sharma, 1997), local surveys (Dena 2007; Obeso, 2008; Rascón and Gómez, 2007), and the trench-calibrated resistivity responses of this survey. The classification resulted in six G.E.U.'s (Table I). The shallower units were correlated with the lithological column observed in the trench. The first unit ($r < 15$ ohm-m) is correlated with a clay dominated layer. The second unit ($15 < r <$

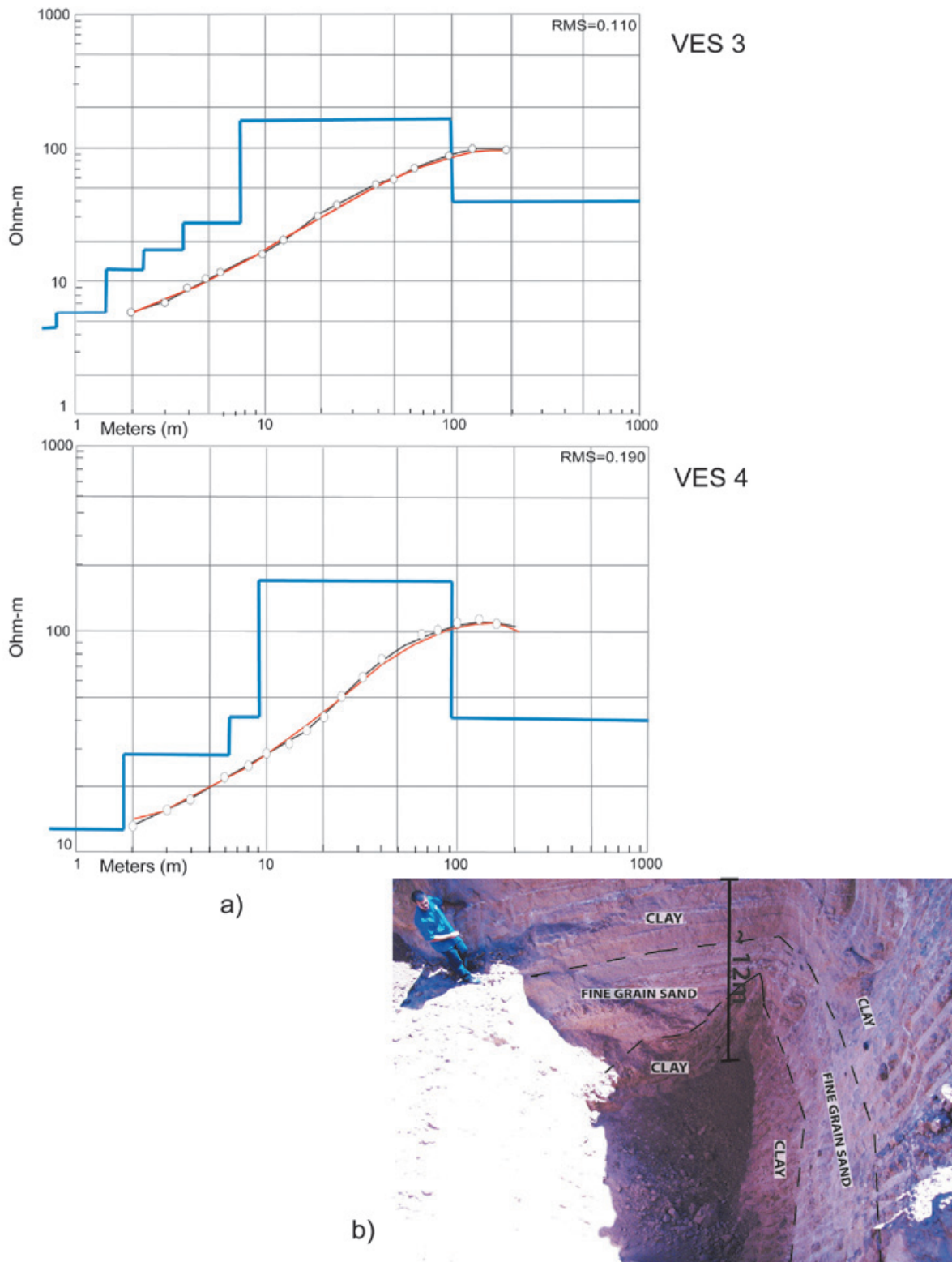


Figure 6. a) Initial forward modeling results. The observed points are represented by white dots, black line represents the resistivity curve of the observed points, red line represents the resistivity curve that best fits to the observed data curve, and the layers model is shown in blue line. b) Photograph of the excavated trench (Test pit) number 2.

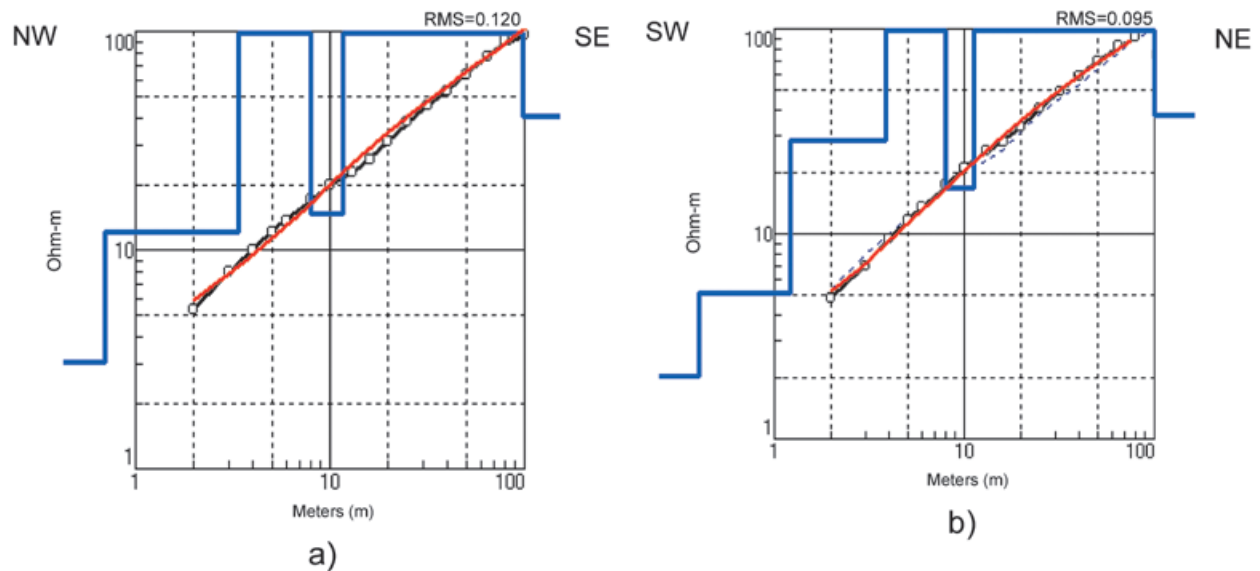


Figure 7. Wenner array VES conducted perpendicular to each other to test for anisotropy in the upper 30 m of depth. The observed points are represented by white dots, black line represents the resistivity curve of the observed points, red line represents the resistivity curve that best fits to the observed data curve, and the layers model is shown in blue line. For location see Figure 1(b).

50 ohm-m) is correlated with a fine grain sand layer, G.E.U. 3 ($50 < r < 80$ ohm-m) is correlated to compacted and cemented fine grain sands according to textural analysis. The deeper units were interpreted in terms of production wells since the excavated trenches did not reach depths greater than 14 m. G.E.U. 4 ($80 < r < 160$ ohm-m) is associated with the presence of medium grain sands with some clay. G.E.U. 5 ($160 < r < 270$ ohm-m) is interpreted as a thick package of non-cemented fine to medium grain sand. Finally, G.E.U. 6 ($30 < r < 70$ ohm-m) is associated with the top boundary of the aquifer, which, according to well data, is composed of medium to coarse grain sands.

Permeability

The permeability was calculated for each time interval with the data collected in the field. The resultant average permeability (2.48 m/d) was determined from 6 interval permeabilities (Table II).

The permeability test (Figure 14a) shows how the infiltration rate depends on the hydraulic head, i.e., the higher the charge, the faster the infiltration. Furthermore, this analysis reveals that permeable layers are found at depths close to the infiltration test depth. The estimated infiltration capacity results (Figure 14 b) display the projected infiltration yields for each inner ring casing diameter considered.

Table 1. Geoelectric Units (G.E.U.).

Unit	Lithology	ρ (Ohm-m) resistivity
G.E.U. 1	Clay (plastic)*	< 15
G.E.U. 2	Fine grain sand with clay*	15 - 50
G.E.U. 3	Fine grain sand compacted and cemented*	50 - 80
G.E.U. 4	Medium grain sand with some clay **	80-160
G.E.U. 5	Fine grain clean sand, not cemented **	160-270
G.E.U. 6	Aquifer (Medium to coarse grain sand)**	30 - 70

Source: *Test Trench, ** Production wells, JMAS.

Table 2. Open pit permeability test results.

Time (min)	Depth to the level (m)	H0-H1 (m)	t0-t1 (min)	C (1/m)	A (m ²)	k (m/min)	k (m/d)
8	0.160	0.600	8	1.5665	0.03243	0.001499	2.16
18	0.340	0.420	10	1.5665	0.03243	0.001672	2.41
28	0.444	0.316	10	1.5665	0.03243	0.001590	2.29
39	0.551	0.209	11	1.5665	0.03243	0.001680	2.42
49	0.620	0.140	10	1.5665	0.03243	0.001752	2.52
66	0.712	0.048	17	1.5665	0.03243	0.002124	3.06
81	0.760	0.000	15	1.5665	0.03243		
						Average	2.48

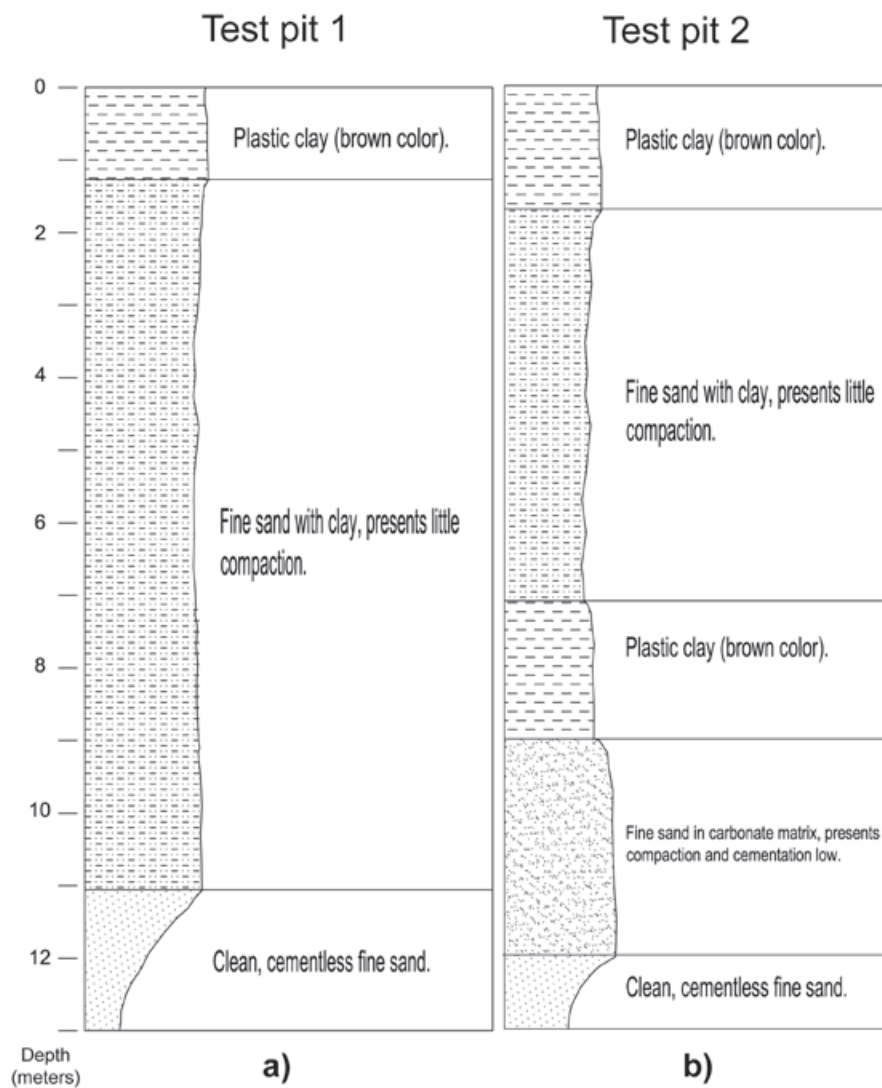


Figure 8. Excavated trench lithologies.

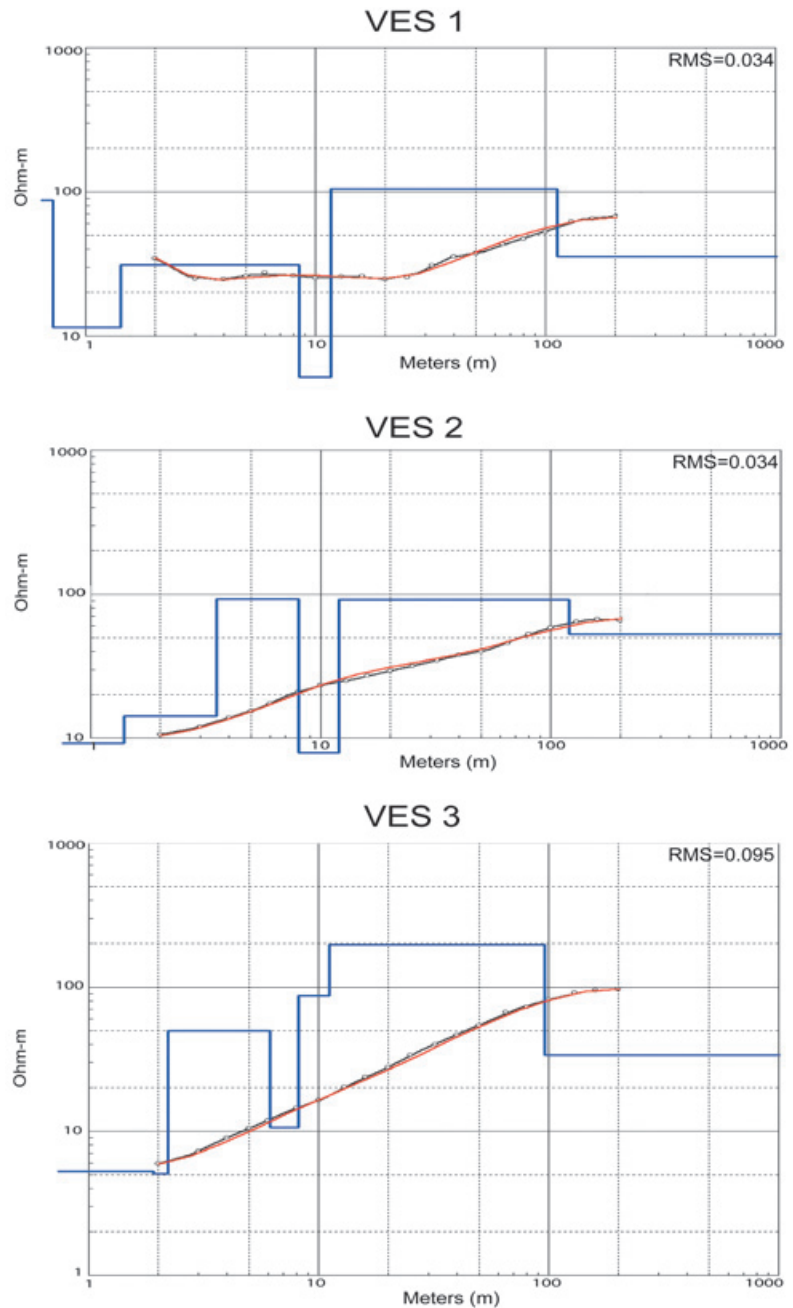


Figure 9. VES 1, VES 2, and VES 3 1D inverted models. The observed points are represented by white dots, black line represents the resistivity curve of the observed points, red line represents the resistivity curve that best fits to the observed data curve, and the layers model is shown in blue line.

Discussion

The application of DC Electrical methods at the El Barreal flooding zone reveals six different G.E.U. (Figures 12 and 13), which were associated with specific lithologies (Table I) identified either in the excavated trenches (Figure 8) or the production wells (Figure 3). The interpretation of these G.E.U., together with the correlation between the 1D inverted models (Figures 9, 10 and 11), revealed the subsurface geometry of the stratigraphic package within the study area. The final stratigraphic sections (Figures 15

and 16) show how the interpreted lithofacies in profiles A-D', B-B', C-C' and B-E' reveal lateral heterogeneity associated with the strong lateral gradients observed in the geophysical profiles between VES1, VES2, VES3, VES4 and VES5 (Figure 12a), VES6, VES2 and VES3 (Figure 12b), VES7 and VES4 (Figure 12c), and between VES6, VES 7, VES8 and VES9 (Figure 13c). On the other hand, stratigraphic sections D-D' and E-D' (Figure 16a and b) appear more homogenous as suggested by geophysical profiles between VES 8 and VES 5 (Figure 13a) and VES9 and VES5 (Figure 13b).

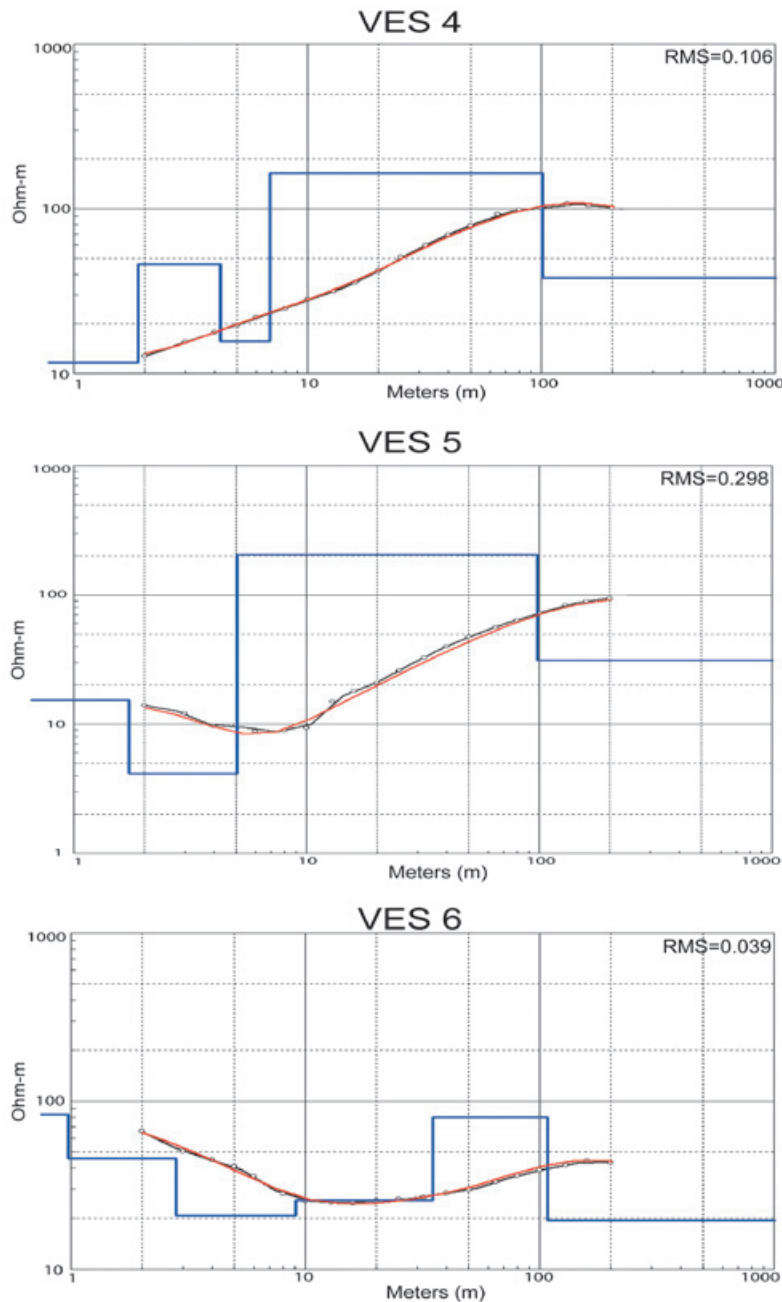


Figure 10. VES 4, VES 5, and VES 6 1D inverted models. The observed points are represented by white dots, black line represents the resistivity curve of the observed points, red line represents the resistivity curve that best fits to the observed data curve, and the layers model is shown in blue line.

The lateral transitions in sections A-D', B-B', C-C' and B-E' are associated with the presence of larger grain sands pinching out into a layer composed of sand and clay. This lateral heterogeneity is more evident in the 3D model of the investigated area (Figure 17). The geometry of the relatively coarse and permeable sand seems to be consistent with the architecture of deposition of prograding deltas and terminal fan deposits developed by ephemeral streams. The strong geophysical gradients might be interpreted as the boundary of a series of paleochannels or ancient prograding deltas, probably developed as a consequence of different flooding events. This interpretation seems to be consistent with the

geomorphologic features observed in the satellite image of the El Barreal watershed (Figure 18).

As an alternate explanation, the observed heterogeneity patterns could also be explained in terms of the presence of Quaternary faults that are common in the region (Seager, 1980; Burgos, 1993; Khatun *et al.*, 2007; McCalpin, 2006). The inferred EFMF, which is 500 Ka old (McCalpin, 2006), passes very close to the area of study (Figures 1a and 2a). Furthermore, it is very possible that the pattern of faulting observed in the northwestern Hueco Bolson (e.g., Seager, 1980), consisting of a series of intrabasin horsts and grabens is also taking place in the El Barreal

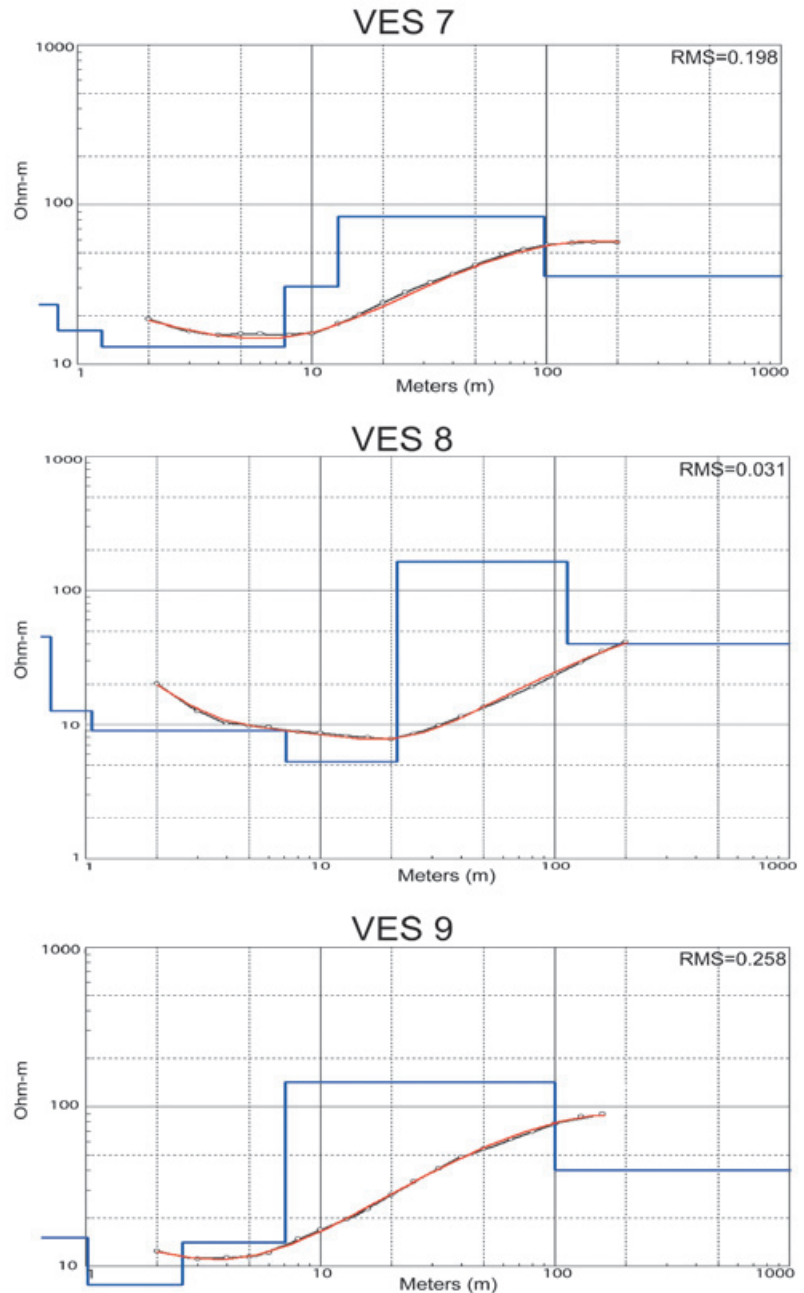


Figure 11. VES 7, VES 8, and VES 9 1D inverted models. The observed points are represented by white dots, black line represents the resistivity curve of the observed points, red line represents the resistivity curve that best fits to the observed data curve, and the layers model is shown in blue line.

zone located within the southwestern Hueco Bolson (Figure 1a), within the Río Grande Rift. The fact that fault scarps are not observed at the surface in the study area could be attributed to recent alluvial processes that have covered them. Other geophysical techniques, such as precision gravity surveys, could help reveal how extensive faulting is within this region.

Regardless of whether the deposition patterns are either attributed to structural or stratigraphic controls or both, a final hydrostratigraphic zoning (Figure 18), useful for the immediate purpose of infiltrating runoff excess into the shallow aquifer,

was developed by integrating the geophysics and permeability results, production well data and geomorphology, into a geographic information system. As a result, two hydrostratigraphic zones are proposed: (I) The area located southeast of VES 3 (green polygon in Figure 18) seems to be the most suitable region to be successfully infiltrated by runoff in terms of the geophysical and direct test findings, and (II) the red polygon (Figure 18), which on the other hand, seems to be overlying a low permeability clay-prone zone, which lacks the potential to effectively support the infiltration well battery design.

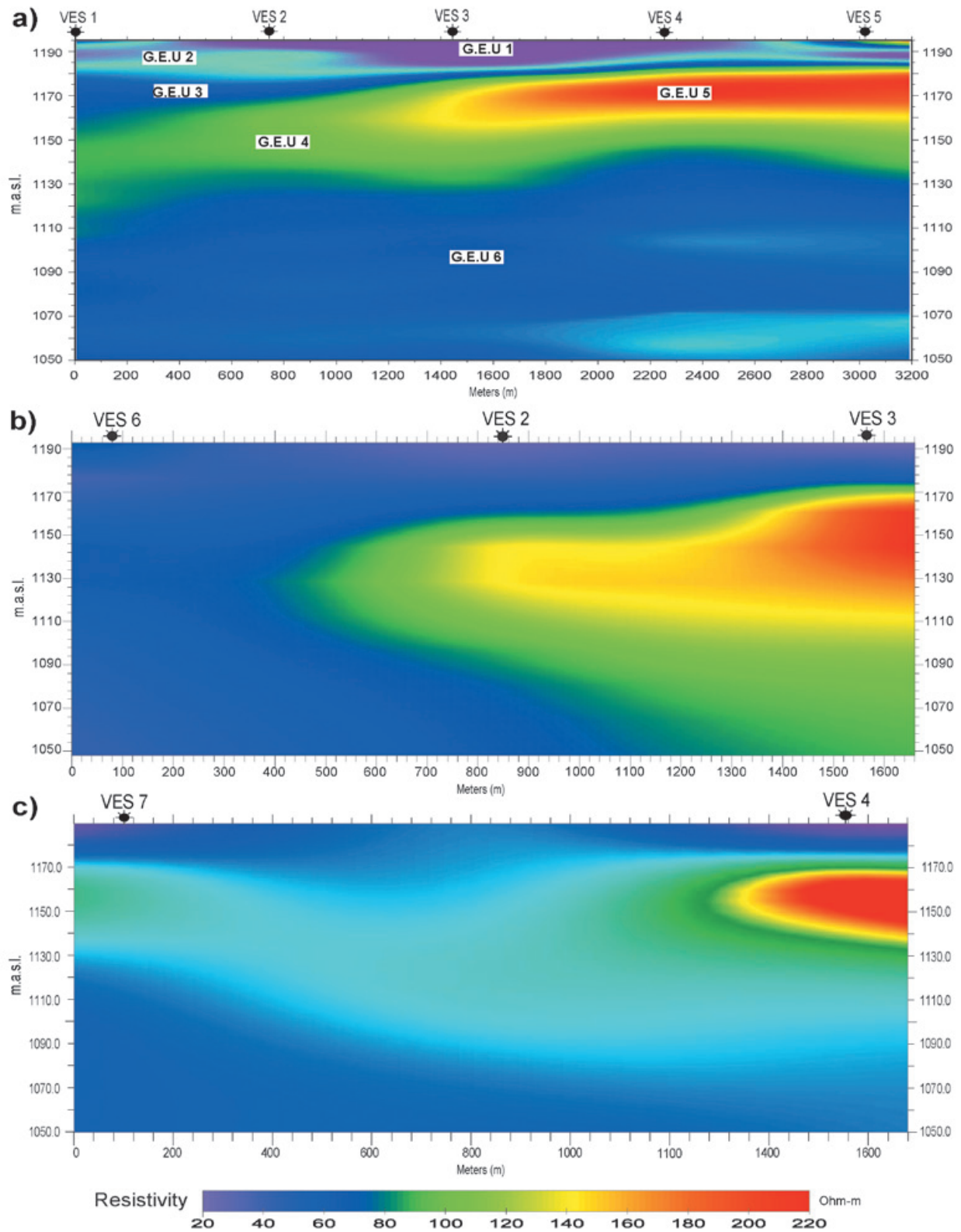


Figure 12. Geoelectric 2D models generated by interpolation between the 1D inverted models. For location see Figure 1(b). Resistivities are represented as the logarithm of the inverted resistivity.

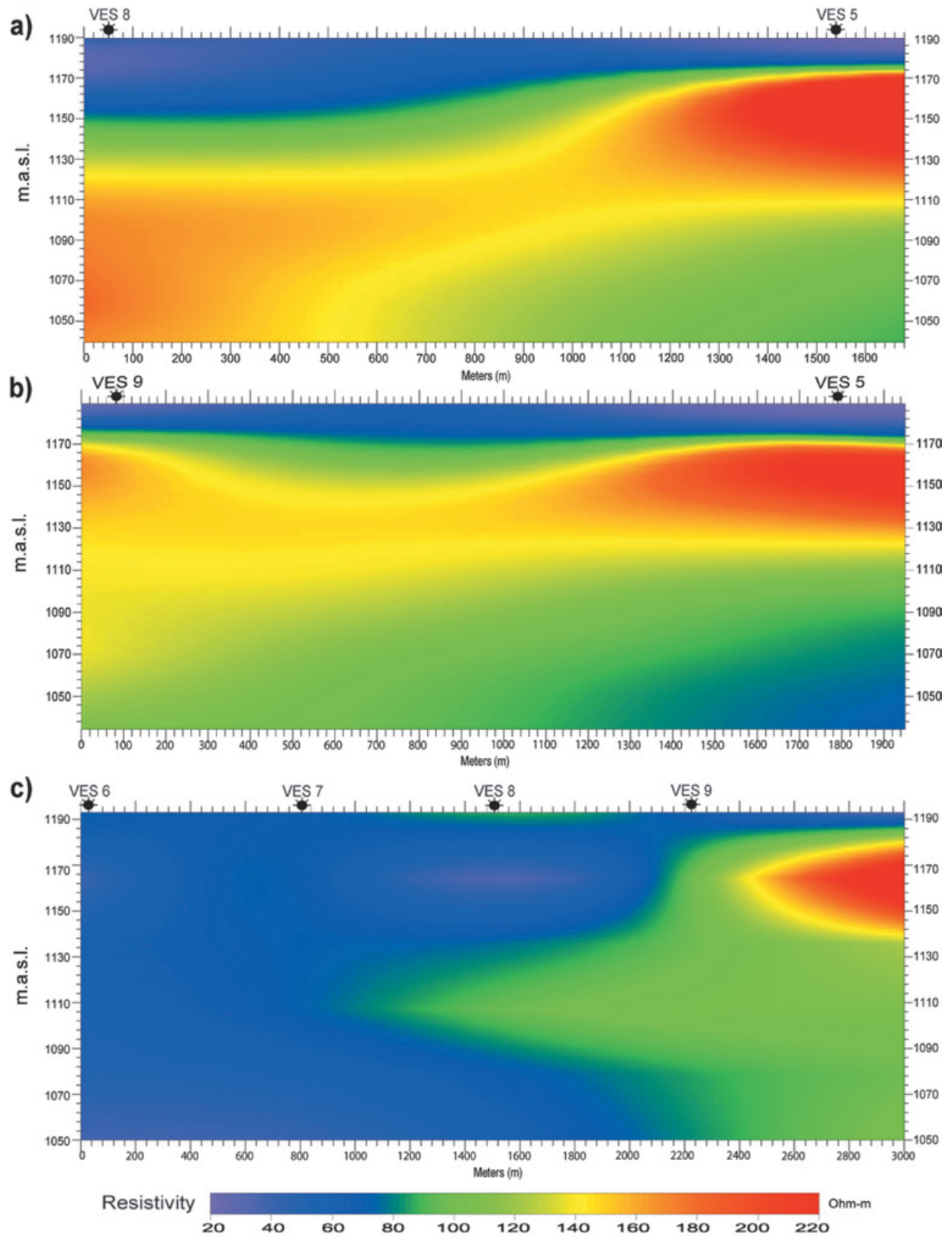


Figure 13. Geoelectric 2D models generated by interpolation between the 1D inverted models. For location see Figure 1(b). Resistivities are represented as the logarithm of the inverted resistivity.

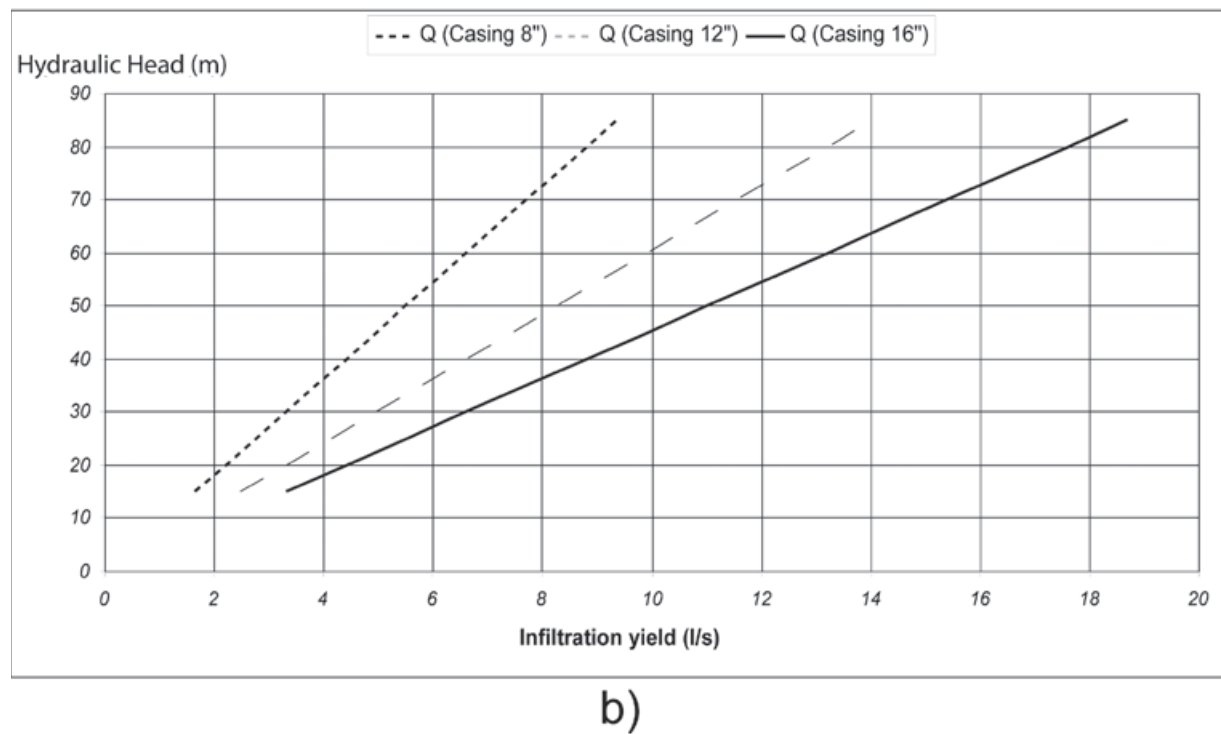
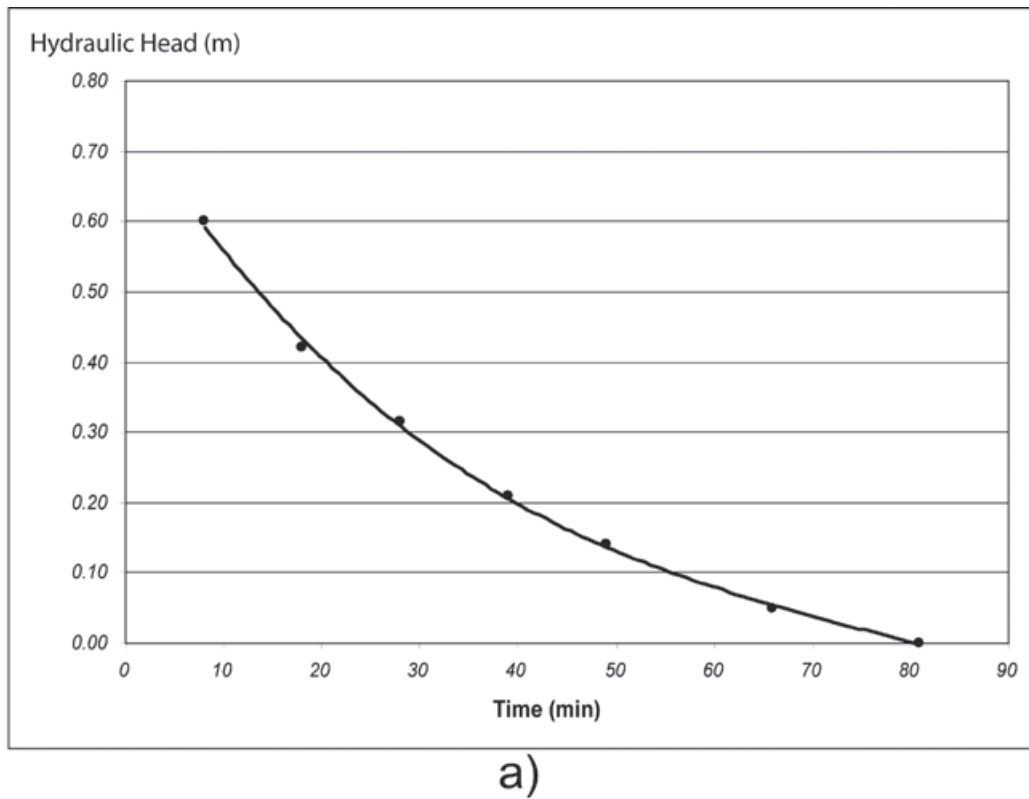


Figure 14. a) Lefranc permeability test pit results. b) Infiltration capacity results.

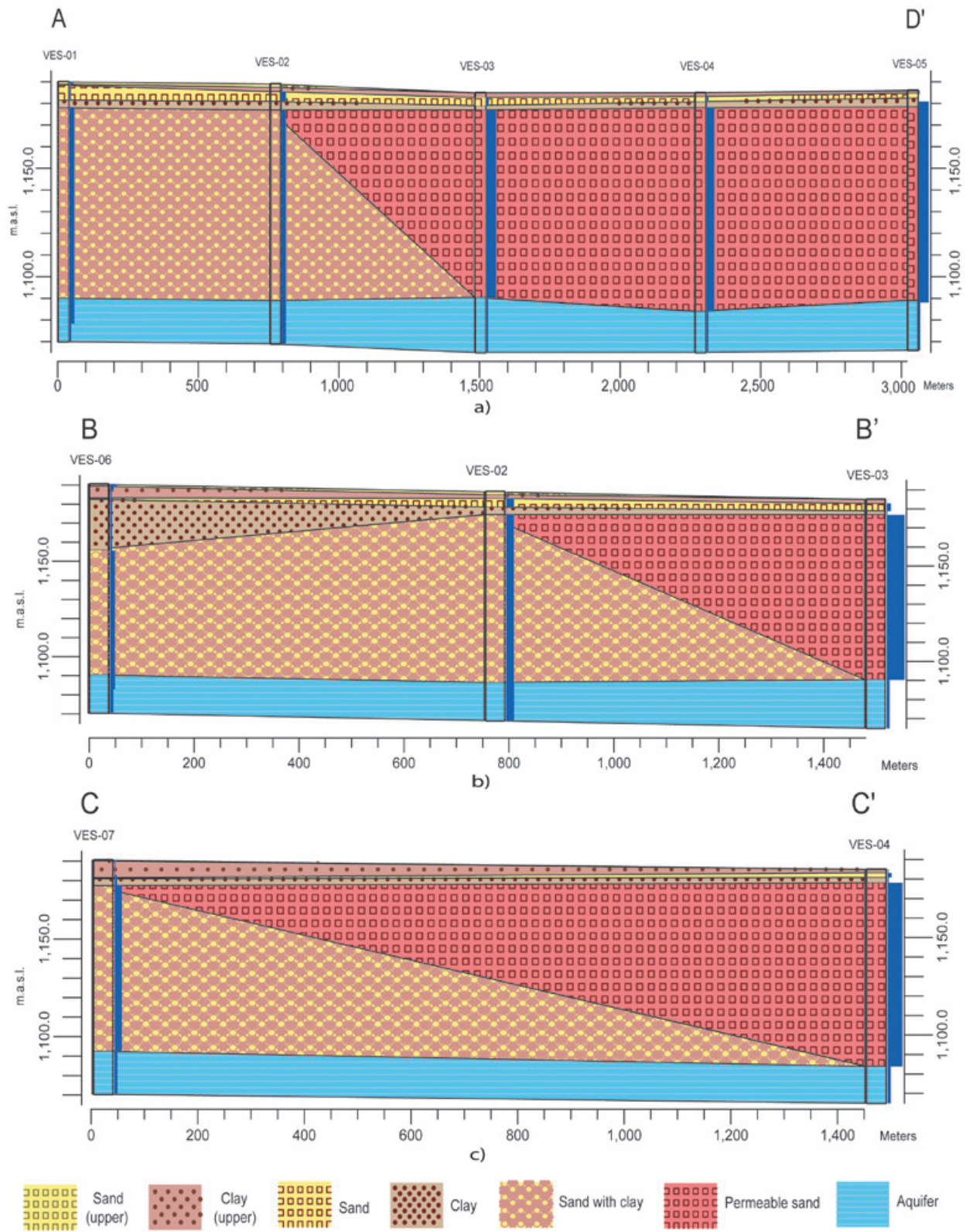


Figure 15. Goelectric stratigraphic profiles. The legend explains the interpreted stratigraphic horizons. The “upper” units are younger strata. The blue columns represent the 1D inverted models, the widths are proportional to the inverted resistivity value. a) Profile A-D’. b) Profile B-B’. c) Profile C-C’. For profile location see Figure 1(b).

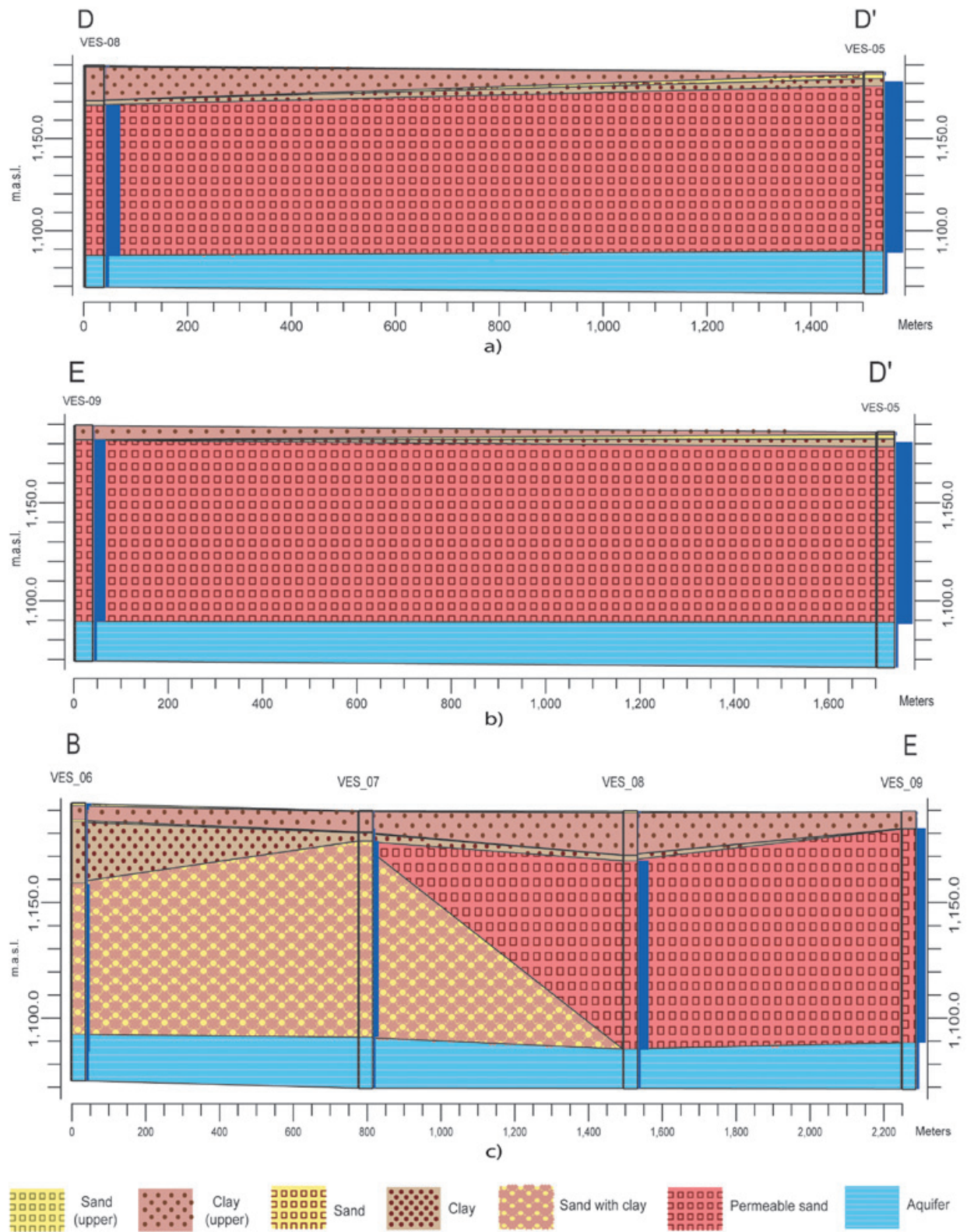


Figure 16. Goelectric stratigraphic profiles. The legend explains the interpreted stratigraphic horizons. The “upper” units are younger strata. The blue columns represent the 1D inverted models, the widths are proportional to the inverted resistivity value. a) Profile D-D’. b) Profile E-D’. c) Profile B-E. For profile location see Figure 1(b).

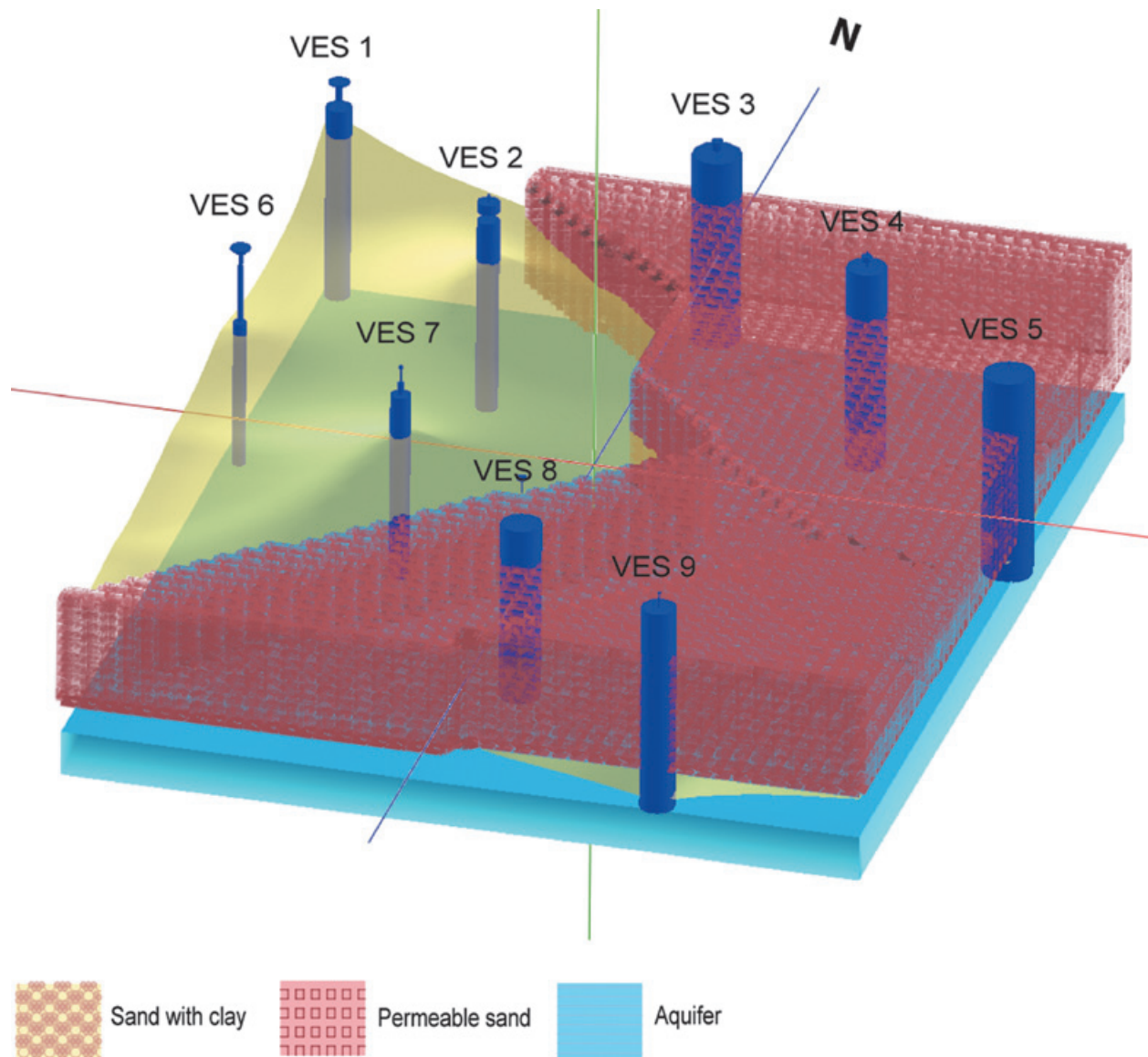


Figure 17. 2D stratigraphic model inferred from geophysics and well data. The widths of the blue columns are proportional to the inverted resistivity value.

Conclusions

The observed lithologies in the trench displayed a good agreement between the modeled resistivity results and the actual underground stratigraphy. However, the main observed disagreement was the presence of fine-grained sand interbedded with a lacustrine sequence, which was initially modeled in the resistivity studies as a single unit. The poor functioning of the absorption wells might suggest they were drilled to a depth that only reached the upper boundary of this fine-grained sand body. Once the observed lithologic

units were input as a starting model into the modeling software, a reasonable fit between the theoretical and the observed curves was obtained (Figures 9 to 11). This is not surprising, since several combinations of resistivity impedances can yield the same result (Telford *et al.*, 1995; Sharma 1997). It is also true that it is very difficult to infer the true underground structure from a single geophysical technique. Nevertheless, the high resistivity layer (greater than 160 ohm-m and nearly 80 m in thickness) was confirmed to be a relatively permeable (2.45 m/d) sand body suitable for infiltration.

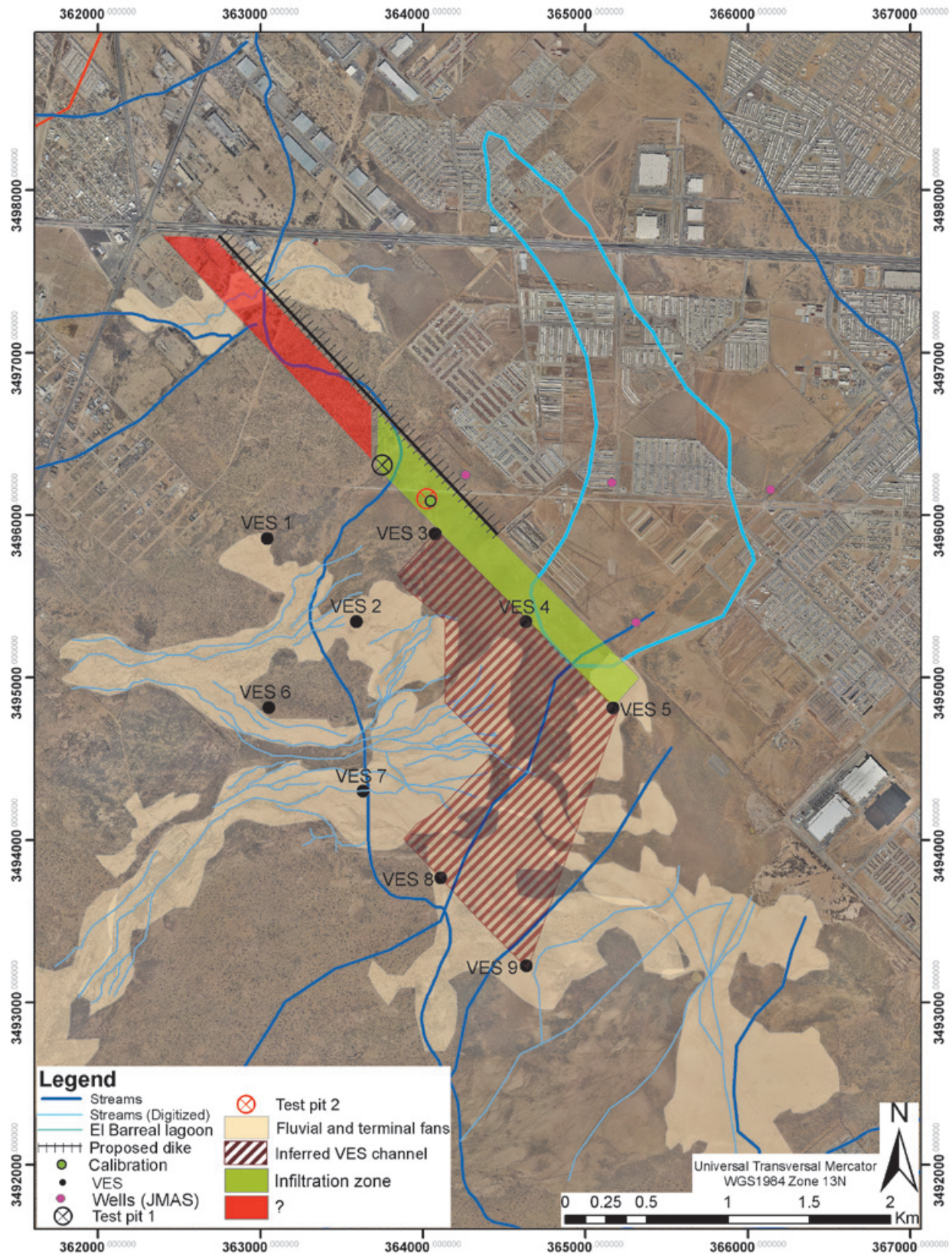


Figure 18. Hydrostratigraphic local scale zoning overlaying 1m pixel size aerial photo. Aerial photo inferred streams are shown in light blue. The green area represents an appropriate infiltration zone in terms of the research results.

We conclude that the DC method was an excellent approach to discriminating between fine and coarse grain materials, however it was limited in resolution. It would be advisable to conduct Electrical Resistivity Tomography (ERT) in the region with an intelligent electrode array capable of yielding profiles with vertical meter resolution. Nevertheless, the DC approach is still an outstanding cost-benefit prospecting tool to provide information on subsurface conditions when tied to existing borehole and other subsurface information. Given the proper subsurface information, this modeling process might reduce the number of direct soundings to only two or three in order to tune the models and generate a final 3D subsurface model with a high degree of certainty.

In terms of our study, our final goal of detecting the depth and extent of a permeable layer in terms of hydrostratigraphic units (H.S.U.) was achieved after integrating the geophysical findings, the remotely sensed and interpreted geomorphology, and a proper geological model into a GIS. This resulted in a bimodal zoning map, which defines the geographical extent of the infiltration prone area (green polygon in Figure 18). Nevertheless, a considerable number of extra DC soundings and/or TDEMs accompanied by ERT profiling are still required to effectively design the entire well infiltration battery with enough capacity to channel surface water into subsurface permeable units in order to provide a feasible solution for the flooding problem in El Barreal zone.

Bibliography

- ABEM, 1993, ABEM Terrameter SAS 300 C: Instruction Manual, NO. JN/9006/9138 5000 12, 64 pp.
- Allen D.B., 2005, Ice age lakes in New Mexico, New Mexico Museum of Natural History and Science Bulletin, 28, p. 107 – 114.
- Averill M.G., 2007, A lithospheric investigation of the southern Río Grande Rift, ETD Collection for University of Texas, El Paso, <http://digitalcommons.utep.edu/dissertations/AAI3273992>.
- Burgos A., 1993, A gravimetric study of the thickness of the unconsolidated materials in the Hueco Bolson aquifer, Juárez area, Chihuahua Mexico. M.S. thesis, The University of Texas at El Paso, 80 pp.
- Buro Nacional Inmobiliario, 2009, Quieren construir en zona inundable del Barreal, <<http://www.buroinmobiliario.com.mx>>
- Castiglia P.J., Fawcett P.J., 2006, Large Holocene lakes and climate change in the Chihuahuan Desert. *Geology* (Boulder), 34, 2, p.113-116.
- Comisión Nacional del Agua (CNA), 2008, Estudio de Factibilidad para el control integral de avenidas en las cuencas Zona I-Anapra y zona II-Centro en Ciudad Juárez, Chihuahua, Reporte Técnico Final, 255 pág.
- Dena O., 2000, Geophysical properties of soils in the upper Río Grande Valley near El Paso, Texas, Department of Geological Science, University of Texas at El Paso, Thesis, 113 pp.
- Dena O.S., 2007, Estudio gravimétrico aplicado a prospección de aguas subterráneas al suroeste de Ciudad Juárez, Reporte Técnico Final, Universidad Autónoma de Ciudad Juárez, 68 pág.
- Doser D.I., Dena-Ornelas O.S., Langford R.P., Baker M.R., 2004, Monitoring of the yearly changes in the electrical properties of the shallow subsurface at two sites near the Río Grande, west Texas, *Journal Envir. and Engineer. Geophysics* 9, 179-190.
- Granillo J.A., 2004, A gravimetric study of the structure of the northeast portion of the Hueco Bolson, Texas employing GIS Technology. M.S. thesis, The University of Texas at El Paso, 141 pp.
- Haenggi W., 2002, Tectonic history of the Chihuahua trough, Mexico and adjacent USA, Part II: Mesozoic and Cenozoic, *Mexican Geological Society Bulletin* No. LV-1, p. 38-94.
- Hawley J.W., 1969, Notes on the geomorphology and the late Cenozoic geology of northwestern Chihuahua: New Mexico Geological Society, 26th Annual Field Conference, Guidebook, p. 131-142.
- Hawley J.W., 1993, Geomorphic setting and late Quaternary history of pluvial-lake basins in the southern New Mexico region. New Mexico Bureau of Mines and Mineral Resources, open-file report 391. p. 28.
- Hawley J.W., Hibbs B.J., Kennedy J.F., Creel B.J., Remmenga M.D., Johnson M., Lee M.M., Dinterman P., 2000, Trans-International Boundary aquifers in southwestern New Mexico: New Mexico Water Resources Research Institute, New Mexico State University, prepared for U. S. Environment Protection Agency-Region 6 an International Boundary and Water Commission; Technical Completion Report-Interagency Contract X-996350-01-3, 126 p.

- Hawley J.W., Hibbs B.J., Kennedy J.F., Creel B.J., 2001, the Mesilla Basin aquifer system of New Mexico, West Texas and Chihuahua –an overview of its hydrogeology framework and related aspects of Aquifers of West Texas: Texas Water Development Board Report 356, p. 76-99.
- Instituto Municipal de Investigación y Planeación (IMIP), 2004, Plan Sectorial de Manejo de Agua Pluvial, 384 pág.
- Instituto Municipal de Investigación y Planeación (IMIP), 2004b, Plan Parcial El Barreal y Oriente San Isidro, 190 pág.
- Juárez Press, 21 de Julio del 2008. No cumplen con ordenamientos para evitar inundaciones, Juárez Press Periodismo Activo, 27 de Marzo del 2010 <<http://www.juarezpress.com/n/227.htm>>
- Keaton J.R., Barnes J., 1996, Paleoseismic Evaluation of the East Franklin Mountains Fault, El Paso, Texas: Final Report, under award, U. S. Geological Survey, National Earthquake Hazards Reduction Program, Program Element III, 1434-94-G-2389.
- Keller G.R., Baldrige S.W., 1999, The Río Grande Rift: A geological and geophysical overview, *Rocky Mountain Geology*, 34, 1, p. 121-130.
- Keller G.R., Morgan P., Seager W.R., 1990, Crustal structure, gravity anomalies, and heat flow in the southern Río Grande rift and their relationship to extensional tectonics, in *Technophysics*, 174, p. 21 - 37.
- Kernodle J.M., 1992, Summary of U.S. Geological Survey ground-water-flow models of basin-fill aquifers in the southwestern alluvial basins region. Colorado, New Mexico, and Texas: U.S. Geological Survey, Open-file Report 90-361, 81 p.
- Khatun S., Doser D.I., Imana E.C., Keller G.R., 2007, Locating faults in the southern Mesilla Bolson, west Texas and southern New Mexico using 3-D modeling of precision gravity data, *J. Envir. and Engineer. Geophys.* 12, 149-161.
- Knowles D.B., Kennedy R.A., 1956, Groundwater resources of the Hueco Bolson, northeast of El Paso, Texas: Texas Board Water Engineering Bull. 5615-265 p.
- Laboratorio de Climatología y Calidad del Aire (LCCA), 2008, Pluviometric records digital database, Departamento de Ingeniería Civil y Ambiental, Universidad Autónoma de Ciudad Juárez (UACJ).
- Loke M.H., 2004, TUTORIAL: 2-D and 3-D electrical imaging surveys. www.geoelectrical.com, pp.29-31
- McCalpin J.P., 2006, Quaternary faulting and Seismic source Characterization in the El Paso-Juarez Metropolitan Area; Collaborative Research with the University of Texas at El Paso, Program Element II: Evaluate Urban Hazard and Risk, final Technical Report, National Earthquake Hazards Reduction Program U. S. Geological Survey.
- Obeso G.J., 2008, Estudio gravimétrico aplicado a prospección de aguas subterráneas al suroeste de Ciudad Juárez. B.S. thesis, Universidad Autónoma de Ciudad Juárez, 70 pág.
- O'Donnell T.M., 1998, Integrated gravity seismic reflection/refraction study of the McGregor geothermal system, southern New Mexico. M. S. thesis, University of Texas at El Paso, 142 pp.
- Palacky G.I., 1987, Resistivity characteristics of geological targets. In: M. Nabighian, Editor, *Electromagnetic Methods in Applied Geophysics-Theory*, Society of Exploration Geophysicists, Tulsa, OK, pp.53-129.
- Rascón E.M., Gómez F.J., 2007, Estudio de Prospección Geofísica para la ubicación de una fuente de abastecimiento para el nuevo campus de Ciudad Universitaria, al sur de Ciudad Juárez. Reporte Interno Final, Junta Municipal de Agua y Saneamiento (JMAS), 39 pág.
- Rascón E.M., 2008, Chief of Department of Geohydrology, Junta Municipal de Agua y Saneamiento (JMAS) de Ciudad Juárez, pers. comm.
- Reeves C.C. Jr., 1969, Pluvial Lake Palomas northwestern Chihuahua, Mexico. *New Mexico Geological Society, 20th Annual Field Conference, Guidebook*. p. 143 -154.
- RockWorks. Earth Science and GIS Software, 2002.<http://www.rockware.com/index.php>.
- Sayre A.N., Livingston P., 1945, Groundwater resources of the El Paso area, Texas, U.S. Geological Survey Water Supply Paper 919, 190 pp.
- Seager W.R., 1980, Quaternary Fault Systems in the Tularosa and Hueco Basins, Southern New Mexico and West Texas, in *Guidebook of the Trans Pecos Region: New Mexico Geological Society*, 5 pp.

- Seager W.R., Morgan P., 1979, Río Grande rift in southern New Mexico, west Texas, and northern Chihuahua. In R.E. Riecker (Editor), Río Grande rift: Tectonics and magmatism. American Geophysical Union, Washington, D.C., pp. 127-143.
- Servicio Geológico Mexicano (SGM), 2008, Carta Magnética de Campo Total Escala 1:50,000 de Ciudad Juárez, Chihuahua.
- Sharma P.V., 1997, Environmental and engineering geophysics, Cambridge University Press, p. 475, ISBN: 0-521-576326.
- Shevnin V.A., Modin I.N., 2003, IPI2win, Program for 1D automatic and manual interpretation of VES curves, Moscow State University, Geological Faculty, Department of Geophysics.
- Shevnin V.A., Delgado Rodríguez O., Mousatov A., Nakamura Labastida E., Mejía Aguilar A., 2003, Oil Pollution using resistivity sounding, *Geofísica Internacional*, 42, 4, pp. 613-642.
- Sinno Y.A., Daggett P.H., Keller G.R., Morgan P., Harder S.H., 1986, Crustal structure of the southern Río Grande rift determined from seismic refraction profiles: *Journal of Geophysical Research*, 91, p. 6143-6156.
- Telford W.M., Geldart L.P., Sheriff R.E., 1995, Applied geophysics, Second Edition, Cambridge University Press, p. 751, ISBN: 0-521-33938-3.
- Uphoff T.J., 1978, Subsurface stratigraphy and structure of the Mesilla and Hueco Bolsons, in the El Paso Region, Texas and New Mexico: MS Thesis, University of Texas at El Paso 66, p.
- Wessel P., Smith W.H.F., 1988, Generic Mapping Tools (GMT), <http://gmt.soest.hawaii.edu/>, School of Ocean and Earth Science and Technology, University of Hawaii at Manoa.

Exploration of subsoil structure in Mexico city using correlation of micrometremors

Francisco J. Chávez-García* and Jorge Aguirre

Received: May 04, 2011; accepted: February 27, 2011; published on line: June 29, 2012

Resumen

Presentamos resultados de la exploración del subsuelo en la zona de lago de la Ciudad de México utilizando correlación de registros de microtremores. Registramos microtremores con estaciones de banda ancha. La duración de los registros varió entre pocos minutos y una hora. Los componentes verticales de los registros se analizaron usando los métodos SPAC e interferometría sísmica para estimar la dispersión de ondas superficiales del medio. Nuestros datos permitieron calcular la correlación cruzada de microtremores para un rango amplio de distancias entre estaciones, entre 10 m y 2 km. Para distancias pequeñas entre estaciones, observamos buena correlación entre registros, lo que permitió determinar de manera confiable la estructura superficial. Nuestros resultados indican que la heterogeneidad lateral de la capa de arcilla superficial es importante, aún para distancias cortas. Para distancias más grandes, no fue posible obtener valores de correlación altos. La correlación cruzada entre dos estaciones requiere que el medio entre ellas sea capaz de propagar ondas de Rayleigh con longitud de onda de dimensión comparable a la distancia entre las estaciones. Nuestros resultados sugieren que no es posible recuperar ondas de Rayleigh a partir de de la correlación de microtremores para longitudes de onda entre 1 y 9 km.

Palabras clave: microtremores, correlación, dispersión de velocidad, estructura del subsuelo, heterogeneidad lateral.

Abstract

We present results of the exploration of the subsoil in the lake bed zone of Mexico City using correlation of microtremors. We recorded microtremors using broad band stations and recording windows between a few minutes and one hour. Vertical components were analyzed using both SPAC and time interferometry to recover Rayleigh wave dispersion. Our measurements allow us to compute correlation of microtremors for a very wide range of distances between stations, from 10 m to almost 2 km. At short distances, we obtained significant correlation and the shallow velocity structure could be well determined. We show that lateral heterogeneities of the clay layer are important even over short distances. At larger distances, it was not possible to obtain good correlation. Correlation between two stations requires that the medium, at the wavelength scale of distance between stations, be able to sustain Rayleigh waves. Our results suggest that Rayleigh waves cannot be retrieved from correlation analyses for wavelengths between 1 and 9 km.

Key words: microtremors, correlation, velocity dispersion, subsoil structure, lateral heterogeneity

F. J. Chávez-García
Instituto de Ingeniería
Universidad Nacional Autónoma de México
Ciudad Universitaria
Delegación Coyoacán, 04510
México D.F., México

*Corresponding author: paco@pumas.ii.unam.mx

J. Aguirre
Instituto de Ingeniería
Universidad Nacional Autónoma de México
Ciudad Universitaria
Delegación Coyoacán, 04510
México D.F. México

Introduction

Site effects play a major role in destructive ground motion in the Mexico City valley. The presence of very soft soil layers amplifies ground motion in the lake bed zone 8 to 50 times in the frequency domain with respect to a hill zone site (e.g., Singh *et al.*, 1988). Because of this amplification, earthquakes with epicenters more than 300 km away may cause damage as important as that observed in September 1985. Amplification in the lake bed zone has been measured using spectral ratios of recorded earthquakes relative to ground motion observed in firm ground (referred to as the hill zone). This approach has allowed characterising site effects in the lake bed zone, due to the presence at the surface of the lake-bed zone of a very thin, extremely soft clay layer, deposited in an ancient lake. The importance of site effects is evident from the fact that in 1985 no damage was observed in the hill or transition zones of the geotechnical zoning of Mexico City. However, the records obtained on the lake-bed zone not only show significantly larger amplitudes than those on hill zone. They also show late, energetic arrivals (with amplitude comparable to those of the intense phases) that increased the duration of ground motion, almost up to three times that observed on firm soil. These two phenomena, amplification and increase of duration, have been the guiding themes of a large amount of research concerning site effects at Mexico City (see for example Kawase and Aki, 1989; Chávez-García and Bard, 1993a, b, 1994; Chávez-García *et al.*, 1995; Singh *et al.*, 1995; Shapiro *et al.*, 1997, 2001; Iida, 1999; Chávez-García and Salazar, 2002).

After the 1985 Michoacán earthquake, site response of Mexico City was the subject of many studies, in an effort to reconcile observed ground shaking with results from model computations. Prediction from numerical models is essential to establish limits to strong ground motion for future earthquakes. A 1D model was used by Seed *et al.* (1988) to model response spectra of recorded ground motion during the 1985 earthquake. These authors showed that an *ad hoc* 1D model could reproduce amplification due to the soft clay layer. However, Kawase and Aki (1989) and Chávez-García and Bard (1994) showed clearly that however useful 1D models were to reproduce observations in the frequency domain, they were wholly inadequate to explain the recorded ground motion (see Chávez-García, 2010 and 2011, for more recent discussions). The reason is that it is not possible to separate site from path effects in this basin. The large heterogeneity associated to the Mexican Volcanic Belt, at the origin of the regional amplification (e.g. Ordaz and Singh, 1992), conditions incident wavefield in

Mexico's basin. Thus, the long duration of ground shaking in this basin results from the interaction of different surface wave modes with the very local soil conditions in Mexico City, blending path and site effects. A few studies have addressed modelling of ground motion in Mexico City including the crustal structure surrounding the basin (e.g., Cárdenas *et al.*, 1997; Chávez-García and Salazar, 2002) showing the large importance of the regional structure that conditions incident ground motion at the base of the very soft soils in the lake bed zone. The very large amplification in the clay layer masks the effect on ground motion of the deeper structure making it difficult to understand the contribution of each factor. To date, however, the more refined and complete model for central Mexico is that published by Furumura and Kennett (1998). These authors computed synthetics for a simplified 3D model of central Mexico that included the correct position of the Transmexican Volcanic Belt, oblique to the subduction. They were able to show that this geometry was important and they could establish a relation between the irregular crustal structure and the incident wave field at Mexico City. However, due to computational restrictions and the large uncertainties of the deeper structure of Mexico City basin, their results are strongly limited.

There is a critical lack of data concerning the deep structure of Mexico City basin. Indeed, were there no computational limitations to model the 3D seismic response of Mexico City basin, we would be embarrassed to propose a geotechnical model with all the necessary details. Most of the available information concerns the surficial clay layer and there is a lack of information concerning the thick (several km) volcanic deposits between the clay and the limestone basement of the basin. After the large 1985, Michoacan, earthquake, Pemex drilled four deep boreholes and recorded several km of seismic reflection lines in the city. The results were discussed by Pérez-Cruz (1988), who identified up to seven sequences of volcanic deposits. However, no information was obtained on shear wave velocities (more important than compressive wave velocities for site response modelling) and no clear idea of the shape of the basin could be inferred from the results. The current building code in Mexico City is based on the dominant period determined at each site, a very stable parameter which is due to the large impedance contrast at the base of the clay layer; usually estimated using spectral ratios (see for example Lermo and Chávez-García, 1993, 1994). However, empirical estimation of site effects has severe limitations (e.g., Chávez-García, 2007, 2011). Empirical methods do not allow us to understand the factors that condition ground shaking. They are not useful to build an accepted

model to simulate together the observed large amplification and the long duration. The current building code relies on average spectral ratios of past earthquakes to predict ground motion for future events. In this approach, the variability among individual site response estimates is swept aside through the computation of average values. For example, Lermo and Chávez-García (1993) showed spectral ratios of earthquake records for soft soil sites in Mexico City relative to a firm site (CU), which is a widely accepted method to estimate local amplification. Those authors showed large differences in the estimated amplification depending on whether the NS or the EW component was used. Those differences are hidden when average horizontal amplification values are computed.

The size of Mexico City, the significance of its infrastructure and the high probability of it being affected by future subduction zone earthquakes make for its large seismic risk. A better understanding of ground motion in Mexico City is necessary to mitigate that risk. If we are able to understand the relation between incident motion, irregular structure and observed surface motion, we may constrain a major factor contributing to destructive ground motion during future earthquakes. This understanding calls for more than mere estimation of local amplification. It requires a better knowledge of the subsoil structure and its integration into simulation models of ground motion. Active exploration methods are out of the question because of their cost, field conditions, background noise, and the size of the region and depth that needs to be investigated. For this reason, the use of passive methods as the analysis of microtremors, also called ambient seismic noise, is very attractive. In this paper we present results of exploration of subsoil in the lake bed zone of Mexico City using correlation of microtremor records. Correlation of microtremors allows investigating shear wave velocity distribution in the subsoil. We present the results of the application of correlation to array recorded microtremors in the lake bed zone of Mexico City, close to its eastern edge. We show that this method is effective for shallow depths and allows constraining lateral heterogeneities within the valley. However, our results indicate that this method fails to obtain useful information for the deeper volcanic layers.

Method

In this paper, we use the SPAC method to determine the subsoil structure from microtremor measurements in Mexico City. Correlation of microtremors has developed into a reliable tool to determine shear wave velocity profiles since the introduction of the SPAC method more than 50 years ago (Aki, 1957). The theory of the SPAC

(SPatial AutoCorrelation) method was thoroughly developed by Aki (1957). The essence of the method is that, when we have records from seismic stations, spaced at a constant distance and forming pairs of stations along different azimuths, it is possible to compute an estimate of the phase velocity of the waves crossing the array, without regard to the direction of propagation of the waves present. The method assumes that the 2D wavefield being recorded by an array of stations is stochastic and stationary, in both space and time.

Let us assume that the microtremors stochastic wavefield is formed by the superposition of many plane surface waves propagating with equal power in all directions of the horizontal plane. All of the waves propagate with the same phase velocity c . Consider the recordings of microtremors at the two locations on the free surface (x, y) and $(x+\xi, y+\eta, t)$. The spatial autocorrelation function, $\phi(\xi, \eta, t)$ is defined as

$$\phi(\xi, \eta, t) = \overline{u(x, y, t)u(x + \xi, y + \eta, t)} \quad (1)$$

where the bar indicates time averaging. Under the assumption that the wavefield is stationary, Aki (1957) showed that the azimuthal average of the spatial autocorrelation function can be written as

$$\bar{\phi}(r) = \frac{1}{2\pi} \int \phi(r, \psi) d\psi \quad (2)$$

where r and ψ are the polar coordinates defined by

$$\xi = r \cos \psi \quad (3)$$

and

$$\eta = r \sin \psi \quad (4)$$

Aki (1957) showed that the azimuthal average of the spatial autocorrelation function, $\bar{\phi}(r)$, is related to the power spectral density of the microtremor wavefield, $\Phi(\omega)$, through

$$\bar{\phi}(r) = \frac{1}{\pi} \int_0^\infty \Phi(\omega) J_0\left(\frac{\omega}{c} r\right) d\omega \quad (5)$$

where J_0 is the Bessel function of the first kind and zero order, and ω is angular frequency. This last equation also applies to the case of dispersive waves, and we need only substitute $c(\omega)$ for c . Assume now that we apply a bandpass filter to the records. The spectral density becomes

$$\Phi(\omega) = P(\omega_0)\delta(\omega - \omega_0) \quad (6)$$

where $P(\omega_0)$ is the power spectral density at frequency ω_0 and $\delta(\cdot)$ is Dirac's function. In this case, the azimuthal average of the spatial correlation function can be written as

$$\bar{\phi}(r) \equiv \bar{\phi}(r, \omega_0) = P(\omega_0)J_0\left(\frac{\omega_0}{c(\omega_0)}r\right) \quad (7)$$

Finally, Aki (1957) defined the autocorrelation coefficients, $\rho(r, \omega_0)$, as

$$\rho(r, \omega_0) = \frac{\phi(r, \psi, \omega_0)}{\phi(0, \psi, \omega_0)} \quad (8)$$

Because $P(\omega_0)$ does not depend on the position (assumption of spatial stationarity), we can finally write the azimuthal average of the correlation coefficients as

$$\rho(r, \omega_0) = J_0\left(\frac{\omega_0}{c(\omega_0)}r\right) \quad (9)$$

This last equation states that, if we are able to compute $\rho(r, \omega_0)$ from microtremor measurements, we can estimate $c(\omega_0)$. However, because the relation between the correlation coefficients and the phase velocity is non linear, an iterative inversion scheme is needed. In this paper we have used the inversion scheme described in detail in Chávez-García *et al.* (2005).

The derivation of the SPAC method was presented in great detail in Aki (1957) and Chouet *et al.* (1998) among others. Eq. (9) offers a way to compute the phase velocity, when we can estimate an azimuthal average of the spatial autocorrelation, for a fixed distance r . This was interpreted, starting with Aki (1965), as requiring several stations, distributed on a circle of radius r , with one station at the center of the circle. Naturally, if data recorded on several circles with different radii are available, an azimuthal average can be computed for each circle, and for a fixed frequency ω_0 , using r as independent variable.

The SPAC method has been used frequently to estimate a phase velocity dispersion of Rayleigh waves (e.g., Ferrazzini *et al.*, 1991; Chouet *et al.*, 1998; Yamamoto, 1998; Morikawa *et al.*, 1998, 2004; Flores Estrella and Aguirre González, 2003; Chávez-García *et al.*, 2005; Apostolidis *et al.*, 2005, Margaryan *et al.*, 2009). This method has also been complemented and/

or compared with horizontal to vertical spectral ratios (HVSR) of microtremors (e.g., Roberts and Asten, 2005, 2007) with $f-k$ (frequency-wavenumber method, e.g., Claproud and Asten, 2009), and with REMI, Refraction Microtremor method, proposed by Louie (2001) in Chávez-García *et al.* (2007). All those results showed SPAC to be very reliable. Once a dispersion curve is estimated, it is possible to invert it using standard methods (e.g., Herrmann, 1985) to obtain a 1D layered structure. The limitation is that the soil profile under the array of stations must be regular enough for a single surface wave mode to dominate the correlation functions. One of the limitations of the SPAC method was the need to use a circular array of stations. However, it has been shown (Ohori *et al.*, 2002; Okada, 2003; Chávez-García *et al.*, 2005) that it is possible to use of the SPAC method without the limitations imposed by the circular array. If the waves that form the microtremors propagate homogeneously in all directions, a single station pair samples all directions of propagation provided that temporal averaging is substituted for the azimuthal averaging. In that case, instead of deploying a circular array and estimating correlation coefficients for a distance equal to the radius of the circle, it is possible to analyse a single station pair as if the distance between the two stations were the radius of a circle of stations. This has increased significantly the applicability of the SPAC method. For example, Chávez-García *et al.* (2006) analysed successfully data recorded by a linear array. Ekström *et al.* (2009) used two-station SPAC to analyse data from USArray including 30,000 station pairs. In a more modest scale, we take advantage of this improvement in this paper.

If correlations in the frequency domain are useful, then because of the Fourier transform, they should also be useful in the time domain. However, the development of correlations in time domain to explore the subsoil has a different history. The first references are related to exploration seismology (e.g., Claerbout, 1968). Time domain correlation was rediscovered by helioseismologists (Duvall *et al.*, 1993), before making its appearance in acoustics and seismology. In addition, time domain correlation of ambient noise has been the object of many theoretical studies that have been able to show its relation with the character of ambient noise and statistical properties of diffusive media. Weaver and Lobkis (2005) retrace briefly this history. The theoretical basis of the method and the conditions for its success have been the object of many papers (e.g., Campillo and Paul, 2003; Wapenaar, 2004; Snieder, 2004; Paul *et al.*, 2005; Sabra *et al.*, 2005; Roux *et al.*, 2005; Bensen *et al.*, 2007; Tsai, 2009, 2010). Time domain cross-correlation of microtremors, or

seismic interferometry, is based on the relation that has been established between the cross-correlation function of a diffusive signal recorded at two sites and the time domain Green's function of the medium between the recording stations. Let us write the cross-correlation of microtremors (which can be shown to behave as a diffusive field) recorded at two locations as

$$C_{ij}(\tau) = \int_0^T v_i(r_1, t) v_j(r_2, t + \tau) dt \quad (10)$$

where t is time, $v_i(r_1, t)$ and $v_j(r_2, t)$ are simultaneous recordings of microtremors at locations r_1 and r_2 , T is the observation period and C_{ij} is the cross-correlation computed between the two traces as a function of τ , the delay time. Among others, Sabra *et al.* (2005) have shown that

$$\frac{dC_{ij}}{dt} \approx -G_{ij}(r_1; r_2, t) + G_{ji}(r_1; r_2, -t) \quad (11)$$

where $G_{ij}(r_1; r_2, t)$ is the time domain Green's function between the two locations. A review paper has been presented in Campillo (2006) and a useful compilation of 73 papers has been printed (Wapenaar *et al.*, 2008). Results have been published from very small inter-station distances (5m in Chávez-García *et al.*, 2006) to very large distances (thousands of km in Shapiro *et al.*, 2005). Applications of this equation are abundant, from local or regional tomography (e.g., Shapiro *et al.*, 2005; Yao *et al.*, 2006; Kang and Shin, 2006; Moschetti *et al.*, 2005; Yang *et al.*, 2007; Prieto and Beroza, 2008) to volcano monitoring (e.g., Sens-Schönfelder and Wegler, 2006; Brenguier *et al.*, 2007) and even to building response (Prieto *et al.*, 2010).

The SPAC method and time domain cross-correlation are not completely independent methods. The data used is often the same and the operation (correlation) between traces is the same. The relation between the two methods has been analysed in Chávez-García and Luzón (2005), Chávez-García and Rodríguez (2007), Yokoi and Margaryan (2008), Prieto *et al.* (2009), and Tsai and Moschetti (2010), among others. It is not the purpose of this paper to review that relation but we did compute time domain correlation functions, where we observed the emergence of the fundamental mode pulse for Rayleigh waves. In this paper we will only show an example of the equivalence of results obtained using cross-correlation in the frequency (SPAC method) and time domains (seismic interferometry). Some station pairs show a lack of correlation in both time and frequency domains, which we interpret in terms of lateral heterogeneity. When lateral

variations occur over a distance larger than the size of the arrays, we may identify it through the comparison among the results for the different arrays. However, if the lateral heterogeneity occurs over a distance smaller than the distance between stations, no correlation is obtained in either frequency or time domains and the method fails.

Data

The studied region is located in the lake bed zone in Mexico City, close to the transition zone, along the trace of the Metro-A line (Figure 1). Triangular and linear arrays were deployed mainly along Ignacio Zaragoza avenue (Figure 2). Array aperture spanned a large range, from 10 to 1,960 m. Two different sensor types were used. Vertical sensors HV1 by Kinometrics (5 s natural period) were used for the arrays smaller than 50 m. For these small arrays, HV1 sensors were installed forming a triangle and all three were cable connected to a single accelerograph. In this case, because the three signals were recorded by the same accelerograph, the sampling for all sensors was simultaneous. For larger triangles, we had to use independent recorders at each measurements point, and therefore had to check a common time base for all the records. We used GPS antennas to synchronize all recorders to GMT. If the accelerograph locks to the time signal received by the GPS antenna, then common time for all the records is guaranteed. There was only one triangle for which one of the accelerographs failed to lock its internal clock to the GPS time signal, and the record had to be discarded. For distances between stations of 60 m and larger, we used triaxial broad band sensors CMG40 by Guralp, able to record faithfully ground velocity down to 0.03 Hz, each one coupled to a different accelerograph. Ground vibration was recorded using K2 and Etna accelerographs by Kinometrics.

A total of nine triangular arrays and two linear arrays were used to record microtremors. Table 1 gives the different sizes of the triangular and linear arrays used and Figure 2 shows their location. At each one of locations S1 to S6 (small green triangles in Figure 2), four or five different triangular arrays with side length from 10 to 45 m were used to record microtremors during 20 min for each array. Additional triangular arrays were deployed at locations A, B, and C (large green triangles in Figure 2). At positions A and B, 10 and 8 triangular arrays respectively were deployed, with side length between 10 and 500 m (Table 1). Figure 2 shows an additional large green triangle, labelled C, where only three triangular arrays (with side lengths of 200, 400, and 500 m) were deployed. All these arrays were used to record microtremors for 20 min for the smaller arrays and 30 min for the larger arrays.

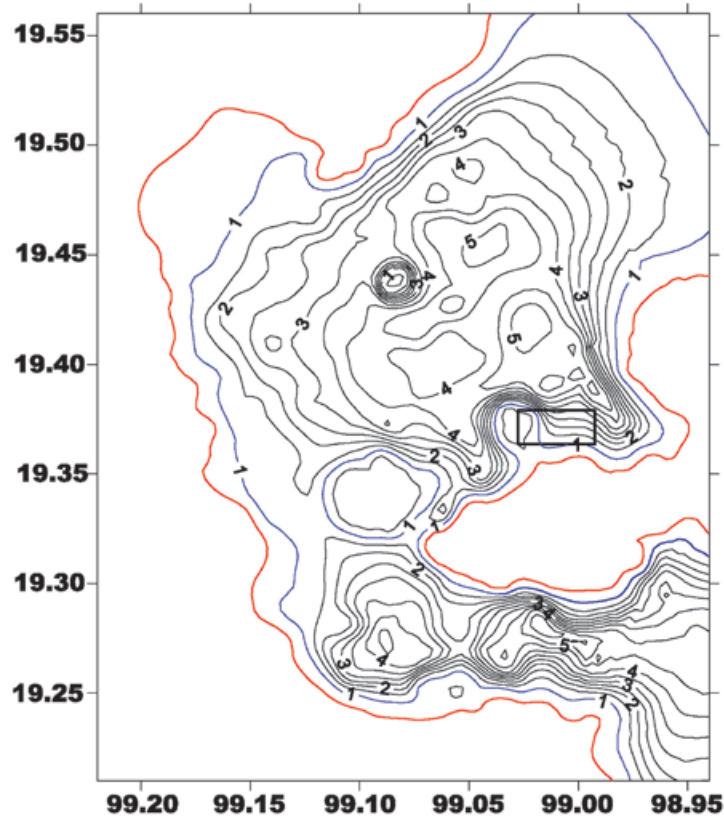


Figure 1. Location of the studied region (black rectangle drawn with thick lines) in Mexico City basin. The solid lines correspond to contours of dominant period within Mexico City lake bed zone, interpolated from available measurements. The lines are labelled with the corresponding period value in s. A red line shows the limit between the hill zone and the transition zone. The line corresponding to 1 s period is drawn with blue; it indicates the limit between transition and lake bed zones.

Table 1. Distances between stations in all of our triangular and linear arrays. At location S1, microtremors were recorded using five different triangular arrays. At locations S2 to S6, four different triangular arrays were used at each site. Locations A, and B included both small and large triangular arrays, with the sizes given in the table. At location C only three large triangular arrays were used to record microtremors. For arrays L1 and L2, four stations were used along a line.

Triangular arrays										
Array	Distance between sensors connected to the same accelerograph in m					Distance between independent stations in m				
S1	10	20	27	35	45					
S2	10	20	26.5	35						
S3	10	20	30	45						
S4	10	20	30	45						
S5	10	20	30	45						
S6	10	20	30	45						
A	10	20	30	40	45	100	200	300	400	500
B	10	20	30	40		60	200	400	500	
C						200	400	500		
Linear arrays										
L1						100	200	300	500	
L2						600	620	750	1220	1360 1960



Figure 2. Arrays used to measure ambient vibration in the lake bed zone of Mexico City. The region plotted corresponds to the black rectangle shown in the previous figure. The North direction is parallel to the ordinate axis, pointing up. At the locations of the green triangles marked with the letters A, B, and C, microtremors were recorded using large triangles (distance between stations between 100 and 500 m). At locations A and B microtremors were also measured using smaller triangles (side length between 10 and 60 m). At locations S1 to S6 microtremors were recorded using triangular arrays with side length between 10 and 45 m. Finally, the blue and red solid lines marked L1 and L2 show the location of the linear arrays where microtremors were recorded with four stations along a line. The distance between station in arrays L1 and L2 varied between 100 m and 1,960 m. Table 1 gives the sizes of all arrays used to record microtremors.

Finally, two additional linear arrays (L1 and L2) were deployed using four stations for each one. Their location is shown with the blue and red lines in Figure 2. The distance between stations is given in Table 1. Array L1, solid blue line in Figure 2, had separation between stations varying between 100 and 500 m. Array L2, solid red line in Figure 2, had separation between stations going from 600 to 1,960 m. The two linear arrays recorded microtremors for one hour.

Frequency and time domain correlation functions were computed for all station pairs. Time windows selected for the analysis had an overlap of 50% of its width, which varied from 60 s for the smaller arrays (smaller than 50 m) and from 240 s for the larger arrays up to the complete record length (1,200 s for arrays S1 to S6, 1,800 s for the large triangles at locations A, B, and C, and 3,600 s for the linear arrays L1 and L2). The use of different window lengths allowed us to check the influence of the record length in the results of the correlation analysis. We verified that our final results did not depend on window length and that they were stable and independent of all processing parameters.

Results

Results for distances smaller than 50 m

Figure 3 shows an example of the correlation coefficients computed from the measurements at location A for distances between stations of 10, 20, 30, and 40 m. This figure shows the average correlation coefficients computed for each distance from the 180 time windows selected for the analysis (60 time windows of 60 s duration with 30 s overlap, for each one of the three station pairs at the same distance for each triangle). The vertical dashed lines in each frame indicate the frequency range for which the corresponding correlation coefficients resemble a J_0 function. On the high frequency end of the plots, we observe that the correlation coefficients become almost flat at a smaller frequency as distance between stations increases: 15 Hz for 10 m, 8 Hz for 20 m, 6 Hz for 30 m, and 4 Hz for 40 m. At low frequencies we observe that correlation drops significantly at about 1 Hz in all four cases shown. This drop in correlation at low frequencies has also been observed by Chávez-García *et al.* (2006), Roberts and Asten (2007),

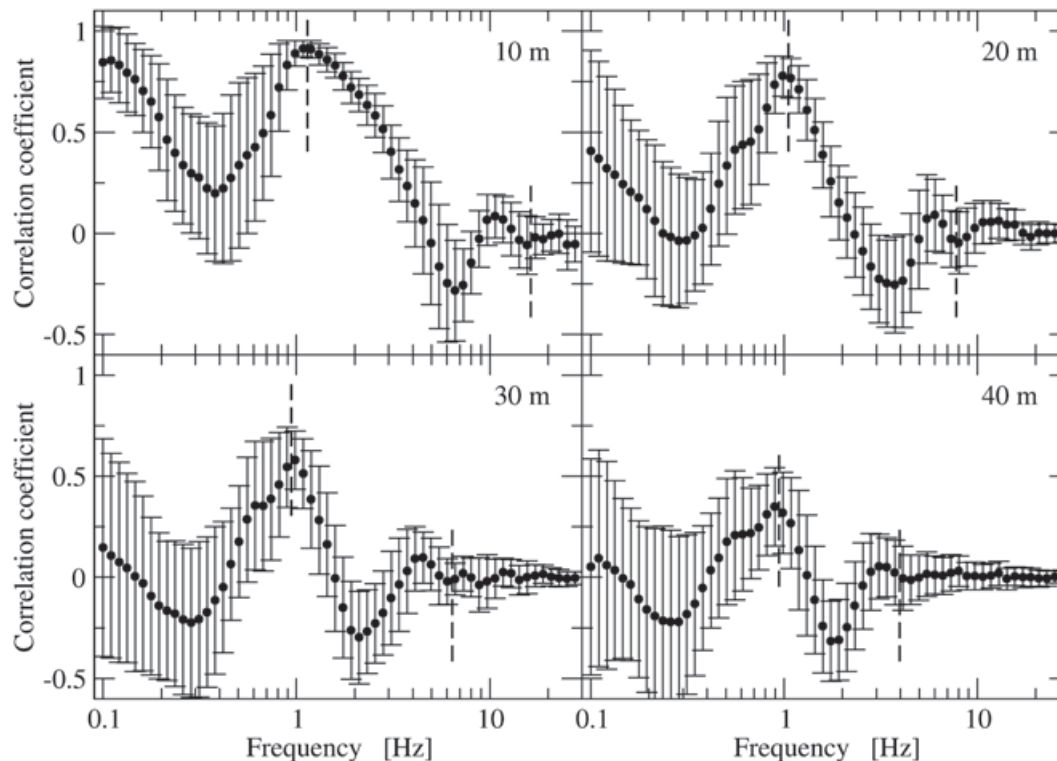


Figure 3. Average cross-correlation coefficients computed for the triangular arrays with side length of 10, 20, 30, and 40 m for location A (Figure 2). The solid circles show mean values and the bars for each symbol indicate the mean value plus or minus one standard deviation computed from 180 measurements for each distance. The two vertical dashed lines in each panel indicate the frequency range for which the correlation coefficients may be inverted to estimate a phase velocity dispersion curve.

and Claprod and Asten (2009). Roberts and Asten (2007) propose that the lowest frequency at which the correlation coefficients take the shape of a Bessel function coincides approximately with the peak values of the horizontal to vertical spectral ratios (HVSr) recorded at the same site. They speculate that high HVSr values imply low amplitudes of vertical component surface-wave motion, which results in the degradation of the correlation coefficients. Our results support this interpretation. As is shown below, for the small triangular arrays at location A, HVSr have a peak at frequencies between 0.4 and 1 Hz, coinciding with the trough in correlation at low frequencies of Figure 3. Similar results were obtained for all small (smaller than 50 m) triangular arrays, with the exception of array S6 as explained below.

Consider now an example of time domain correlation. Figure 4 shows average time domain correlation for all station pairs for the five triangles with size smaller than 50 m at location A (Figure 2), plotted at the corresponding distance between stations. They correspond then to the correlation coefficients shown in Figure 3. Again, each trace is the average for all possible station pairs at the corresponding distance. The pulse

corresponding to the Rayleigh wave mode is clearly observed. The phase velocity of this pulse can be measured in Figure 4, it is about 100 m/s. Figure 5 shows the Fourier amplitude spectra of the four traces shown in Figure 4. The Rayleigh wave pulse apparent in Figure 4 has energy in the frequency band from 1 to 10 Hz, although the largest amplitudes occur between 1 and 4 Hz.

We inverted a phase velocity from the computed correlation coefficients at each location using eq. (9). Figure 6 shows the phase velocity dispersion curves derived from the small arrays (smaller than 50 m) with the exception of array S6. Figure 6 shows almost flat dispersion curves in the frequency range from 0.7 to 4 Hz. The frequency range for which results could be obtained is different for each measurement point. However, minimum (about 40 m) and maximum (about 140 m) wavelengths are similar for all cases. This was expected. The resolution of an array for correlation of microtremor measurements is a function of wavelength, as explained in detail in Henstridge (1979) and Chávez-García *et al.* (2005). The phase velocities that were obtained are also quite different

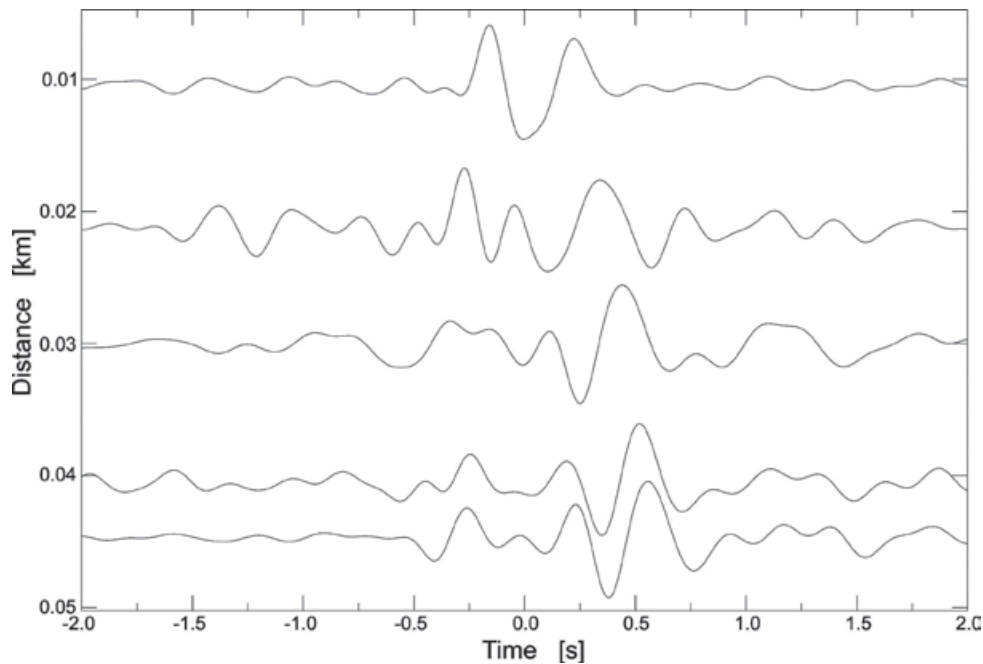


Figure 4. Seismic section formed with the average correlation functions computed in time domain for station pairs from the small triangular arrays installed at location A (Figure 2). Each trace is plotted at the corresponding inter station distance and is the average of 180 correlations computed for each distance. We observe a clear pulse with a phase velocity of about 100 m/s.

among the different measurements points, from 60 to 220 m/s at 2 Hz. This result suggests significant lateral heterogeneity, with shear wave velocity of the topmost layer varying according to the location of the array. We can compare the frequency range for which a phase velocity could be estimated at point A in Figure 6 (between 1 and 3.4 Hz) with the frequency band for which a Rayleigh pulse is estimated using time domain correlation with the same microtremor records (shown in Figure 5). The lower frequency limit is the same, about 1 Hz. However, time domain correlation shows that the Rayleigh pulse has significant energy at least up to 10 Hz, whereas frequency domain results do not go above 3.4 Hz. The reason is that frequency domain correlation requires that the phase difference between the two records be unambiguously measured. This is not the case for wavelengths smaller than half the distance between the two stations, which violate the spatial version of the fundamental sampling theorem, as explained in detail in Chávez-García and Rodríguez (2007). However, the phase velocity estimated from the seismic section in Figure 5 coincides well with the results from SPAC for array A. The results from SPAC and time domain correlation are compatible.

Figure 6 does not show results for measurements at array S6. A 200 s window of raw microtremor data recorded at this array for 10 m distance between stations is shown

in Figure 7, as an example of the records at that location. The records in this figure are dominated by very large amplitude transients, common to the three stations. We verified that these transients correspond to trucks and cars going by in the large Zaragoza Avenue; arrival time increases with distance to this avenue. Correlation between the traces is strongly affected by these signals which are certainly not aleatory (we can easily identify the same pulse in the three stations) and originate from a moving point source. The basic hypothesis of the SPAC method, waves propagating with equal power in all directions, is violated and no significant result could be obtained for this array.

Results for distances larger than 50 m

Let us consider now the results for station pairs separated a distance larger than 50 m. The results for these station pairs were not very good. The triangular arrays at locations A, B, and C included distances between 60 and 500 m (see Table 1). We computed correlations between the records in time and frequency domains, testing windows of different length for the analysis. We could not obtain significant correlation for any case. A possible reason for this lack of correlation could be that the microtremor records were not long enough. The recording time for the larger triangles at the locations of arrays A, B, and C was between 900 and 1,800 s.

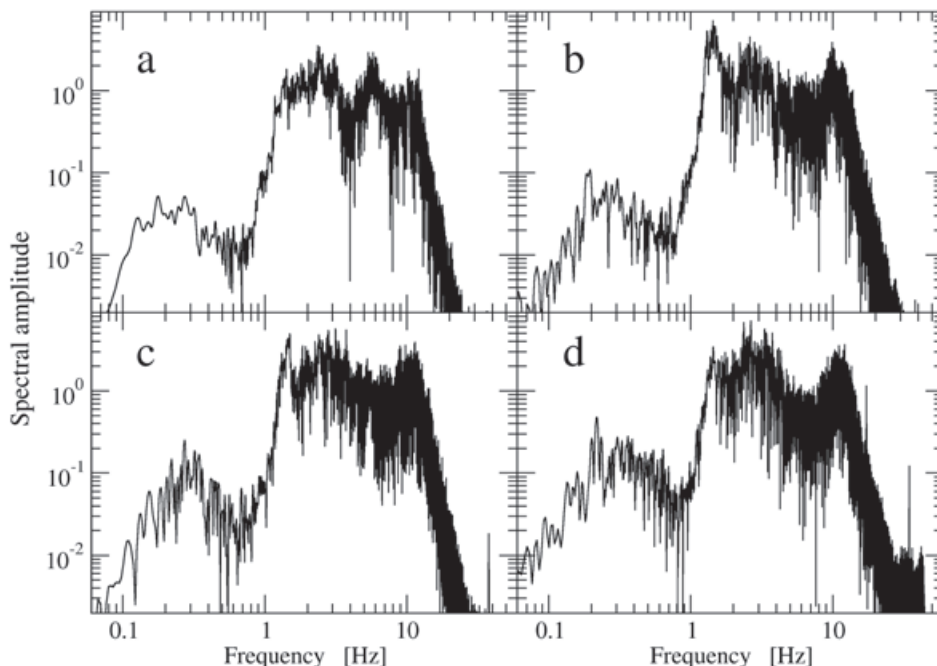


Figure 5. Example of the spectral amplitudes computed by Fourier transforming the traces shown in the preceding figure. a) Fourier amplitude spectrum of the trace plotted at 10 m distance in Figure 4. b) Fourier amplitude spectrum of the trace plotted at 30 m distance in Figure 4. c) Fourier amplitude spectrum of the trace plotted at 40 m distance in Figure 4. d) Fourier amplitude spectrum of the trace plotted at 45 m distance in Figure 4.

In order to check whether the total length of microtremor recording was a problem, we planned two additional arrays, L1 and L2. These arrays were two lines of four stations each. The total length of these arrays was 500 m for L1 and 1,960 m for L2. One hour of microtremors were recorded simultaneously in the four stations of each linear array. We computed correlation

coefficients for all station pairs for arrays L1 and L2 (the corresponding distances are given in Table 1) averaging results for windows of different duration selected from the records. We tested window durations between 240 and 3,600 s. An example of the results is given in Figure 8. This figure shows average correlation coefficients determined for four different station pairs from

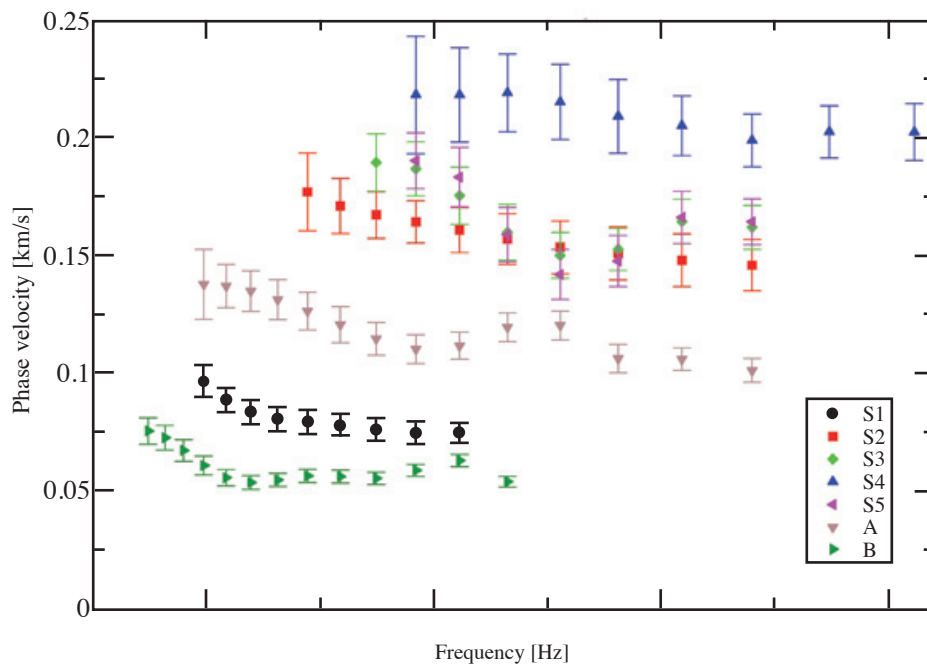


Figure 6. Phase velocity dispersion curves estimated from the inversion of the correlation coefficients obtained for triangular arrays with side length smaller than 50 m. We observe significant lateral heterogeneity in the studied region.

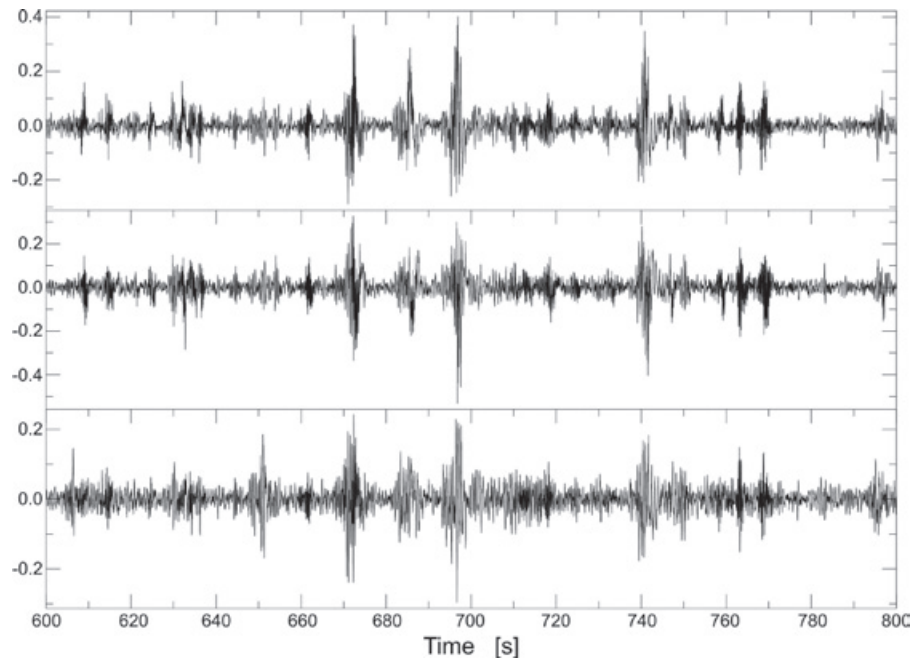


Figure 7. A 200 s window as an example of the microtremor records obtained for array S6. The traces shown correspond to the triangle with the sensors separated 10 m and are plotted as recorded, with no processing. We observe that very large pulses dominate all three traces. The arrival time of these pulses increases with distance to Ignacio Zaragoza avenue. We verified that those pulses correspond to vehicles in that avenue. Because the microtremor records are dominated by these pulses, they violate the hypotheses required by the SPAC method, and no dispersion curve could be estimated from the records obtained at location S6.

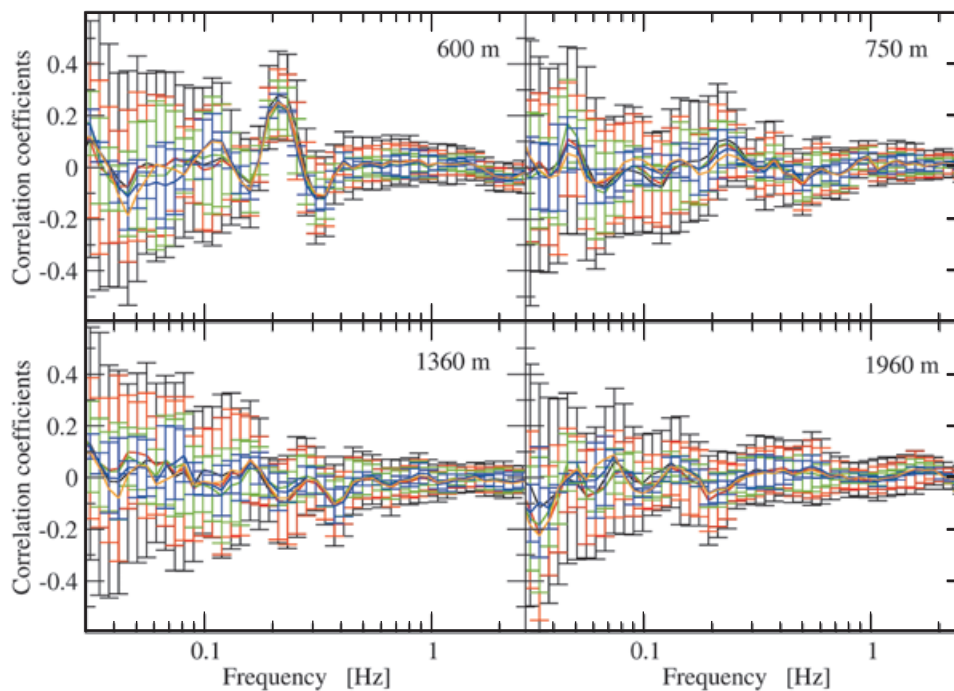


Figure 8. Average cross-correlation coefficients computed for station pairs separated distances of 600 m, 750 m, 1360 m and 1960 m, for linear array L2. The different lines correspond to different window lengths analysed, all of them with 50% overlap between windows. Black lines: average of 29 windows 240 s wide. Red lines: average of 14 windows 480 s wide. Green lines: average of 6 windows 960 s wide. Blue lines: average of 3 windows 1800 s wide. The orange lines correspond to the correlation of the complete records as a single window of 1-hour length. We observe a very good agreement among all the lines for each distance, indicating that window length is not a significant parameter in the results. We observe that only for 600 m distance significant correlation is obtained between 0.2 and 0.4 Hz.

array L2. Each solid line in this figure corresponds to average correlation coefficients computed using a different number of windows of different duration, between 240 and 3,600 s. The good agreement among all five curves indicates that the window length has no significant effect on the results. Thus the lack of correlation observed for the triangular arrays at locations A, B, and C was not the result of the limited recording time. The correlation coefficients in Figure 8 are not similar to a J_0 Bessel function, with the exception of a narrow frequency band (between 0.2 and 0.4 Hz) for the station pair at a distance of 600 m in Figure 8. Similar results were obtained for all station pairs from arrays L1 and L2. The correlation coefficients that were computed were not useful to invert a phase velocity dispersion curve based on eq. (9).

Even if the correlation coefficients from array L1 and L2 were inadequate for an inversion to obtain a phase velocity dispersion curve, for some station pairs, the observed correlation coefficients showed the expected behaviour, i.e., a shape similar to a J_0 function, at least for small

frequency windows, as shown for 600 m distance in Figure 8. Figure 9 shows the same correlation coefficients computed for the separation distance of 600 m for array L2. In this figure we have superposed a J_0 function, manually fitted to the observations by changing the abscissa of each point while keeping the ordinates constant. This modified Bessel function is shown with solid green circles in Figure 9 in the frequency range 0.17 to 0.4 Hz. For each of these points, a phase velocity could be estimated from the comparison between the argument of the original J_0 function and the value of the abscissa of that same point after being fitted to the observed correlation coefficients, using the relation between the argument of the Bessel function and the term $\omega r/c$. Using this non-standard procedure, we could obtain some estimates of phase velocity for distances of 100, 200, 300, and 500 m for array L1, and for 600 m for array L2, only for five out of the ten distances for which data were recorded in these arrays, and only five out of 22 distances larger than 50 m including measurements for locations A, B, and C.

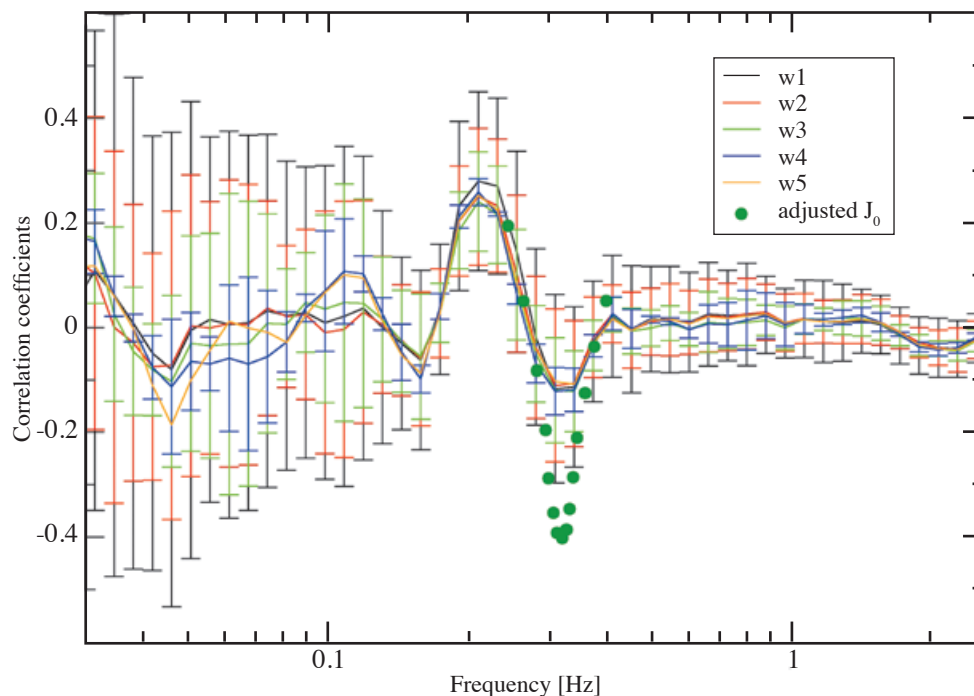


Figure 9. Example of the manual fit of the abscissae of a J_0 function (solid circles) to the average observed correlation coefficients. The solid lines with error bars repeat the average correlation coefficients and standard deviations shown in Figure 8 for the station pair at a distance of 600 m in array L2. As explained in the figure caption of Figure 8, the different lines correspond to different window lengths analysed, all of them with 50% overlap between windows. The green solid circles show selected points of a Bessel function of first kind and zero order whose abscissae have been changed to fit as closely as possible the observed correlation coefficients, while keeping the amplitudes unaffected. An estimate of phase velocity may be computed from the comparison between the original argument of each point of the Bessel function and its abscissa after being fitted to the observed correlation coefficients.

The results for the five distances for which phase velocity dispersion could be estimated using this non-standard procedure are shown in Figure 10. The different symbols identify the corresponding station pair for which the phase velocity could be estimated. The frequency range of these estimates is very small, except for 100 m distance for array L1. Contrary to what was observed for small distances between stations, all the different estimates shown in Figure 10 are in good agreement among them, forming a single phase velocity dispersion curve. Phase velocity is almost constant at 75 m/s for frequencies larger than 0.8 Hz, in good agreement with a couple of the dispersion curves shown in Figure 6 for the smaller arrays. For frequencies smaller than 0.8 Hz, phase velocity in Figure 10 increases up to 450 m/s, indicating a significant velocity contrast below the soft surficial layer. However, because the phase velocity curve remains steep at low frequencies, it does not constrain the velocity below the sediments.

Velocity models

The phase velocity dispersion curves we estimated are consistent between our small and large arrays. However, although a significant velocity contrast below is clearly identified, the results

are unable to constrain the velocity of the deeper medium. Moreover, because the phase velocity estimates shown in Figure 10 were obtained using a manual fit of the Bessel function, they are less reliable than the phase velocities shown in Figure 6, obtained using a formal inversion scheme based on eq. (9). For these reasons, we have not tried to estimate a 1D layered model from the inversion of the phase velocity dispersion curves. Rather, we propose the model shown in Table 2, based on the phase velocity dispersion estimated in Figure 10. A single layer over a half space model is the simplest model that can fit the observed dispersion. This proposed model constrained the velocity of the soft layer to 75 m/s, to fit the Rayleigh phase velocity observed at frequencies larger than 1 Hz in Figure 10. The shear wave velocity of the half space must be larger than 500 m/s but is otherwise unconstrained. We took density values adequate for the soil layer and half space from Pérez-Cruz (1988). We computed phase velocity dispersion for the fundamental Rayleigh wave mode for the model in Table 2, varying the thickness of the layer until a reasonable fit was obtained. The computed dispersion curve is shown with a solid black line in Figure 10. Even if the model of Table 2 is not well constrained, the agreement between observed and computed phase velocity dispersion is quite good.

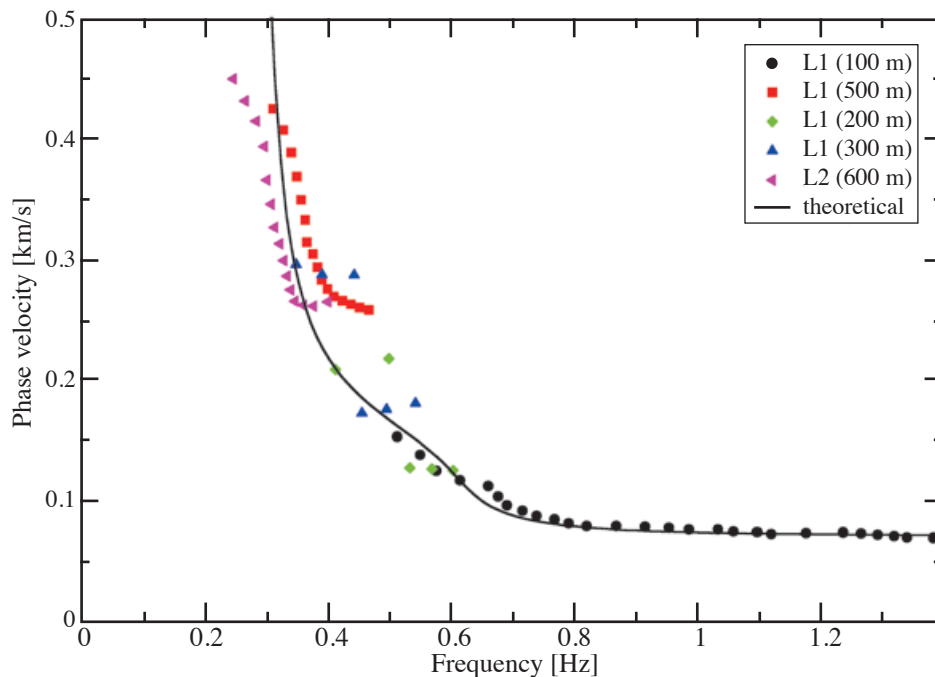


Figure 10. Phase velocity dispersion curves estimated from the manual fitting of a J_0 function to the correlation coefficients determined for distances larger than 50 m. Only five station pairs, out of 22 (see Table 1), showed a small frequency range for which a J_0 function could be fitted manually. From that fit we determined the phase velocity dispersion curves shown in this figure. The different symbols identify the corresponding array and distance between stations. The solid line corresponds to the fundamental mode of Rayleigh waves computed for the model given in Table 2. The agreement between the observed and computed dispersion is good.

Table 2. A possible one-layer model for the studied region based on the dispersion curve determined for arrays L1 and L2. The shear-wave velocity of the half space is unconstrained.

H [m]	α [m/s]	β [m/s]	ρ [gm/cm ³]
62.0	800.0	75.0	1.8
-	1,413.7	816.2	2.0

The simple model of Table 2 is also compatible with the phase velocity dispersion estimated from the smaller arrays. Figure 11 shows the estimates of phase velocity dispersion obtained from our small arrays (those shown in Figure 6) together with phase velocity dispersion curves computed for the fundamental mode of Rayleigh waves for models very similar to that in Table 2. The only change made was on the shear wave velocity of the soft layer. All other parameters of the model were kept constant. The shear wave velocity used for the layer is indicated next to each dispersion curve. We observe quite a good fit to the observed dispersion. This fit could be

improved, were we to tweak the thickness of the soft layer but we do not think this to be useful at this stage because the model remains not well constrained. Figures 10 and 11 do show, however, that a model similar to that in Table 2 explains our observations and quantifies the lateral variation of the shear wave velocity of the topmost layer.

The results for our larger arrays are disappointing. At low frequencies the phase velocity dispersion curve is very steep, indicating a large impedance contrast at the base of the clay layer. That impedance contrast is the reason for the large amplification of seismic ground motion in the lake bed zone, which in a model such as that in Table 2 is equal to the impedance contrast between the layer and its substratum. Our results fail to constrain the shear wave velocity in the half-space. As explained in detail in Chávez-García (2011), if we cannot constrain the shear wave velocity below the soft sediments, we cannot compute the expected amplification. We expected that larger distances between stations would allow us to correlate waves propagating through the substratum. This is not the case.

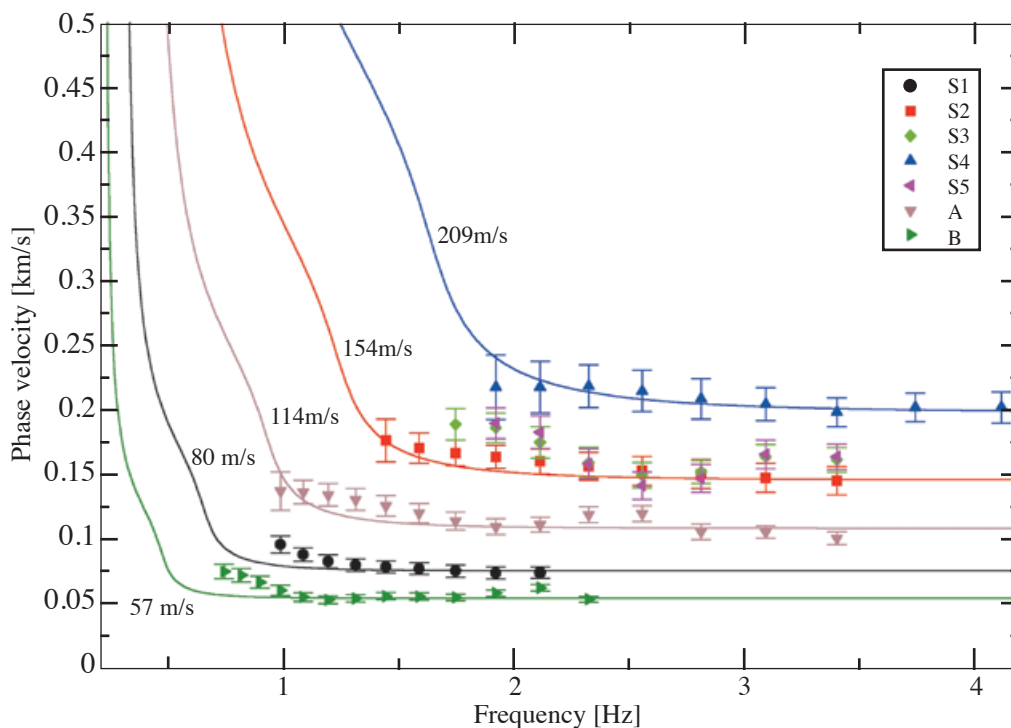


Figure 11. The symbols show the phase velocity dispersion curves estimated from the correlation of seismic noise in the frequency domain from triangular arrays with side length smaller than 50 m. They repeat the results shown in Figure 6. We have now included, with solid lines, theoretical dispersion curves for the fundamental Rayleigh wave mode computed for models similar to that shown in Table 2. We only changed the shear wave velocity value for the soft soil layer and kept all other parameters the same. Instead of the value of 75 m/s given in Table 2 for the shear wave velocity of the soft layer, the value shown next to each solid line was used to compute phase velocity dispersion

The lack of correlation between our stations for distances larger than 600 m is similar to the results presented in Chávez-García and Quintanar (2010). Those authors computed correlation between stations separated from 5 to several hundred km. One of the arrays whose data they analysed crossed Mexico City. They observed a lack of correlation between stations closer than 10 km, even if the same stations showed good correlation with more distant stations. They ascribed the lack of correlation to strong lateral heterogeneities, expected for the thick volcanic sediment sequence below the clay layer in Mexico City basin. Chávez-García and Quintanar (2010) concluded that the heterogeneity of the deep structure of the Mexican Volcanic Belt inhibited the propagation of Rayleigh waves with wavelengths smaller than 9 km.

In the case of our results, Figure 10 shows a phase velocity of 400 m/s at 0.4 Hz. This implies a wavelength of 1 km, which is about the longest wave for which we obtain correlation among our stations. Considering together our results with those of Chávez-García and Quintanar (2010), we may conclude that there is a wavelength range between 1 and 9 km, for which no correlation is observed for microtremor records in Mexico City basin. However, information for this wavelength range is needed to constrain the shear-wave velocity structure of the volcanic

sediments below the clay layers in the lake bed zone. This is a very significant problem and one that remains a challenge.

HVSR

Finally, we computed horizontal to vertical spectral ratios (HVSR) using the microtremor records where three-component ground motion was recorded. We estimated dominant period in the studied region from the large peaks observed in the HVSR. This is not incompatible with the interpretation of the records in terms of Rayleigh waves, as required by the SPAC method. It has been shown that HVSR gives stable results independently of the predominant propagation mode, body or surface waves (Chávez-García, 2009). Figure 12 shows the map distribution of dominant period obtained from our measurements. We observe significant variations, from 0.8 s on Ignacio Zaragoza avenue up to almost 5 s for the measurements at the stations for the linear arrays L1 and L2. Dominant period varies rapidly over short distances. The dominant period value computed for the model of Table 2 (which does not correspond to a specific site but is mostly based on the results for array L1) is 3 s, in good agreement with the empirical values shown in Figure 12. We have superposed in this figure the dominant period curves shown in Figure 1, included in the Distrito Federal building code.

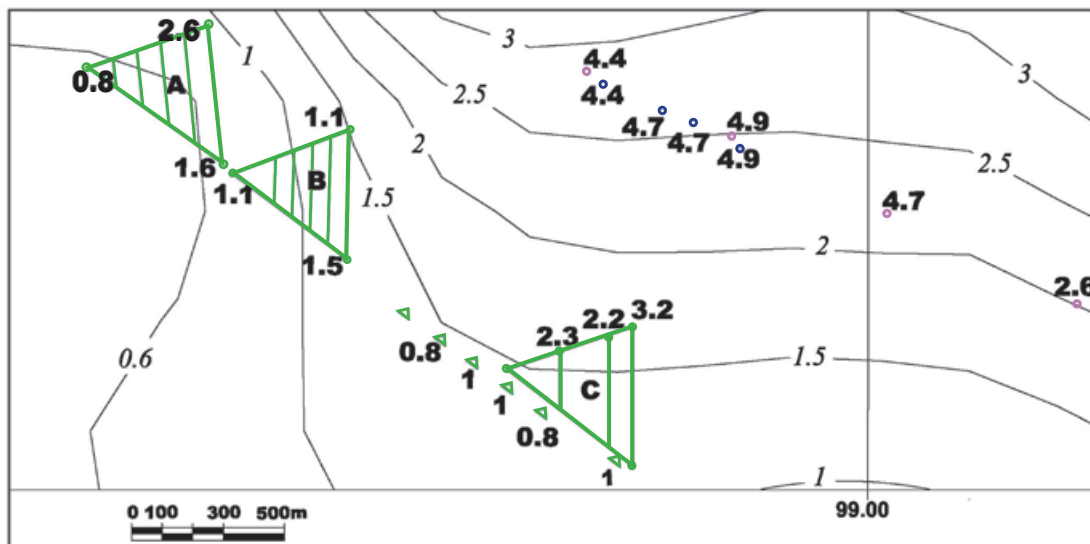


Figure 12. Dominant period map obtained using HVSR with the microtremors recorded in all the arrays. The region plotted corresponds to the black rectangle shown in Figure 1. The North direction is parallel to the ordinate axis, pointing up. The location of the arrays used in this study are shown with the large green triangles marked A, B, and C. The small green triangles indicate the location of arrays S1 to S6. The open red and blue circles indicate the location of the linear arrays L1 and L2 respectively. The bold numbers indicate the values of dominant period in s determined from HVSR for our measurements. The solid black lines, together with the numbers in cursive font, show the contours of dominant period obtained from Distrito Federal building code. They are the same curves shown in Figure 1. We observe a significant disagreement between our measurements and the contour lines, interpolated from much sparser measurements.

These curves are the result of the interpolation of available measurements, which are quite sparse in our studied region. This explains the large difference between our measurements of dominant period and the interpolated curves. These discrepancies suggest that additional measurements of dominant period are needed in the lake bed zone of Mexico City.

Conclusions

We have presented the results of subsoil exploration in the lake bed zone of Mexico City using correlation of microtremors recorded with arrays of stations. 46 independent triangular arrays and two linear arrays were installed with inter station distances between 10 m and almost 2 km. Microtremors were recorded for a few minutes at the smaller arrays and one hour at the larger arrays. Vertical components were analyzed using the SPAC method to recover Rayleigh wave dispersion. Our measurements allowed us to compute correlations of microtremors for a very wide range of distances between stations, from 10 m to 2 km.

Good results were obtained for distance between stations smaller than 50 m. The shallow velocity structure could be well determined from correlation analyses. Moreover, we obtained evidence of significant lateral heterogeneity in the clay layer. We showed that the velocities estimated using time domain cross-correlation, seismic interferometry, were compatible with the results from the SPAC method.

For distance between stations larger than 50 m, it was not possible to obtain good correlation. We only observed correlation coefficients similar to a Bessel function in small frequency ranges for five different distances (between 100 and 600 m) out of the 22 distance for which we recorded data. We demonstrated that this lack of correlation was not due to the duration of the microtremor records in the field. For those five different station pairs, we manually fitted a Bessel function to the narrow range of useful correlation coefficients and estimated from that phase velocity values in the frequency range from 0.3 to 1.4 Hz. The result shows that there is a significant impedance contrast at the base of the soft surficial sediments. However, our measurements are unable to constrain the velocity below those sediments. If we cannot determine the shear wave velocity of both sediments and basement, it is not possible to compute expected amplification. These results are disappointing. Our analysis indicates that the most likely cause is lateral heterogeneity of the sediments below the soft clay layers. Mexico City basin includes several km of volcanic sediments

between the very soft clay layer at the surface in the lake bed zone and the limestone basement of the basin. Correlation between two stations requires that the medium, at the wavelength scale of distance between stations, be able to sustain Rayleigh waves. The large heterogeneity expected for volcanic sediments must affect surface wave propagation for wavelengths larger than 1 km in such a way that Rayleigh waves cannot be retrieved from frequency or time domain correlations. This conclusion is similar to those of Chávez-García and Quintanar (2010), who observed a lack of correlation in Mexico City for Rayleigh wavelengths smaller than 9 km. Our results show that we need an alternative method to investigate the subsoil structure for the wavelength range between 1 and 9 km.

We used the records obtained using triaxial sensors to estimate dominant period from horizontal to vertical spectral ratios. The results are compatible with those from correlation analyses. Our measurements provide reliable constraints on the variation of dominant period in the studied region. Dominant period changes significantly over short distances, similarly to the change of shear wave velocity of the topmost layers identified from correlation analyses. This was to be expected close to the edges of the ancient lake, where we anticipate rapid lateral variations in the subsoil structure. Our values for dominant period are quite different from the smooth curves included in Distrito Federal building code. The curves from the building code were interpolated from very few measurements in the studied region. This suggests that additional measurements of dominant period are needed in the lake bed zone of Mexico City. This is important because the building code specifies design spectra in terms of dominant frequency.

Finally, the correlation method, as any other method in Geophysics, has significant limitations. In the case of Mexico City, the determination of the velocity structure below the clay layer remains a challenge. That structure is important because it conditions the incident wavefield below the clay layer and is necessary to compute expected amplification.

Acknowledgements

We gratefully acknowledge the help of Antonio Valverde, Horacio Mijares, and Ricardo Vázquez Rosas for their help during the many days of field work. The comments by four anonymous reviewers were very helpful to improve our manuscript. Part of this research was supported by Instituto de Ingeniería, UNAM, through its fund for internal research projects 2010, project 0542.

Bibliography

- Aki K., 1957, Space and time spectra of stationary stochastic waves, with special reference to microtremors, *Bull. Earthquake Res. Inst. Univ. Tokyo*, 25, 415–457.
- Aki K., 1965, A note on the use of microseisms in determining the shallow structure of the earth's crust, *Geophysics*, 30, 665–666.
- Apostolidis P., Raptakis D., Pandi K., Manakou M., Ptilakis K., 2005, Definition of subsoil structure and preliminary ground response in Aigion city (Greece) using microtremors and earthquakes, *Soil Dyn. Earthq. Engng.*, 26: 922–940.
- Bensen G.D., Ritzwoller M.H., Barmin M.P., Levshin A.L., Lin F., Moschetti M.P., Shapiro N.M., Yang Y., 2007, Processing seismic ambient noise data to obtain reliable broad-band surface wave dispersion measurements, *Geophys. J.* 169, 1239–1260, doi 10.1111/j.1365-246X.2007.03374.x.
- Brenguier F., Shapiro N.M., Campillo M., Nercessian A., Ferrazzini V., 2007, 3D surface wave tomography of the Piton de la Fournaise volcano using seismic noise correlations, *Geophys. Res. Lett.*, 34, L02305.
- Campillo M., Paul A., 2003, Long range correlations in the diffuse seismic coda, *Science*, 299, 547–549.
- Campillo M., 2006, Phase and correlation in 'random' seismic fields and the reconstruction of the Green's function, *Pure Appl. Geophys.*, 163, 475–502.
- Cárdenas M., Chávez-García F.J., Gusev A., 1997, Regional amplification of ground motion in central Mexico: results from coda magnitude data and preliminary modeling, *J. Seism.*, 1, 341–355.
- Chávez-García F.J., Bard P.-Y., 1993a, Gravity waves in Mexico City? I. Gravity perturbed waves in an elastic solid, *Bull. Seism. Soc. Am.*, 83, 1637–1655.
- Chávez-García F.J., Bard P.-Y., 1993b, Gravity waves in Mexico City? II. Coupling between an elastic solid and a fluid layer, *Bull. Seism. Soc. Am.*, 83, 1656–1675.
- Chávez-García F.J., Bard P.-Y. 1994, Site effects in Mexico City eight years after the September 1985 Michoacán earthquakes, *Soil Dyn. Earthquake Eng.*, 13, 229–247.
- Chávez-García, F.J. and L. Salazar (2002). Strong motion in central Mexico: a model based on data analysis and simple modelling, *Bull. Seism. Soc. Am.*, 92, 3087–3101.
- Chávez-García, F.J. y F. Luzon (2005). On the correlation of seismic microtremors, *J. Geophys. Res.*, 110, B11313, doi: 10.1029/2005JB003671.
- Chávez-García, F.J. (2007). Site effects: from observations and modelling to accounting for them in building codes, in K.D. Ptilakis (ed.) *Earthquake Geotechnical Engineering, 4th International Conference of Earthquake Geotechnical Engineering - Invited lectures*, vol. 6 of the series Geotechnical, Geological and Earthquake Engineering, ISBN: 978-1-4020-5892-9, ISSN 1573-6059, DOI 10.1007/978-1-4020-5893-6, Springer, 53-72.
- Chávez-García, F.J. and M. Rodríguez (2007). The correlation of microtremors: empirical limits and relations between results in frequency and time domains, *Geophys. J. Int.*, 171, 657–664.
- Chávez-García, F.J. (2009). Ambient noise and site response: from estimation of site effects to determination of the subsoil structure, en M. Mucciarelli, M. Herak y J. Cassidy (eds.) *Increasing seismic safety by combining engineering technologies and seismological data*, NATO Science for Peace and Security Series C: Environmental Security, ISBN 978-1-4020-9193-3 Springer Science+Business Media B.V., 53-71.
- Chávez-García, F.J. (2010). Site response at Mexico City. Progress made and pending issues, *Joint Conference Proceedings, 7th International Conference on Urban Earthquake Engineering (7CUUE) & 5th International Conference on Earthquake Engineering (5ICEE)*, 3-5 de marzo, Tokyo Institute of Technology, Tokyo, Japón, 81-88.
- Chávez-García, F.J. y L. Quintanar (2010). Velocity structure under the Trans-Mexican Volcanic Belt. Preliminary results using correlation of noise, *Geophys. J. Int.*, 183, 1077-1086, doi: 10.1111/j.1365-246X.2010.04780.x.
- Chávez-García, F.J. (2011). Site effects due to topography and to soft soil layers: progress made and pending issues. A personal perspective, conferencia estado-del-arte invitada en *5th International Conference on Earthquake Geotechnical Engineering*, ISBN 978-956-7141-18-0, Chilean Geotechnical Society, 105-136.

- Chávez-García, F.J., J. Ramos Martínez, and E. Romero-Jiménez (1995). Surface wave dispersion analysis in Mexico City, *Bull. Seism. Soc. Am.*, 85, 1116–1126.
- Chávez-García, F.J., M. Rodríguez, M. and W.R. Stephenson (2005). An alternative approach to the SPAC analysis of microtremors: exploiting stationarity of noise, *Bull. Seism. Soc. Am.*, 95, 277–293.
- Chávez-García, F.J., M. Rodríguez, and W.R. Stephenson (2006). Subsoil structure using SPAC measurements along a line, *Bull. Seism. Soc. Am.*, 96, 729–736.
- Chávez-García, F.J., T. Domínguez, M. Rodríguez, and F. Pérez (2007). Site effects in a volcanic environment: a comparison between HVSR and array techniques at Colima, Mexico, *Bull. Seism. Soc. Am.*, 97, 591–604, doi: 10.1785/0120060095.
- Chouet, B., G. DeLuca, G. Milana, P. Dawson, M. Martini, and R. Scarpa (1998). Shallow velocity structure of Stromboli volcano, Italy, derived from small-aperture array measurements of Strombolian tremor, *Bull. Seism. Soc. Am.*, 88, 653–666.
- Claerbout J.F., 1968, Synthesis of a layered medium from its acoustic transmission response, *Geophysics*, 33, 264–269.
- Claprod, M. and M.W. Asten (2009). Initial results from spatially averaged coherency, frequency-wavenumber, and horizontal to vertical spectrum ratio microtremor survey methods for site hazard study at Launceston, Tasmania, *Exploration Geophysics*, 40, 132–142, *Butsuri-Tansa*, 62, 132–142, *Mulli-Tamsa*, 12, 132–142.
- Duvall T.L., S.M. Jefferies, J.W. Harvey, and M.A. Pomerantz (1993). Time–distance helioseismology, *Nature*, 362, 430–432.
- Ekström, G., G.A. Abers, and S.C. Webb (2009). Determination of surface-wave velocities across USArray from noise and Aki’s spectral formulation, *Geophys. Res. Lett.*, 36, L18301, doi:10.1029/2009GL039131.
- Ferrazzini, V., K. Aki, and B. Chouet (1991). Characteristics of seismic waves composing Hawaiian volcanic tremor and gas-piston events observed by a near-source array, *J. Geophys. Res.*, 96, 6199–6209.
- Flores Estrella, H. and J. Aguirre-González (2003). SPAC: an alternative method to estimate earthquake site effects in Mexico City, *Geofis. Int.*, 42, 227–236.
- Furumura, T., and B. L. N. Kennett (1998). On the nature of regional seismic phases. III. The influence of crustal heterogeneity on the wavefield for subduction earthquakes: the 1985 Michoacan and 1995 Copala, Guerrero, Mexico earthquakes, *Geophys. J. Int.*, 135, 1060–1084.
- Henstridge, D.J. (1979). A signal processing method for circular arrays, *Geophysics*, 44, 179–184.
- Herrmann, R.B. (1985). Computer programs in Seismology, 8 vols., Saint Louis University.
- Iida, M. (1999). Excitation of high-frequency surface waves with long duration in the Valley of Mexico, *J. Geophys. Res.*, 104, 7329–7345.
- Kang, T.S. and J.S. Shin (2006). Surface-wave tomography from ambient seismic noise of accelerograph networks in southern Korea, *Geophys. Res. Lett.*, 33, L17303, doi:10.1029/2006GL027044.
- Kawase, H. and K. Aki (1989). A study on the response of a soft soil basin for incident S, P, and Rayleigh waves with special reference to the long duration observed in Mexico City, *Bull. Seism. Soc. Am.*, 79, 1361–1382.
- Lermo J. and F.J. Chávez-García (1993). Site effect evaluation using spectral ratios with only one station, *Bull. Seism. Soc. Am.*, 83, 1574–1594.
- Lermo, J. and F.J. Chávez-García (1994). Site effect evaluation at Mexico City: dominant period and relative amplification from strong motion and microtremor records, *Soil Dyn. & Earthq. Engrg.*, 13, 413–423.
- Louie, J.N. (2001). Faster, better: shear-wave velocity to 100 meters depths from refraction microtremor arrays, *Bull. Seism. Soc. Am.*, 91, 347–364.
- Margaryan, S., T. Yokoi, and K. Hayashi (2009). Experiments on the stability of the spatial autocorrelation method (SPAC) and linear array methods and on the imaginary part of the SPAC coefficients as an indicator of data quality, *Explor. Geophys.*, 40, 121–131; *Butsuri-Tansa*, 62, 121–131; *Mulli-Tamsa*, 12, 121–131.
- Morikawa, H., K. Toki, S. Sawada, J. Akamatsu, K. Miyakoshi, J. Ejiri, and D. Nakajima

- (1998). Detection of dispersion curves from microseisms observed at two sites, in *The effects of surface geology on seismic motion; Proc. of the 2nd. Intl. Symp. on the effects of surface geology on seismic motion*, K. Irikura, K. Kudo, H. Okada, and T. Sasatani (Editors) 2, 719–724.
- Morikawa, H., S. Sawada, and J. Akamatsu (2004). A method to estimate phase velocities of Rayleigh waves using microseisms simultaneously observed at two sites, *Bull. Seism. Soc. Am.*, 94, 961–976.
- Moschetti, M.P., M.H. Ritzwoller, and N.M. Shapiro (2005). California surface wave tomography from ambient seismic noise: tracking the progress of the USArray transportable network, *EOS, Trans. Am. geophys. Un.*, 86(52), Fall Meet. Suppl., Abstract S31A-0276.
- Ohori M., A. Nobata, and K. Wakamatsu (2002). A comparison of ESAC and FK methods of estimating phase velocity using arbitrarily shaped microtremor arrays, *Bull. Seism. Soc. Am.*, 92, 2323–2332.
- Okada H. (2003) *The microtremor survey method*, Soc. of Expl. Geophys. of Japan, translated by K. Suto, Geophys. Monograph Series No. 12, Soc. of Expl. Geophys., Tulsa.
- Ordaz, M. and S.K. Singh (1992). Source spectra and spectral attenuation of seismic waves from Mexico earthquakes, and evidence of amplification in the hill zone of Mexico City, *Bull. Seism. Soc. Am.*, 82, 24–43.
- Paul, A., M. Campillo, L. Margerin, and E. Larose (2005). Empirical synthesis of time-asymmetrical Green's functions from the correlation of coda waves, *J. Geophys. Res.*, 110, B08302, doi:10.1029/2004JB003521.
- Pérez-Cruz, G.A. (1988). Estudio sismológico de reflexión del subsuelo de la Ciudad de México, M.Eng. Thesis, Facultad de Ingeniería, UNAM, 81 pp.
- Prieto, G.A. and G.C. Beroza (2008). Earthquake ground motion prediction using the ambient seismic field, *Geophys. Res. Lett.*, 35, L14304, doi:10.1029/2008GL034428.
- Prieto, G.A., J.F. Lawrence, and G.C. Beroza (2009). Anelastic Earth structure from the coherency of ambient seismic field, *J. Geophys. Res.*, 114, B07303, doi:10.1029/2008JB006067.
- Prieto, G.A., J.F. Lawrence, A.I. Chung, and M.D. Kohler (2010). Impulse response of civil structures from ambient noise analysis, *Bull. Seism. Soc. Am.*, 100, 2322–2328, doi:10.1785/0120090285.
- Roberts, J.C. and M.W. Asten (2005). Estimating the shear velocity profile of Quaternary silts using microtremor array (SPAC) measurements, *Exploration Geophysics*, 36, 34–40, *Butsuri-Tansam* 58, Mulli-Tamsa, 8.
- Roberts, J.C. and M.W. Asten (2007). Further investigation over Quaternary silts using the spatial autocorrelation (SPAC) and horizontal to vertical spectral ratio (HVSR) microtremor methods, *Exploration Geophysics*, 38, 175–183.
- Roux, P., K.G. Sabra, W.A. Kuperman, and A. Roux (2005). Ambient noise correlations in free space: theoretical approach, *J. acoust. Soc. Am.*, 117, 79–84.
- Sabra, K.G., P. Gerstoft, P. Roux, W.A. Kuperman, and M.C. Fehler (2005). Extracting time-domain Green's function estimates from ambient seismic noise, *Geophys. Res. Lett.*, 32, L03310, doi:10.1029/2004GL021862.
- Seed, H.B., M.P. Romo, J.I. Sun, A. Jaime, and J. Lysmer (1988). Relationships between soil condiriont and earthquake ground motion, *Earthquake Spectra*, 4, 687–729.
- Sens-Schönfelder, C. and U. Wegler (2006). Passive image interferometry and seasonal variations of seismic velocities at Merapi Volcano, Indonesia, *Geophys. Res. Lett.*, 33, L21302.
- Shapiro, M.N., M. Campillo, A. Paul, S.K. Singh, D. Jongmans, and F.J. Sánchez-Sesma (1997). Surface wave propagation across the Mexican Volcanic Belt and the origin of the log-period seismic-wave amplification in the Valley of Mexico, *Geophys. J. Int.*, 128, 151–166.
- Shapiro, N.M., K.B. Olsen, and S.K. Singh (2001). Evidence of the dominance of higher-mode surface waves in the lake-bed zone of the valley of Mexico, *Geophys. J. Int.*, 147, 517–527.
- Shapiro, N.M., M. Campillo, L. Stehly, and M.H. Ritzwoller (2005). High-resolution surface-wave tomography from ambient seismic noise, *Science*, 307, 1615–1618, doi:10.1126/science.1108339.
- Singh, S.K., E. Mena, and R. Castro (1988). Some aspects of the source characteristics and ground motion amplifications in and near Mexico City from acceleration data of

- the September, 1985, Michoacan, Mexico earthquakes, *Bull. Seism. Soc. Am.*, 78, 451–477.
- Singh, S.K., R. Quaas, M. Ordaz, F. Mooser, D. Almora, M. Torres, and R. Vásquez (1995). Is there truly a 'hard' rock site in the Valley of Mexico?, *Geophys. Res. Lett.*, 22, 481–484.
- Snieder, R. (2004). Extracting the Green's function from the correlation of coda waves: a derivation based on stationary phase, *Phys. Rev. E*, 69, doi:10.1103/PhysRevE.69.046610.
- Tsai, V.C. (2009). On establishing the accuracy of noise tomography travel-time measurements in a realistic medium, *Geophys. J. Int.*, 178, 1555–1564, doi: 10.1111/j.1365-246X.2009.04239.x.
- Tsai, V.C. (2010). The relationship between noise correlation and the Green's function in the presence of degeneracy and the absence of equipartition, *Geophys. J. Int.*, 182, 1509–1514, doi: 10.1111/j.1365-246X.2010.04693.x.
- Tsai, V.C. and M.P. Moschetti (2010). An explicit relationship between time-domain noise correlation and spatial autocorrelation (SPAC) results, *Geophys. J. Int.*, 182, 454–460, doi: 10.1111/j.1365-246X.2010.04633.x.
- Wapenaar, K. (2004). Retrieving the elastodynamic Green's function of an arbitrary inhomogeneous medium by cross correlation, *Phys. Rev. Lett.*, 93(25), Article 254301.
- Wapenaar, K., D. Draganov, and J.O.A. Robertsson (eds.) (2008). *Seismic interferometry: history and present status*, SEG Geophysics Reprint Series No. 26, Tulsa, Oklahoma.
- Weaver R.L. and O.I. Lobkis (2005). Fluctuations in diffuse field-field correlations and the emergence of the Green's function in open systems, *J. Acoust. Soc. Am.*, 117, 3432–3439.
- Yamamoto, H. (1998). An experiment for estimating S-wave velocity structure from phase velocities of Love and Rayleigh waves in microtremors, in *The effects of surface geology on seismic motion*; Proc. of the 2nd. Intl. Symp. on the Effects of Surface Geology on Seismic Motion, K. Irikura, K. Kudo, H. Okada, and T. Sasatani (Editors), Rotterdam, Balkema, 2, 705–71.
- Yang, Y., M.H. Ritzwoller, A.L. Levshin, and N.M. Shapiro (2007). Ambient noise Rayleigh tomography across Europe, *Geophys. J. Int.*, 168, 259–274, doi: 10.1111/j.1365-246X.2006.03203.x.
- Yao, H., R.D. van der Hilst, and M.V. De Hoop (2006). Surface-wave array tomography in SE Tibet from ambient seismic noise and twostation analysis: I—Phase velocity maps, *Geophys. J. Int.*, 166, 732–744.
- Yokoi, T. and S. Margaryan (2008). Consistency of the spatial autocorrelation method with seismic interferometry and its consequence, *Geophys. Prospecting*, 56, 435–451, doi:10.1111/j.1365-2478.2008.00709.x.

Vertical structure of tidal flows at the entrance to Guaymas Bay, Mexico

José Gómez-Valdés*, Juan A. Dworak, Heriberto J. Vázquez and Manuel Paz

Received: June 06, 2011; accepted: February 07, 2012; published on line: June 29, 2012

Resumen

Se estudia la estructura vertical de los flujos de marea a partir de 144 días de observaciones realizadas por un ADP anclado al fondo en la entrada de la Bahía de Guaymas, cuya área es de 33.6 km² y se encuentra en una región semiárida. Se aplicaron métodos de análisis armónico a las series de tiempo de velocidad y a las series de tiempo de elevación del nivel del mar, para extraer los parámetros de las elipses de marea y para calcular amplitudes y fases de la marea. También se analizaron dos series de tiempo del nivel del mar adicionales obtenidas antes del experimento en sitios interiores de la bahía. Las corrientes barotrópicas de marea de mayor importancia fueron la K₁ y la M₂, estuvieron alineadas con la topografía de la entrada y mostraron amplitudes máximas de 7.8 ± 0.2 cm s⁻¹ y 7.4 ± 0.3 cm s⁻¹, respectivamente. Mientras que la corriente de agua somera de mayor importancia fue la M₄, con una amplitud máxima de 1.0 ± 0.2 cm s⁻¹. Debido a que la bahía cumple con la condición de cuerpo de agua pequeño, los principales movimientos de marea mostraron características de onda estacionaria. La estructura del perfil vertical de la corriente fue parabólico, lo que sugiere que la corriente barotrópica fue afectada por procesos de capa límite, además el perfil promedio de las corrientes confirmó la formación de una circulación estuarina inversa. Las corrientes de marea diurnas rotaron contra las manecillas del reloj en la capa superior y con las manecillas del reloj en la capa inferior, lo que sugiere que fueron moduladas por la estratificación.

Palabras clave: mareas, corrientes, laguna semiárida, Golfo de California, Bahía de Guaymas.

Abstract

A 144-day bottom-mounted ADP experiment at the entrance to Guaymas Bay was used to examine the vertical structure of the tidal flows of a small basin (33.6 km²) located in a semiarid region. Harmonic analysis techniques were used to extract the tidal ellipse parameters of the time series of ADP and to determine amplitude and phase of the tidal components of additional time series of tide height from two sites on the inner side of the bay taken before the experiment. The K₁-current and the M₂-current were the tidal currents of foremost importance; they were aligned with topography and showed amplitudes of 7.8 ± 0.2 cm s⁻¹ and 7.4 ± 0.3 cm s⁻¹, respectively. The M₄-current was the principal shallow water tidal current with amplitude of 1.0 ± 0.2 cm s⁻¹. Because of the small embayment condition, the main tidal motions showed characteristics of a standing wave. The vertical structure of the tidal currents was parabolic, which suggests that the barotropic tidal currents were affected by boundary layer process, furthermore, the mean current profile confirmed previous indication of an inverse estuarine circulation. The diurnal currents rotated anticlockwise in the upper layer and clockwise in the lower layer, which suggests that they were modulated by stratification.

Key words: tides, tidal current, semiarid lagoon, Gulf of California, Guaymas Bay.

J. Gómez-Valdés*
H.J. Vázquez
Centro de Investigación Científica
y de Educación Superior de Ensenada
Carretera Tijuana Ensenada No. 3918
Zona Playitas, C.P. 22860
Ensenada, Baja California
México
Tel: +52-6461750500
Fax: +52-6461750547

*Corresponding author: jgomez@cicese.mx

J.A. Dworak
M. Paz
Instituto Tecnológico de Guaymas
Km 4, Carr. al Varadero Nacional, 85950
Guaymas, Sonora
México
Tel: +52-6222216480, +52-6222215367
Fax: +52-6222216221

Introduction

Guaymas Bay (Figure 1) is a small semiarid coastal lagoon well connected to the Gulf of California by a single inlet. The basin has an area of 33.6 km². The inlet is 1.2 km wide, 13 m deep, and 2 km long. The bay features two shallow lagoons, one stemming to the west, the Guaymas Lagoon, and the other one to the northeast, the Empalme Lagoon, a relic of the Matape River's delta. Beyond the Empalme lagoon there is a very shallow body of water, the Estero el Rancho. Guaymas Bay is one of the main Mexico's fishing harbors with ample urban activity. On this bay, high rainfall takes place mainly from July to September and is scarce the rest of the year; freshwater entering the bay is mostly from runoff during the rainy season. The climate is semiarid with a yearly average temperature of ~ 25 °C, reaching the maximum temperatures (~ 32 °C) in August; during summer and autumn evaporation exceeds precipitation (Roden, 1958; Castro *et al.*, 1994). The predominant winds are from SSW during spring and summer, NW during autumn, and N during winter.

Few reports on physical process of Guaymas Bay have been found in the literature, Valle-Levinson *et al.* (2001) documented the oceanographic

conditions at the entrance to the bay for a lunar day in June 1999 and in February 2000. They found a reversal in water exchange patterns in late spring with respect to late winter. In late spring, an inverse estuarine circulation was established. In contrast, the literature about the Gulf of California, the adjacent sea of Guaymas Bay, is abundant. For example, the basic aspects of the tides of the Gulf of California are well known, the type of the tides off Guaymas Bay is mixed, mainly diurnal (Marinone, 1997).

Acoustical Doppler Profiler (ADP) observations at straits and inlets have been carried out frequently over the last decade, see e.g., Tsimplis (2000), Winant and Gutierrez de Velasco (2003), and Carrillo Gonzalez *et al.* (2007). These studies have revealed that the vertical structure of the tidal signal is complicated and varies, for example, by boundary layer and stratification effects. The main goal of the present study includes an analysis of the sea surface elevation and the vertical structure of the currents at the inlet of Guaymas Bay in which the focus of attention is on the tidal frequencies, using data from a bottom-mounted ADP, upward-looking, during the summer and autumn of 2000. Since tidal flows are determinant for the sediment budget and the dispersion of contaminants (Dyer

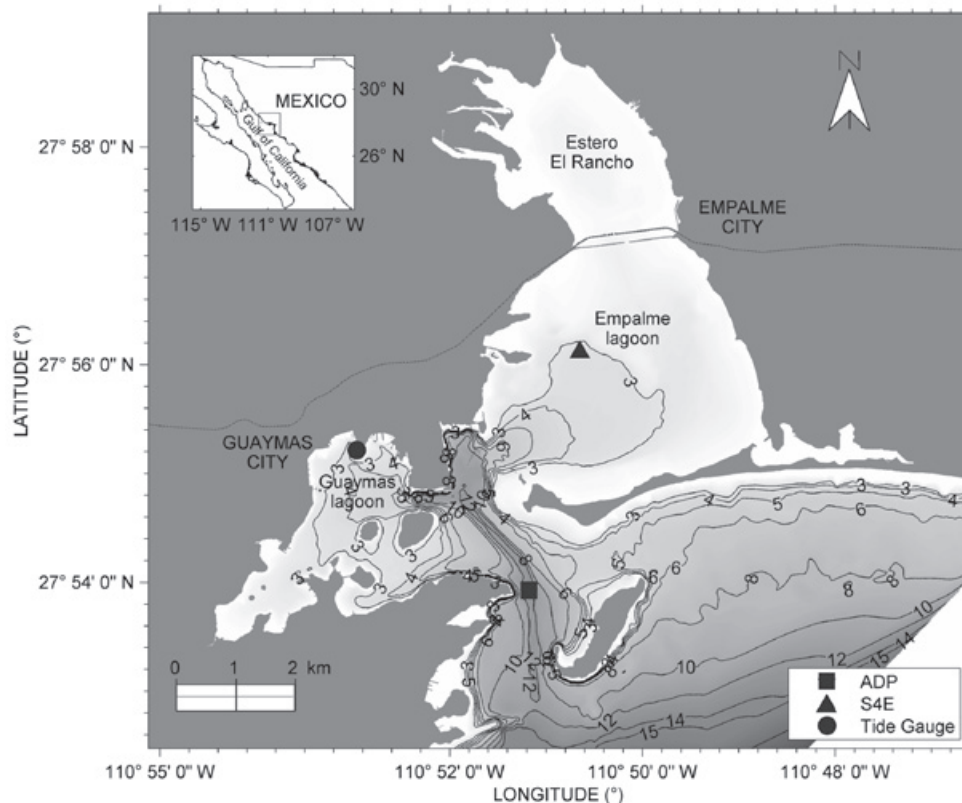


Figure 1. Geographical location of Guaymas Bay at the Gulf of California. Bathymetry with respect to LLW is displayed. The locations of the ADP, tide gauge, and S4 pressure sensor are also shown.

1997, 1-4 pp.), the correct separation of tidal motions from the long-term ADP mooring might provide a better understanding of the tidal-induced flows in this bay. In addition, the time series of the vertical structure of the currents provides an opportunity to test for the inverse estuarine circulation reported by Valle-Levinson *et al.* (2001).

Data and methods

A time series of velocity from a 1,500 kHz ADP, bottom-mounted, upward looking, at the entrance to Guaymas Bay, was the main data set used in this study. The time series spanned from 28 June 2000 to 19 November 2000. The instrument was deployed in the middle part of the navigation channel, at 0.95 m above the bottom, where the average water column depth was 13.2 m with respect to Mean Sea Level. The depth bin was 0.5 m, with a blanking distance of 0.40 m. The sampling frequency was 2 Hz and 2 min averages were stored each 20 min. Data reduction for the ADP included the removal of the upper 10 % water column due to the side-lobe effect. Because the first and the deepest bins were considered inaccurate, they were removed. Thus, the actual depth range of the profiles was from 1.85 m from the bottom up to 11.35 m.

The ADP also registered sea surface elevation. To provide a better description of the tide in the bay, sea surface elevation data from two instruments deployed in the inner lagoons were also used. A long-time series, from 28 February 1970 to 25 November 1976, from a tide gauge at Guaymas Lagoon, as well as a short-time series, from 13 May 1999 to 19 June 1999, from an InterOcean S4 pressure sensor at Empalme Lagoon, were used. The location of these instruments are shown in Figure 1.

Sea surface level data was smoothed with a running-mean filter and sampled to hourly records. Tidal constituents amplitude and phase lag (A_k , g_k) were extracted from the time series by least-squares fitting, using a Rayleigh criterion of one and including nodal corrections (Godin, 1972; Foreman, 1977; Pawlowicz *et al.*, 2002). Constituents P_1 and K_2 were estimated by inference, as suggested by Foreman *et al.* (1995). The internal relations between constituents P_1 and K_1 and between K_2 and S_2 taken from Godin *et al.* (1980) were used.

Reduction of tidal currents data was similar to the one performed on sea surface elevation data. To study the vertical structure of the tidal currents, the ellipse characteristics were extracted from the records of each bin using the least-square technique (Godin, 1988; Pawlowicz *et al.*, 2002).

Results

A global view of the relative importance of the principal currents in the study area can be obtained from Figure 2, in which the spectra of sea surface elevation and vertically-integrated velocity are shown. Both spectra show high variance in low-frequency and tidal bands. The sea surface elevation spectrum shows a peak about 0.0403 cph (diurnal band) with the greatest variance, a second peak about 0.0806 cph (semidiurnal band), and a third peak about 0.1610 cph (quarter-diurnal band), whereas the kinetic energy spectrum shows that diurnal and semidiurnal motions are of the same magnitude. In the latter spectrum, it is also noteworthy the relatively high energy in the quarter-diurnal band. Since tidal motions are dominant on those spectra, our main goal here is to study these flows.

Sea surface elevation

Amplitude and phase of the main diurnal and semidiurnal constituents for the inlet site, Empalme Lagoon site, and Guaymas Lagoon site are shown in Tables 1-3, respectively. The dominant diurnal constituents are K_1 and O_1 , its amplitudes at inlet site are about 27 and 19 cm, respectively. There are no significant differences in the amplitudes of the diurnal tides over the bay. The phase lag of K_1 between inlet site and Guaymas Lagoon site and between inlet site and Empalme Lagoon site are ~ 3 degrees and ~ 0 degrees, respectively. The dominant semidiurnal constituents are M_2 and S_2 , its amplitudes at the inlet site are about 14 and 11 cm, respectively. Because of the bottom friction effect, there is a small reduction of the amplitude of the M_2 at the inner basins. The phase lag of M_2 between inlet site and Guaymas Lagoon site is 5 degrees, whereas it is 1 degree between inlet site and Empalme which is lower than the phase lag error at the Empalme site.

The characteristics of the tide of Guaymas Bay are as follows. Using the form number $(K_1 + O_1)/(M_2 + S_2)$, following Defant (1958), the type of tide is identified as mixed, predominantly diurnal. The fortnightly variation for semidiurnal tides $(|(M_2 + S_2) / (M_2 - S_2)| > 8)$ is higher than for diurnal tides $(|(K_1 + O_1) / (K_1 - O_1)| > 5)$ at all sites. Furthermore, M_4 tidal constituent is the one with the highest amplitude (~ 1 cm) for the shallow-water constituents. It is also noteworthy that the non-linear response of the water body to harmonic forcing is weak, as M_4 has practically the same amplitude throughout the basin and $M_4 / M_2 \sim 1 / M_2$. The phase difference between $2M_2$ and M_4 is about 310 degrees throughout the basin, which implies that Guaymas Bay is an ebb-dominant system according to Friedrichs and Aubrey (1988).

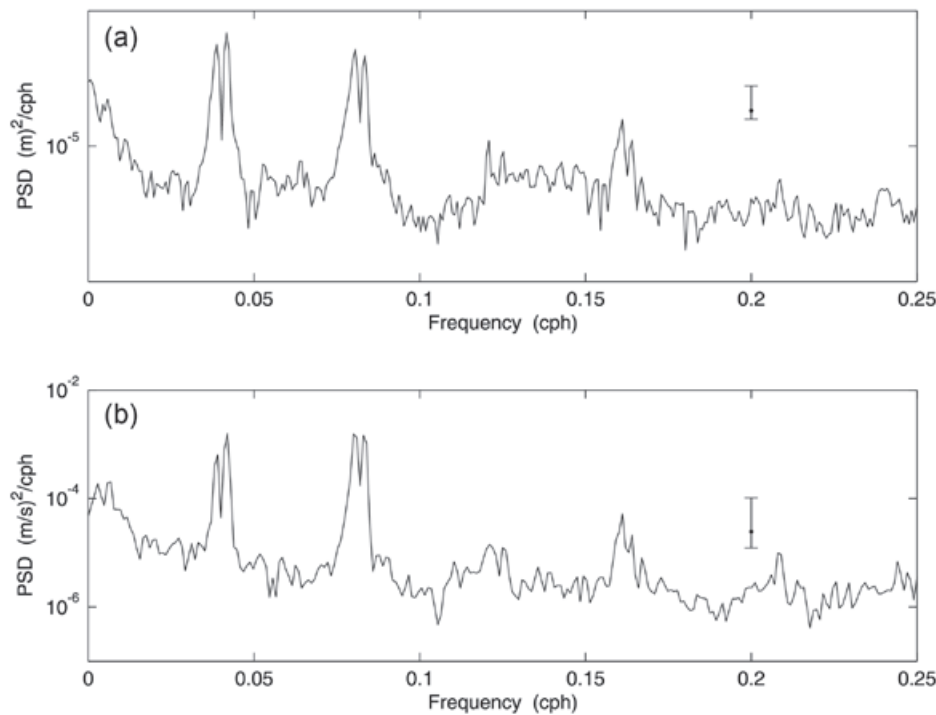


Figure 2. Spectral density estimates for (a) the sea surface elevation and (b) the velocity at the entrance to Guaymas Bay, using an ADP record 144-day long.

Table 1. Tidal constituents for the sea surface level at the entrance to Guaymas Bay. Amplitude (A) and phase lag (g) values and their respective errors (δa , δg) are shown.

Constituent	Freq (cph)	A (cm)	δa (cm)	g (°)	δg (°)
Q1	0.0372185	3.4	1.3	134	19
O1	0.0387307	18.8	1.2	166	4
K1	0.0417807	27.3	1.1	178	2
N2	0.0789992	3.6	0.4	165	6
M2	0.0805114	13.8	0.4	156	1
S2	0.0833333	11.1	0.4	134	2
M4	0.1610228	1.2	0.1	1	6

Phases are relative to UT. Time zone Z = -7. Tidal amplitude and phase are reported at 95 % confidence. Tidal constituents are above the noise level (signal-to-noise ratio > 1).

Tidal currents

The mean current (Z_0) and the vertical profile of the percentage of explained variance are shown in Figure 3. On the average, in the upper layer an input flow is established while in the lower layer there is an output flow. The thickness of the lower layer is greater than the thickness of the

upper layer. The explained variance reaches its highest value at the middle of the water column. The hypothesis is that the combined effect on the tidal currents by bottom stress and surface stress in conjunction with stratification generates the observed patterns, where stratification is related to a gravitational flow induced by evaporation in the inner basins.

Table 2. Tidal constituents for the sea surface elevation at the Empalme Lagoon. Amplitude (A) and phase lag (g) values and their respective errors (δa , δg) are shown.

Constituent	Freq (cph)	A (cm)	δa (cm)	g (°)	δg (°)
Q 1	0.0372185	4.5	0.3	155	4
O1	0.0387307	19.4	0.3	168	1
K1	0.0417807	26.3	0.3	180	1
N2	0.0789992	3.7	0.3	167	5
M2	0.0805114	12.6	0.4	157	2
S2	0.0833333	9.9	0.4	145	2
M4	0.1610228	1.2	0.3	6	14

Phases are relative to UT. Time zone Z = -7. Tidal amplitude and phase are reported at 95 % of confidence. Tidal constituents are above the noise level (signal-to-noise ratio > 1).

Table 3. Tidal constituents for the sea surface elevation at the Guaymas Lagoon. Amplitude (A) and phase lag (g) values and their respective errors (δa , δg) are shown.

Constituent	Freq (cph)	A (cm)	δa (cm)	g (°)	δg (°)
Q1	0.0372185	3.6	0.2	161	2
O1	0.0387307	18.5	0.2	167	1
K1	0.0417807	27.9	0.2	183	0
N2	0.0789992	3.6	0.1	171	2
M2	0.0805114	13.5	0.1	160	1
S2	0.0833333	10.7	0.1	140	1
M4	0.1610228	1.4	0.1	26	2

Phases are relative to UT. Time zone Z = -7. Tidal amplitude and phase are reported at 95 % of confidence. Tidal constituents are above the noise level (signal-to-noise ratio > 1).

Two configurations of currents are presented: 1) the vertically-integrated velocity and 2) the velocity vertical profile. Table 4 shows the ellipse characteristics for the vertically-integrated velocity at the entrance to the bay. The most energetic components are K_1 ($\sim 8 \text{ cm s}^{-1}$) and M_2 ($\sim 7 \text{ cm s}^{-1}$). The diurnal tidal currents rotate anticlockwise (semiminor axis > 0), whereas the semidiurnal tidal currents rotate clockwise (semiminor axis < 0). The orientation of the tidal ellipses (Φ) is consistent with the bathymetric features along the main channel. The phase difference between the sea surface elevation and the velocity for the component

M_2 and for the component K_1 are about 80° and 90° , respectively. The latter component shows a standing wave behavior. M_4 -current shows an amplitude $\sim 1 \text{ cm s}^{-1}$; because $m = 0$, it is completely elongated without rotation.

Figure 4 exhibits the vertical structure of the ellipse characteristics of the main diurnal and semidiurnal components. The semimajor axis magnitude reveals the following order $K_1 \approx M_2 > S_2 > O_1$, fluctuating between 8.3 cm s^{-1} and 4.4 cm s^{-1} . The semiminor axis magnitude is almost the same (0.4 cm s^{-1}) for the four components, fluctuating between -0.7 cm s^{-1} and $+0.7 \text{ cm s}^{-1}$.

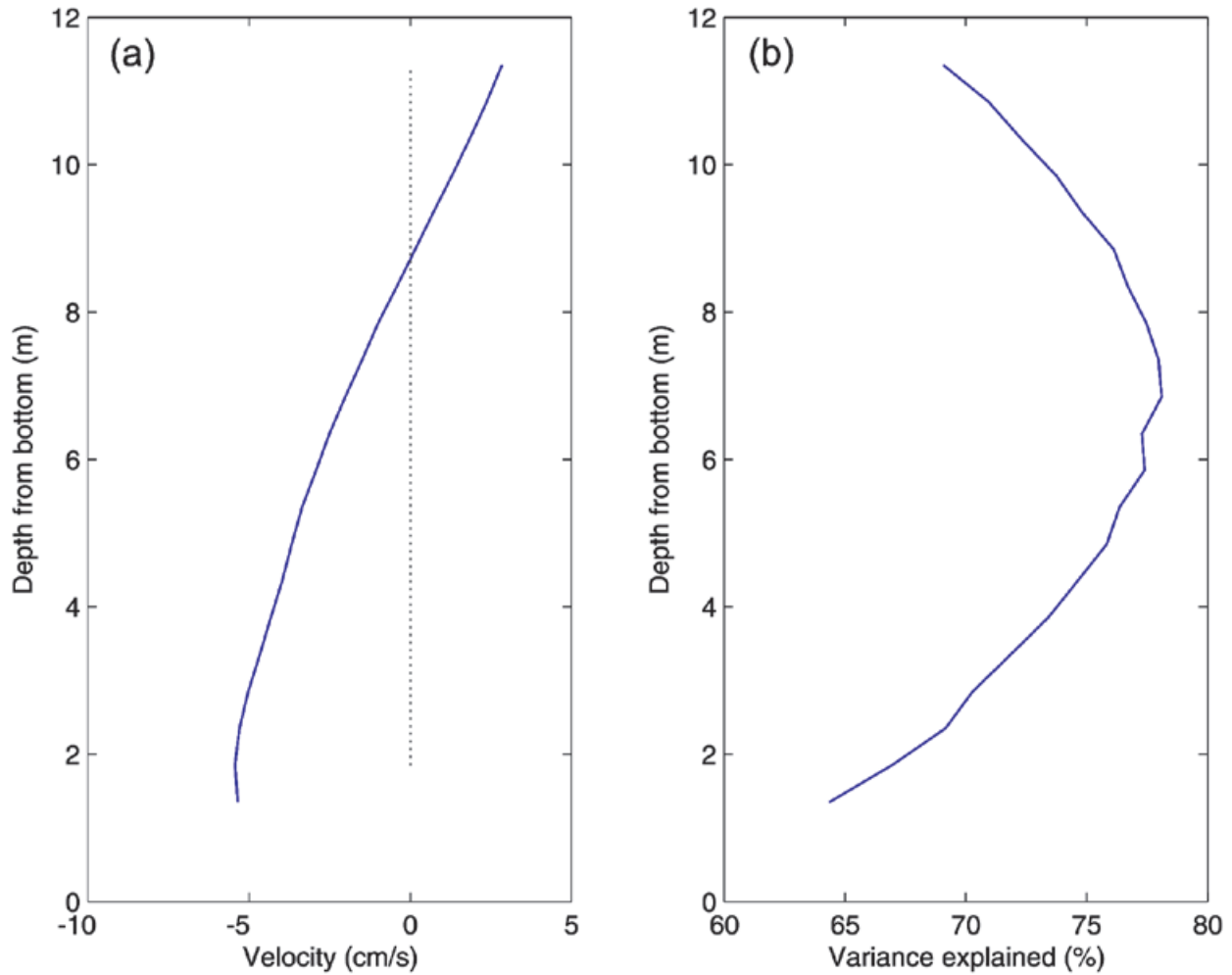


Figure 3. (a) Mean current (cm s^{-1}) and (b) percentage of explained variance.

Table 4. Tidal ellipse parameters for the vertically-integrated current at the entrance to Guaymas Bay. M is the semimajor axis, m is the semiminor axis, Φ is the inclination with respect to the East, and g is the phase lag; δM , δm , $\delta \Phi$, and δg are estimate errors.

Constituent	M (cm s^{-1})	δM (cm s^{-1})	m (cm s^{-1})	δm (cm s^{-1})	Φ ($^{\circ}$)	$\delta \Phi$ ($^{\circ}$)	g ($^{\circ}$)	δg ($^{\circ}$)
Q_1	0.7	0.46	0.3	0.25	84	37	55	55
O_1	4.9	0.53	0.4	0.28	93	3	75	7
K_1	7.8	0.50	0.4	0.25	93	2	85	4
N_2	2.0	0.30	-0.1	0.24	93	7	79	10
M_2	7.4	0.34	-0.4	0.28	96	2	76	3
S_2	6.3	0.38	-0.3	0.23	97	2	51	3
M_4	1.0	0.24	0.0	0.14	100	7	290	12

Phases are relative to UT. Time zone $Z = -7$. Tidal ellipse parameters are reported at 95 % confidence. Tidal constituents are above the noise level (signal-to-noise ratio > 1).

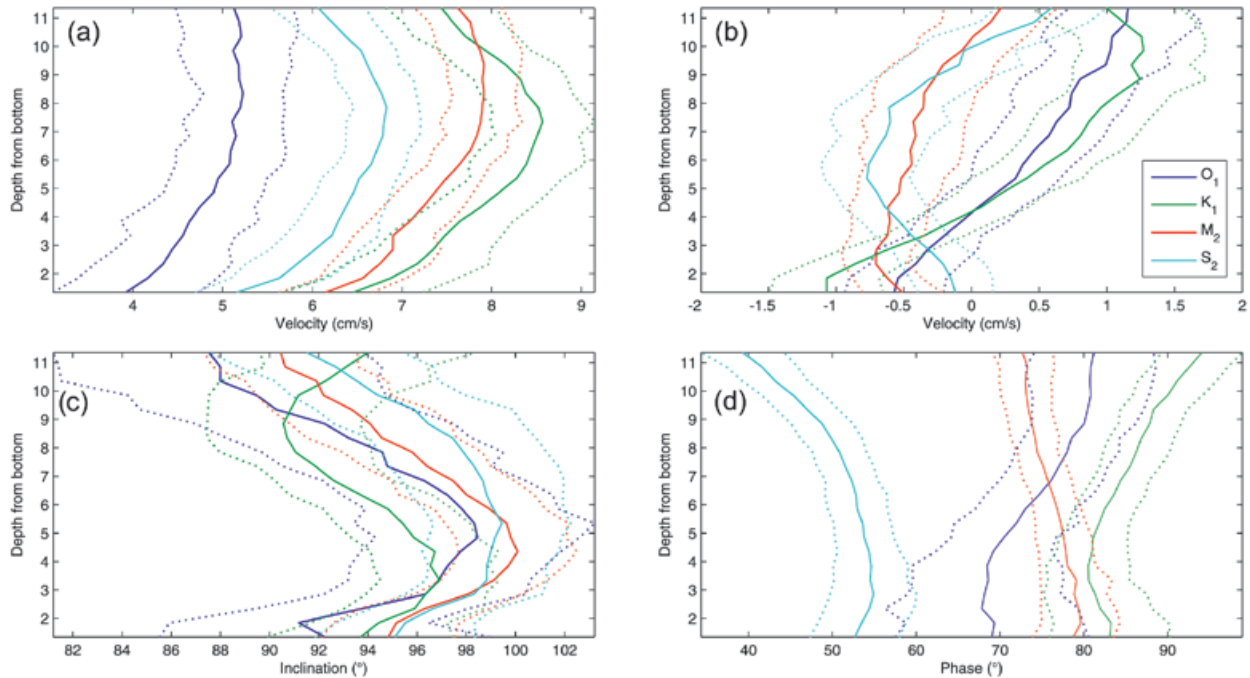


Figure 4. Vertical structure of the ellipse characteristics for the main tidal currents: (a) semimajor axis (cm s^{-1}), (b) semiminor axis (cm s^{-1}), (c) orientation of the semimajor axis, in degrees relative to East, positive counterclockwise, and (d) phase relative to tidal potential at Greenwich, in degrees. The dashed lines are the demarcation of the errors.

s^{-1} . All components show a parabolic profile. They are affected by boundary layer process (see e.g., Prandle, 2009). It is noteworthy that the magnitude of K_1 -current is maximal at the middle of the water column. Diurnal components reveal anticlockwise rotation at the upper half of the water column and clockwise at the lower half, whereas the semidiurnal components show predominantly clockwise rotation in the entire water column. The orientation of the major axis is depth dependent and is consistent with the course of the main channel. The phase lag of the diurnal components diminishes from the surface to the bottom, whereas for semidiurnal components the phase lag is almost constant along the water column. It is also noteworthy that there is a phase lag difference of 30° between components M_2 and S_2 . This result is explained by differences in their respective forcing mechanism: the Moon generates M_2 and the Sun generates S_2 .

Discussion

Based on a 144-day ADP dataset at the inlet of Guaymas Bay, tides, tidal currents and its vertical structure have been presented for the first time.

The diurnal component K_1 and the semidiurnal component M_2 are the dominant tidal motions. K_1 and M_2 exhibit a standing wave behavior. It is very well known that tidal dynamics in coastal waters depends on basin shape. To measure the relative importance of basin shape in the tidal flow field, Fagherazzi *et al.* (2003) define the adimensional parameter $\alpha = \omega L / (g H)^{1/2}$, where ω is the tidal frequency, L is the basin length, g is gravity, and H is depth. If α is small ($O(10^{-3})$), then the water level is in phase at every point in the basin. Taking representative values for the inlet of Guaymas Bay as $L \sim 3$ km, $H \sim 10$ m, it is found that for the diurnal tide ($\omega = 7.2 \times 10^{-5} \text{ s}^{-1}$), $\alpha = 0.002$; thus, the short embayment hypothesis is valid for the inlet. Under these conditions, the tide is a standing wave. Therefore K_1 is standing in Guaymas Bay because its wavelength is larger than the length of the basin.

The M_2 tidal component also holds the small embayment hypothesis ($\alpha = 0.004$) and the phase shift between the inlet and the boundaries is small. Under this theory the velocity (U) scales as ωL . This length scale is related to the tidal excursion ($E = u T / \pi$), which is ~ 2 km for the diurnal components and ~ 1 km for the

semidiurnal tides. As comparison, Fagherazzi *et al.* (2003) report that in San Diego Bay the M_2 tidal component is a standing wave. They report that $\alpha = 0.015$ for the semidiurnal tide. In Laguna San Ignacio, a small coastal lagoon on the Pacific coast of the Baja California peninsula, main tidal waves are also close to standing (Winant and Gutierrez de Velasco, 2003).

The M_4 tidal component, an overtide associated to the M_2 tidal component, is the shallow-water constituent of foremost importance. Overtides have been observed in coastal lagoons of the Gulf of California (Sandoval and Gómez-Valdés, 1997; Gómez-Valdés *et al.*, 2003; Dworak and Gómez-Valdés, 2003; Dworak and Gómez-Valdés, 2005). For example, Dworak and Gómez-Valdés (2003) report that in Yavaros Bay, the M_4 tidal component is $\sim 2 \text{ cm s}^{-1}$, and that at the inlet of this lagoon, M_2 tidal current is $\sim 30 \text{ cm s}^{-1}$. In Guaymas Bay, the most important shallow water component is the overtide M_4 with magnitude $\sim 1 \text{ cm s}^{-1}$. Thus the non-linear interactions are stronger in Yavaros Bay than in Guaymas Bay. This discrepancy between these two systems is explained for the fact that the linear momentum is stronger in the former system than in the latter. On the other hand, the $2M_2 - M_4$ phase relationship at the inlet for the sea surface elevation is of the order of 300 degrees, whereas for the velocity is of the order of 150 degrees. Hence the water body is ebb-dominant (Friedrichs and Aubrey, 1988), favorable to maintain healthy water quality in the bay. However, the tidal excursion for all components is not larger than the inlet length suggesting that exchange between the inner lagoons and the ocean might not be as adequate enough for maintaining the bay water quality. As well as in a stratified system, the relationship between flood and ebb are more complex, both processes are modified by baroclinic pressure gradient forces and by vertical mixing (Cudeback and Jay, 2000). In addition, because Li and Zhong (2009) demonstrate that fortnightly fluctuations of the tidal currents modify the residual current in estuaries (coastal lagoon), the strong spring-neap cycle in Guaymas Bay might have an important influence on the water exchange.

In the homogenous case, ellipse properties of tidal currents change with depth because of boundary layer effects (Prandle, 1982). The parabolic structure of the tidal currents is explained for the effect of the wind stress in the upper layer and the effect of the bottom stress in the lower layer. Under these conditions, the pressure gradient force induced a maximum of velocity at the middle of the water column (Kundu, 1990, 268 pp.). In the homogenous case, stratification modifies the tidal ellipse characteristics (Souza and Simpson, 1996).

The diurnal currents rotate anticlockwise in the upper layer and clockwise in the lower layer. The pattern of the rotatory diurnal current is similar to the pattern of the rotary semidiurnal current in Rhine ROFI (Souza and Simpson, 1996), which is a very well known site where stratification effects are important in the tidal motions. The two-layer pattern at the inlet is in agreement with results obtained from an experiment of a lunar day at the entrance to the Guaymas Bay (Valle-Levinson *et al.*, 2001), which implies that wind stress, bottom friction and stratification might be included in theoretical or numerical studies on tidal dynamics in semiarid coastal lagoon.

Acknowledgments

The field experiment was partially supported by CONACyT, México, grants P50185-2005 and CB-2007-82529, Cuerpo Académico Manejo de Zona Costera (SEP-PROMEP), and CICESE. J. Gómez-Valdés was visiting scholar at ITG during June 2010, when the final version of this paper was prepared. M. F. Lavín (Editor) and two anonymous referees helped to improve the manuscript.

Bibliography

- Carrillo González F., Ochoa J., Candela J., Badan A., Sheinbaum J., González Navarro J.I., 2007, Tidal currents in the Yucatan Channel. *Geofísica Internacional*, 3, 199-209.
- Castro R., Lavin M.F., Ripa P., 1994, Seasonal heat balance in the Gulf of California. *J. Geophys. Res.* 99, 3,249-3,261.
- Cudaback C.N., Jay D.A., 2000, Tidal asymmetry in an estuarine pycnocline: Depth and thickness. *J. Geophys. Res.*, 105, 26,237-26,251.
- Defant A., 1958, Ebb and Flow. The tides of earth, air, and water. The University of Michigan Press, USA, 121 pp.
- Dworak J.A., Gómez-Valdés J., 2003, Tide-induced residual current in a coastal lagoon of the Gulf of California. *Estuarine, Coastal Shelf Sci.* 57, 1-11.
- Dworak J.A., Gómez-Valdés J., 2005, Modulation of shallow water tides in inlet-basin system with a mixed tidal regime. *J. Geophys. Res.* 110, Doi:10.1029/2003JC001865.
- Dyer K. R., 1997, Estuaries a Physical Introduction. Wiley, Chichester, 195 pp.
- Fagherazzi S., Wiber P.L., Howard A.D., 2003, Tidal field in a small basin. *J. Geophys. Res.* 108, doi:10.1029/2002JC001340.

- Foreman M.G.G., 1977, Manual for Tidal Heights Analysis and Prediction. Pac Mar Sci Rep 77-10, Inst Of Ocean Sci, Patricia Bay, Sidney, B. C., 69 pp.
- Foreman M.G.G., Crawford W.R., Marsden R.F., 1995, De-tiding: Theory and practice. In: Lynch D.R. and Davies A.M. (Editors) Quantitative Skill Assessment for Coastal Ocean Models, Coastal Estuarine Studies 47, AGU, Washington, D.C., pp. 203-239.
- Friedrichs C.T., Aubrey D.G., 1988, Non-linear tidal distortion in shallow well-mixed estuaries: a synthesis. *Estuarine, Coastal Shelf Sci.*, 27, 521-545.
- Godin G., 1972, The Analysis of Tides. Univ of Toronto Press, Toronto, 264 pp.
- Godin G., 1988, Tides. Anadyomene, Ottawa, 349 pp.
- Godin G., Paz-Vela R., Rodríguez N., Ortiz M., 1980, Revisión de los datos de mareas para la costa occidental de México disponibles en el CICESE e interpretación de los resultados (in Spanish). Centro de Investigación y de Educación Superior de Ensenada, Ensenada, B. C., México. 63 pp.
- Gómez-Valdés J., Delgado J.A., Dworak J.A., 2003, Overtides, compound tides, and tidal residual current in Ensenada de la Paz, Baja California Sur, Mexico. *Geofísica Internacional*, 42, 623-634.
- Kundu P.K., 1990, Fluid mechanics. Academic Press, San Diego, 638 pp.
- Li, M., L. Zhong, 2009. Flood-ebb and spring-neap variations of mixing, stratification and circulation in Chesapeake Bay. *Cont. Shelf Res.* 1, 4-14 pp.
- Marinone S.G., 1997, Tidal residual currents in the Gulf of California: is the M_2 tidal constituent sufficient to induce them? *J. Geophys. Res.* 102, 8,611-8,623.
- Pawlowicz R., Beardsley B., Lentz S., 2002, Classical tidal harmonic analysis including error estimates in MATLAB using T_TIDE. *Comput. Geosci.* 28, 929-937.
- Prandle D., 1982, The vertical structure of tidal currents and other oscillatory flows. *Cont. Shelf Res.* 1, 191-207.
- Prandle D., 2009, Estuaries. Dynamic, Mixing, Sedimentation and Morphology. The vertical structure of tidal currents. Cambridge University Press, Cambridge, 236 pp.
- Roden G.I., 1958, Oceanographic and meteorological aspects of the Gulf of California. *Pacific Sci.* 12, 21-45.
- Sandoval F.J., Gómez-Valdés J., 1997, Tides and tidal currents in Ensenada de la Paz lagoon, Baja California Sur, Mexico. *Geofísica Internacional*, 36, 37-47.
- Souza A.J., Simpson J.H., 1996, The modification of tidal ellipses by stratification in the Rhine ROFI. *Cont. Shelf Res.*, 16, 997-1,007.
- Tsimplis M.N., 2000, Vertical structure of tidal currents over the Camarinal Sill at the Strait of Gibraltar. *J. Geophys. Res.*, 105, 19, 709-19 728.
- Valle-Levinson A., Delgado J.A., Atkinson L., 2001, Reversing water exchange patterns at the entrance to a semiarid coastal lagoon. *Estuarine, Coastal Shelf Sci.*, 53, 825-838.
- Winant C.D., Gutiérrez de Velasco G., 2003, Tidal dynamics and residual circulation in a well-mixed inverse estuary. *J. Phys. Oceanogr.*, 33, 1,365-1,379.

Shallow travel-time tomography below southern Mexico

Eduardo Huesca-Pérez* and Allen Husker

Received: July 25, 2011; accepted: May 03, 2012; published on line: June 29, 2012

Resumen

Se desarrollaron dos tomografías de tiempo de viaje para las ondas P y S, así como un mapa del cociente Vp/Vs en el sur de México. Se utilizaron datos provenientes de la red temporal de banda ancha Meso-American Subduction Experiment (MASE). Los perfiles de las tomografías tienen su origen en la costa del Pacífico y corren tierra adentro 205 km perpendiculares a la trinchera; muestrean hasta una profundidad de 55 km. Los resultados muestran, para ambas ondas, velocidades altas desde la costa hasta 40 km en la sección descendiente de la placa subducida de Cocos, una anomalía lenta para la onda P entre los 50 km y 90 km, por arriba del doblez donde la placa se vuelve subhorizontal y velocidades bajas para las ondas P y S por encima de la placa entre los 90 km y 205 km desde la costa. El mapa del cociente de Vp/Vs exhibe dos zonas de valores altos: (1) la región donde la placa desciende desde la costa hasta 60 km; y (2) entre los 90 km y 160 km, donde se han detectado los Tremores No-Volcánicos (NVT). Por otro lado, se encuentran valores bajos de Vp/Vs donde la placa dobla (60 km – 90 km), lo que probablemente indica que la corteza está seca y sometida a esfuerzos intensos. Se estimaron valores normales de Vp/Vs en la corteza al norte de 160 km de la costa, a pesar de que existe mucha evidencia de alta presión de fluidos en aquella región. Este hecho, muy probablemente, describe una combinación de reducciones proporcionales entre las velocidades de P y S debido a altas temperatura y bajas presiones efectivas.

Palabras clave: tomografía sísmica de tiempo de viaje, cociente de Vp/Vs, tremor no-volcánico, prueba de checkerboard.

Abstract

P and S wave travel-time tomographies as well as a Vp/Vs ratio image of the crust below southern Mexico were developed using data from the Meso-American Subduction Experiment (MASE) broad-band temporary network. The profile used in the tomography starts at the Pacific coast and runs 205 km inland perpendicular to the trench with a depth of 55 km. Results show fast P and S-wave velocities from the coast to 40 km inland in the descending section of the Cocos slab, a low P-wave anomaly between 50 km and 90 km above the corner where the slab becomes subhorizontal and low P and S-wave velocities above the slab between 90 and 205 km. The Vp/Vs image shows two areas with high values: (1) the zone where the slab descends from the coast to 60 km inland; and (2) between 90 km – 160 km from the coast where Non-Volcanic Tremors (NVT) are also found to occur. Low Vp/Vs values are found where the slab bends (60 km – 90 km) probably due to it being a highly stressed, dry region of the crust. Normal Vp/Vs values are found within the crust farther than 160 km from the coast despite strong evidence of high pore fluid pressure in that region. This is probably due to the proportional reduction of the P-wave velocity with the S-wave velocity due to high temperature and low effective pressure.

Key words: travel-time seismic tomography, Vp/Vs ratio, non-volcanic tremor, checker board test.

E. Huesca-Pérez*
Posgrado en Ciencias de la Tierra
Instituto de Geofísica
Universidad Nacional Autónoma de México
Ciudad Universitaria
Delegación Coyoacán, 04510
México D.F., México
*Corresponding autor: ehuesca@gmail.com

A. Husker
Instituto de Geofísica
Universidad Nacional Autónoma de México
Ciudad Universitaria
Delegación Coyoacán, 04510
México D.F., México

Introduction

The Mexican subduction zone has one of the few flat slab segments in the world (e. g. Gutscher *et al.*, 2000). The flat tectonic configuration of the Cocos slab below Mexico affects a wide geographic area of the overriding crust and knowledge of its geometry is important. Pérez-Campos *et al.* (2008) provided detailed seismic observations of the portion of the Cocos slab zone with the flat segment. They found in a receiver function study the subducting slab dipping at a 15° angle into the mantle, turning flat approximately 70 km from the coast at ~40 km depth. The slab remains flat until 300 km inland from the coast where it turns to steep subduction and descends into the mantle. The flat slab is mechanically decoupled from the upper crust by a very thin low viscosity zone (Song *et al.*, 2009; Kim *et al.*, 2010), probably generated by dewatering processes. It is well known that the Cocos slab is highly hydrated (Jödicke *et al.*, 2006; Manea *et al.*, 2010; Kim *et al.*, 2010) and releases its fluid content into the upper continental crust while subducting. The dehydration process makes the continental crust undergo chemical and elastic parameter changes affecting the seismic wave propagation velocities.

There is ample evidence of fluids present in the slab and the continental crust. For example, Kim *et al.* (2010) in a receiver function study find moderate to high V_p/V_s values in the upper subducted oceanic crust indicating that there exists elevated pore pressure due to fluid saturation. Iglesias *et al.* (2010) detect low shear wave velocities south of the Trans-Mexican Volcanic Belt (TMVB) over the flat section of the subducted oceanic crust that they correlate to dewatering processes from the slab. Those findings concur with a Magnetotelluric (MT) study done by Jödicke *et al.* (2006) that finds the presence of conductive anomalies that they interpret as slab-released fluids stored in the overlying continental crust. Jödicke *et al.* (2006) propose that the fluids in the MT study are thought to be progressively discharged by metamorphic dehydration of the underlying oceanic crust due to lithostatic pressure squeezing of open pores and cracks of sediments and basalts and intense “bend faulting”.

The isolated conductivity anomalies found by Jödicke *et al.* (2006) north of 105 km from the coast coincide with an area where dehydration phase changes were inferred (Manea *et al.*, 2010). This is the region where NVT energy distribution has been detected in Guerrero, Mexico within the flat slab region, 85 km to 160 km from the coast (Husker *et al.*, 2012; Kostoglodov *et al.*, 2010; Payero *et al.*, 2008). The existence of NVT could be related to the fluids released by dehydration during phase changes in the slab (Manea *et al.*, 2004; Manea *et al.*, 2010).

In this study we perform body wave tomography using P- and S-wave arrival times. Pore fluid pressure in the crust affects the velocity of seismic waves so a travel-time tomography study can provide information about the location and distribution of fluid-rich areas. The data used come from the MASE network that consisted of a 100-station seismic broadband array that was deployed during 2005 – 2007 across central Mexico (Figure 1). The array is oriented nearly perpendicular (~N16°E) to the Middle America Trench (MAT) from Acapulco on the Pacific coast to Tempoal, near the Gulf of Mexico in the north with a density of 5 – 6 km spacing between stations.

Data and Method

In order to develop the tomographic images we read the P and S wave arrival times from Mexican earthquakes registered by the MASE array. To constrain the inversion from the south, we employed the seismicity at the Mexican Pacific coast and from the north we used the seismicity of the Trans-Mexican Volcanic Belt (TMVB), the seismicity of the Valley of Mexico and one earthquake from the Gulf of Mexico (Figure 1). The Pacific seismicity comes from a catalog of Mexican earthquakes (Iglesias *et al.*, 2010) that were relocated with the double difference method (Waldhauser and Ellsworth, 2000) using the velocity model of Campillo *et al.* (1996). The Servicio Sismológico Nacional (SSN) reported 303 earthquakes in Mexico with $M \geq 4.5$ during December 2004 to April 2007. Of these events, only 90 could be relocated with an RMS < 0.5 s (Iglesias *et al.*, 2010). Only events that occurred 400 km (~4° epicentral distance, profile labeled A'A in Figure 1) from the nearest station of the MASE network were used. The majority of the events occurred at the coast, and so arrivals in the northern MASE stations were non-impulsive and could not be accurately determined.

To constrain the model using arrival times from the north, the TMVB earthquakes were employed. The TMVB seismicity comes from a catalog compiled with data from the Red Sísmica del Valle de México. The earthquakes in the area are relocated by Zenón Jiménez (unpublished catalog, personal communication) using a velocity model obtained for the region by Z. Jiménez (unpublished velocity model, personal communication). There were 32 earthquakes registered in the February 2005 to May 2007 period with M between 2.9 and 4.1. Because the low magnitude and low signal to noise ratio only ten earthquakes could be used in the inversion.

The total number of seismic rays obtained were 1951 for the P waves and 1344 for the S waves (Figure 2). The 400 km epicentral

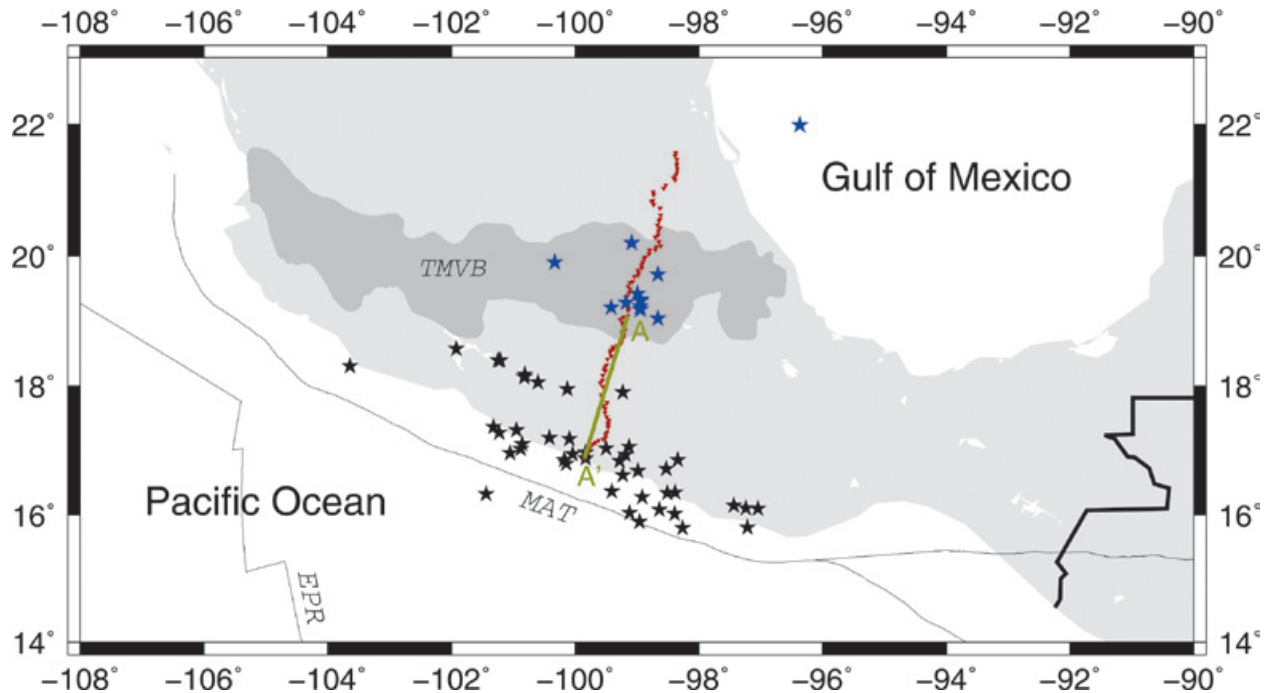


Figure 1. Map of southern Mexico showing the position of the profile of the tomography (green line labeled A'A), the MASE stations (red dots) and the seismicity used as input data (black stars, rays coming from the south; blue stars, ray coming from the north). EPR, East Pacific Rise; MAT, Middle-America Trench; TMVB, Trans-Mexican Volcanic Belt.

distance restriction limited the data set to mostly horizontal seismic rays, so multiple oblique ray-crossings that are sensitive to both vertical and lateral velocity variations could be obtained. There is good azimuthal ray coverage south of the TMVB. However seismicity is deficient to the north with just a few events between the Gulf of Mexico and the TMVB (Figure 1).

The seismograms employed were band-pass filtered between 1 and 10 Hz to remove high frequency noise and long period signals so that the time of the first arrival could be read clearly. The difference between theoretical (Campillo *et al.*, 1996) and observed arrival times, ΔT , was used as input data. Topography and the mean of the travel time were also removed from ΔT in order to account for travel time differences due to elevation and to avoid the regional offset in velocities from the Campillo *et al.* (1996) model and hypocentral errors. The topography was accounted for by assuming that regions above sea level have the same velocity as the top layer of the crustal model.

The study area consisted of a profile that runs -5 km off the coast of Acapulco, parallel to the MASE line (N16.7°E) to just south of south of Trans-Mexican Volcanic Belt (TMVB) covering a total horizontal distance of 210 km. It was not

possible to include the region north of the TMVB due to the sparse seismic activity there. The model extends to a depth of 55 km including the crust and a small part of the upper mantle. The model space was a two dimensional 15 km x 15 km grid of points and consisted of 68 grid points in all.

In order to locate station and grid spacing in kilometers instead of degrees, stations were mapped onto a flat surface using a Mercator projection with stations at the equator of the projection in order to minimize distortions in distance. The origin of the coordinate system was fixed at the Acapulco seismic station from the MASE array. A 2-D seismic ray-tracer pseudo-bending algorithm (Um and Thurber, 1987) was used to determine the ray path between the source and the receiver using the Campillo *et al.* (1996) velocity model. Because it is a shear-wave model, the corresponding P-wave vertical velocity structure was computed assuming a V_p/V_s of 1.73 (Poisson solid, i. e. the Lamé constants λ and μ are equal $V_p/V_s = \sqrt{3} \approx 1.73$). The ray tracing was performed by minimizing travel time differences by perturbing the ray path in segments (Eberhart-Phillips, 1993). In order to perform the inversion, the damped least square method (LSQR) of Paige and Saunders (1982) was used. A 2-D Gaussian filter was applied after inverting to smooth sharp shapes to get

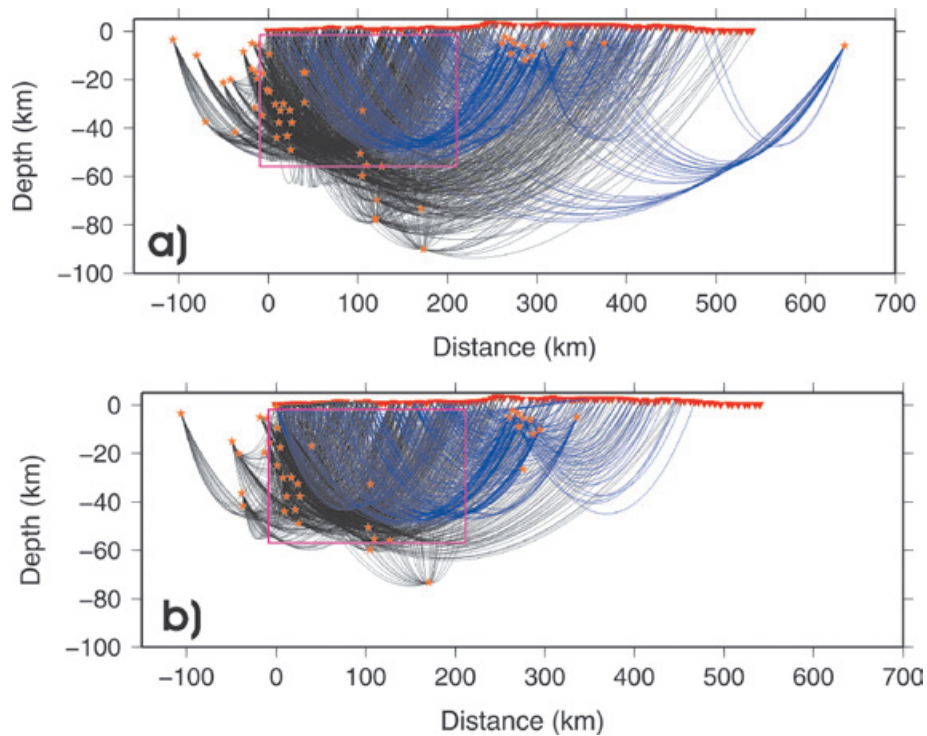


Figure 2. a) 1951 P-wave ray paths; and b) 1344 S-wave ray paths used in this study. Zero represents the first station (ACAP) of the MASE line and the origin of the tomographic profile. Black ray paths represent seismic waves coming from the south while the blue ones are coming from the north. Inverted red triangles are MASE stations; orange stars are the hypocenters. The pink rectangle shows the area encompassed by the tomographic profile.

a more robust average velocity structure. We also performed a checkerboard resolution test to ensure robustness of the results.

Results

Figures 3 and 4 show the P- and S-wave tomograms, respectively. The black continuous line represents the top of the subducted Cocos slab for comparison (Pérez-Campos *et al.*, 2008). The color scale varies from high velocity (blue) to low velocity (red). The mean velocity has been removed, so it is not possible to distinguish average velocity difference from the background model.

Figure 3 shows the P-wave tomogram where fast velocities are observed in the section of the descending slab close to the coast (blue region between 0 – 40 km). Above the corner where the slab turns horizontal there are low P-wave velocities (red-orange region between 50 km to 90 km inland). Over the flat part of the slab there is a region of slightly low velocities (red-orange region between 90 km to 160 km inland) followed by extremely low velocities to the north more than 160 km inland (red region between 160 – 205 km).

The S-wave (Figure 4) velocities exhibit some differences from the P-waves (Figure 3). In the descending slab there are fast velocities between the coast (A') to 80 km inland and 5 km to 30 km depth (blue region in Figure 4) and low velocities

more than 30 km depth (red-orange region). To the north, the tomogram shows normal velocities just above the bending section of the slab (as depicted by the green region between 80 km to 110 km inland) and almost near-normal S-wave velocities above the flat section of the slab more than 110 km inland (red-orange region).

Figure 5 shows the V_p/V_s ratio along the profile. In the image two high V_p/V_s ratio bands are formed. The first of them emerges along the dipping segment of the subducted slab (between 0 and 60 km inland) and the second between 90 and 160 km inland and both bands showing ratios greater than 1.76. Between 160 km and 205 km from the coast the V_p/V_s ratio shows almost no anomaly as depicted by the green color that corresponds to a Poisson solid. This is due to the low values in both the P- and S-wave velocities. Between 60 km and 90 km from the coast the V_p/V_s ratio shows a low anomaly with values below 1.73 just above where the slab becomes flat shown as yellow. This anomaly is due to low P-wave velocities and almost no affected S-wave velocities.

Resolution tests

We determined the resolution of the inversion using a checkerboard test (Hearn and Clayton, 1986). The checkerboard is an extreme velocity test because it has singularities at jumps between slow and fast anomalies that are not likely in nature. The resolution, in this test, of

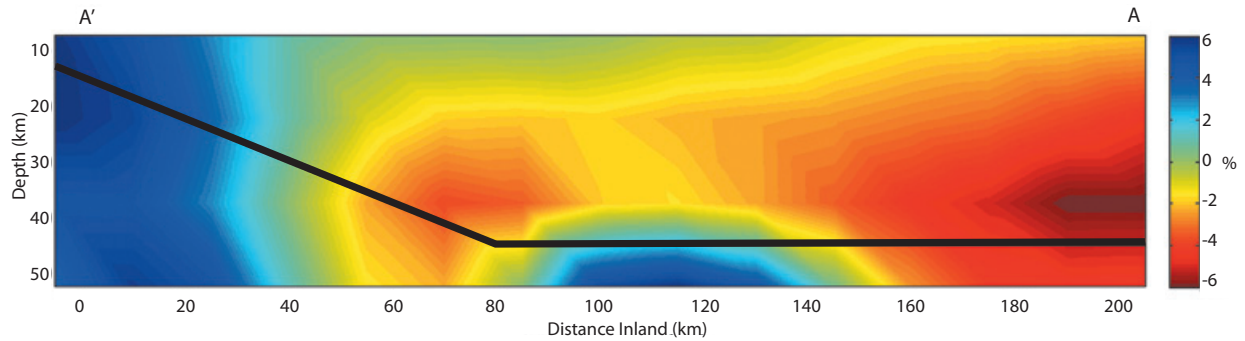


Figure 3. P wave travel time tomography. Colors represent variation of the P-wave velocity perturbation to the *Campillo et al.* (1996) background velocity model. The black continuous line represents the position of the top of the subducting Cocos slab (*Pérez-Campos et al.*, 2008). The blue and red colors represent the maximum positive and negative velocity differences from the background model, in percentage. The horizontal distance has its origin at the coast and runs inland corresponding to the profile A'A in figure 1.

a given region is found by creating a synthetic forward model of anomalies where a series of boxes are positively or negatively perturbed over and below a certain input average velocity model. The position of the original checkerboard is marked as light gray lines in Figures 6 and 7. Then, synthetic travel times are found using this synthetic structure where the ray paths are those used in the tomography. The synthetic travel times are then inverted to determine how well the synthetic velocity structure is recovered and a Gaussian filter is used to replicate the procedure used for the tomographic inversion of the real data.

The checkerboard inversions indicate that anomalies of 30 km x 30 km for the P-wave (Figure 6 panel **a**) and 50 km x 30 km for the S-wave (Figure 7 panel **b**) can be resolved in most of the profile. It is difficult to resolve smaller coherent structures as shown for the S-wave case in panel a Figure 7. Due to deficient ray coverage to the north of the profile, neither the

P-wave nor the S-wave can recover structures less than 60 km horizontal x 30 km vertical in that region (panels **c** in Figures 6 and 7). The smearing and distorted boxes amplitudes come mainly from the lack of crossing rays (sparse in the north (> 120 km) in the inversion) which is the greatest source for error in a tomographic inversion. In general more fine structures can be recovered in the southern portion of the profile due to the larger number of crossing raypaths (Figure 2). The relative strength of the velocity perturbation within the profile is reduced from 8 to 4% because of the smearing of the image (*Husker and Davies*, 2009) which gives a 4% of error in the velocity amplitude.

Discussion

In this study we obtained an image of the velocity structure as well as a map of the V_p/V_s distribution in the upper mantle, the subducted slab and crust below southern Mexico. The results show low velocity just above the slab for both

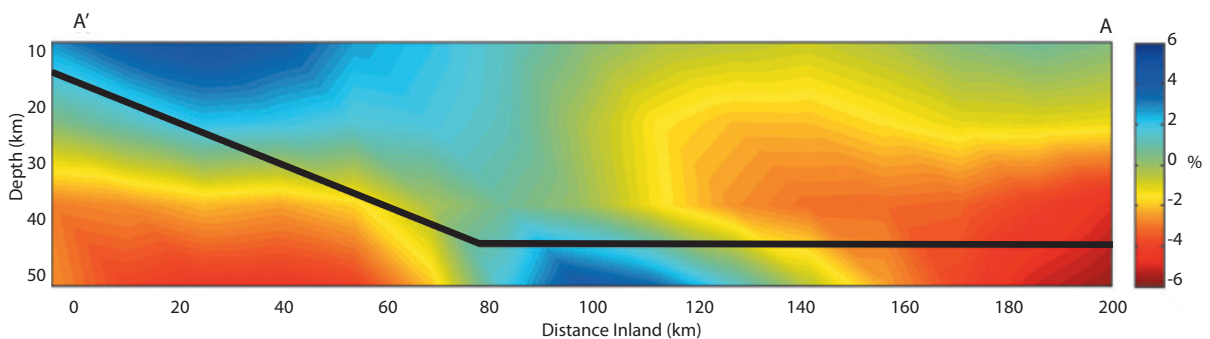


Figure 4. S wave travel time tomography. Colors represent variation of the S-wave velocity perturbation to the *Campillo et al.* (1996) background velocity model. The black continuous line represents the position of the top of the subducting Cocos slab (*Pérez-Campos et al.*, 2008). The blue and red colors represent the maximum positive and negative velocity differences from the background model, in percentage. The horizontal distance has its origin at the coast and runs inland corresponding to the profile A'A in figure 1.

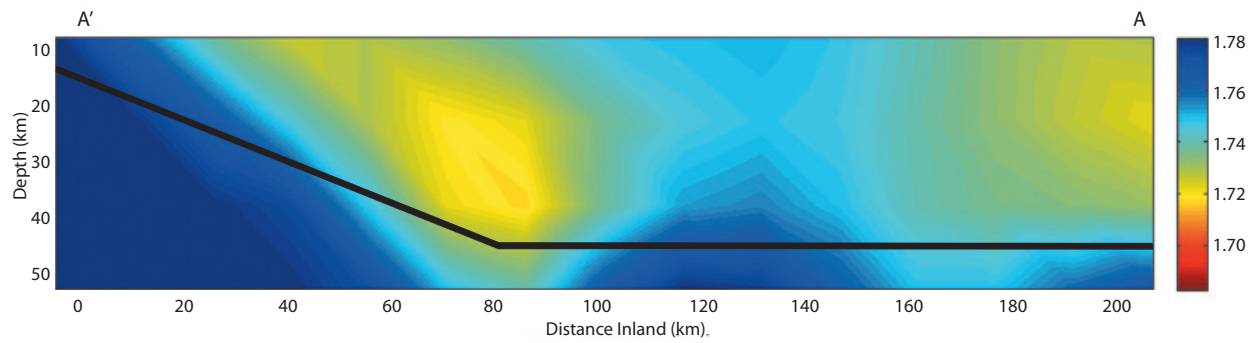


Figure 5. The color image represents the V_p/V_s ratio inversion. Green is no anomaly (Poisson solid). Blue is a high ratio whereas yellow to red are low. Black line is the position of the top of the Cocos slab (Perez-Campos *et al.*, 2008) for comparison. Label A'A refers to profile line in figure 1.

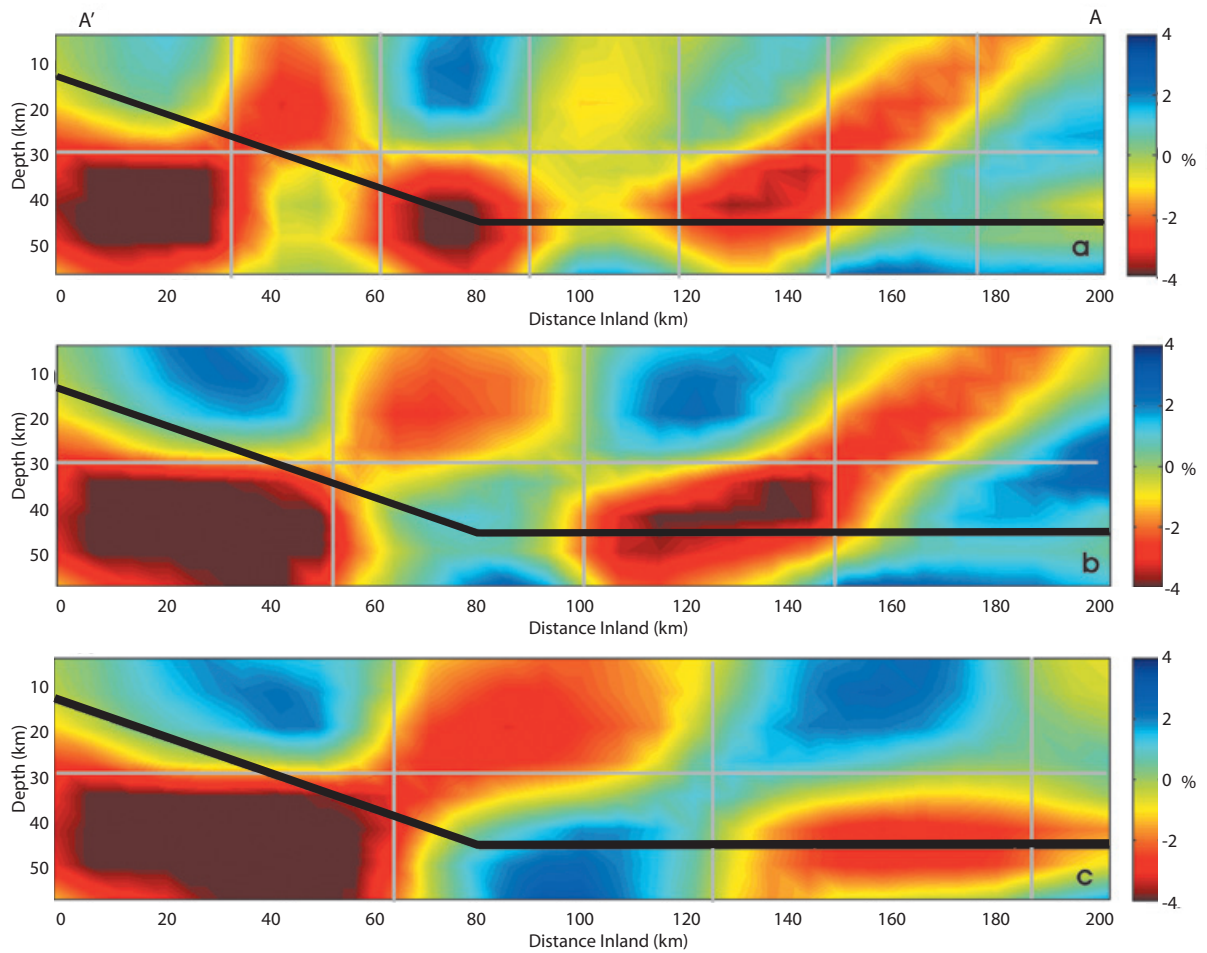


Figure 6. Checkerboard test for P-wave travel time tomography. The test consists of alternating boxes of high (blue) and low (red) velocity perturbations ($\pm 8\%$) of the background velocity model. The synthetic test is designed to show the ability of the inversion to resolve structures. Panels **a**, **b** and **c** show boxes sizes of 30 km x 30 km, 50 km x 30 km and 60 km x 30 km, respectively. Light grey lines denote the position of the original checkerboard.

waves to the north between 100 km and 205 km from the coast (A') (P and S, Figures 3 and 4). These features coincide with observations in previous studies (e. g. Jödicke *et al.*, 2006; Manea *et al.*, 2010) that suggest fluids released into the continental crust from the oceanic crust (see Figure 8, yellow area in panel d and big blue drops panels **c** – **d**). This dehydration process, represented as blue drops in Figure 8, tends to occur in several areas with different amounts of water discharge (Manea *et al.*, 2010).

There is evidence of water in the crust above nearly the entire portion of the flat slab. Manea *et al.* (2010) define two principal dewatering pulses (at 90 km – 120 km and 140 km – 180 km) associated with mineral phase changes whereas Jödicke *et al.* (2006) find a long elongated (100 km – 205 km) area of high conductivity (yellow) due to fluid presence over a larger area than reported by Manea *et al.* (2010) and confirmed here by the

tomography. The southern dewatering pulses are near a zone detected by Kim *et al.* (2010) with high Poisson's ratio in the slab that is associated with a fluid-enriched slab that releases water into the crust between 55 km – 80 km from the coast. Song *et al.* (2009) also report a fluid saturated slab and a high pore-fluid pressure zone near the coast that they interpret as trapped fluid in the down-going portion of the slab, which is released when the slab becomes flat.

Figure 5 shows the Vp/Vs ratio distribution map. Two high Vp/Vs ratio are present: (1) between the coast (A') and 60 km inland, and (2) between 90 and 160 km from the coast. The south Vp/Vs anomaly (0 – 60 km) coincides with the descending slab, which carries large amounts of water with it and where the 2006 Slow Slip Event (SSE) occurred (see also panels **c** and **d**, Figure 8). The SSE aligns with an ultra slow velocity layer (USL) found between the slab

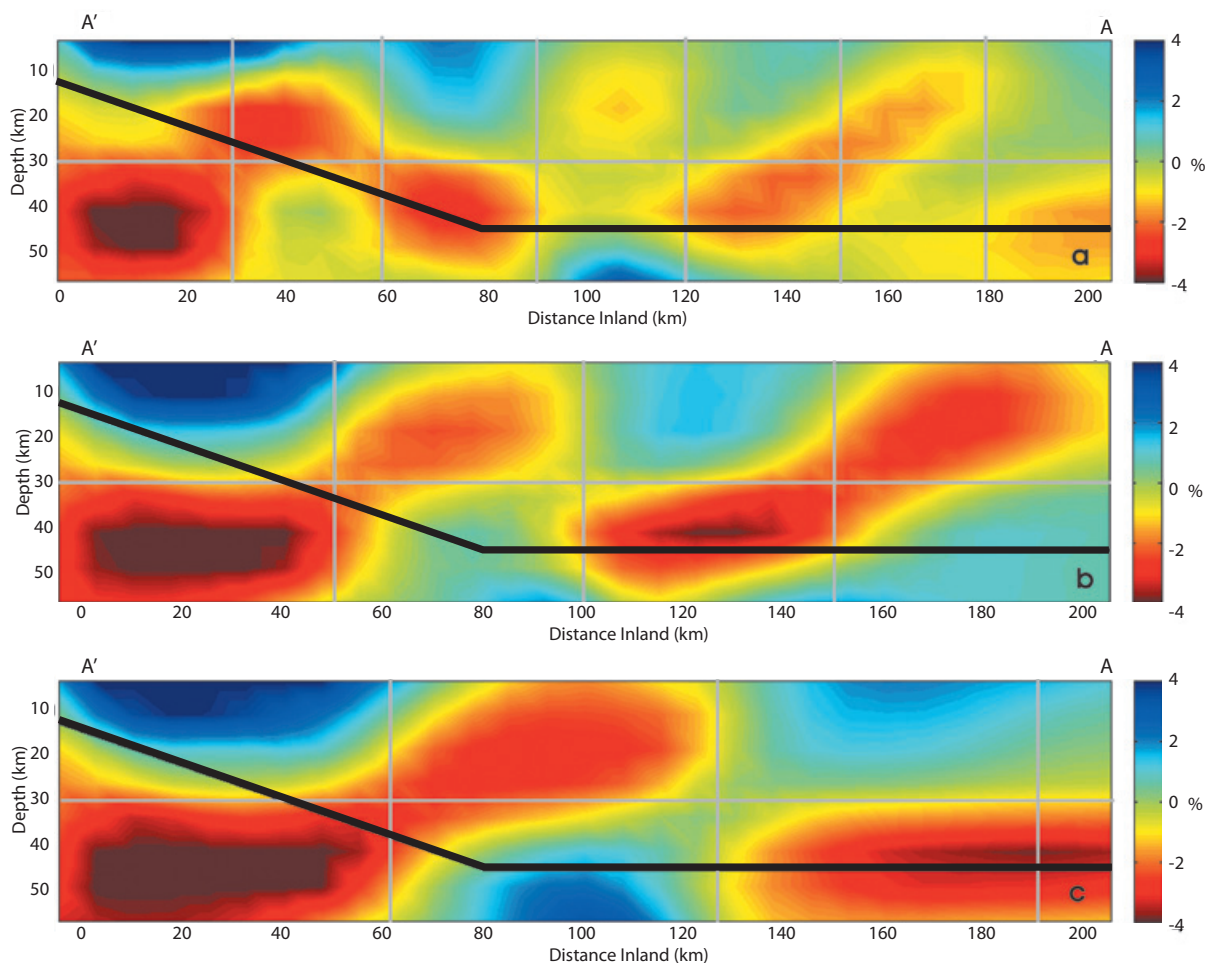


Figure 7. Checkerboard test for S-wave travel time tomography. The test consists of alternating boxes of high (blue) and low (red) velocity perturbations ($\pm 8\%$) of the background velocity model. The synthetic test is designed to show the ability of the inversion to resolve structures. Panels **a**, **b** and **c** show boxes sizes of 30 km x 30 km, 50 km x 30 km and 60 km x 30 km, respectively. Light grey lines denote the position of the original checkerboard.

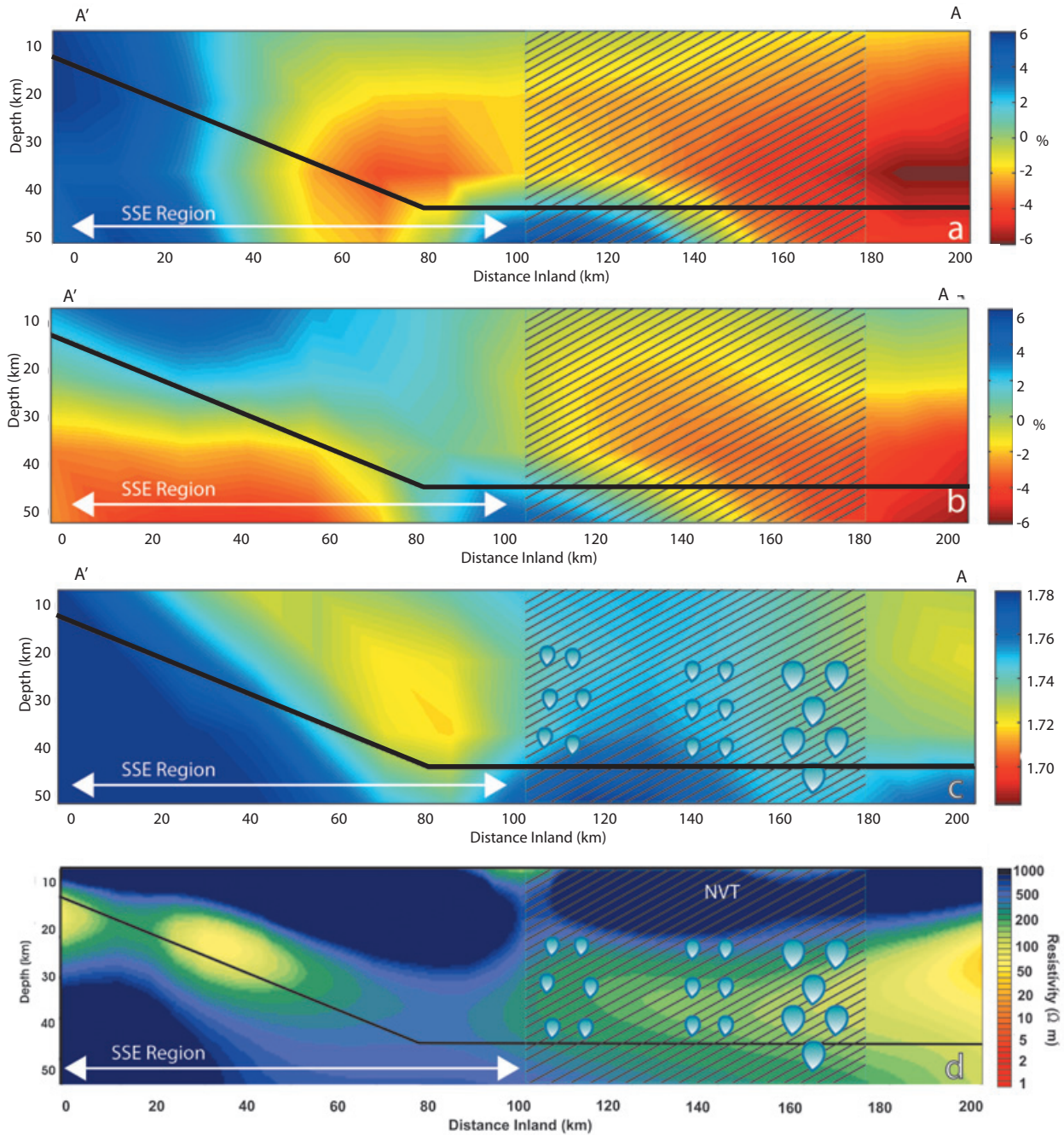


Figure 8. Interpretative comparison diagram that depicts several relevant results. The figure superimposes the tomography results (panels **a** and **b**) and the V_p/V_s ratio map (panel **c**) with the location of the NVT of *Husker et al.* (2012) delimited by the diagonal hatching and the results of *Manea et al.* (2010) where they find the presence of fluid release from the slab (blue drops panels **c** and **d**). The drops' sizes represents the quantity of liquid being released. Panel **d** shows the magnetotelluric (MT) study of *Jödicke et al.* (2006). White arrows indicate the extension of the Slow Slip Events (SSE), from the coast to 100 km inland as suggested by *Kim et al.* (2010).

and the overriding plate (Song *et al.*, 2009). USL's are evidence of high pore fluid pressure that releases partially its fluid content into the overriding crust lowering Vs and increasing the Vp/Vs ratio. Due to resolution problems it was not possible to determine the Vp/Vs ratio within USL.

The northern Vp/Vs anomaly (between 90 and 160 km, Figure 8) is high because Vs is low (Figure 8, panel **b**) indicating the presence of fluids in agreement with the other studies already mentioned. However, Vp is also somewhat low and becomes increasingly lower to the north (Figure 8, panel **a**) until Vp/Vs returns to the input value of a Poisson solid (1.73) north of 160 km (green-yellow area in Figures 5 and 8, panel **c**). The reason for the decrease in Vp is probably a combination of increased pore fluid pressure and temperature. When rock changes from dry to fluid saturated, Vs drops. However, once it is fluid saturated, Vp depends more strongly on changes in pressure and temperature than Vs (Vanorio *et al.*, 2005). Vp has been observed to decrease with decreases in differential pressure, which is lithostatic pressure minus pore pressure (Prasad and Manghnani, 1997). Horizontally within the crust, the lithostatic pressure does not change, but evidence of increased fluid content further than ~160 km from the coast (Jödicke *et al.*, 2006; Manea and Manea, 2010) suggests an increase in pore pressure, which drops the differential pressure. The simultaneous drop in differential pressure and increase in temperature with distance from the coast as inferred from Manea and Manea (2010), explains why Vp lowers with distance from the coast.

The one low Vp/Vs ratio seen as a yellow region at 80 km from the coast in Figure 5 is due to a low Vp anomaly that exists in a mostly dry media (Jödicke *et al.*, 2006; Manea and Manea, 2010) where Vs has normal values. The low Vp is probably due to a high stress regime above the bending portion of the slab where it becomes subhorizontal creating thick cracks. Thick cracks lower Vp (Shearer, 1988). The overriding crust, 40 km from the coast directly above the slab corner, seems to be in an extensive regime which is consistent with focal mechanisms of the little seismicity observed within the overriding plate (Singh and Pardo, 1993; Pérez-Campos *et al.*, 2008; Pacheco *et al.*, 2010). Singh and Pardo (1993) suggested that the extensional regime of the upper continental plate could be a consequence of trench retreat or tectonic erosion of the leading edge of the continent.

The NVT zone is located between 85 km and 160 km (Kostoglodov *et al.*, 2010; Husker *et al.*, 2012; diagonal-hatching Figure 8, panels **a** – **d**). The NVT energy bursts, in general, coincide with

a low S-wave velocity that corresponds to a high Vp/Vs ratio between 85 km – 160 km (> 1.73). The energy of the NVT bursts (diagonal-hatching, Figure 8) occurs within two fluid release pulses from the slab where temperature is near 450°C (Manea and Manea, 2010). It is unclear why the high energy NVT bursts are limited mostly to the region with high Vp/Vs. Beyond 160 km from the coast the tomography shows thermal effects of the slab hinge point, where it plunges abruptly into the mantle (Manea and Manea, 2010). The hinge point area undergoes a series of dehydration pulses between ~100 and 150 km depth (Manea and Manea, 2010) from the slab into the mantle wedge where ultramafic rocks serpentinize (Hacker *et al.*, 2003) ascending into the upper mantle and continental crust just under the active volcanoes of the TMVB. This temperature increase observed between 160 km – 205 km from the coast, induces crustal water to be super critical, increasing pore pressure and reducing Vp. The pressure and thermal conditions may indicate a limit to the presence of NVT north of 160 km from the coast.

Conclusions

Two tomography images were developed using P- and S-wave arrival times as well as a Vp/Vs ratio map below southern Mexico that sample the subducted slab and the continental crust. The tomograms show low velocity for both waves north of 100 km from the coast that suggests the presence of fluids in the crust in agreement with previous studies (e. g., Manea *et al.*, 2010; Jödicke *et al.*, 2006). A low P-wave velocity in the crust was found ~80 km from the coast just where the slab bends to become subhorizontal. A reduced S-wave velocity was not found there giving a low Vp/Vs ratio suggesting the existence of a strong stress regime that creates thick-cracks in the zone (Singh and Pardo, 1993; Pardo and Suárez, 1995; Pérez-Campos *et al.*, 2008; CMT Mexican Project). Thick cracks tend to lower Vp proportionally more than Vs (Shearer, 1988).

Two high Vp/Vs ratios are present: (1) between the coast and 70 km inland that coincides with the descending oceanic crust which carries large amounts of water where the S-wave velocity is drastically reduced and a high Poisson's ratio was detected by Kim *et al.* (2010) and where the 2006 SSE occurred; and (2) between ~100 and 160 km from the coast. Although there are evidence of fluids over almost the entire flat section of the slab (~100 to 300 km from the coast), the high Vp/Vs ratio is limited to ~100 and 160 km from the coast because of higher temperatures inferred by Manea and Manea (2010) and pore pressure north of 160 km which tend to decrease Vp. The high Vp/Vs zone (between 110 and 160 km from the coast) also corresponds to the NVT

zone (Kostoglodov *et al.*, 2010). We suggest that it is aligned to this zone due to a limit set by temperature and pressure.

Acknowledgements

We would like to thank Dr. Arturo Iglesias Mendoza for providing his seismic catalogue for Mexican earthquakes during the period 2005 – 2007 and for all his valuable advices during the development of this study. We also thank Dr Luis Quintanar Robles and the Servicio Sismológico Nacional (SSN) for providing the catalogue of the Valley of Mexico whose data has been employed in this study. Finally we thank the MASE team whose seismograms have been employed. This research was supported by CONACYT CVU 177244.

Bibliography

- Bernabei M., Botti A., Bruni F., Ricci M.A., Soper A. K., 2008, Percolation and three-dimensional structure of supercritical water, *Phys. Rev. E*, 78, 021505, 10.1103/PhysRevE.78.021505.
- Campillo M., Singh S.K., Shapiro N., Pacheco J., Hermann R.B., 1996, Crustal structure south of the Mexican volcanic belt, based on group velocity dispersion. *Geofísica Internacional*, 35, 4, 361- 370.
- Eberhart-Phillips D., 1993, Local earthquake tomography: earthquake source regions, in *Seismic Tomography: Theory and Practice*, edited by H. M. Lyer and K. Hirahara.
- Gutscher M.A., Spakman W., Bijwaard H., Engdahl E.R., 2000, Geodynamics of flat subduction: Seismicity and tomographic constraints from the Andean margin, *Tectonics*, 19, 814-833.
- Hacker B.R., Abers G.A., Peacock S.M., 2003, Subduction factory, 1, Theoretical mineralogy, densities, seismic wave speeds, and H₂O contents, *J. Geophys. Res.*, 108(B1), 2029, doi:10.1029/2001JB001127.
- Hearn Thomas M., Clayton Robert W., 1986, Lateral variations in southern California. I. Results for the upper crust from Pg waves. *Bull. Seis. Soc. Amer.* Vol. 76, No. 2. 495 – 509.
- Husker A., Davis P.M., 2009, Tomography and thermal state of the Cocos plate subduction beneath Mexico City, *J. Geophys. Res.*, 114, B04306, doi: 10.1029/2008JB006039.
- Husker A.L., Kostoglodov V., Cruz-Atienza V.M., Legrand D., Shapiro N.M., Payero J.S., Campillo M., Huesca-Pérez E., 2012, Temporal variations of non-volcanic tremor (NVT) locations in the Mexican subduction zone: Finding the NVT sweet spot, *Geochem. Geophys. Geosyst.*, 13, Q03011, doi:10.1029/2011GC003916.
- Iglesias A., Clayton R.W., Pérez-Campos X., Singh S.K., Pacheco J.F., García D., Valdés-González C., 2010, S wave velocity structure below central Mexico using high-resolution surface wave tomography, *J. Geophys. Res.* 115, no. B06307, doi 10.1029/2009JB006332.
- Jödicke H., Jording A., Ferrari L., Arzate J., Mezger K., Ruoke L., 2006, Fluid release from the subducted Cocos plate and partial melting of the crust deduced from magnetotelluric studies in southern Mexico: Implications for the generation of volcanism and subduction dynamics, *J. Geophys. Res.* 111, no. B08102, doi 10.1029/2005JB003739.
- Kim Y., Clayton R.W., Jackson J.M., 2010, Geometry and seismic properties of the subducting Cocos plate in central Mexico, *J. Geophys. Res.*, 115, B06310, doi: 10.1029/2009JB006942.
- Kostoglodov V., Husker A., Shapiro N.M., Payero J.S., Campillo M., Cotte N., Clayton R., 2010, The 2006 slow slip event and nonvolcanic tremor in the Mexican subduction zone, *Geophys. Res. Lett.*, 37, L24301, doi: 10.1029/2010GL045424.
- Manea V.C., Manea M., Kostoglodov V., Currie C.A., Sewell G., 2004, Thermal structure, coupling and metamorphism in the Mexican subduction zone beneath Guerrero. *Geophys. J. Int.* 158, 775 – 784. doi: 10.1111/j.1365-246X.2004.02325.x.
- Manea V.C, Manea M., 2010, Flat-Slab Thermal Structure and Evolution Beneath Central Mexico. *Pure Appl. Geophys.*, Springer Basel AG. Doi: 10.1007/s00024-010-0207-9.
- Pacheco J.F., Singh S.K., 2010, Seismicity and state of stress in Guerrero segment of the Mexican subduction zone, *J. Geophys. Res.*, 115, B01303, doi:10.1029/2009JB006453.
- Paige Ch. C., Saunders M.A., 1982, LSQR: An Algorithm for Sparse Linear Equations and Sparse Least Squares. *ACM Transactions on Mathematical Software*, 8, 1, 43 – 71.
- Pardo M., Suárez G., 1995, Shape of the subducted Rivera and Cocos plates in southern Mexico: Seismic and tectonic implications. *J. Geophys. Res.*, 100, 12357 – 12373.

- Payero J., Kostoglodov V., Shapiro N., Mikumo T., Iglesias A., Pérez-Campos X., Clayton R., 2008, Non-Volcanic tremor observed in the Mexican subduction zone. *Geophys. Res. Lett.* 35, L07305.
- Prasad M., Manghnani M.H., 1997, Effects of pore and differential pressure on compressional wave velocity and quality factor in Berea and Michigan sandstones, *Geophysics*, 62 (4), 1,163 - 1,176.
- Pérez-Campos X., Kim Y.H., Husker A., Davis P.M., Clayton R.W., Iglesias A., Pacheco J.F., Singh S.K., Manea V.C., Gurnis M., 2008, Horizontal subduction and truncation of the Cocos plate beneath central Mexico, *Geophys. Res. Lett.* 35, doi 10.1029/2008GL035127.
- Shearer P., 1988, Cracked media, Poisson's ratio and the structure of the upper oceanic crust. *Geoph. J.*, 92, 357 - 362.
- Singh S.K., Pardo M., 1993, Geometry of the Benioff zone and state of stress in the overriding plate in central Mexico. *Geophys. Res. Lett.*, 20, 1483 - 1486.
- Song T.R.A., Helmberger D.V., Brudzinski M.R., Clayton R.W., Davis P., Pérez-Campos X., Singh S.K., 2009, Subducting Slab Ultra-Slow Velocity Layer Coincident with Silent Earthquakes in Southern Mexico. *Science*, vol. 324, 502 - 506.
- Um J., Thurber C., 1987, A Fast Algorithm For Two-Point Seismic Ray Tracing, *Bull. Seis. Soc. Amer.*, Vol. 77, 3, 972-986.
- Vanorio T., Virieux J., Capuano P., Russo G., 2005, Three-dimensional seismic tomography from P wave and S wave microearthquake travel times and rock physics characterization of the Campi Flegrei Caldera, *J. Geophys. Res.*, 110, B03201, doi: 10.1029/2004JB003102.
- Waldhauser F., Ellsworth W.L., 2000, A double-difference earthquake location algorithm: Method and application to the northern Hayward fault, *Bull. Seism. Soc. Amer.*, 90, 1,353-1,368.

Trace elements geochemistry and origin of volcanic units from the San Luis Potosí and Río Santa María volcanic fields, Mexico: the bearing of ICP-QMS data

Alfredo Aguillón-Robles*, Margarito Tristán-González, Rubén Alfonso López-Doncel, María Elena García-Arreola, Joselin de Lourdes Almaguer-Rodríguez and René C. Maury

Received: July 27, 2011; accepted: March 15, 2012; published on line: June 29, 2012

Resumen

Dos campos volcánicos importantes separados por una estructura volcánico-tectónica se desarrollaron en la porción meridional de la Mesa Central durante el Cenozoico en la etapa de máxima extensión continental, correspondiente a la porción SE de la Provincia de Cuencas y Sierras en la porción suroriental de la Sierra Madre Occidental. Las rocas volcánicas asociadas a estas estructuras tectónicas varían en composición desde basaltos subalcalinos a basanitas o andesitas basálticas hasta riolitas emplazadas desde el Eoceno y extendiéndose hasta el Cuaternario durante cinco eventos volcánicos. A partir de análisis químicos de unidades volcánicas representativas de los complejos volcánicos en el estado de San Luis Potosí, se interpreta que el vulcanismo derivó de la fusión de la cima del manto y por metasomatismo de la base de la corteza, ligado con grados pequeños de cristalización fraccionada, dando como resultado una diversidad magmática y multiepisódica durante el tiempo y espacio, que se asociaron a estructuras volcánicas de la región de San Luis Potosí. La interpretación conjunta a los análisis químicos obtenidos por diferentes técnicas para elementos mayores y para elementos traza por el método ICP-QMS, ha ayudado a proponer nuevos modelos sobre el origen y emplazamiento de unidades volcánicas existentes en la región.

Palabras clave: campos volcánicos, unidades volcánicas, elementos traza, ICP-QMS, San Luis Potosí, México.

Abstract

Two main volcanic fields separated by a volcano-tectonic structure were emplaced in the southern part of San Luis Potosí state during the Cenozoic peak of continental extension in the SE portion of the Sierra Madre Occidental. The Eocene to Quaternary volcanic rocks associated to these structures range in composition either from subalkaline basalts to basanites or from basaltic andesite to rhyolites, and were emplaced during five magmatic events. New trace element analyses obtained by the ICP-QMS method show that the three oldest ones, ranging in age from middle Eocene to late Oligocene, emplaced potassic calc-alkaline intermediate to evolved lavas. These originated from subduction-related mafic magmas through open-system fractional crystallization coupled with assimilation and possibly melting of the continental crust. The two youngest volcanic phases (Miocene and Quaternary) emplaced intraplate subalkaline to alkaline basalt and basanites derived from variable melting degrees of enriched mantle.

Key words: volcanic fields, volcanic units, trace elements, ICP-QMS, San Luis Potosí, Mexico.

A. Aguillón-Robles*
M. Tristán-González
R. A. López-Doncel
Ma. E. García-Arreola
Instituto de Geología
Universidad Autónoma de San Luis Potosí
Av. Dr. Manuel Nava #5, Zona Universitaria
San Luis Potosí, S.L.P.
México
*Corresponding author: aaguillon@uaslp.mx
E-mail: mtristan@uaslp.mx
rlopez@uaslp.mx; maria.garcia@uaslp.mx

J. L. Almaguer-Rodríguez
Área Ciencias de la Tierra; DES Ingeniería
Universidad Autónoma de San Luis Potosí
Av. Dr. Manuel Nava #8
Zona Universitaria
San Luis Potosí, S.L.P.
México
E-mail: almaguerjocelyn@gmail.com

R. C. Maury
Université Européenne de Bretagne
Université de Brest
CNRS; UMR 6538 Domaines Océaniques
Institut Universitaire Européen de la Mer
Place N. Copernic
29280 Plouzané
France
E-mail: maury@univ-brest.fr

Introduction

Two main large volcanic structures are located in the southern portion of the San Luis Potosí State. The formation of the San Luis Potosí Volcanic Field (SLPVF) started during the Eocene with the eruption of andesitic lava flows (Labarthe-Hernández *et al.*, 1982; Tristán-González *et al.*, 2009a). Andesites, dacites and rhyolites were emplaced until late Oligocene (Labarthe-Hernández *et al.*, 1982; Tristán-González, 1986; Aranda-Gómez *et al.*, 1989; Labarthe-Hernández *et al.*, 1991; 1992; Tristán-González *et al.*, 2009a). They are either overlain or crosscut by basaltic intraplate lavas emitted sporadically from Miocene to Pleistocene. The building of the second structure, the Río Santa María Volcanic Field (RSMVF), was initiated by middle Eocene andesitic lava eruptions and followed by the emplacement of voluminous felsic volcanics during the Oligocene. These include a large volume of rhyolitic pyroclastic flows overlain by trachytic and andesitic lava flows. The pyroclastic eruptions were responsible of the Caldera Milpa Grande collapse (Grassel, 1979; Labarthe-Hernández *et al.*, 1984; Tristán-González, 1987; Labarthe-Hernández *et al.*, 1989). The RSMVF volcanism ended with sporadic andesitic lava flows interbedded with rhyodacites and basaltic andesites.

The previously mentioned volcanic fields are separated by the Villa de Reyes Graben volcano-tectonic structure (VRG) which shows a dominant NE-SW trend. The SLPVF and the western portion of the RSMVF were affected by high angle NW-SE normal faults and the blocks were tilted towards the NE (Figure 1). This system formed a complex pattern of domino faults and narrow tectonic grabens. In some of these grabens, the emplacement of rhyolitic pyroclastic flows, were alternated with basaltic lava flows, forming a typical bimodal volcanic association (Tristán-González, 1986; Aguirre-Díaz and Labarthe-Hernández, 2003; Torres-Aguilera, 2005; Torres-Hernández *et al.*, 2006; Tristán-González *et al.*, 2006; Tristán-González, 2008; Tristán-González *et al.*, 2008; Rodríguez-Ríos and Torres-Aguilera, 2009).

These volcanic events occurred in the southern portion of the Mesa Central Physiographic Province (MC, Figure 1). This area is considered as belonging to the Magmatic Province of the Sierra Madre Occidental (SMOc), the origin of which has been discussed by several authors (Cameron *et al.*, 1980; Cameron and Hanson, 1982; Graham *et al.*, 1995; Smith *et al.*, 1996; Ruiz *et al.*, 1988; 1990; Bryan *et al.*, 2000, 2002; Ferrari *et al.*, 2002; 2005). Three alternative models have been proposed to explain the origin of the voluminous silicic volcanic cover of the SMOc. The first one involves partial melting of the continental crust (Cameron *et al.*, 1980;

Cameron and Hanson, 1982). It implies the uprising of large amounts of basaltic magmas from the mantle, which provided the heat necessary to melt the crust. The second hypothesis postulates that the felsic magmas, mainly rhyolitic, derived from the fractional crystallization of basaltic magmas generated in the mantle, with little or not contribution of the continental crust (Smith *et al.*, 1996; Ruiz *et al.*, 1988; 1990; Bryan *et al.*, 2002). In the third (and the most complex) model, magmas originated by partial melting of the base of the lithosphere mixed with existing magmas of felsic composition, and were extruded through faults and fissures associated to the cortical extension (Aranda-Gómez *et al.*, 2007; Aguillón-Robles *et al.*, 2009; Tristán-González *et al.*, 2009b).

The volcanism associated to the formation of the SLPVF, intermediate to felsic in composition, is considered as a product of the partial melting of the Precambrian lower continental crust (Ruiz *et al.*, 1988; Aguillón-Robles *et al.*, 1994; 1996; 1997; Orozco-Esquivel *et al.*, 2002). Although fractional crystallization processes operated at a smaller scale, their influence was significant in the evolution of these magmas (Verma, 1984; Rodríguez-Ríos *et al.*, 2007; Aguillón-Robles *et al.*, 2009).

Given the existing controversy on the origin of the volcanism for this portion of the SMOc, we have used the ICP-QMS method recently developed in UASLP (Universidad Autónoma de San Luis Potosí) to obtain a set of new trace element data. The aim of this article is to show that these data allow us to constrain the various petrogenetic models discussed above, and to better understand the relationship between the activity of the volcanic fields and the volcano-tectonic structure of Villa de Reyes Graben.

Sampling of the geologic units

We sampled some representative volcanic units of the volcanic fields of SLP and Río Santa María, as well as volcanic units associated to the formation of Villa de Reyes Graben (Figure 1). The stratigraphy of this region was studied in detail by Labarthe-Hernández *et al.* (1982) and Tristán-González *et al.* (2009a); the names of the volcanic units were taken from the original work (Labarthe-Hernández, *et al.*, 1982), which was named by petrographic criteria; however, subsequently chemical analysis showed they have different composition, as in the case of units named as Casita Blanca andesite, Portezuelo latite and Ojo Caliente trachyte, which fall in the field from basaltic-andesite to rhyolite (Figure 2), to update their names would be necessary to reinterpret them, because this nomenclature has been used in this way throughout the past

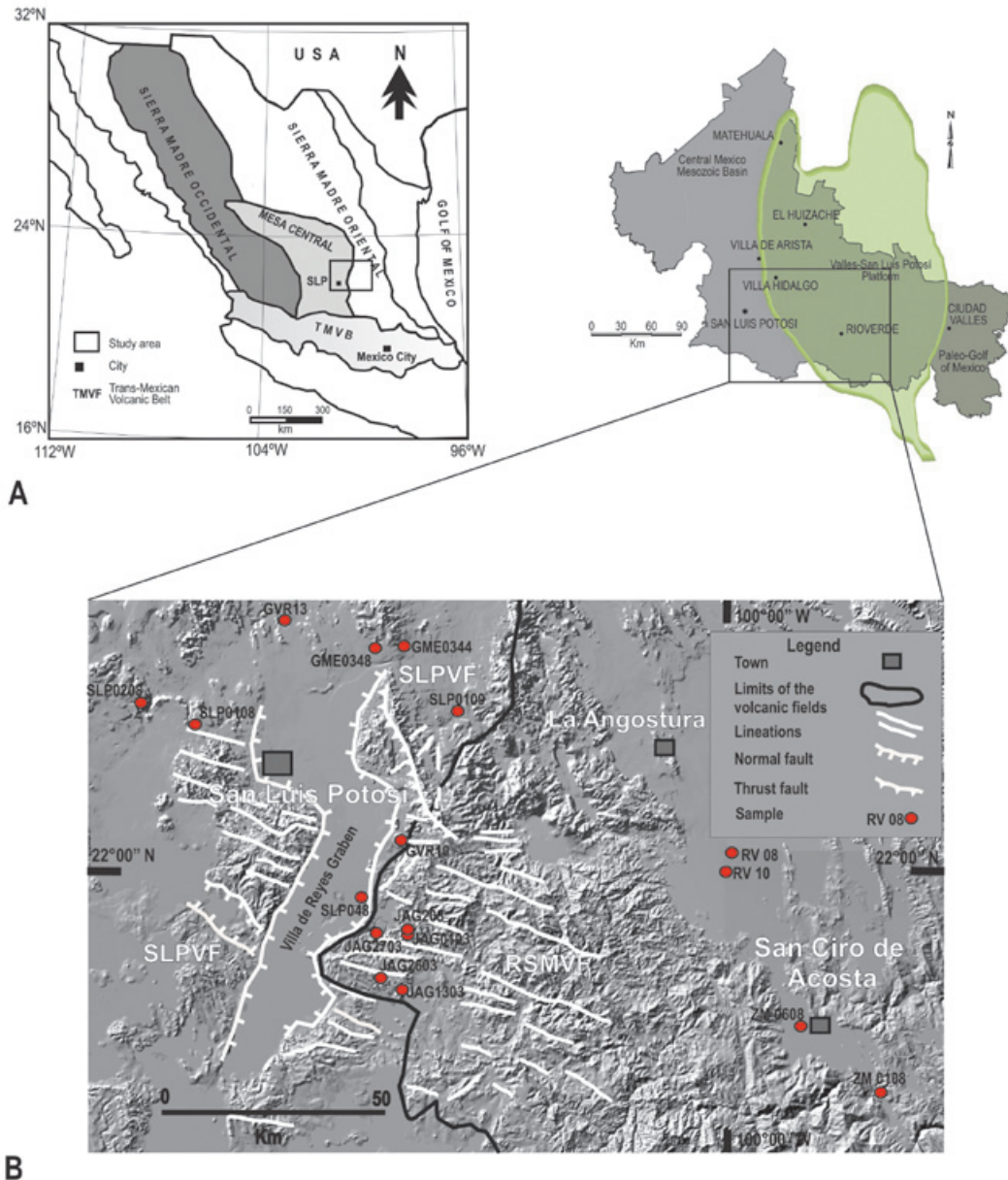


Figure 1. Location of San Luis Potosí (SLPVF) and Río Santa María Volcanic Fields (RSMVF). A: position and relationships with the main physiographic provinces (left) and paleogeographic structures (right) from northern Mexico (modified after Tristán *et al.*, 2009b); B: location of the main volcano-tectonic structures of the southern part of San Luis Potosí state (modified after Tristán-González *et al.*, 2009a).

literature. We collected 18 volcanic rock samples, which include: two basaltic-andesitic lava flows located in the SLPVF; three recent samples associated to "maar" type structures emplaced between 1.50 and 0.59 Ma (Tristán-González *et al.*, 2009a); nine samples from the RSMVF, among which five are lava flows from Ojo Caliente unit (trachytic magma; Labarthe-Hernández *et al.*, 1982) and four others are basaltic lava samples erupted along the regional faults and/or NW-SE trending fissures. The latter appeared event during the late Miocene (Barboza-Gudiño pers. com.), and are interpreted here for the first time

as associated to the final volcanic events in this area. Finally, we sampled dacitic lavas associated to the VRG volcano-tectonic structure.

Casita Blanca andesite

Labarthe-Hernández *et al.* (1982) have termed Casita Blanca andesite a serie of andesitic to basaltic lava flows which mark the beginning of the SLPVF vulcanism. One of these lava flows crops out in the northwestern and northern parts of the volcanic field and in some stratigraphic windows located to the east of the SLPVF in

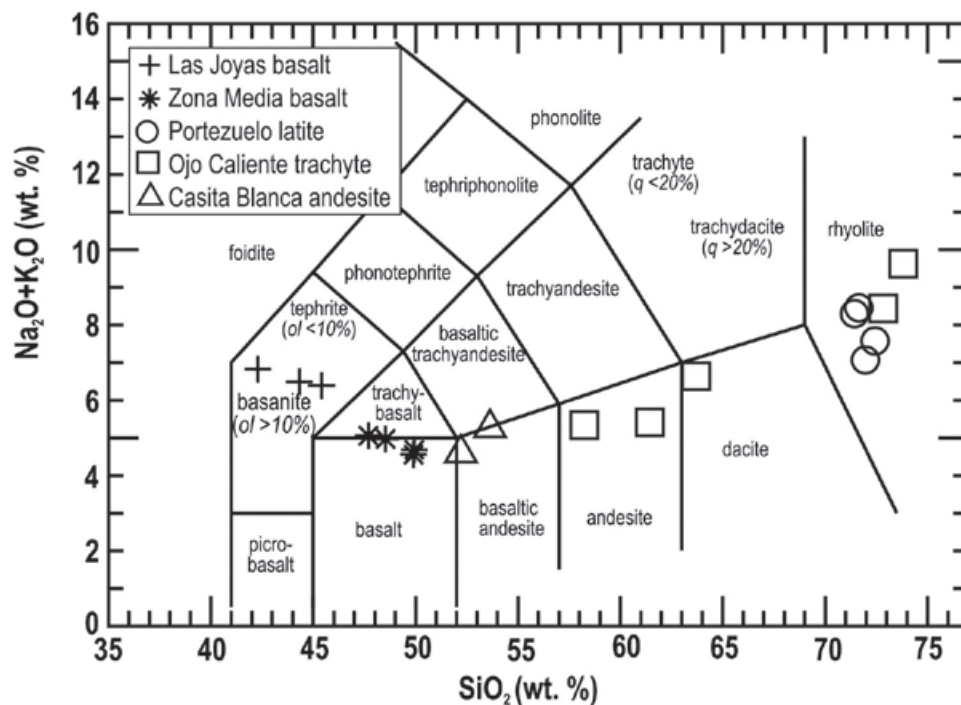


Figure 2. TAS (total alkalis vs. silica; Le Bas *et al.*, 1986) diagram for San Luis Potosí, Río Santa María and Villa de Reyes Graben lava samples. Volatile-free analyses recalculated using the SINCLAS program (Verma *et al.*, 2002).

the vicinity of Cerro de San Pedro (Labarthe-Hernández *et al.*, 1982; Tristán-González *et al.*, 2009b). It is a moderately porphyritic rock of greenish dark gray color, with *ca.* 5 modal % of phenocrysts of biotite and plagioclase in an aphanitic microlitic matrix, composed of plagioclase and biotite. The top of this flow ranges from 20 to 80 m thick, which rests over Mesozoic marine rocks and continental lacustrine sediment, contains abundant vesicles, some of them filled up with chalcedony. Whole rock K-Ar ages of 45.5 ± 1.1 ; 44.4 ± 1.0 , and 42.4 ± 1.0 (middle Eocene) have been reported (Tristán-González *et al.*, 2009a).

Ojo Caliente trachyte

This name applies to a *ca.* 180 m thick pile of trachytic lava flows which crop out mainly in the western portion of the RSMVF (Labarthe-Hernández *et al.*, 1982); although in the present study, the collected samples classify as andesite, dacites and rhyolites (Figure 2). This unit overlies rhyolitic pyroclastic flows, the emplacement of which marked the start of volcanic activity in this volcanic field around 32 Ma (Labarthe-Hernández *et al.*, 1982; Tristán-González *et al.*, 2009a). These light gray colored moderately porphyritic lava contains *ca.* 5 modal% phenocrysts of sanidine and clinopyroxenes sometimes altered to iron oxides, set in a devitrified groundmass. Corresponding whole rock isotopic ages are 31.8 ± 0.7 and 31.6 ± 0.7 Ma, *i.e.* early Oligocene (Tristán-González *et al.*, 2009a).

Portezuelo latite

Although the volcanic unit referred to as Portezuelo latite outcrops are within the SLPVF; its emplacement was associated to the main extension event which formed the volcano-tectonic structure of the VRG. Thus, its main outcrops are located all along this graben (Labarthe-Hernández *et al.*, 1982; Tristán-González, 1986; 2008; Tristán-González *et al.*, 2009b). This unit is associated to a *ca.* 440 m thick pile of porphyritic lava flow of rhyolitic composition. These light gray color porphyritic rocks contain 10 to 15 modal% phenocrysts of sanidine, plagioclase and subordinated quartz, set in a microlitic groundmass bearing plagioclase, magnetite, zircon and apatite (Labarthe-Hernández *et al.*, 1982); in this study all the samples were according to their geochemistry classified as rhyolites. The corresponding whole rock ages range from 30.6 ± 1.5 to 31.0 ± 0.7 Ma, *i.e.* early Oligocene (Labarthe-Hernández *et al.*, 1982; Tristán-González *et al.*, 2009a).

Zona Media basalt

The unit known as Zona Media basalt is a pile of fissural lava flows of basaltic-andesitic composition which were emitted from scoria cones and of blocky lava flows extruded along NW-SE trending faults and/or fissures. These lava flowed within depressions dug into sediments associated to the Valles-San Luis Potosí Platform, near San Ciro and Angostura SLP (Figure 1). This volcanic unit, located at the NE border of the RSMVF, has

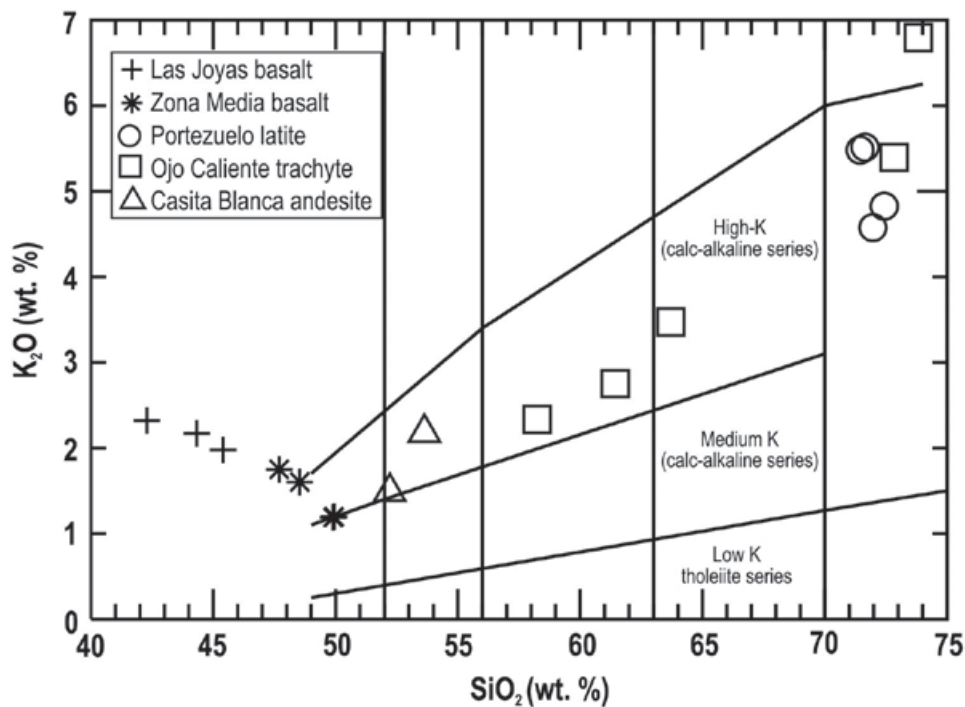


Figure 3. K₂O vs. SiO₂ diagram (Peccerillo and Taylor, 1976) of San Luis Potosí and Río Santa María lavas, showing the features of low-K, medium-K and high-K (potassic) calc-alkaline series.

been associated to a Miocene intraplate event subsequent to volcanism of the SLPVF. These porphyritic basalt and andesites contain ca. 20 modal% phenocrysts of plagioclase, olivine and augite, embedded in a fine-grained plagioclase- and augite-bearing microlitic groundmass (Sánchez-García, 2009).

Las Joyas basalt

The youngest volcanic event recognized in the southern portion of the SLP state emplaced the Las Joyas basalt, a set of Quaternary pyroclastic flows and lava flows associated to "maar" type volcanic structures (Labarthe-Hernández *et al.*, 1982). These vesicular basaltic lava flows contain a few percent phenocrysts of olivine altered to iddingsite, set in a groundmass bearing calcic plagioclase together with pigeonite and/or augite. They filled up the depressions of the local rugged topography, and were only covered in some sites by recent alluvial deposits. The whole rock K-Ar isotopic ages obtained for this volcanic unit are 1.50 ± 0.8 Ma; 1.01 ± 0.08 Ma and 0.59 ± 0.06 Ma (Tristán-González *et al.*, 2009a).

Analytical Methods

Major elements analyses (Table 1) were obtained by X-ray fluorescence at the Institute of Geology UNAM (Universidad Nacional Autónoma de México). The samples were finely powdered in an agate grinder. The details of the analytical method are reported by Lozano and Bernal (2005). The trace element analyses (Table 2)

were performed at the Geochemical Laboratory in the Institute of Geology of the UASLP (LGIG), by the ICP-QMS (Thermo Scientific Serie X2, inductively coupled plasma- quadrupole mass spectrometer) method. The analytical techniques are described in Almaguer-Rodríguez (2010).

Major element data

The samples are rather fresh, with LOI values (loss of ignition at 1,000°C) ranging from slightly negative values up to 2.60 and exceptionally to 3.22 wt.% (Table 1). Samples from Casita Blanca, Ojo Caliente and Portezuelo units are silica-oversaturated basaltic andesites, andesites, dacites and rhyolites (Figure 2). All of them display the usual major element features of K-rich calc-alkaline series (Figure 3; Peccerillo and Taylor, 1976), with typically low Na₂O/K₂O ratios. The alumina saturation index $[Al_2O_3/(CaO+K_2O+Na_2O)]$ ratio range from 0.86 to 1.01 for the silica-rich units; a single sample (JAG27-03), has been determined as peralkaline $[(Na_2O+K_2O)/Al_2O_3 > 1]$. In Harker diagrams (not shown), TiO₂, Fe₂O₃*, MgO, MnO, and CaO display negative correlations with SiO₂, while K₂O (Figure 3) and to a lesser extent Na₂O (not shown) positive ones; the decrease of compatible elements and the increase of incompatible elements (mainly large ion lithophile elements) with SiO₂ are potentially consistent with assimilation, fractional crystallization or coupled (AFC) processes. The Differentiation Index (DI) of Thornton and Tuttle (1960), varies from 58.6 to 89.7 for felsic units (Portezuelo latite and Ojo

Table 1. Major element analyses of representative San Luis Potosí, Río Santa María and Villa de Reyes Graben lavas. Analytical method described in the text. Total iron as Fe₂O₃.

Sample	SLP0108	SLP0208	JAG0103	JAG0203	JAG1303	JAG2603	JAG2703	SLP0108A	GVR10
Rock*	BA	BA	A	A	R	D	R	R	R
GU**	Tcb	Tcb	Toc	Toc	Toc	Toc	Toc	Tlp	Tlp
Lat. N	22.2741°	22.2918°	21.8914°	21.8853°	21.7850°	21.8036°	21.8875°	22.2889°	22.0572°
Long W	101.1541°	101.1981°	100.7207°	100.7161°	100.7333°	100.7730°	100.7805°	101.2055°	100.7350°
Major elements (wt.%)									
SiO ₂	53.32	51.82	59.30	56.50	70.40	61.00	72.79	70.65	70.50
TiO ₂	3.41	1.59	1.46	2.04	0.31	0.92	0.28	0.56	0.34
Al ₂ O ₃	14.11	16.27	14.65	14.32	13.24	15.10	12.67	13.69	13.15
Fe ₂ O ₃	12.24	9.38	8.42	10.36	3.98	8.15	3.03	3.24	4.22
MnO	0.17	0.13	0.12	0.14	0.03	0.10	0.03	0.01	0.03
MgO	3.24	7.49	2.50	3.02	0.14	0.94	0.15	0.27	0.26
CaO	7.30	8.22	5.12	5.75	0.68	3.54	0.37	1.83	1.53
Na ₂ O	3.06	3.08	2.50	2.85	2.87	2.96	2.72	2.90	2.68
K ₂ O	2.16	1.47	2.60	2.21	5.16	3.27	6.64	5.43	4.70
P ₂ O ₅	1.15	0.40	0.35	0.45	0.04	0.24	0.02	0.19	0.14
LOI	0.06	0.25	2.61	2.05	2.30	3.22	0.09	1.37	1.80
Total	100.22	100.10	99.63	99.69	99.15	99.44	99.66	100.14	99.35
Major elements to 100% free volatiles (calculated with SINCLAS program****)									
SiO ₂	53.635	52.216	61.439	58.241	72.835	63.701	73.83	71.643	72.427
TiO ₂	3.430	1.599	1.513	2.103	0.321	0.961	0.286	0.569	0.349
Al ₂ O ₃	14.197	16.388	15.178	14.761	13.698	15.768	12.858	13.885	13.509
Fe ₂ O ₃	4.723	3.43	3.538	4.199	2.125	3.720	1.710	1.719	2.177
FeO	6.827	5.413	4.666	5.831	1.793	4.310	1.230	1.406	1.942
MnO	0.171	0.132	0.124	0.144	0.031	0.104	0.032	0.007	0.031
MgO	3.259	7.542	2.590	3.113	0.145	0.982	0.157	0.273	0.267
CaO	7.345	8.285	5.305	5.927	0.704	3.697	0.378	1.857	1.572
Na ₂ O	3.081	3.104	2.590	2.938	2.969	3.091	2.758	2.941	2.753
K ₂ O	2.176	1.484	2.694	2.278	5.338	3.415	6.738	5.512	4.824
P ₂ O ₅	1.156	0.406	0.363	0.464	0.041	0.251	0.021	0.189	0.144
CIPW normative minerals (calculated from SINCLAS program)									
qz	10.801	1.088	20.778	15.863	33.042	22.404	60.079	29.481	34.007
or	12.859	8.77	15.92	13.462	31.546	20.181	0.136	32.574	28.532
ab	26.07	26.265	21.916	24.860	25.123	26.155	25.03	24.886	23.295
an	18.481	26.4	21.832	20.36	3.225	16.701	1.864	7.978	6.858
ne	---	---	---	---	---	---	---	---	---
c	---	---	---	---	1.854	0.866	8.216	0.156	1.24
di	8.377	9.599	1.715	4.873	---	---	---	---	---
hy	7.371	18.928	8.995	9.422	1.425	5.892	2.077	0.915	1.913
ol	---	---	---	---	---	---	---	---	---
mt	6.847	4.973	5.129	6.088	3.081	5.393	1.963	2.492	3.156
il	6.514	3.037	2.874	3.994	0.610	1.825	0.583	1.081	0.663
ap	2.678	0.941	0.841	1.075	0.095	0.582	0.053	0.438	0.334
Mg#	45.973	71.294	49.735	48.761	12.599	28.883	14.672	25.712	19.684
DI	49.73	36.123	58.614	54.185	89.711	68.740	85.245	86.941	85.834
ASI	0.804	0.917	1.010	0.940	1.015	1.073	0.860	0.980	0.996

Caliente trachyte) and from 36.1 to 49.7 for the old mafic unit (Casita Blanca andesite).

The young mafic samples Zona Media basalt and Las Joyas basalt units include silica-saturated subalkaline basalts and silica-undersaturated (ne-normative) alkaline basalts, basanites and trachy-basalt (Figure 2), which display high contents in incompatible major element oxides (TiO₂, Na₂O, K₂O; P₂O₅). Their FeO*/MgO ratios are rather low (less than 1.3)

and their Mg numbers are scattered from 75.0 to 61.9. In contrast to the former group, they display relatively high Na₂O/K₂O ratios (from 1.8 to 2.8). In Harker diagrams (not shown), TiO₂, Fe₂O₃*, MgO and P₂O₅ as well as K₂O and K₂O + Na₂O (Figure 3) display negative correlations with SiO₂. The two latter ones are not consistent with differentiation- or assimilation-related processes, but could indicate variations in partial melting degrees of an ultramafic source.

Table 1A. Major element analyses (continued).

Sample	GVR13	SLP048	RV08	RV10	ZM0108	ZM0608	SLP0109	GME0344	GME0348
Rock*	R	R	B, subal	B, alk	B, subal	TB, pot	BSN, bsn	BSN, bsn	BSN, mnp
GU**	Tlp	Tlp	ZMb	ZMb	ZMb	ZMb	Qbj	Qbj	Qbj
Lat. N	22.4558°	21.9511°	22.0359	22.0066	21.5010°	21.6501°	22.2900°	22.4075°	22.4075°
Long W	100.9641°	100.8137°	100.0428	100.0985	99.6666°	99.7833°	100.6235°	100.7273°	100.7831°
Major elements (wt.%)									
SiO ₂	69.85	70.81	49.40	47.60	49.619	46.937	43.354	44.80	41.90
TiO ₂	0.46	0.454	1.94	2.04	1.835	2.04	3.233	2.30	2.96
Al ₂ O ₃	13.29	13.723	15.60	13.98	15.239	14.391	13.364	14.00	11.85
Fe ₂ O ₃	4.56	4.272	11.85	12.10	11.929	11.192	13.136	13.40	13.50
MnO	0.04	0.043	0.17	0.19	0.155	0.152	0.189	0.21	0.20
MgO	0.36	0.358	6.29	8.60	7.563	9.966	8.468	7.78	12.90
CaO	1.71	1.301	9.40	8.90	8.972	8.919	9.365	9.80	8.70
Na ₂ O	2.42	2.791	3.45	3.30	3.346	3.25	4.224	4.35	4.46
K ₂ O	4.44	5.431	1.18	1.57	1.181	1.721	2.121	1.95	2.30
P ₂ O ₅	0.17	0.148	0.41	0.58	0.364	0.562	1.199	0.91	1.15
LOI	2.51	1.11	-0.09	0.03	-0.11	0.86	0.94	0.67	-0.38
Total	99.81	100.441	99.60	98.89	100.093	99.99	99.593	100.17	99.54
Major elements to 100% free volatiles (calculated with SINCLAS program***)									
SiO ₂	71.961	71.434	49.937	48.534	49.903	47.698	44.32	45.41	42.294
TiO ₂	0.474	0.458	1.961	2.08	1.846	2.073	3.305	2.331	2.988
Al ₂ O ₃	13.692	13.844	15.77	14.254	15.326	14.624	13.662	14.191	11.962
Fe ₂ O ₃	2.292	2.25	4.25	4.35	4.241	4.004	4.926	5.05	5.039
FeO	2.165	1.854	6.954	7.187	6.979	6.631	7.651	7.678	7.728
MnO	0.041	0.043	0.172	0.194	0.156	0.154	0.193	0.213	0.202
MgO	0.371	0.361	6.358	8.769	7.606	10.128	8.657	7.886	13.021
CaO	1.762	1.312	9.502	9.075	9.023	9.064	9.574	9.933	8.782
Na ₂ O	2.493	2.816	3.488	3.365	3.365	3.303	4.318	4.409	4.502
K ₂ O	4.574	5.479	1.193	1.601	1.188	1.749	2.168	1.976	2.322
P ₂ O ₅	0.175	0.149	0.414	0.591	0.366	0.571	1.226	0.922	1.161
CIPW normative minerals (calculated from SINCLAS program)									
qz	35.493	30.76	---	---	---	---	---	---	---
or	27.031	32.379	7.05	9.461	7.021	10.336	12.812	11.677	13.722
ab	21.095	23.828	29.514	27.204	28.474	22.338	13.209	14.228	3.206
an	7.598	5.536	23.849	19.06	23.204	19.91	11.492	13.094	5.573
ne	---	---	---	0.687	---	3.039	12.638	12.503	18.900
c	1.855	1.252	---	---	---	---	---	---	---
di	---	---	16.569	17.667	15.373	16.957	22.257	24.162	24.063
hy	2.299	1.768	6.921	---	8.506	---	---	---	---
ol	---	---	5.25	14.293	6.918	16.353	11.333	10.45	18.867
mt	3.323	3.262	6.162	6.306	6.148	5.805	7.142	7.321	7.305
il	0.90	0.87	3.724	3.95	3.506	3.937	6.277	4.427	5.675
ap	0.405	0.345	0.959	1.369	0.848	1.323	2.84	2.136	2.69
Mg#	23.399	25.766	61.974	68.503	66.017	73.137	66.854	64.675	75.021
DI	83.619	86.967	36.564	37.352	35.495	35.713	38.659	38.408	35.828
ASI	1.049	0.967	0.804	0.731	0.816	0.745	0.610	0.625	0.548

* Chemical classification of rock types are presented according to total alkalis vs. silica diagram (Le Bas *et al.*, 1986); BA, basaltic-andesite; A, andesite; R, rhyolite; D, dacite; TB, trachy-basalt; BSN, basanite; mnp, melanephelinite; alk, alkali; subal, subalkali. ***Geologic Unit the stratigraphy of the volcanic fields reported by Labarthe-Hernández *et al.* (1982); and Tristán-González *et al.* (2009a); Tcb, Casita Blanca andesite; Toc, Ojos Caliente trachyte; Tlp, Portezuelo latite; ZMb, Zona Media basalt; Qbj, Las Joyas basalt (see the text). ****SINCLAS Program by Verma *et al.* (2002). Mg# = $100(\text{Mg}^{2+}/\text{Mg}^{2+}+\text{Fe}^{2+})$; FeO = $\text{Fe}_2\text{O}_3(\text{total}) \times 0.85$. DI, differentiation index, DI = $qz + or + ab + ne + lc$ (Thornton y Tuttle, 1960). ASI, alumina saturation index = $\text{Al}_2\text{O}_3/(\text{K}_2\text{O} + \text{Na}_2\text{O} + \text{CaO})$.

Trace element data

The trace element data for the analyzed samples, combined with the major element features discussed above, allows us to distinguish two lava types. The first group corresponds to old calc-

alkaline potassic lavas ranging in composition from Casita Blanca andesite to felsic lavas (Portezuelo latite and Ojo Caliente trachyte). It displays variable enrichment in Rb, Th, Yb and Ba, the contents of which increase together with SiO₂ contents during magmatic differentiation

and/or assimilation and mixing (Figure 4). The second group corresponds to the young subalkaline/alkaline lavas (Zona Media basalt and Las Joyas basalt). These are less evolved than the calc-alkaline ones according to their rather high contents in Ni, Cr and Co (Table 2). They also display high contents in most incompatible elements and especially in Nb (Figure 4).

In the multielement plots normalized to the Primitive Mantle (Figure 5; Sun and McDonough, 1989), calc-alkaline lavas display highly fractionated patterns, with positive spikes for most large ion lithophile elements (LILE, especially Rb, K and Pb), and strong negative anomaly in high field strength elements (HFSE:

Nb, Ta, P, Zr, Hf and Ti). These features, as well as their highly fractionated rare earth element (REE) patterns, are characteristic of subduction-related calc-alkaline magmas. In addition, negative anomalies in Sr and Eu can indicate plagioclase fractionation during differentiation, while similar negative anomalies in Ti and P can be due to iron oxides and apatite fractionation, respectively. The patterns of the young subalkaline/alkaline lavas are enriched in the most incompatible elements. The highest enrichments are observed for Ba, Nb and Ta, and the light REE (Figure 5). Such features are typical of intraplate alkali basalts and related "OIB-type" lavas (Sun and McDonough, 1989; Wilson, 1989).

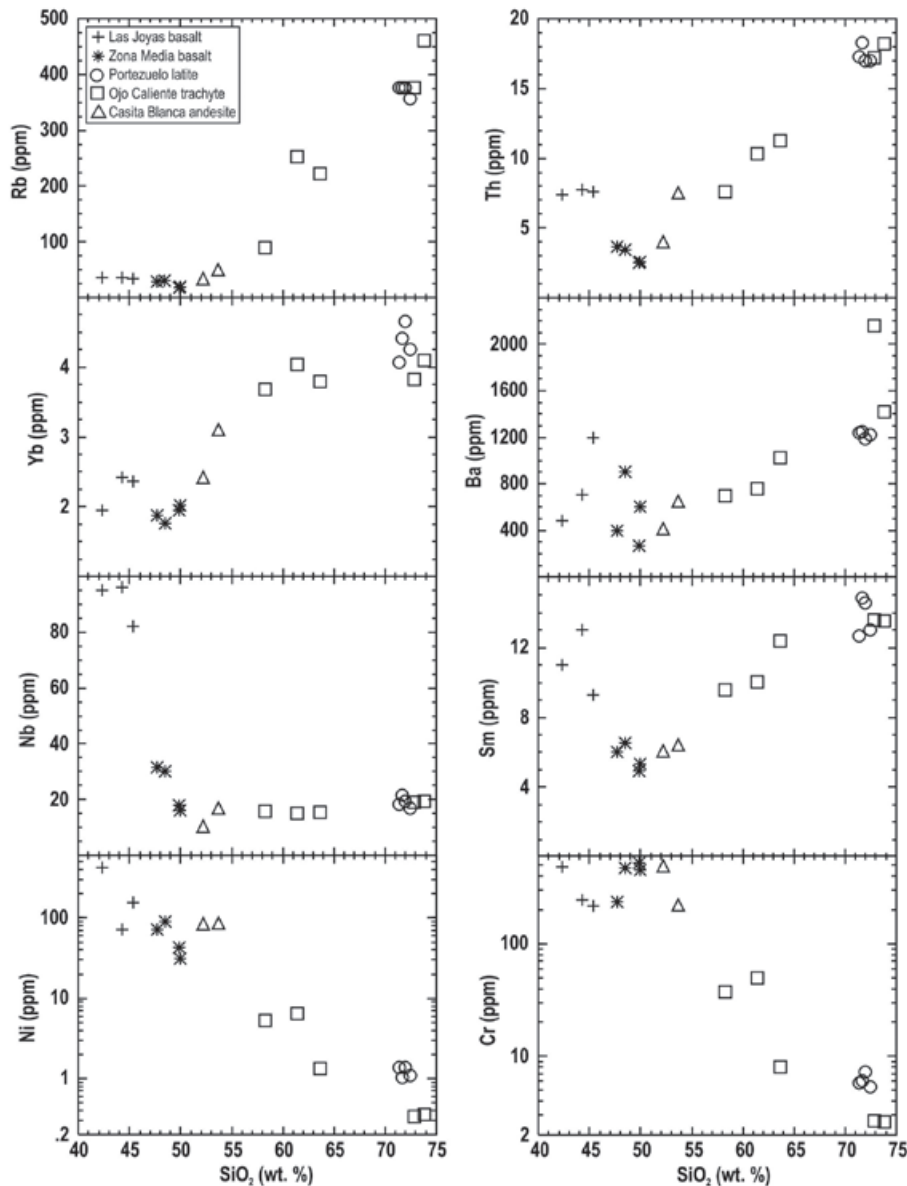


Figure 4. Plots of a selection of incompatible trace elements (ppm) vs. SiO₂ (wt. %). See text for explanations.

Table 2. Trace element analyses (ppm) of representative San Luis Potosí, Río Santa María and Villa de Reyes Graben volcanic rocks. Analytical method described in the text.

Sample	SLP0108	SLP0208	JAG0103	JAG0203	JAG1303	JAG2603	JAG2703	SLP0108A	GVR10
Rock*	BA	BA	A	A	R	D	R	R	R
GU**	Tcb	Tcb	Toc	Toc	Toc	Toc	Toc	Tlp	Tlp
Trace elements (ppm)									
Ba	658.39	410.52	757.25	699.77	2157.89	1022.22	1414.36	1243.65	1223.83
Rb	49.58	33.63	253.51	90.10	375.67	222.45	460.92	376.13	356.21
Sr	870.83	535.76	378.72	346.51	114.22	343.96	42.23	184.62	157.50
Y	36.75	15.67	28.16	26.20	29.11	29.42	30.98	33.49	33.73
Zr	238.67	233.01	421.57	425.64	433.29	464.87	295.18	121.73	135.82
Nb	16.46	10.43	15.24	15.67	19.20	15.55	19.46	21.38	16.97
Th	7.55	4.02	10.33	7.64	17.22	11.24	18.19	18.25	17.01
Pb	8.24	5.59	13.49	9.24	24.54	15.69	23.06	25.67	25.94
Ni	87.86	83.57	6.52	5.25	0.34	1.33	0.36	1.03	1.09
V	204.79	149.12	58.28	71.19	5.51	22.64	12.41	13.86	11.73
Cr	222.98	489.89	49.95	37.03	2.68	7.98	2.60	6.00	5.31
Hf	5.57	4.27	0.00	8.11	8.13	7.58	6.09	2.94	3.09
Cs	0.58	0.58	5.29	6.13	7.37	6.52	8.83	7.91	7.98
Ta	0.99	1.16	1.41	1.40	1.99	1.48	2.01	2.16	1.90
Co	30.75	35.72	26.27	26.29	0.79	11.32	0.55	3.15	3.10
U	0.22	1.02	2.55	1.75	3.12	3.40	4.88	3.56	2.89
Rare earth elements (ppm)									
La	30.96	24.40	42.43	59.01	117.58	86.17	104.49	111.94	94.14
Ce	71.85	52.84	90.56	83.94	125.76	111.55	129.29	141.44	121.19
Pr	10.35	5.44	9.39	8.71	14.40	12.41	14.62	15.24	13.01
Nd	36.39	28.08	48.12	44.61	66.83	59.27	68.70	75.15	64.40
Sm	6.88	6.08	10.06	9.59	13.58	12.39	13.54	14.84	13.03
Eu	2.39	1.52	1.93	1.93	1.78	2.15	1.38	1.86	1.67
Gd	6.93	5.49	8.98	8.47	11.03	10.32	10.69	12.35	10.84
Tb	1.06	0.75	1.24	1.16	1.44	1.37	1.44	1.64	1.48
Dy	6.11	4.31	7.02	6.55	7.74	7.40	7.79	8.87	8.20
Ho	1.27	0.84	1.36	1.29	1.41	1.38	1.45	1.65	1.54
Er	3.36	2.39	3.97	3.67	4.01	3.84	4.14	4.65	4.43
Tm	0.49	0.33	0.54	0.50	0.55	0.53	0.56	0.61	0.59
Yb	3.19	2.42	4.04	3.68	3.83	3.80	4.09	4.41	4.26
Lu	0.47	0.31	0.53	0.48	0.51	0.49	0.52	0.55	0.54

* Chemical classification of rock types are presented according to total alkalis vs. silica diagram (Le Bas *et al.*, 1986); BA, basaltic-andesite; A, andesite; R, rhyolite; D, dacite; TB, trachy-basalt; BSN, basanite; mnp, melanephelinite; alk, alkali; subal, subalkali. ** Geologic Unit the stratigraphy of the volcanic fields reported by Labarthe-Hernández *et al.* (1982); and Tristán-González *et al.* (2009a); Tcb, Casita Blanca andesite; Toc, Ojos Caliente trachyte; Tlp, Portezuelo latite; Qbj, Las Joyas basalt (see the text).

Discussion

It is important to obtain a large set of trace element data for the study of magmatic rocks because (i) they are much more numerous (*ca.* 80) than the major elements, (ii) they belong to several chemical groups with specific properties (e.g. the LILE, HFSE and REE), (iii) some of them, especially the HFSE, are relatively immobile during alteration, hydrothermalism and metamorphism, and therefore are good indicators of the nature of the protolith of old igneous rocks, and finally (iv) because of their concentrations, they vary considerably during magmatic processes such as partial melting, fractional crystallization, magma mixing and metasomatism. One of the most reliable analytical methods for them is the inducted coupled plasma - Quadrupole Mass

Spectrometry (ICP-QMS, already implemented in the LGIG, UASLP). The method ICP-QMS used for this study (Almaguer-Rodríguez, 2010) is based on the combination of the procedures used for the ICP-AES at the Université de Bretagne Occidentale at Brest France (Cotten *et al.*, 1985; inducted coupled plasma - atomic emission spectroscopy) and for the ICP-MS method at the University of Arizona (1997).

The volcanic units associated to the formation event of the San Luis Potosí Volcanic Field (Labarthe-Hernandez *et al.*, 1982; Tristán-González *et al.*, 2009a), have been emplaced simultaneously with other volcanic units that are associated either to the Río Santa María Volcanic Field (Labarthe-Hernandez *et al.*, 1989; Tristán-González, 1987) or to the main extension event

Table 2A. Trace element analyses (continued).

Sample	GVR13	SLP048	RV08	RV10	ZM0108	ZM0608	SLP0109	GME0344	GME0348
Rock*	R	R	B, subal	B, alk	B, subal	TB, pot	BSN, bsn	BSN, bsn	BSN, mnp
GU**	Tlp	Tlp	ZMb	ZMb	ZMb	ZMb	Qbj	Qbj	Qbj
Trace elements (ppm)									
Ba	1185.24	1237.95	603.78	901.47	271.30	396.22	709.43	1200.00	485.00
Rb	376.57	376.24	19.25	30.12	17.86	28.45	35.60	34.50	36.50
Sr	156.91	141.71	610.49	862.84	524.28	774.81	1198.58	995.00	976.00
Y	39.84	32.21	22.80	15.95	14.34	14.33	22.78	32.50	30.00
Zr	82.92	118.20	165.38	198.64	166.31	210.68	387.53	265.00	335.00
Nb	19.28	18.33	16.29	30.32	18.08	31.41	95.93	82.00	95.00
Th	16.99	17.29	2.60	3.43	2.49	3.66	7.73	7.60	7.40
Pb	25.74	27.59	2.27	3.18	2.15	2.38	4.82	---	---
Ni	1.39	1.36	31.35	89.05	42.41	70.71	71.22	156.00	424.00
V	16.48	13.59	165.42	167.85	168.32	167.24	196.32	202.00	197.00
Cr	7.29	5.84	450.28	468.89	514.62	236.12	246.24	216.00	480.00
Hf	2.06	2.66	3.01	3.22	2.98	3.48	7.38	---	---
Cs	8.77	8.02	0.32	0.71	0.14	0.48	0.71	---	---
Ta	2.12	1.98	1.627	2.88	1.91	3.12	6.43	---	---
Co	2.24	2.65	45.86	59.58	52.30	56.53	58.26	44.00	57.00
U	3.66	3.98	0.75	1.10	0.75	1.28	2.40	---	---
Rare earth elements (ppm)									
La	102.95	95.12	21.98	33.04	19.19	28.47	102.20	60.00	60.00
Ce	134.37	121.13	42.10	59.59	39.34	55.22	124.66	105.00	114.00
Pr	14.19	12.94	4.38	6.14	3.98	5.65	12.71	---	---
Nd	71.40	64.36	22.37	31.71	20.90	29.34	66.25	40.00	57.50
Sm	14.58	12.66	5.34	6.57	4.93	6.05	12.99	9.30	11.00
Eu	1.68	1.60	1.61	1.88	1.45	1.72	3.52	2.94	3.38
Gd	12.51	10.54	5.23	5.81	4.76	5.44	10.93	8.10	9.10
Tb	1.71	1.42	0.73	0.75	0.66	0.71	1.34	---	---
Dy	9.53	7.82	4.14	3.95	3.86	3.92	6.68	6.10	6.20
Ho	1.81	1.48	0.79	0.73	0.74	0.73	1.14	---	---
Er	5.04	4.23	2.17	1.99	2.06	2.02	2.99	2.80	2.70
Tm	0.67	0.58	0.29	0.25	0.28	0.26	0.36	---	---
Yb	4.65	4.07	2.02	1.76	1.95	1.87	2.42	2.36	1.95
Lu	0.58	0.52	0.26	0.22	0.27	0.24	0.29	---	---

* Chemical classification of rock types are presented according to total alkalis vs. silica diagram (Le Bas *et al.*, 1986); BA, basaltic-andesite; A, andesite; R, rhyolite; D, dacite; TB, trachy-basalt; BSN, basanite; mnp, melanephelinite; alk, alkali; subal, subalkali. ** Geologic Unit in the stratigraphy of the volcanic fields reported by Labarthe-Hernández *et al.* (1982); and Tristán-González *et al.* (2009a); Tcb, Casita Blanca andesite; Toc, Ojos Caliente trachyte; Tlp, Portezuelo latite; ZMb, Zona Media basalt; Qbj, Las Joyas basalt (see the text).

of the volcano-tectonic structure of Villa de Reyes Graben (Tristán-González, 1986; 2008). The corresponding structures have been identified in the southern portion of San Luis Potosí state (Figure 1), where five successive volcanic stages have been recognized (Tristán-González *et al.*, 2009b).

Subalkaline and alkaline basalts, basanites and trachybasalts of intraplate type were emplaced during the two youngest stages, which occurred during the Miocene (23 to 21 Ma) in the RSMVF and the Quaternary in the SLPVF (Tristán-González *et al.*, 2009a). Both Miocene and Quaternary lavas were considered as derived from a progressive partial melting of a peridotitic mantle (Aranda-Gómez *et al.*, 2005). Our new

data support this interpretation. Indeed, the REE and multielement patterns of these lavas (Figure 5) are rather smooth. They display no evidence of interaction with the continental crust, which would have resulted in positive LILE and negative HFSE anomalies, and more generally in a somewhat erratic behavior of incompatible trace elements. In addition, the variations observed in incompatible trace element plots (Figure 6) are consistent with variable partial melting degrees and limited fractional crystallization processes. The studied alkaline lavas are fairly similar to the Encinos Volcanic Field hawaiites located in the north of the San Luis Potosí state, which in addition have experienced some crustal contamination (Luhr *et al.*, 1994).

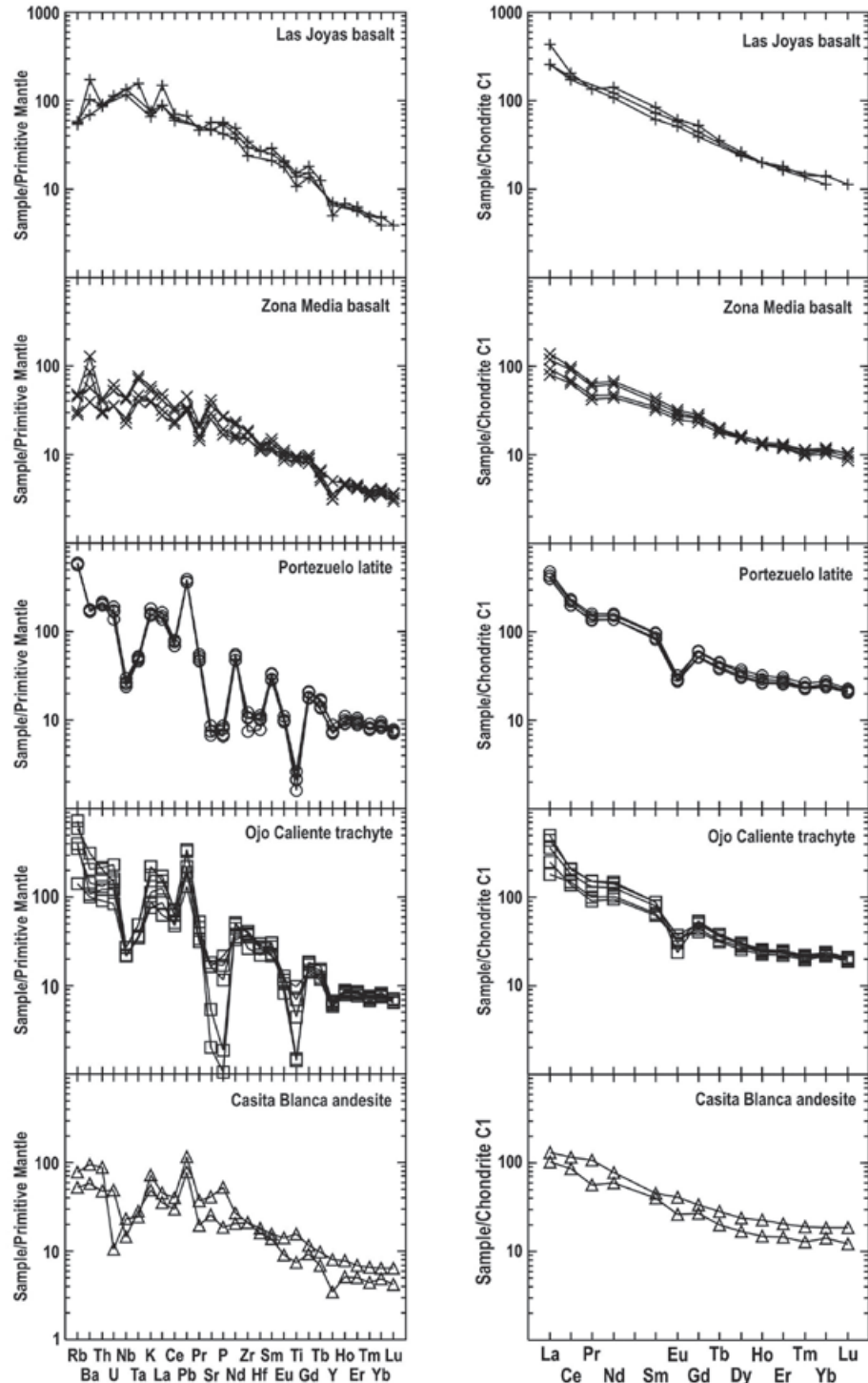


Figure 5. Primitive Mantle -normalized multielement plots and C1 chondrite-normalized rare earth element patterns. Normalization values from Sun and McDonough (1989).

The three older volcanic events emplaced successively (i) the Casita Blanca andesite (mid Eocene); (ii) dacitic to rhyolitic domes and pyroclastic deposits between 32 and 28 Ma in the SLPVF and contemporaneous trachytes and rhyolites in the RSMVF, such as the Ojo Caliente trachyte (Labarthe-Hernandez *et al.*, 1982; Tristán-González *et al.*, 2009a), and the Portezuelo latite associated to the main extension

event that originated the VRG (Tristán-González, 1986); and finally (iii) rhyolitic magmas extruded between 28 and 26 Ma (Labarthe-Hernández *et al.*, 1982; Tristán-González *et al.*, 2009a), which belong to a bimodal volcanic series (Tristán-González, 2008; Tristán-González *et al.*, 2009a; Rodríguez-Ríos and Torres-Aguilera, 2009). All these potassic calc-alkaline lavas display typical fractionated REE and multielement

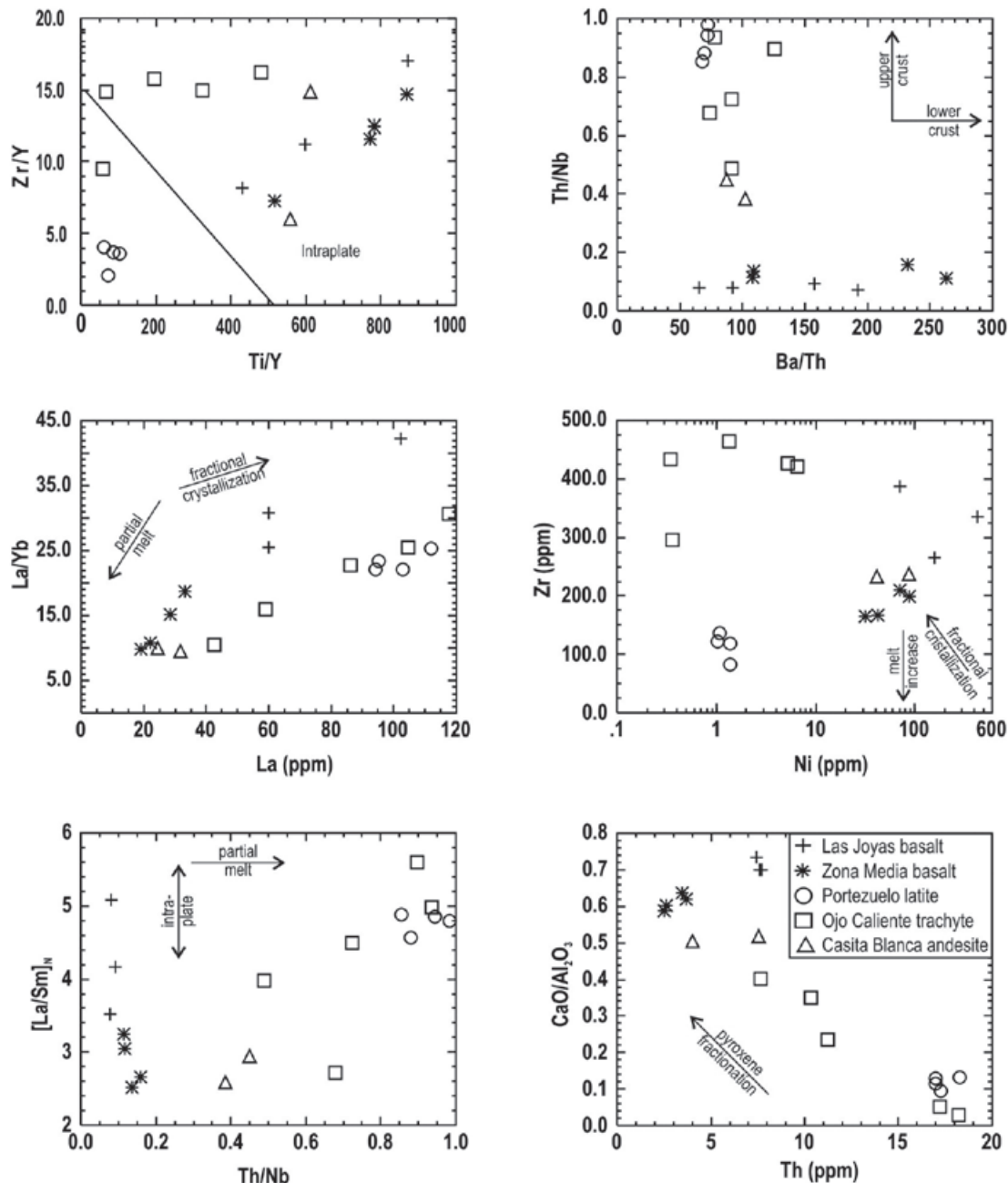


Figure 6. Rectangular plots for selected incompatible element concentrations and ratios; showing the features of intraplate volcanism (Zr/Y vs. Ti/Y; [La/SM]_n vs. La diagrams); or magma generation by AFC in the lower or upper crust (La/Yb vs. La; Zr vs. Ni diagrams). The CaO/Al₂O₃ vs. Th diagram displays features associated to partial melting following clinopyroxene depletion in the source (Luhr *et al.*, 1995).

patterns (Figure 5). These patterns are consistent with their derivation from a mantle source metasomatized by LILE- and LREE- rich hydrous fluids and/or magmas ascending from a subducted oceanic slab. The intermediate/evolved character of these lavas, their low MgO, Ni, Cr and Co contents, their negative Sr, Eu, Ti and P anomalies, as well as their

trends in Figure 6 incompatible element plots, are consistent with their derivation from mafic magmas through fractionation of a plagioclase – olivine – pyroxene – titanomagnetite – apatite phenocryst assemblage (Aranda-Gómez *et al.*, 2007; Aguillón-Robles *et al.*, 2009). However, the displays in Figure 6 plots suggests that their evolution was controlled by more complex

petrogenetic processes than closed-system fractional crystallization. Those can include assimilation coupled with fractional crystallization (AFC; DePaolo, 1981) or melting-assimilation-storage-homogenization (MASH; Hildreth and Moorbath, 1988), both of them involving the chemical contribution of the lower or upper continental crust (Medina-Romero *et al.*, 2005; Aguillón-Robles *et al.*, 2009).

Conclusions

Combined major and trace element data allow us to divide the five magmatic events which emplaced the volcanic fields of San Luis Potosí and Río Santa María from Eocene to Pleistocene into two groups. The three oldest ones, ranging in age from middle Eocene to late Oligocene, emplaced potassic calc-alkaline intermediate (andesitic) to evolved (trachytic and rhyolitic) lavas. These originated from subduction-related mafic magmas through open-system fractional crystallization coupled with assimilation and possibly melting of the continental crust. In addition, mixing with the magma chamber may have contributed to the genesis of dacitic and trachytic lavas extruded along the SLPVF and RSMVF (Portezuelo latite and Ojo Caliente trachyte; Aguillón-Robles *et al.*, 2009). Later, a fast extensional event formed a faulting pattern used for the ascent of magmas from the two youngest volcanic phases (Miocene and Quaternary). These emplaced mostly OIB-type subalkaline to alkaline basalt and basanites which derived from variable melting degrees of enriched mantle and experienced limited amounts of fractionation. The association between cortical extension and OIB-type intraplate magmatism is typical feature of the evolution of the Mesa Central of Mexico (Luhr *et al.*, 1994; Tual, 2010; Rodríguez-León, 2012).

Acknowledgments

We thank José Rafael Barboza-Gudiño, Director of the Instituto de Geología, at the Universidad Autónoma de San Luis Potosí for the logistical and financial support to carry out the fieldwork and chemical analyses in the laboratory; and two anonymous reviewers for their comments and suggestions that allowed us to improve the final version of this manuscript. We are grateful to Erasmo Mata-Martínez technician of the Instituto de Geología at UASLP, for preparing the samples used in this work. To Blanca Lizeth Tristán-Hernández by the english text suggestions.

Bibliography

Aguillón-Robles A., Aranda Gómez J.J., Solorio Munguía J.G., 1994, Geología y tectónica de un conjunto de domos riolíticos del Oligoceno

medio en el sur del Estado de San Luis Potosí, México. *Rev. Mex. Cienc. Geol.*, 11(1), 29-42.

Aguillón-Robles A., De la Huerta-Cobos M.L., Aranda Gómez J.J., 1997, Características geológicas de los domos félsicos del Campo Volcánico de San Luis Potosí. *Actas INAGEQ*, 3, 103-111.

Aguillón-Robles A., Rodríguez-Ríos R., Leroy J.L., Aranda Gómez J.J., Marín-Solis J.D., 1996, Geología y características geoquímicas del Centro Volcánico de Pinos, Zac. *Actas INAGEQ*, 2, 3-8.

Aguillón-Robles A., Tristán-González M., Aguirre-Díaz G.J., Bellon H., 2009, Syn-extensional intra-plate trachydacite-rhyolitic dome volcanism of the Mesa Central, southern Sierra Occidental volcanic province, Mexico. *J. Volcanol. Geother. Res.*, 187, 33-52.

Aguirre-Díaz G.J., Labarthe-Hernández G., 2003, Fissure ignimbrites: fissure-source origin for voluminous ignimbrites of the Sierra Madre Occidental and its relationship with Basin and Range faulting. *Geology*, 31, 773-776.

Almaguer-Rodríguez J.L., 2010, Estudio geoquímico de elementos traza en unidades volcánicas del CVSLP: método ICP-MS (validación del método): San Luis Potosí, México. Tesis Ingeniería Geológica, Facultad de Ingeniería, UASLP, 89 pp.

Aranda-Gómez J.J., Aranda-Gómez J.M., Nieto-Samaniego A.F., 1989, Consideraciones acerca de la evolución tectónica durante el Cenozoico de la Sierra de Guanajuato y la parte meridional de la Mesa Central, México, Méx. *Boletín Instituto de Geología, UNAM*, 8, 33-46.

Aranda-Gómez J.J., Luhr J.M., Housh T.B., Valdez-Moreno G., Chávez-Cabello G., 2005, El volcanismo tipo intraplaca del Cenozoico tradio en el centro y norte de México: una revisión. *Bol. Soc. Geol. Mex.*, 3, 187-226.

Aranda-Gómez J.J., Molina-Garza R., McDowell F.W., Vasallo-Morales L.F., Ortega-Rivera M.A., Solorio-Munguía J.G., Aguillón-Robles A., 2007, The relationships between volcanism and extension in the Mesa Central: the case of Pinos Zacatecas, Mexico. *Rev. Mex. Cienc. Geol.*, 24(2), 216-233.

Bryan S.E., Ewart A., Stephe C.J., Parianos J., Downes P.J., 2000, The Whitsunday Volcanic Province, central Queensland, Australia: Lithological and Stratigraphic investigations of a silicic-dominated large igneous province. *J. Volcanol. Geother. Res.*, 99, 55-78.

- Bryan S.E., Riley T.R., Jerram D.A., Leat P.T., Stephens C.J., 2002, Silicic volcanism: an undervalued component of large igneous province and volcanic rifted margins, en Menzies, M.A., Klemperer, S.L., Ebinger, C.J., Baker J. (eds.), *Magmatic Rifted Margins. Geol. Soc. Am. Spec. Paper*, 362, 99-120.
- Cameron K.L., Cameron C., Babgy W.C., Moll E.J., Drake R.E., 1980, Petrologic characteristics of mid-Tertiary volcanic suites, Chihuahua, Mexico. *Geology*, 8, 87-91.
- Cameron K.L., Hanson G.N., 1982, Rare earth element evidence concerning the origin of voluminous mid-Tertiary rhyolitic ignimbrites and related volcanic rocks, SMO, Chihuahua, Mexico. *Geochim. Cosmochim. Acta*, 46, 1489-1503.
- Cotten J., Le Dez A., Bau M., Caroff M., Maury R.C., Dulski P., Fourcade S., Bohn M., Brousse R., 1995, Origin of anomalous rare-earth element and yttrium enrichments in subaerially exposed basalts: evidence from French Polynesia. *Chem. Geology*, 119, 115-138.
- DePaolo D.J., 1981, Trace element and isotopic effects of combined wallrock assimilation and fractional crystallization. *Earth Planet. Sci. Lett.*, 53, 189-202.
- Ferrari L., López-Martínez M., Rosas-Elguera J., 2002, Ignimbrite flare up and deformation in the southern Sierra Madre Occidental, western Mexico: implications for the late subduction history of the Farallon plate. *Tectonics*, 21(4), 17-24, doi: 10.1029/2001TC001302.
- Ferrari L., Valencia-Moreno M., Bryan S., 2005, Magmatismo y tectónica de la Sierra Madre Occidental y su relación con la evolución de la margen occidental de Norteamérica. *Bol. Soc. Geol. Mex.*, LVII (3), 343-378.
- Graham I.J., Cole J.W., Briggs R.M., Gamble J.A., Smith I.E.M., 1995, Petrology and petrogenesis of volcanic rocks from Taupo Volcanic Zone: a review. *Jour. Volcanol. Geother. Res.*, 68, 59-87.
- Grassel P.C., 1979, The reconnaissance geology of the La Salitrera Mining District, San Luis Potosí, Mexico: Houston, U.S.A. Master of Sciences thesis, University of Texas, 251 pp.
- Hildreth W., Moorbath S., 1988, Crustal contributions to arc magmatism in the Andes of central Chile. *Contrib. Mineral. Petrol.*, 98, 455-489.
- Labarthe-Hernández G., Jiménez-López L.S., 1991, Cartografía geológica 1:50,000 de las hojas Cerrito de Bernal, Santo Domingo, El Estribo y La Herradura, Estado de San Luis Potosí. Instituto de Geología, UASLP, Folleto Técnico 113, 62 pp.
- Labarthe-Hernández G., Jiménez-López L.S., 1992, Características físicas y estructura de lavas e ignimbritas riolíticas en la Sierra de San Miguelito, S. L. P. Instituto de Geología, UASLP, Folleto Técnico 114, 31 pp.
- Labarthe-Hernández G., Tristán-González M., Aranda-Gómez J.J., 1982, Revisión estratigráfica del Cenozoico de la parte central del estado de San Luis Potosí. Instituto de Geología, UASLP, Folleto Técnico 85, 208 pp.
- Labarthe-Hernández G., Tristán-González M., Aguillón-Robles A., Jiménez-López L.S., Romero A., 1989, Cartografía geológica 1:50 000 de las hojas El Refugio y Mineral El Realito, estados de San Luis Potosí y Guanajuato. Instituto de Geología, UASLP, Folleto Técnico 112, 76 pp.
- Labarthe-Hernández G., Tristán-González M., Aguillón-Robles A., 1984, Cartografía Geológica 1:50,000 Hoja Salitrera, S.L.P. Instituto de Geología y Metalurgia, UASLP, Folleto Técnico 94, 85 pp.
- Le Bas M.J., Le Maitre R.W., Streckeisen A., Zanettin B., 1986, A chemical classification of volcanic rocks based on the total alkali-silica diagram. *Jour. Petrol.*, 27, 745-750.
- Lozano R., Bernal J.P., 2005, Characterization of a new set of eight geochemical reference materials for XRF major and trace element analysis. *Rev. Mex. Cienc. Geol.*, 22, 329-344.
- Luhr J.F., Aranda-Gómez J.J., Housh T.B., 1995, San Quintin Volcanic Field, Baja California Norte, México: Geology, Petrology and Geochemistry. *J. Geophys. Res.*, 100(B6), 10353-10380, doi: 10.1029/95JB00037.
- Luhr J.F., Aranda-Gómez J.J., Piere J.G., 1994, Spinel-Iherzolite-bearing Quaternary volcanic centers in San Luis Potosí, Mexico 1. *Geology, Mineralogy, and Petrology. J. Geophys. Res.*, 94(B6), 7916-7940, doi: 10.1029/JB094iB06p07916.
- Medina-Romero E., Aguillón-Robles A., Tristán-González M., Bellon H., Cotten J., 2005, Características geoquímicas del vulcanismo

- intermedio en la porción poniente del Campo Volcánico Río Santa María, en la región meridional del Estado de San Luis Potosí. *Actas INAGEQ*, 11, p. 108.
- Orozco-Esquivel M.T., Nieto-Samaniego A.F., Alaniz-Alvarez S.A., 2002, Origin of rhyolitic lavas in the Mesa Central, Mexico, by crustal melting related to extension. *Jour. Volcanol. Geother. Res.*, 118, 37-56.
- Peccerillo A., Taylor S.R., 1976, Geochemistry of Eocene calcalkaline volcanic rocks from the Kastamonu area, northern Turkey. *Contrib. Mineral. Petrol.*, 58, 63-81.
- Rodríguez-Ríos R., Aguillón-Robles A., Leroy J.L., 2007, Evolución petrológica y geoquímica de un complejo de domos topacíferos en el Campo Volcánico de San Luis Potosí (México). *Rev. Mex. Cienc. Geol.*, 24(3), 328-343.
- Rodríguez-Ríos R., Torres-Aguilera J.M., 2009, Evolución petrológica y geoquímica del vulcanismo bimodal oligocénico en el Campo Volcánico de San Luis Potosí (México). *Rev. Mex. Cienc. Geol.*, 26 (3), 658-673.
- Ruiz J., Patchett P.J., Arculus R.J., 1988, Nd-Sr isotope composition of lower crustal xenoliths: evidence for the origin of mid-Tertiary felsic volcanics in Mexico. *Contrib. Mineral. Petrol.*, 99, 36-43.
- Ruiz J., Patchett P.J., Arculus R.J., 1990, Reply to "Comments on Nd-Sr isotopic composition of lower crustal xenoliths: evidence for the origin of mid-Tertiary felsic volcanics in Mexico", by K.L. Cameron and J.V. Robinson. *Contrib. Mineral. Petrol.*, 104, 615-618.
- Sánchez-García A.C., 2009, Descripción de posibles fallas sismogénicas regionales en la Zona Media del Estado de San Luis Potosí, SLP. Tesis Ingeniería Geológica, Facultad de Ingeniería, UASLP, 80 pp.
- Smith R.D., Cameron K.L., McDowell F.W., Niemeyer S., Sampson D.E., 1996, Generation of voluminous silicic magmas and formation of mid-Cenozoic crust beneath north-central Mexico-evidence from ignimbrites, associated lavas, deep crustal granulites, and mantle pyroxenites. *Contrib. Mineral. Petrol.*, 123, 375-389.
- Sun S.S., McDonough W.F., 1989, Chemical and isotopic systematics of oceanic basalts: implications for mantle composition and processes; In Saunders, A.D.; Norry, M.J. (eds), 1989; Magmatism in the Ocean Basins. *Geol. Soc. Spec. Paper Publication*, 42, 313-345.
- Rodríguez-León L., 2012, Evolución geológica del Campo Volcánico Salinas - Villa de Ramos. Maestría en Ciencias en Geología Aplicada, UASLP, 76 pp.
- Thornton C.P., Tuttle O.F., 1960, Chemistry of igneous rocks. I. Differentiation index. *Am. Jour. Sci.*, 258, 664-684.
- Torres-Aguilera J.M., 2005, Caracterización petrográfica y geoquímica del vulcanismo bimodal en el semigraben de Bledos, en el Campo Volcánico de San Luis Potosí: San Luis Potosí, México. Tesis de Maestro en Ciencias, Facultad de Ingeniería, UASLP, 159 pp.
- Torres-Hernández J.R., Labarthe-Hernández G., Aguillón-Robles A., Gómez-Anguiano M., Mata-Segura J.L., 2006, The pyroclastic dikes of the Tertiary San Luis Potosí volcanic field: Implications on the emplacement of Panalillo ignimbrite. *Geofís. Intl.*, 45, 243-253.
- Tual T., 2010, Quelles sont les relations entre les volcanisme paléogène et néogène du Champ volcanique de San Luis Potosi (México). Mémoire Master 2; Institute Universitaire Européen de la Mer, Université de Bretagne Occidentale, Brest France, 57 pp.
- Tristán-González M., 1986, Estratigrafía y tectónica del Graben de Villa de Reyes, en los estados de San Luis Potosí y Guanajuato, México: San Luis Potosí, México. Instituto de Geología y Metalurgia, UASLP, Folleto Técnico 107, 91 pp.
- Tristán-González M., 1987, Cartografía geológica "Hoja Tierra Nueva", S.L.P., Esc. 1:50,000. Instituto de Geología, UASLP, Folleto Técnico 109, 103 pp.
- Tristán-González M., 2008, Evolución tectono-magmática durante el Paleógeno en la porción sur-oriental de la Mesa Central. Tesis Doctoral, Centro de Geociencias, UNAM, 207 pp.
- Tristán-González M., Labarthe-Hernández G., Aguillón-Robles A., Torres-Hernández J.R., Aguirre-Díaz G., 2006, Diques piroclásticos en fallas de extensión alimentadores de ignimbritas en el occidente del Campo Volcánico del Río Santa María, S.L.P. *GEOS*, 26, p. 163.
- Tristán-González M., Aguirre-Díaz J.G., Labarthe-Hernández G., Aguillón-Robles A., 2008, Tectono-volcanic control of fissure type vents for the 28 Ma Panalillo ignimbrite in the Villa de Reyes Graben, San Luis Potosí, Mexico. *Earth and Environmental Science*, 3, doi:10.1088/1755-1307/3/1/012026.

Tristán-González M., Aguillón-Robles A., Barboza-Gudiño J.R., Torres-Hernández J.R., Bellon H., López-Doncel R.A., Rodríguez-Ríos R., Labarthe-Hernández G., 2009a, Geocronología y distribución espacial del Campo Volcánico de San Luis Potosí. *Bol. Soc. Geol. Mex.*, 61(3), 287-303.

Tristán-González M., Aguirre-Díaz G.J., Labarthe-Hernández G., Torres-Hernández J.J., Bellon H., 2009b, Post-Laramide and pre-Basin and Range deformation and implications for Paleogene (55-25 Ma) volcanism in central Mexico: A geological basis for a volcano-tectonic stress model. *Tectonophysics*, 471, 136-152, doi: 10.1016/j.tecto.2008.12.021.

University of Arizona, 1997, Rock digestion: The University of Arizona: actualización 28 de abril de 1997, <https://sites.google.com/a/email.arizona.edu/ruizresearchgroup/misc-procedures/rock-digestion>.

Verma S.P., 1984, Sr and Nd isotopic evidence for petrogenesis of Mid-Tertiary felsic volcanism in the mineral district of Zacatecas, Zac. (Sierra Madre Occidental), Mexico. *Isotopic Geosciences*, 1, 37-53.

Verma S.P., Sotelo-Rodríguez Z.T., Torres-Alvarado I.S., 2002, SINCLAS: Standard Igneous Norm and Volcanic Rock Classification System. *Comput. Geosci.*, 28(5), 711-715.

Wilson M., 1989. Igneous petrogenesis. A global tectonic approach. Unwin Hyman, London, 466 p.